Characterisation of Liquid Distribution and Behaviour within Randomly Packed Columns using Electric Impedance Tomography

by

Johannes Hendrik Lamprecht

Dissertation presented for the Degree

of

DOCTOR OF PHILOSOPHY

(CHEMICAL ENGINEERING)

in the Faculty of Engineering
at Stellenbosch University

Supervisor

Professor A.J Burger

April 2022

DECLARATION

By submitting this thesis electronically, I declare that the entirety of the work contained therein is my own, original work, that I am the sole author thereof (save to the extent explicitly otherwise stated), that reproduction and publication thereof by Stellenbosch University will not infringe any third-party rights and that I have not previously in its entirety or in part submitted it for obtaining any qualification.

April 2022

ABSTRACT

The optimum design of column internals plays a prominent role in the economic viability of distillation setups, due to such internals' notable contribution to both operating and capital costs. Progression in both our understanding and characterisation of column internals is therefore paramount. Both hydrodynamic and kinetic characterisation methodologies consider the influence of the vapour-liquid interface, whether directly (effective interfacial area) or indirectly (pressure drop and liquid hold-up).

Most of the random packing literature, however, focuses on the evaluation of macro parameters (e.g. pressure drop, holdup, flow rates, packing dimensions and fluid physical properties), with notably less attention to the fluid behaviour at a micro level (e.g. droplet formation, distribution and rivulet formation). This limits the fundamental basis of the available models, introducing numerous regressed empirical constants. In other words, while modern random packing designs are strongly influenced by the optimisation of inter-packing droplet and rivulet formation, the available mathematical models lack predictive capabilities of such micro-behaviour.

Against this background, and in pursuit of a better understanding of fluid behaviour and distribution in random packing, an Electrical Impedance Tomography (EIT) measurement system was designed and constructed to visualize and quantify liquid distribution behaviour inside randomly packed columns. The EIT system was preferred to conventional X-Ray tomography, due to **a)** safety, **b)** cost-effectiveness, and **c)** simplicity, while it can be utilised for both conducting and non-conducting liquids.

The sensor of the EIT system consisted of a stainless-steel wire matrix, installed at a horizontal plane directly below 3m random packing in a 400mm diameter column. It provided 1369 measuring points, with measuring frequencies of 207 Hz and 21 Hz for conductive and non-conductive liquids, respectively. The data were processed using 2-D and 3-D image processing algorithms to enable quantification of individual liquid elements. The individual elements were evaluated based on their reconstructed volume, surface area and sphericity.

The experimental characterisations were used to evaluate the liquid distributions inside two types of industrial random packing, FlexiRing® and Intalox® Ultra, at sizes ranges between 1.5" to 2.5". The evaluations considered various liquid- and vapour loadings using both water and ethylene glycol to vary the liquid physical properties; water being electrically conductive and ethylene glycol being predominantly non-conductive.

The presented results show increased element uniformity in favour of the Intalox® Ultra throughout and illustrated the presence of a force-balance transition in the mechanism of liquid hold-up creation. This indicated the transition from conglomerating inter-packing liquid (IPL) streams, towards droplet-

creation. The onset of this transition was found distinctly related to the relative velocity profiles and vapour - liquid shear forces of the respective packings.

The contribution of droplets in the inter-packing space to the total vapour-liquid interfacial area was also evaluated. The Intalox® Ultra presented *ca* 17% and 9.4% increase in total reconstructed surface area for the respective 2" and 1.5" equivalent comparisons with FlexiRing® (for the air-water system). This confirmed the applicability of the EIT characterisation system for both hydrodynamic and kinetic prototyping.

Several novel contributions were developed in this work. These are:

[1] The development of a characterisation methodology based on EIT for better understanding of inter-packing liquid distributions.

[2] Novel experimental inter-packing distribution data for IPL element-volumes and -areas and their relation to:

   i. packing type,
   ii. liquid and vapour loadings, and
   iii. liquid physical properties.

[3] Presenting the existence of a packing-specific transitional point, based on liquid and vapour loadings, where the mechanism of liquid hold-up changes. This point marks the cross-over between the conglomeration of inter-packing liquid elements into streams, and their break-up/ redistribution into smaller elements. This alludes to a possible increase in interfacial turbulence (decreasing liquid phase resistance to mass transfer) while adding to the understanding of the pressure drop mechanisms in packed columns.

[4] Presenting the total IPL element-surface area as a comparative kinetic characterisation parameter for use in prototyping. This is posed to assist in the design of future packings, in finding the optimum packing area and structure to minimize entrainment and maximize efficiency.

OPSOMMING

Optimum ontwerp van interne strukture in kolomme is van kritiese belang vir die ekonomiese lewensvatbaarheid van distillasie opstellings, vanweë sodanige strukture se beduidende bydrae tot die kapitaal- en onderhoudskostes. Vooruitgang in die gepaardgaande karakterisering van interne strukture bly derhalwe steeds belangrik.

Die bestaande hidrodinamiese- en kinetiese karakteriseringsmetodologieë word beide beïnvloed deur vloeistof-gas interaksies. Hierdie interaksies word direk en indirek aangespreek deur die effektiewe area, drukval en vloeistof inhoud. Die bestaande literatuur rakende ongeordende pakking fokus egter grotendeels op makro- of oorkoepelende eienskappe (totale effektiewe area, drukval en die totale vloeistof inhoud), met aansienlik minder navorsing wat die uitwerking van druppel-formasie en druppel-verspreidings beskou. Die tekort aan genoegsame data rakende hierdie verspreidings beperk dus fundamentele modellering en noodsaak die gebruik van empiriese korrelasies.

Teen hierdie agtergrond, en in 'n poging om die vloeistofgedrag en -verspreiding in ongeordende pakking beter te verstaan, is 'n Elektriese Impedansie Tomografie (EIT) meetsisteem ontwerp en gebou om die vloeistofverspreidings in die tussen-spasies van ongeordende pakking te visualiseer en te karakteriseer. Die EIT sisteem bied die voordeel van **a)** veiligheid, **b)** koste-effektiwiteit en **c)** eenvoud bo die bestaande X-straal metodes, en is toepasbaar op vloeistowwe wat onderskeidelik elektries-geleidend en nie-geleidend is.

Die sensor van die EIT sisteem het bestaan uit 'n vlekvrye staal draadmatriks, horisontaal geïnstalleer in 'n 400mm deursnit kolom en direk onder 'n gepakte hoogte van 3 m. Die matriks het beskik oor 1369 meetpunte, met meet-frekwensies van 207 Hz en 21 Hz vir geleidende en nie-geleidende vloeistowwe onderskeidelik. Die metings is verwerk met gevorderde 2-D en 3-D beeldverwerking algoritmes, waarvolgens die individuele vloeistof elemente gekarakteriseer is volgens hul volume, oppervlak area en sferisiteit.

Die eksperimentele karakterisering van vloeistof-druppel verspreidings in ondersoek binne industriële FlexiRing® en Intalox® Ultra pakkings met groottes van 1.5“ tot 2.5“. Die evaluasie het vloeistowwe met veranderende fisiese eienskappe en lug beskou, teen verskillende vloeitempo's. Die vloeistowwe was onder meer elektries-geleidende water en nie-geleidende etileen-glikol.

Die resultate toon 'n aansienlike verbeterings in druppel uniformiteit ten gunste van die Intalox® Ultra en illustreer ook die teenwoordigheid van 'n kragte-balans oorgang wat die volumetriese vloeistofinhoud beïnvloed. Hierdie oorgang behels 'n verandering vanaf druppel-samesmelting tot opbreek en verdeling, en is afhanklik van die snelheidsprofiel en sleurkragte.

Die bydrae van die tussen-pakking druppels tot die totale damp-vloeistof oppervlakarea is ook ondersoek, met die Intalox® Ultra wat onderskeidelik 17% en 9.4% meer oppervlakarea toon teenoor die 2” en 1.5” FlexiRing® (vir die lug-water sisteem). Hierdie dien as bevestiging van die bruikbaarheid van die EIT sisteem vir beide hidrodinamiese en kinetiese prototipe-ontwikkeling.

Die nuwe bydraes, soos ontwikkel in hierdie werk, word gelys as:

[1] Die ontwikkeling van ’n EIT karakteriseringsmetode vir tussen-pakking vloeistof verspreidings.

[2] Tussen-pakking vloeistof-element verspreidings i.t.v. oppervlak area en volume en hul verband met:

i. tipe pakking,
ii. vloeistof- en gasvloeitempo’s, en
iii. vloeistof fisiese eienskappe.

[3] Bewyse rakende die bestaan van ’n pakking-spesifieke oorgangspunt, waar die meganisme van volumetriese vloeistofinhoud verander vanaf druppel-samesmelting tot opbreek en verdeling. Hierdie fenomeen dui op ’n moontlike verandering in tussenvlak turbulensie terwyl dit ook bydra tot ’n beter verstaan van die meganisme van drukval in gepaktye kolomme.

[4] Die voorstelling van die totale tussen-pakking area van vloeistof-elemente as ’n kinetiese parameter vir gebruik in prototipe ontwikkeling. Die metode word voorgestel om te help met die ontwerp van toekomstige pakkings, deur die optimum pakkingsarea en -struktuur te identifiseer om meesleuring te minimeer en effektiwiteit te maksimeer.

ACKNOWLEDGEMENTS

I could not have completed this project without the assistance, encouragement and support of my family, friends and colleagues. I would like to thank and honour the following people:

My supervisor Prof A.J. Burger: Thank you for taking the red pill with me and wandering down the rabbit hole. We definitely took the road less travelled.

The workshop staff at Process Engineering, Mr. Jos Weerdenberg and Mr Anton Cordier, Mr. Alvin Petersen and Mr. Oliver Jooste: Thank you for teaching me a wide variety of technical skills. I will always cherish the time you all invested in me.

Dr. Herman Franken, Nardus Uys, Jason Smit: For sharing your endless technical expertise with me, when I was not yet worthy. It remains a debt that I can never repay.

My fiancé, Danielle de Klerk: For your love and encouragement and everything in between. For the late nights and comfort when things tough. YOU remain the best thing to have come from my time at Stellenbosch. I could never have completed this journey without you.

To my parents: Thank you for your support and encouragement throughout my life. “If I have seen further than others, it is because I was standing on the shoulders of Giants” Isaac Newton

Then lastly, to my Heavenly Father: Thank you for blessing me with these people and the privilege to pursue this endeavour. “The things that I am afraid of are afraid of you”.

TABLE OF CONTENTS

Abstract ..... **ii**

Opsomming ..... **iv**

Table of Contents ..... **vii**

List of Figures ..... **xii**

List of Tables ..... **xxv**

Glossary ..... **xxvi**

Column Flow Definitions xxx

Greek Symbols xxx

Dimensionless Numbers xxx

1. Introduction **1**

1.1 Problem Statement 1

1.2 Introduction to Flow Imaging in Columns 4

1.3 The Link Between Kinetics, Hydrodynamics and Tomography 5

1.4 Aims and Objectives 6

1.5 Scope and Limitations 7

1.5.1 Random Packing Considered 8

1.5.2 Vapour-liquid Systems Considered 8

1.5.3 Range of Operation 8

1.5.4 Limitations 8

1.6 Novel Contributions 9

1.7 Foreword on Electronic Circuitry Development and Image Processing 9

2. Characterisation of Column Internals – An Overview **10**

2.1 Column-Internals 10

2.1.1 Tray Columns 10

2.1.2 Packed Columns 11

2.2 Column-Internal Characterisation 13

2.2.1 Kinetic Characterisation 15

2.2.2 Hydrodynamic Characterisation 18

3. Multiphase Flow Imaging 27

3.1 Vapour-Liquid Flow Patterns 27

3.2 Multiphase Flow Measurement 29

3.2.1 Phase Fraction Measurement 29

3.2.2 Tomographic Imaging of Multiphase Flow 31

3.3 X-Ray Imaging in Columns 33

3.4 Basics of Electrical Impedance 33

3.4.1 Electrical Resistance 35

3.4.2 Electrical Reactance 36

3.4.3 Significance of Impedance Measurements 38

3.5 Electrical Impedance Tomography (EIT) in Chemical Engineering 39

3.6 Electrical Tomography Imaging in Columns 40

3.7 Improving Multiphase Measurements for Column-Internals 40

4. Development of Electrical and Electronic Equipment 43

4.1 Method of Impedance Measurement: Auto Balancing Bridge 44

4.2 Circuitry Description and Design 47

4.2.1 Proof of Concept 47

4.2.2 Small Scale Modular Design (8x8 Modular Design) 57

4.2.3 Pilot-scale Circuitry 65

5. Mechanical Design and Experimental Setup 72

5.1 Wire-Mesh Grid Design for EIT Sensing 72

5.2 Pilot Plant Layout and Operation 78

5.2.1 Process Flow 79

5.2.2 Component Choices 80

5.2.3 Random Packing 81

5.2.4 Testing Procedure 82

6. Data and Image Processing 84

6.1 Image Processing Methodology 84

6.1.1 Block 3.1: Import to PC 85

6.1.2 Block 3.2: Combining Text files 85
6.1.3 Block 3.3: Matrix Creation 85
6.1.4 Block 3.4: Matrix Manipulation 86
6.1.5 Block 3.5: Phase Distribution to Evaluate Liquid Hold-up 87
6.1.6 Block 3.6: 3D Image Processing 88
6.1.7 Block 3.7 & 3.8: Distribution Plots 89
6.2 Generated Outputs and Definitions 89
6.3 Assumptions & Limitations 90
7. Verification of Equipment and Methods 92
7.1 Method Verification and Mesh-Grid Validation using Pressure Drop 92
7.2 Liquid Hold-up vs Element Liquid Hold-up 94
7.2.1 Conclusion on Hold-up Validation 97
7.3 Repeatability 98
7.4 Bimodal Comparison 99
7.5 Grid Evaluation and Validation 100
7.6 Hydrodynamic Characterisation of Wall-Effects 102
7.7 Maldistribution Evaluation 104
7.7.1 Liquid and Vapour Loadings 105
7.7.2 Packing type 108
7.8 Discussion of Additional Assumptions 110
8. Final Experimental Results 112
8.1 Foreword 113
8.2 Hydraulic characterisation through tomography 113
8.2.1 Cumulative IPL element-volume Comparison without Vapour 115
8.2.2 Effect of Vapour Loading on Cumulative IPL element-volume 125
8.2.3 Cumulative IPL Element-surface Area Comparison 130
8.3 Mass Transfer Implication 132
8.4 Industrial Significance 136
9. Conclusion 137

9.1 Novel Contributions 139

9.2 Recommendation for Improvements to the EIT System: 139

10. References 140

11. Appendix A: Packed Column 11-153

11.1 Experimental setup accuracies 11-153

11.2 Experimental Procedure 11-153

11.2.1 Liquid Loadings 11-153

11.2.2 Packing Loadings 11-153

11.2.3 EIT Calibrations 11-154

11.2.4 Start-up 11-154

11.2.5 Experimental 11-154

12. Appendix B: Electronics 12-155

12.1 PCB Testing 12-159

12.2 Circuit Linearity 12-161

12.3 Grid Testing 12-162

12.4 Wire-mesh Explanation 12-163

12.5 Power Delivery Problems 12-164

13. Appendix C: Computational 13-165

13.1 Matlab Version 13-165

13.2 Computational requirements 13-165

14. Appendix D Graphical Results 14-166

14.1 Liquid Hold-up 14-166

14.1.1 Air/Water 14-166

14.1.2 Air/Ethylene Glycol 14-169

14.2 Volume based CDF: Effects of Vapour 14-170

14.2.1 2.5” Intalox® Ultra (O) 14-170

14.3 Area based CDF 14-171

14.3.1 IPL element-surface area: Water without vapour 14-171

14.3.2 Water: 1.5” FlexiRing® and Intalox® Ultra A 14-172

14.3.3 Water: 2” FlexiRing® and Intalox® Ultra L 14-173
14.3.4 Characterisation based on varying packing size: Water 14-174
14.3.5 IPL element-surface area: Ethylene Glycol 14-175
14.3.6 Ethylene Glycol: 2” FlexiRing® and Intalox® Ultra L 14-176
14.4 IPL Element-Surface Area-CDF: Effects of Vapour 14-177
14.4.1 Air/Water: 2” FlexiRing® and Intalox® Ultra L 14-177
14.4.2 Air/Water: 1.5” FlexiRing® and Intalox® Ultra A 14-179
14.4.3 Air/Water: 2.5” Intalox® Ultra (O) 14-180
14.4.4 Ethylene Glycol/Air:2” FlexiRing® and Intalox® Ultra L 14-181
14.5 Number based CDF 14-183
14.5.1 IPL element-volume 14-183
14.5.2 IPL element-surface area 14-189
14.6 Probability Density Functions 14-195
14.6.1 Element Volume: Water without vapour 14-195
14.7 Distribution analysis 14-200
14.7.1 Water: 2” FlexiRing® 14-200
14.7.2 Water: Intalox® Ultra L 14-201
14.7.3 Water: Intalox® Ultra A 14-202
14.7.4 Water: 1.5” FlexiRing® 14-203
14.8 Appendix E :Three-dimensional Interactive Projections 14-204
14.8.1 Liquid distributor 14-204
14.8.2 Full Column 14-205
14.8.3 Wire-mesh grid 14-206

LIST OF FIGURES

Figure 1.1: The Ratio of effective interfacial area to apparent interfacial area for A) Intalox® Ultra L and O at F_s =1.8 $(m.s^{-1})\cdot(kg.m^{-3})^{0.5}$ [3], and B) Raschig Super Ring® [4]..... 3

Figure 1.2 : A computed tomography illustration, where measurements are taken alternating the activated node (1-8) while measuring continuously across the other nodes (1-8). The image then reconstructed using specialised algorithms. 4

Figure 1.3: A schematic of a conventional wire-mesh sensor depicting two layers of perpendicular electrodes (X and Y), separated in the Z-direction. The wire-mesh sensor thereby provides measurement at each of the perpendicular points where the X and Y electrodes cross..... 5

Figure 1.4: A schematic of the link between hydrodynamics, kinetics, and tomography within packed columns. 6

Figure 2.1: Roadmap of the column internal literature section of this dissertation..... 14

Figure 2.2: Pressure drop of 1.5" FlexiRing® using an air / water system as reference. The data have been obtained from Lamprecht [2] 19

Figure 2.3: Liquid Hold-up data for 1.5" FlexiRing® using an air / water system as reference. The data were reproduced from Lamprecht [2]. 20

Figure 3.1: Schematic of the multiphase flow regimes present in pipes. A) Vertical B) Horizontal. Redrawn from Da Silva [57] 28

Figure 3.2:A radiation attenuation depiction showing cross-sectional phase area measurements. 30

Figure 3.3: A schematic of conventionally computed tomography systems used in XT-scan and X-Ray systems [138, 11]. The signal emitter is shown rotating to evaluate the system from all angles. The data from the various angles are then combined into a single 2D image. 31

Figure 3.4 Electrical Impedance vector diagram [64] showing the contributions of both the real and imaginary constituents of electrical flow. The real component is analogous to conventional electrical resistance and the imaginary to the contribution of capacitance and inductance. 35

Figure 3.5: The graphical illustration of a conductivity measurement cell where the evaluated resistance is a function of the area of the fluid contacting the electrodes. 36

Figure 3.6:An electrical circuit depicted a capacitor [14]. 37

Figure 3.7: An electrical circuit depicted an inductor [14]. 38

Figure 3.8: Categories of description and discussion in this work related to the development of the EIT sensor and data-processing systems. 42

Figure 4.1: An electrical drawing depicting impedance measurement using an auto-balancing bridge. 44

Figure 4.2: Effect of changes in capacitance on the frequency response of an auto-balancing bridge. 46

Figure 4.3: Effect of changes in resistance on the frequency response of an auto-balancing bridge. 46

Figure 4.4: A summary for the electrical development methodology. This methodology progresses from first principal basic engineering to the design and implantation. 47

Figure 4.5: OpenEMS model showing the expected voltage across a liquid element (water droplet). The voltage measured by the measurement electrode was used to evaluate the feasible ranges of capacitance and resistance that the sensor was likely to encounter. 48

Figure 4.6: OpenEMS model predicting capacitance based on both relative permittivity and the cross-sectional radius of a liquid droplet. 50

Figure 4.7: Response of disturbance cross-sectional diameter on capacitance. The graph depicts a linear tend thereby suggesting that the liquid cross-section can be correlated based on a capacitance reading.....50

Figure 4.8: Voltage distribution model from OpenEMS considering the voltages experienced by other electrodes not in contact with the liquid droplet. 51

Figure 4.9 : Schematic of the LTspice XVII model, with various blocks numbered to guide discussions in this section of the thesis. The model was solved in the Laplace domain 53

Figure 4.10: The single-channel experimental circuitry used to evaluate the components and pre-feasibility of the method..... 55

Figure 4.11: Conductivity readings from prototype sensor based on the measured voltage output. 56

Figure 4.12 Capacitance readings from prototype sensor based on the measured voltage output. 56

Figure 4.13 : Small scale schematic of the wire-mesh EIT system. Block 2.4 refers to the circuitry developed in section 4.2.1.2, while the other blocks depict the peripherals used to log the data and control the various sensing channels. 58

Figure 4.14: Effect of Sampling speed on the accurate sampling a wave; A) sample at 10kHz wave at 148kHz; B) sample 10Khz wave at 30kHz..... 60

Figure 4.15: A) Auto-balancing bridge PCB, and B) Logging PCB, C) Small-scale wire mesh grid; Electrode spacing =10mm; Wire diameter 0.625mm. Gap between electrode planes 2mm 62

Figure 4.16: Signal response of air, i.e., no liquid on the grid. On the small-scale wire mesh grid; Electrode spacing =10mm; Wire diameter 0.625mm. Gap between electrode planes 2mm. 63

Figure 4.17: Signal response 100k resistance and 1pF capacitor in parallel. The response shows little variation in the readings and depicts long plateaus which are key for stability..... 63

Figure 4.18: Signal response of water using A) conductivity; B) capacitance. The respective measurements were taken high and low pass filters and consequently only depict the values for capacitance and resistance. 64

Figure 4.19: Pilot-scale sensor circuitry where M1 refers to the “master node” that controls the cycle times of the other nodes i.e. “slave nodes” (S1-S4) 66

Figure 4.20: Pseudo droplet calibration blocks showing point evaluations for a variety of simulated droplet sizes..... 67

Figure 4.21: Cross sectional diameter-based calibrations using the millivolts recorded on the sensor for A) the capacitance circuitry and B) the conductivity circuitry. 68

Figure 4.22: Arduino code flow diagram presenting the sampling logic. 69

Figure 5.1: Schematic of Wire-mesh grid developed in this chapter. The schematic shows toe perpendicular planes of electrodes (Y&X). The separate planes are kept from touching by separating them by 2mm. The “gap” at the crossing points thereby creates the effective sampling zone. 73

Figure 5.2: Wire mesh grid design: A) Bottom view, and B) Top view. The schematic depicts the tensioning system and PCB’s for simplified connections. 74

Figure 5.3: POM 10mm deformation model as projected by Autodesk Inventor. The Red indicating areas of maximum deformation under tensioning stress. 75

Figure 5.4: Mesh-grid spacing at the bottom of the distillation column showing the detection area. 75

Figure 5.5: Image of sensor grid installation with the Sinusoidal packing support grid used by Lamprecht [2] and Minne [5]. This support grid was later replaced with a woven support grid. 76

Figure 5.6: Image of sensor grid installation at the bottom of the distillation column. The electrodes are illustrated moving through the flange and onto the PCB’s. The G-claps are sued to seal the column with compression force. 76

Figure 5.7: Packed column experimental setup at Stellenbosch University..... 78

Figure 6.1: Flow diagram of post-processing and imaging. The diagram is explaining using the block approach suggested in Section 1.7. 84

Figure 6.2: Three-dimensional binary matrix depicting a matrix of voltage values over time. 86

Figure 6.3: Expanded 3D matrix. The matrix depicts the cross-sectional liquid comprised area over time. 86

Figure 6.4: Detection range of the of the mesh-matrix within the column. The detection area is 380 x 380mm square block within a 396mm internal diameter column. 87

Figure 6.5:Graphical representation of the 3D matrix of inter-packing liquid elements. Top isometric view. The elongated elements depicted stream-like behaviour and the “shorter” elements depicting droplets 88

Figure 6.6: A) Cumulative IPL element-volume distributions using air / water at zero vapour loading on Intalox® Ultra size A; B) Cumulative element-surface area distributions using air / water at zero vapour loading on Intalox® Ultra size A; 89

Figure 7.1 : Validation and verification roadmap for the succeeding section, illustrating the respective sections and their focus. 92

Figure 7.2: Comparison between the dry-bed pressure drop data from this study, and that of Lamprecht [2].The data were collected on 1.5” FlexiRing® and compared to 50mm Rings using the Billet model [38] 93

Figure 7.3 : Comparison between the irrigated pressure drop data from this study, and that of Lamprecht [2] . The data were collected on 1.5” FlexiRing® All loadings in $m^3/m^2/h$ 93

Figure 7.4: Intalox® Ultra size O , literature liquid hold-up vs element-liquid hold-up from this study; air / ethylene glycol;A)6 $m^3.m^{-2}.h^{-1}$; B) 37 $m^3.m^{-2}.h^{-1}$; C) 73 $m^3.m^{-2}.h^{-1}$; D) 98 $m^3.m^{-2}.h^{-1}$; E) 122 $m^3.m^{-2}.h^{-1}$ 95

Figure 7.5 : Comparison of 1.5” FlexiRing®, literature liquid hold-up vs element-liquid hold-up from this study; water/air; A) 6 $m^3.m^{-2}.h^{-1}$; B) 37 $m^3.m^{-2}.h^{-1}$; C) 73 $m^3.m^{-2}.h^{-1}$; D) 98 $m^3.m^{-2}.h^{-1}$; E) 122 $m^3.m^{-2}.h^{-1}$ 96

Figure 7.6: Intalox® Ultra size O liquid hold-up vs element liquid hold-up; water/air; 122 $m^3.m^{-2}.h^{-1}$. 98

Figure 7.7: Repeatability of 3D- image processing using a cumulative IPL element-volume analysis; air / water 99

Figure 7.8: Comparison of the element liquid hold-up from capacitance and conductivity of Intalox® Ultra size O using the air / water system. The liquid loading L is depicted in $m^3/m^2/hr$ 100

Figure 7.9: IPL element-volume recreation: water / air 101

Figure 7.10: IPL element-volume recreation: ethylene glycol / air 101

Figure 7.11: Wall-effect evaluated by grouping the total IPL liquid volume collected in concentric circles throughout the column. 102

Figure 7.12: Wall-effect evaluation using element liquid hold-up; $F_s = 0$ $(m.s^{-1})\cdot(kg.m^{-3})^{0.5}$ 103

Figure 7.13: Ratio of average- to perimeter element liquid hold-up 103

Figure 7.14: Maldistribution at 6 $m^3.m^{-2}.h^{-1}$ compared to the liquid distributor; Normalized liquid flow; Maximum total flow =1. 105

Figure 7.15: Normalized volume distribution of Intalox® Ultra size O evaluated with air / water at 37 $m^3.m^{-2}.h^{-1}$. A) F_s =0 $(m.s^{-1})\cdot(kg.m^{-3})^{0.5}$; B) F_s = 2.4$(m.s^{-1})\cdot(kg.m^{-3})^{0.5}$; C) F_s =3.1 $(m.s^{-1})\cdot(kg.m^{-3})^{0.5}$ 106

Figure 7.16 : HETP comparison of 1.5" and 2.5" Intalox® Ultra on a liquid phase mass transfer limited system – The Aqueous desorption of isobutyl acetate into air; Recreated from Lamprecht [17] . A) 23 m3/m2/hr B) 36 m3/m2/hr 107

Figure 7.17: Normalized Distribution of Intalox® Ultra size O evaluated with air / water at 98 $m^3.m^{-2}.h^{-1}$: A) F_s =0 $(m.s^{-1})\cdot(kg.m^{-3})^{0.5}$; B) F_s = 2.1 $(m.s^{-1})\cdot(kg.m^{-3})^{0.5}$; C) F_s =3.7 $(m.s^{-1})\cdot(kg.m^{-3})^{0.5}$; D) F_s =3.2 $(m.s^{-1})\cdot(kg.m^{-3})^{0.5}$ 108

Figure 7.18: Normalized distribution of air / water at 37 $m^3.m^{-2}.h^{-1}$. F_s =0 $(m.s^{-1})\cdot(kg.m^{-3})^{0.5}$; A) 2" FlexiRing® ; B) Intalox® Ultra size L. 109

Figure 7.19: Parentage distribution of air / water at 37 $m^3.m^{-2}.h^{-1}$. F_s =0 $(m.s^{-1})\cdot(kg.m^{-3})^{0.5}$; A) 2" FlexiRing® ; B) Intalox® Ultra size L. 109

Figure 8.1: Summary of the structure for IPL element-volume results presented within this chapter 115

Figure 8.2: Cumulative IPL element-volume distributions using air / water at zero vapour loading A) Intalox® Ultra size A; B) 1.5" FlexiRing®; C) Intalox® Ultra size L; D) 2" FlexiRing® ; E) Intalox® Ultra size O; 116

Figure 8.3: Cumulative IPL element-volume distributions using air / water at zero vapour loading considering Intalox® Ultra size A vs. 1.5" FlexiRing® @ A) 37 $m^3.m^{-2}.h^{-1}$; B) 73$m^3.m^{-2}.h^{-1}$; C) 98$m^3.m^{-2}.h^{-1}$; D) 122$m^3.m^{-2}.h^{-1}$;..... 117

Figure 8.4: Cumulative IPL element-volume distributions using air / water at zero vapour loading considering Intalox® Ultra size L vs. 2" FlexiRing® @ A) 6$m^3.m^{-2}.h^{-1}$; B) 37 $m^3.m^{-2}.h^{-1}$; C) 73$m^3.m^{-2}.h^{-1}$; D) 98$m^3.m^{-2}.h^{-1}$; E) 122$m^3.m^{-2}.h^{-1}$; 118

Figure 8.5 : Cumulative element-volume distributions using water at zero vapour loading; Intalox® Ultra size L; differential number-based; A) CDF; B) PDF 119

Figure 8.6: Cumulative IPL element-volume distributions using water at zero vapour loading : A) Intalox® Ultra size A and L @ 37 $m^3.m^{-2}.h^{-1}$; B) 1.5" &2" FlexiRing® @ 37 $m^3.m^{-2}.h^{-1}$; C) Intalox® Ultra size A and L @ 98 $m^3.m^{-2}.h^{-1}$; D) 1.5" &2" FlexiRing® @ 98 $m^3.m^{-2}.h^{-1}$; E) Intalox® Ultra sizes A, L and O @ 37 $m^3.m^{-2}.h^{-1}$; F) Intalox® Ultra sizes A, L and O @ 98 $m^3.m^{-2}.h^{-1}$; 120

Figure 8.7 : Cumulative IPL element-volume distributions using air / ethylene glycol at zero vapour loading; A) Intalox® Ultra size L; B) 2" FlexiRing®; C) Intalox® Ultra size O; D) liquid distribution @ 6$m^3.m^{-2}.h^{-1}$;..... 122

Figure 8.8 : Cumulative IPL element-volume distributions using air / ethylene glycol at zero vapour loading considering Intalox® Ultra size L vs. 2" FlexiRing® @ A) 37 $m^3.m^{-2}.h^{-1}$; B) 73$m^3.m^{-2}.h^{-1}$; C) 98$m^3.m^{-2}.h^{-1}$; D) 122$m^3.m^{-2}.h^{-1}$; 123

Figure 8.9: Cumulative IPL element-volume distributions using ethylene-glycol at zero vapour loading A) Intalox® Ultra size L and O @ 37 $m^3.m^{-2}.h^{-1}$; B) Intalox® Ultra size L and O @ 98 $m^3.m^{-2}.h^{-1}$; C) Intalox® Ultra size L and O @ 122$m^3.m^{-2}.h^{-1}$;..... 124

Figure 8.10 : Cumulative IPL element-volume distributions for air water; A) Intalox® Ultra size L @ 37 $m^3.m^{-2}.h^{-1}$; B) 2" FlexiRing® @ 37 $m^3.m^{-2}.h^{-1}$; 125

Figure 8.11: Figure 8.10 continues ; C) Intalox® Ultra size L @ 73 $m^3.m^{-2}.h^{-1}$; D) 2" FlexiRing® @ 73 $m^3.m^{-2}.h^{-1}$; E) Intalox® Ultra size L @ 98 $m^3.m^{-2}.h^{-1}$; F) 2" FlexiRing® @ 98 $m^3.m^{-2}.h^{-1}$; G) Intalox® Ultra size L @ 122 $m^3.m^{-2}.h^{-1}$; H) 2" FlexiRing® @ 122 $m^3.m^{-2}.h^{-1}$; 126

Figure 8.12 : Cumulative IPL element-volume distributions for air / water; A) Intalox® Ultra size A @ 37 $m^3.m^{-2}.h^{-1}$; B) 1.5" FlexiRing® @ 37 $m^3.m^{-2}.h^{-1}$; C) Intalox® Ultra size A@ 73 $m^3.m^{-2}.h^{-1}$; D) 1.5" FlexiRing® @ 73 $m^3.m^{-2}.h^{-1}$; E) Intalox® Ultra size A@ 98 $m^3.m^{-2}.h^{-1}$; F) 1.5" FlexiRing® @ 98$m^3.m^{-2}.h^{-1}$; 127

Figure 8.13 : Figure 8.12 Continues; G) Intalox® Ultra size A @ 122 $m^3.m^{-2}.h^{-1}$; H) 1.5" FlexiRing® @ 122$m^3.m^{-2}.h^{-1}$. 128

Figure 8.14: Cumulative IPL element-volume distributions for air / ethylene glycol; A) Intalox® Ultra size L @ 37 $m^3.m^{-2}.h^{-1}$; B) 2" FlexiRing® @ 37 $m^3.m^{-2}.h^{-1}$; C) Intalox® Ultra size L@ 73 $m^3.m^{-2}.h^{-1}$; D) 2" FlexiRing® @ 73 $m^3.m^{-2}.h^{-1}$; E) Intalox® Ultra size L@ 98 $m^3.m^{-2}.h^{-1}$; F) 2" FlexiRing® @ 98$m^3.m^{-2}.h^{-1}$;..... 129

Figure 8.15 : Figure 8.14 Continues; G) Intalox® Ultra size L@ 122 $m^3.m^{-2}.h^{-1}$; H) 2" FlexiRing® @ 122$m^3.m^{-2}.h^{-1}$. 130

Figure 8.16:Total IPL element-surface area ratio for air / water: Intalox® Ultra size L and 2" FlexiRing® @ F_s =1.8 $(m.s^{-1})\cdot(kg.m^{-3})^{0.5}$; Intalox® Ultra size A and 1.5" FlexiRing® at F_s =1 $(m.s^{-1})\cdot(kg.m^{-3})^{0.5}$;..... 134

Figure 8.17: Total IPL element-surface area ratio for water: Intalox® Ultra size O and 2" FlexiRing® at F_s =1.8 $(m.s^{-1})\cdot(kg.m^{-3})^{0.5}$;..... 135

Figure 8.18: Total IPL element-surface area comparison; air / water Intalox® Ultra size L and 2" FlexiRing® @ F_s =1.8 $(m.s^{-1})\cdot(kg.m^{-3})^{0.5}$; ethylene glycol Intalox® Ultra size L and 2" FlexiRing® at F_s =0.8 $(m.s^{-1})\cdot(kg.m^{-3})^{0.5}$..... 136

Figure 12.1 : Main motherboard PCB 12-155

Figure 12.2: Slave motherboard PCB..... 12-156

Figure 12.3: Auto-balancing bridge PCB 12-157

Figure 12.4: Arduino PCB 12-158

Figure 12.5: De-mux timing 12-159

Figure 12.6: Mux- switching time 12-159

Figure 12.7: Response time of capacitance circuitry 12-160

Figure 12.8: De-loading time of capacitance circuitry 12-160

Figure 12.9: Capacitance linear voltage response to input voltage. 12-161

Figure 12.10: Conductivity linear voltage response to varying input voltage 12-161

Figure 12.11: Grid harmonics without excitation signal. F_v = 1.8 and L=98$m^3m^{-2}h^{-1}$ 12-162

Figure 12.12: Wire-mesh grid 12-163

Figure 12.13: Impedance 12-164

Figure 14.1: Intalox® Ultra size O liquid holdup vs element liquid holdup; water/air; 37 $m^3m^{-2}h^{-1}$. 14-166

Figure 14.2: Intalox® Ultra size O liquid holdup vs element liquid holdup; water/air; 98 $m^3m^{-2}h^{-1}$; 14-166

Figure 14.3: Intalox® Ultra size O liquid holdup vs element liquid holdup; water/air; 122 $m^3m^{-2}h^{-1}$; 14-167

Figure 14.4: Intalox® Ultra L; element liquid hold-up; air / water 14-167

Figure 14.5 : 2” FlexiRing® element liquid hold-up; air / water 14-168

Figure 14.6: Intalox® Ultra A; element liquid hold-up; air / water 14-168

Figure 14.7: Intalox® Ultra L element liquid hold-up; air/ ethylene glycol 14-169

Figure 14.8: 2” FlexiRing®; element liquid hold-up; air/ ethylene glycol 14-169

Figure 14.9: Cumulative IPL element-volume distributions using air / water and Intalox® Ultra size O A) 37 $m^3.m^{-2}.h^{-1}$; B) 73 $m^3.m^{-2}.h^{-1}$; C) 122 $m^3.m^{-2}.h^{-1}$; 14-170

Figure 14.10 : Cumulative IPL element-surface area distributions using air / water at zero vapour loading A) Intalox® Ultra size A; B) 1.5” FlexiRing®; C) Intalox® Ultra size L; D) 2” FlexiRing® ; e) Intalox® Ultra size O; 14-171

Figure 14.11 : Cumulative IPL element-surface area distributions using air / water at zero vapour loading considering Intalox® Ultra size A vs. 1.5" FlexiRing® @ A) 37 $m^3.m^{-2}.h^{-1}$; B) 73$m^3.m^{-2}.h^{-1}$; C) 98$m^3.m^{-2}.h^{-1}$; D) 122$m^3.m^{-2}.h^{-1}$; 14-172

Figure 14.12: Cumulative IPL element-surface area distributions using air / water at zero vapour loading considering Intalox® Ultra size L vs. 2" FlexiRing® @ A) 6$m^3.m^{-2}.h^{-1}$; B) 37 $m^3.m^{-2}.h^{-1}$; C) 73$m^3.m^{-2}.h^{-1}$; D) 98$m^3.m^{-2}.h^{-1}$; E) 122$m^3.m^{-2}.h^{-1}$;..... 14-173

Figure 14.13 : Cumulative IPL element-surface area distributions using water at zero vapour loading A) Intalox® Ultra sizes A, L and O @ 37 $m^3.m^{-2}.h^{-1}$; B) 1.5" &2" FlexiRing® @ 37 $m^3.m^{-2}.h^{-1}$; C) Intalox® Ultra sizes A, L and O @ 98 $m^3.m^{-2}.h^{-1}$ D) 1.5" &2" FlexiRing® @ 98 $m^3.m^{-2}.h^{-1}$. 14-174

Figure 14.14 : Cumulative IPL element-surface area distributions using air / ethylene glycol at zero vapour loading; A) Intalox® Ultra size L; B) 2" FlexiRing® ; C) Intalox® Ultra size O. 14-175

Figure 14.15 : Cumulative IPL element-surface area distributions using air/Ethylene Glycol at zero vapour loading considering Intalox® Ultra size L vs. 2" FlexiRing® @ A) 37 $m^3.m^{-2}.h^{-1}$; B) 73$m^3.m^{-2}.h^{-1}$; C) 98$m^3.m^{-2}.h^{-1}$; D) 122$m^3.m^{-2}.h^{-1}$. 14-176

Figure 14.16: Cumulative IPL element-surface area distributions for air / water; A) Intalox® Ultra size L @ 37 $m^3.m^{-2}.h^{-1}$; B) 2" FlexiRing® @ 37 $m^3.m^{-2}.h^{-1}$; C) Intalox® Ultra size L @ 73 $m^3.m^{-2}.h^{-1}$; D) 2" FlexiRing® @ 73 $m^3.m^{-2}.h^{-1}$; E) Intalox® Ultra size L @ 98 $m^3.m^{-2}.h^{-1}$; F) 2" FlexiRing® @ 98 $m^3.m^{-2}.h^{-1}$ 14-177

Figure 14.17: Figure 14.16 Continues; G) Intalox® Ultra size L @ 122 $m^3.m^{-2}.h^{-1}$; H) 2" FlexiRing® @ 122 $m^3.m^{-2}.h^{-1}$. 14-178

Figure 14.18 : Cumulative IPL element-surface area distributions for air water; A) Intalox® Ultra size A @ 37 $m^3.m^{-2}.h^{-1}$; B) 1.5" FlexiRing® @ 37 $m^3.m^{-2}.h^{-1}$; C) Intalox® Ultra size A@ 73 $m^3.m^{-2}.h^{-1}$; D) 1.5" FlexiRing® @ 73 $m^3.m^{-2}.h^{-1}$; E) Intalox® Ultra size A@ 98 $m^3.m^{-2}.h^{-1}$; F) 1.5" FlexiRing® @ 98$m^3.m^{-2}.h^{-1}$ 14-179

Figure 14.19 : Figure 14.18 Continues; G) Intalox® Ultra size A @ 122 $m^3.m^{-2}.h^{-1}$; H) 1.5" FlexiRing® @ 122$m^3.m^{-2}.h^{-1}$. 14-180

Figure 14.20: Cumulative IPL element-surface area distributions using air / water and Intalox® Ultra size O A) 37 $m^3.m^{-2}.h^{-1}$; B) 73 $m^3.m^{-2}.h^{-1}$; C) 98 $m^3.m^{-2}.h^{-1}$; 14-180

Figure 14.21: Cumulative IPL element-surface area distributions for air/ ethylene glycol; A) Intalox® Ultra size L @ 37 $m^3.m^{-2}.h^{-1}$; B) 2" FlexiRing® @ 37 $m^3.m^{-2}.h^{-1}$; C) Intalox® Ultra size L@ 73 $m^3.m^{-2}.h^{-1}$; D) 2" FlexiRing® @ 73 $m^3.m^{-2}.h^{-1}$; E) Intalox® Ultra size L@ 98 $m^3.m^{-2}.h^{-1}$; F) 2" FlexiRing® @ 98$m^3.m^{-2}.h^{-1}$;..... 14-181

Figure 14.22: Figure 14.21 Continues; G) Intalox® Ultra size L@ 122 $m^3.m^{-2}.h^{-1}$; H) 2" FlexiRing® @ 122$m^3.m^{-2}.h^{-1.}$ 14-182

Figure 14.23: Cumulative IPL element-volume distributions using air / water at zero vapour loading A) Intalox® Ultra size A; B) 1.5" FlexiRing®; C) Intalox® Ultra size L; D) 2" FlexiRing® ; E) Intalox® Ultra size L; 14-183

Figure 14.24: Cumulative IPL element-volume distributions using air / ethylene glycol at zero vapour loading; A) Intalox® Ultra size L; B) 2" FlexiRing® ; C) Intalox® Ultra size O. 14-184

Figure 14.25 : Cumulative IPL element-volume distributions for air water; A) Intalox® Ultra size L @ 37 $m^3.m^{-2}.h^{-1}$; B) 2" FlexiRing® @ 37 $m^3.m^{-2}.h^{-1}$; C) Intalox® Ultra size L @ 73 $m^3.m^{-2}.h^{-1}$; D) 2" FlexiRing® @ 73 $m^3.m^{-2}.h^{-1}$; E) Intalox® Ultra size L @ 98 $m^3.m^{-2}.h^{-1}$; F) 2" FlexiRing® @ 98 $m^3.m^{-2}.h^{-1}$;..... 14-185

Figure 14.26: Figure 14.25 Continues; G) Intalox® Ultra size L @ 122 $m^3.m^{-2}.h^{-1}$; H) 2" FlexiRing® @ 122 $m^3.m^{-2}.h^{-1}$; 14-186

Figure 14.27 : Cumulative IPL element-volume distributions for air water; A) Intalox® Ultra size A @ 37 $m^3.m^{-2}.h^{-1}$; B) 1.5" FlexiRing® @ 37 $m^3.m^{-2}.h^{-1}$; C) Intalox® Ultra size A@ 73 $m^3.m^{-2}.h^{-1}$; D) 1.5" FlexiRing® @ 73 $m^3.m^{-2}.h^{-1}$; E) Intalox® Ultra size A@ 98 $m^3.m^{-2}.h^{-1}$; F) 1.5" FlexiRing® @ 98$m^3.m^{-2}.h^{-1}$; 14-187

Figure 14.28: Figure 14.27 Continues; G) Intalox® Ultra size A @ 122 $m^3.m^{-2}.h^{-1}$; H) 1.5" FlexiRing® @ 122$m^3.m^{-2}.h^{-1}$. 14-188

Figure 14.29: Cumulative IPL element-volume distributions using air / water and Intalox® Ultra size O A) 37 $m^3.m^{-2}.h^{-1}$; B) 73 $m^3.m^{-2}.h^{-1}$; C) 122 $m^3.m^{-2}.h^{-1}$; 14-188

Figure 14.30 : Cumulative IPL element-surface area distributions using air / water at zero vapour loading A) Intalox® Ultra size A; B) 1.5" FlexiRing®; C) Intalox® Ultra size L; D) 2" FlexiRing® ; E) Intalox® Ultra size L; 14-189

Figure 14.31: Cumulative IPL element-surface area distributions using air / ethylene glycol at zero vapour loading; A) Intalox® Ultra size L; B) 2" FlexiRing® ; C) Intalox® Ultra size O. 14-190

Figure 14.32: Cumulative IPL element-surface area distributions for air water; A) Intalox® Ultra size L @ 37 $m^3.m^{-2}.h^{-1}$; B) 2" FlexiRing® @ 37 $m^3.m^{-2}.h^{-1}$; C) Intalox® Ultra size L @ 73 $m^3.m^{-2}.h^{-1}$; D) 2" FlexiRing® @ 73 $m^3.m^{-2}.h^{-1}$; E) Intalox® Ultra size L @ 98 $m^3.m^{-2}.h^{-1}$; F) 2" FlexiRing® @ 98 $m^3.m^{-2}.h^{-1}$;..... 14-191

Figure 14.33: Figure 14.32 Continues; G) Intalox® Ultra size L @ 122 $m^3.m^{-2}.h^{-1}$; H) 2" FlexiRing® @ 122 $m^3.m^{-2}.h^{-1}$; 14-192

Figure 14.34: Cumulative IPL element-surface area distributions for air water; A) Intalox® Ultra size A @ 37 $m^3.m^{-2}.h^{-1}$; B) 1.5" FlexiRing® @ 37 $m^3.m^{-2}.h^{-1}$; C) Intalox® Ultra size A@ 73 $m^3.m^{-2}.h^{-1}$; D) 1.5" FlexiRing® @ 73 $m^3.m^{-2}.h^{-1}$; E) Intalox® Ultra size A@ 98 $m^3.m^{-2}.h^{-1}$; F) 1.5" FlexiRing® @ 98$m^3.m^{-2}.h^{-1}$; 14-193

Figure 14.35: Figure 14.34 Continues; G) Intalox® Ultra size A @ 122 $m^3.m^{-2}.h^{-1}$; H) 1.5" FlexiRing® @ 122$m^3.m^{-2}.h^{-1}$. 14-194

Figure 14.36: Cumulative IPL element-surface area distributions using air / water and Intalox® Ultra size O A) 37 $m^3.m^{-2}.h^{-1}$; B) 73 $m^3.m^{-2}.h^{-1}$; C) 122 $m^3.m^{-2}.h^{-1}$; 14-194

Figure 14.37 : Probability density function for the air / water system using 1.5" FlexiRing® A) 37 $m^3.m^{-2}.h^{-1}$; B) 73 $m^3.m^{-2}.h^{-1}$; C) 98 $m^3.m^{-2}.h^{-1}$; D) 122$m^3.m^{-2}.h^{-1}$; 14-195

Figure 14.38: Probability density function for the air / water system using 1.5" Intalox® Ultra A) 37 $m^3.m^{-2}.h^{-1}$;B) 73 $m^3.m^{-2}.h^{-1}$;C) 98 $m^3.m^{-2}.h^{-1}$ D) 122$m^3.m^{-2}.h^{-1}$; 14-196

Figure 14.39 : Probability density function for the air / water system using 2” Intalox® Ultra; A) 6 $m^3.m^{-2}.h^{-1}$; B) 37 $m^3.m^{-2}.h^{-1}$;C) 73 $m^3.m^{-2}.h^{-1}$;D) 98 $m^3.m^{-2}.h^{-1}$ E) 122$m^3.m^{-2}.h^{-1}$;..... 14-197

Figure 14.40: Probability density function for the air / water system using 2” FlexiRing® A) 6 $m^3.m^{-2}.h^{-1}$; B) 37 $m^3.m^{-2}.h^{-1}$;C) 73 $m^3.m^{-2}.h^{-1}$;D) 98 $m^3.m^{-2}.h^{-1}$ E) 122$m^3.m^{-2}.h^{-1}$;..... 14-198

Figure 14.41: Probability density function for the air / water system using 2.5” Intalox® Ultra; A) 6 $m^3.m^{-2}.h^{-1}$; B) 37 $m^3.m^{-2}.h^{-1}$;C) 73 $m^3.m^{-2}.h^{-1}$;D) 98 $m^3.m^{-2}.h^{-1}$ E) 122$m^3.m^{-2}.h^{-1}$;..... 14-199

Figure 14.42 : 2” FlexiRing® distribution with water. A) 37 $m^3.m^{-2}.h^{-1}$; B) 73 $m^3.m^{-2}.h^{-1}$; C) 98 $m^3.m^{-2}.h^{-1}$; D) 122 $m^3.m^{-2}.h^{-1}$. 14-200

Figure 14.43: Intalox® Ultra L distribution with water. A) 37 $m^3.m^{-2}.h^{-1}$; B) 73 $m^3.m^{-2}.h^{-1}$; C) 98 $m^3.m^{-2}.h^{-1}$; D) 122 $m^3.m^{-2}.h^{-1}$. 14-201

Figure 14.44: Intalox® Ultra A distribution with water. A) 37 $m^3.m^{-2}.h^{-1}$; B) 73 $m^3.m^{-2}.h^{-1}$; C) 98 $m^3.m^{-2}.h^{-1}$; D) 122 $m^3.m^{-2}.h^{-1}$. 14-202

Figure 14.45: 1.5” FlexiRing® distribution with water. A) 37 $m^3.m^{-2}.h^{-1}$; B) 73 $m^3.m^{-2}.h^{-1}$; C) 98 $m^3.m^{-2}.h^{-1}$; D) 122 $m^3.m^{-2}.h^{-1}$. 14-203

LIST OF TABLES

Table 2.1: Random packings according to generation (Lamprecht [2] and Erasmus [20]) [22, 23]. 12

Table 2.2: The evolution of structured packing from the 1940's to current day [2] [20] [22, 23]. 13

Table 2.3:A summary of the predictive correlations for effective interfacial area found in literature [17]. 17

Table 3.1: Comparison of tomography methods found in literature [14, 10, 11]. 32

Table 3.2: Comparison: Impedance vs. Resistance. 34

Table 3.3: Impedance decomposition table, showing the implications of the respective conductivity and capacitance measurements. 39

Table 3.4: Literature conductivity and electrical Permittivity, as measured for various liquids. 39

Table 4.1: Outline of this chapter and the reasoning behind each development section. 43

Table 4.2: Standard deviations of calibration curves for both capacitance and resistance channels. 70

Table 5.1: FEM deformation analysis. 74

Table 5.2: Summary of the design parameters and their reasoning related to the mesh grid 77

Table 5.3: Vapour and liquid physical properties. 81

Table 8.1: Hydrodynamic characterisation limitation summary. 114

Table 8.2: Table providing the corresponding IPL element-surface area within the Appendix, to the equivalent IPL element-volume sections in this section. 131

Table 8.3: Kinetic characterisation can/cannot table. 133

Table 11.1 : Packed column measurement accuracies based on Minne [5] 11-153

GLOSSARY

Symbol	Description	Units
A	Absorption factor	
a_e	Effective interfacial mass transfer area	m^2 or m^2/m^3
a_G	Effective vapour area	m^2/m^3
a_L	Effective liquid area	m^2/m^3
a_p	Geometric area of packing, as stated by manufacturers	m^2/m^3
a_w	Wetted geometric area of packing	m^2/m^3
C_1	Regressed packing specific parameter	
CFD	Cumulative density function	
CPF	Cumulative probability function	
C_i^*	Equilibrium concentration of component i	mol/m^3
$c_{i,1}$	Concentration of solute at the inlet	g/m^3
$c_{i,1}$	Concentration of solute at the outlet	g/m^3
d_1	Regressed parameter for Linek equations	-
d_2	Regressed parameter for Linek equations	-
d_{32L}	Sauter mean bubble diameter of large bubbles	m
d_{32S}	Sauter mean bubble diameter of small bubbles	m
De_G	Eddie diffusivity of vapour mixing	m^2/s
d_h	Hydraulic diameter of dumped packing	m
$D_{i,L}$	Liquid phase diffusivity of component i	m^2/s
d_p	Diameter of packing	m
E_B	Point efficiency fraction due to bubbles	%
E_{ML}	Murphree liquid efficiency	%
E_{MV}	Murphree vapour efficiency	%
E_O	Section efficiency	%
E_{OG}	Point efficiency	%
EIT	Electrical impedance tomography	
E_{SB}	Point efficiency from small bubbles	%
f_j	Fraction of vapour jetting	
F_s	F factor, product of the superficial gas velocity and square root of gas density	$kg^{0.5}\,m^{-0.5}\,s^{-1}$
F_s'	F factor, product of the superficial gas velocity and square root of gas density (Imperial Units)	$lb_m^{0.5}.ft^{-0.5}.s^{-1}$
F_{SB}	Fraction Small bubbles	
FF	Fraction of flooding F factor	
g	Gravity acceleration	m/s^2

Symbol	Description	Units
G	Gas flow rate	kg/h
G'	Vapour flow rate per bubbling area	$kmol.m^{-2}s^{-1}$
G_m	Gas molar flow rate	mol /h
$\dot{G}$	Gas loading rate	$m^3m^{-2}h^{-1}$
H	Packed column height	m
H_c	Henry's constant (concentration definition)	
h_{cl}	Height of clear liquid in a tray column	m
HETP	Height equivalent of theoretical plate	m
h_f	Froth height in meters	m
h_f'	Froth height in inches	inches
h_{FL}	Liquid hold-up in a packed column at flooding	m^3/m^3
h_L	Liquid hold-up in a packed column	m^3/m^3
h_{LS}	liquid hold-up in a packed column at the onset of the loading point	m^3/m^3
HTU_G	Height of vapour transfer unit	m
HTU_{OG}	Height of overall vapour transfer unit	m
HTU_L	Height of liquid transfer unit	m
HTU_{OL}	Height of overall liquid transfer unit	m
h_w	Weir height	m
h_w'	Weir height in inches	inches
IPL	Inter-packing liquid	
K	Equilibrium K value(y/x)	
k_i	Rate constant	m/s
k_G	Vapour mass transfer mass transfer coefficient	m/s
k_L	Liquid mass transfer coefficient	m/s
k_La	Volumetric liquid mass transfer coefficient	1/s
k_{LLB}	k_L for large bubbles	1/s
K_{OL}	Overall liquid mass transfer coefficient	m/s
K_{OL}'	Overall liquid mass transfer coefficient using mole fractions	$mol.m^{-2}.s^{-1}$
$K_{OG}a$	Volumetric overall vapour mass transfer coefficient	1/s
K_{OG}	Overall vapour mass transfer coefficient	m/s
L	Liquid flow rate	kg/h
L'	Liquid flow rate per bubbling area	$kmol.m^2s^{-1}$
L_f	Volumetric liquid flow rate per unit average flow width	m^2/s
L_m	Liquid molar flow rate	mol/h
$\dot{L}$	Partial pressure of component i at the phase interphase	Pa
m_i	Slope of the equilibrium line	mol/mol
$\dot{M}_G$	Vapour mass flow rate	kg/s

Symbol	Description	Units
N_i	Specific absorption rate	mol/(m^2.s)
n_i	Molar absorption rate of component i	mol/s
N_{IB}	Number of bubbles entering the froth	
$(N_i)_x$	Molar flux of component i, in direction x	Mol.m^{-2}.s^{-1}
$\overline{N_f}$	Number of large bubbles leaving the froth	
$\overline{N_s}$	Number of small bubbles leaving the froth	
NTU_G	Number of vapour mass transfer units	
NTU_{OG}	Number of overall vapour mass transfer units	
NTU_{OL}	Number of overall liquid mass transfer units	
NTU_L	Number of liquid mass transfer units	
NTU_L'	Number of liquid mass transfer units, with the assumption that liquid flows in as plug flow and that there is no vertical liquid mixing	
p	Hole Pitch in sieve trays	m
$P_{i,I}$	Partial pressure of component i at the phase interphase	Pa
$P_{i,G}$	Partial pressure of component i in the bulk gas phase	Pa
P_i^*	Partial Pressure of equilibrium	Pa
P_T	Total pressure	Pa
Q_L	Liquid flow rate	m^3/s
Qwl'	Load per weir length	Gpm/ft
t_G	Average vapour residence time	s
t_{GLB}	Average large bubble residence time	s
t_L	Average liquid residence time	s
T_s	Tray Spacing	m
$u_{V,Fs}$	Superficial gas velocity the loading point	m/s
u_g	Superficial gas velocity	m/s
u_h	Velocity of vapour leaving perforations	m/s
u_L	Superficial liquid velocity	m/s
$u_{S,G}$	Superficial gas velocity in tray columns	m/s
$u_{V,FL}$	Superficial gas velocity at flooding	m/s
V_G	Vapour volumetric flow rate	m^3/s
V_L	Liquid volumetric flow rate	m^3/s
V_{LB}	Volume of large bubbles	m^3
V_{SB}	Volume of small bubbles	m^3
W	Weir length	m

Symbol	Description	Units
$x_{i,L}$	Mole Fraction of component I in the liquid phase	Mol/mol
x*	Equilibrium liquid mole fraction	mol/mol
X*	Equilibrium liquid mole Ratio	Equilibrium mol solute in the liquid per mol solvent free solvent
y	Mole fraction of the vapour phase	Mol/mol
Y	Mole ratio of a set component in the vapour phase	Mol solute in the vapour per mol solvent free vapour
$\overline{y_t}$	Average mole fraction	
y*	Mole fraction of the vapour in equilibrium with the liquid	Mol/mol
z	Directional variable	m
dz	Spatial vector	m
Z	Length of liquid flow path	m

Symbol	Description	Units
a_e	Effective interfacial mass transfer area	m^2 or m^2/m^3
a_p	Geometric area of packing, as stated by manufacturers	m^2/m^3
a_w	Wetted geometric area of packing	m^2/m^3
$D_{i,L}$	Liquid phase diffusivity of component i	m^2/s
d_p	Diameter of packing	m
EIT	Electrical impedance tomography	
F_s	F factor, product of the superficial gas velocity and square root of gas density	$kg^{0.5}\ m^{-0.5}\ s^{-1}$
HETP	Height equivalent of theoretical plate	m

COLUMN FLOW DEFINITIONS

Symbol	Name and Physical Interpretation	Definition
$\underline{F_s}$	**Vapour flow factor;** Based on superficial velocity	$u_S * \sqrt{\rho_v}$

GREEK SYMBOLS

Symbol	Description	SI Units
æ	Element-surface area or the IPL surface area measured with the EIT system	m^2
α	Liquid hold-up volume fraction	m^3/m^3
β	Vapour hold-up in froth	ft^3/ft^2
μ	dynamic viscosity	$kg.m^{-1}s^{-1}$
αe	Effective liquid volume fraction	
δ	Film thickness	m
ε	Bed voidage	m^3/m^3
λ	Stripping factor	
ν_L	Kinematic viscosity	m^2/s
ρ_G	Gas phase density	kg/m^3
ρ_L	Liquid phase density	kg/m^3
$\rho_{Mol,\,L}$	Molar density of liquid	$kmol/m^3$
$\rho_{Mol,V}$	Molar density of vapour	$kmol/m^3$
σ	Surface tension	N/m
υ_e	Element-volume or the IPL volume measured with the EIT system	ml
hε	Element liquid hold-up or the liquid holdup measured with the EIT system	

DIMENSIONLESS NUMBERS

Symbol	Name and Physical Interpretation	Definition
Ca	**Capillary;** Ratio of viscosity to surface tension	$\mu_L * \frac{u_L}{\sigma}$
Fr	**Froude;** Ration of inertia to gravity acceleration	$u_L^2 * \frac{a_p}{g}$
Ga	**Galileo;** Ratio of buoyancy to viscosity	$dp_3 * g_p/\upsilon_L^2$
kσ	Ratio of gravity to surface tension	$\rho_L * \frac{g}{a_p^2 * \sigma_L}$
Re	**Reynolds;** Ratio of inertia to viscosity	$\frac{u_L}{a_P * \upsilon_L}$
Sc	**Schmidt;** Ratio of momentum to diffusivity	$\frac{\mu_L}{\rho_L * D_{i,L}}$
We	**Weber;** Ratio of inertia to surface tension	$u_L^2 * \frac{\rho_L}{\sigma_L * a_P}$
Pe_G	**Peclet;** Ratio of axial dispersion by flow	$u_s * \frac{Z^2}{De_G(T_s - h_f)}$

For Danni

"One is reminded, at a level deeper than all words, how making a living and making a life sometimes point in opposite directions."

Pico Iyer

1. INTRODUCTION

Separating components through selective evaporation and condensation is essential to the chemical refining industry, with examples pertaining to distillation, absorption, and stripping. Their widespread use and economic scaling capabilities motivate continuous systematic optimization [1], intending to improve and ensure financial viability.

Many factors influence the economic viability of distillation systems, with the most notable being their relatively high energy consumption [1]. Ever increasing energy costs consequently motivate the continued focus on the improvement of such systems. Vessel modifications are often infeasible for existing installations, limiting improvements to their internals. Progress in column-internals thereby lead to both the prolonged economic viability of existing (retrofitted) columns and reduced operating and capital costs for new installations.

Performance characterisation parameters are employed to assess, compare, and model new column internal designs. These parameters quantify performance improvements and advance the field by highlighting critical design aspects, on which future designs may build. As a result, performance characterisation and column-internal design are mutually dependent.

Randomly packed columns are of particular interest in this study. Their characterisations are conventionally separated into two interdependent parameter sets, namely *hydrodynamic* and *kinetic*. Hydrodynamic parameters predominantly influence the column width and thereby the throughput/ capacity. These include pressure drop, liquid hold-up, entrainment, and flooding [2]. Alternatively, kinetic parameters contribute to the column height (separation efficiency) and extend to both liquid and vapour phase mass transfer coefficients, the effective interfacial area, and their combined efficiencies in HETP.

These hydrodynamic and kinetic characterisations are conventionally evaluated, independently, and often require separate and specialized experimental setups. This is done to limit the variability in physical properties to isolate the individual effects.

1.1 PROBLEM STATEMENT

Both *kinetic* and *hydrodynamic* characterisation parameters illustrate an intricate dependence on the distribution of the vapour-liquid interface, whether direct, as in the effective interfacial area (a_e), or indirectly through parameters such as pressure drop and liquid hold-up. However, the available literature exclusively focuses on the overall effective surface area (m^2/m^3) or overall liquid hold-up (m^3/m^3) and neglects the individual contributions of the liquid droplets between the packing pieces (inter-packing). The only exception being the comparison of the ratio of effective-to-apparent interfacial area showing the combined effects without isolating the individual contributions of the liquid droplets, streams, and

film coatings [3, 4]. Although historically sufficient for column design and sizing, current characterisation methods fail to highlight the complex interactions between the vapour-liquid mixture and the packing geometry [5].

Fourth-generation packings are designed to capitalize on droplet creation between packing elements, with the resulting effective interfacial area extending to twice the packing surface area (apparent area) [3, 4]. Modern packings are consequently able to produce sizable amounts of surface area through inter-packing droplet formation. The importance of these droplets, our understanding of their behaviour, and their quantification is therefore apparent. This is exemplified in the packing specific comparison of the effective interfacial area to the specific outer area (a_e/a_p), presented in Figure 1.1.The presented graphs are based on the findings by Nieuwoudt et al. (2018) and Kolev et al. (2006) on Intalox® Ultra and Raschig Super Ring® respectively.

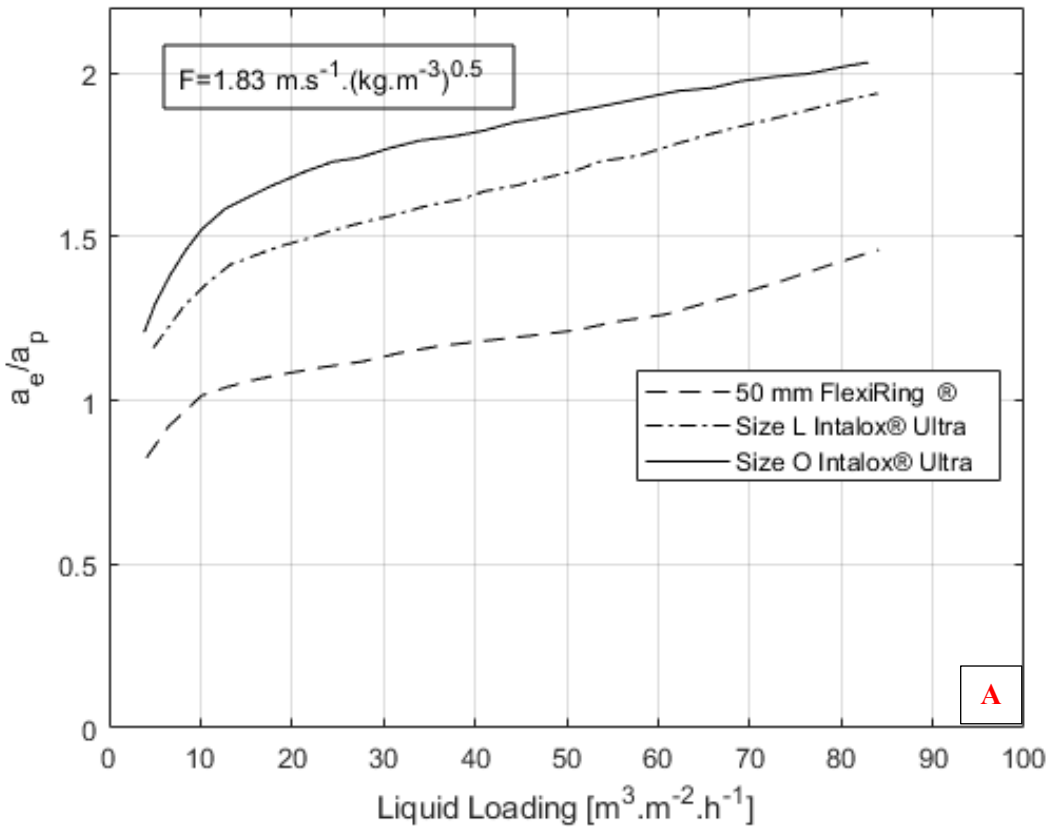

Figure 1.1A: The Ratio of effective interfacial area to apparent interfacial area for Intalox® Ultra L and O at F_s =1.8 $(m.s^{-1})\cdot(kg.m^{-3})^{0.5}$ [3]

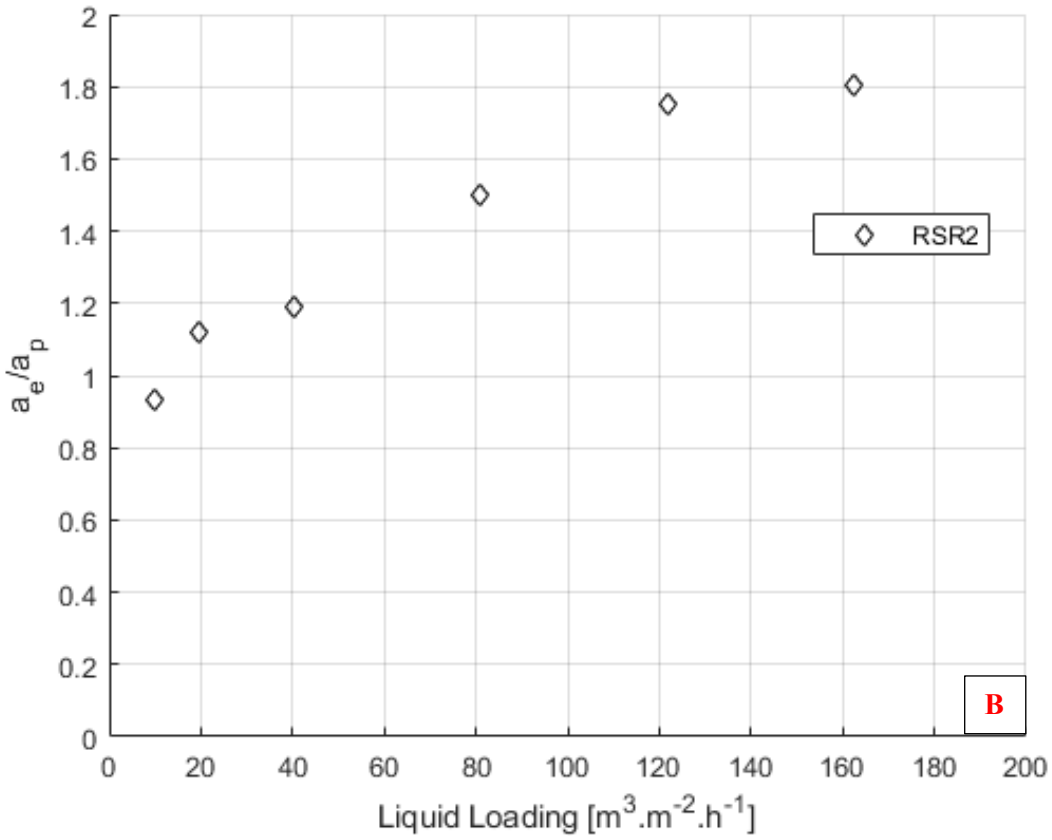

Figure 1.1B: The Ratio of effective interfacial area to apparent interfacial area for Raschig Super Ring® [4]

Inter-packing droplets influence both liquid hold-up, pressure drop, and the effective interfacial area; however, their presence and characterisation in randomly packed columns are still limited. This is likely due to the perceived experimental difficulties in their experimental quantification. The subsequent study set out to characterize random packing through the evaluation of the inter-packing liquid (IPL) behaviour. This was achieved by adapting and incorporating multiphase flow imaging and processing into packed column characterisation. Electrical Impedance Tomography (EIT) with a wire-mesh sensor grid was consequently chosen for use in characterisation.

The product of the abovementioned EIT is a holistic characterisation system capable of cost-effectively evaluating:

[1] Conventional column tomography, including maldistribution, and wall effects,

[2] Conventional hydrodynamic parameters, i.e., liquid hold-up,

[3] Size (volume and surface area) distributions of the inter-packing droplets,

[4] The total inter-packing area (non-effective).

1.2 Introduction to Flow Imaging in Columns

The visual representation of column inner workings has been the centre of various studies since the 1950s. Column imaging research has subsequently progressed from the use of coloured dies and floating balls to represent fluid streamlines, toward X-ray and tracer imagery [6, 7, 8, 9, 10]. Modern studies focus on tomography, which in its most simplistic sense, utilises numerous measurements from various angles to reproduce an image in a 2D or 3D vector space. A simplified representation of the tomography method is presented in Figure 1.2.

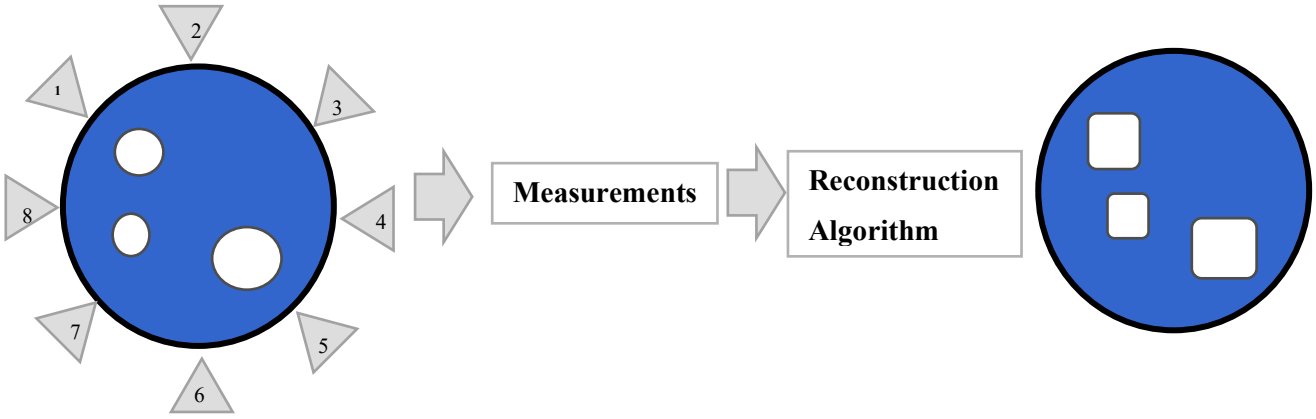

Figure 1.2 : A computed tomography illustration, where measurements are taken alternating the activated node (1-8) while measuring continuously across the other nodes (1-8). The image then reconstructed using specialised algorithms.

Radiation based tomography techniques are widely used throughout literature to evaluate column flow due to the excellent spatial resolutions (1% of diameter) [11, 10, 9]. Although historically slow, numerous advances by Janzen et al. (2013) have improved imaging times to upwards of 2000 frames per second [11]. This was accomplished by rotating both the emitter and detector at high speeds around the column.

Radiation based tomography was deemed unfit for packed column characterisations due to the **a)** inherent safety risks related to the handling of high energy radioactive emissions, **b)** high equipment cost, and **c)** scaling complexity of large rotating systems. Therefor an electrical tomography approach, using complex electrical impedance, was chosen to address these concerns. The EIT approach uses either high-speed conductivity or capacitance measurements for imaging, activating a single electrode with an electrical (sinusoidal) wave (Figure 1.2) and measuring the resulting electrical field through the other sensing nodes (2 to 8). This process is repeated until all the nodes have been activated at least once.

Electrical tomography has been used industrially in applications ranging from airlift- [12] to trickle bed reactors [13] and structured-packed columns [10]. These evaluations produced comparable phase distribution data to radiation tomography at reduced costs, lower complexity, and less safety concerns

[10]. Conventional electrical tomography, however, suffers from considerably lower spatial resolutions (5% of diameter). This hinders conventional EIT for use in packed columns, as the industrial minimum diameter to limit wall effects is widely considered to be 400mm [2] and thus a minimum resolution of 20mm is attainable with the conventional approach.

The spatial resolution restrictions of conventional electrical tomography were overcome by incorporating a wire-mesh electrode configuration [14]. A schematic of the wire-mesh array is provided in Figure 1.3. This configuration creates an effective sensing area around each of the "wire cross points" in Figure 1.3 and utilizes the same electrical principle of impedance. Wire-mesh electrical tomography systems can attain spatial resolutions (electrode spacing) down to 2mm [14] .

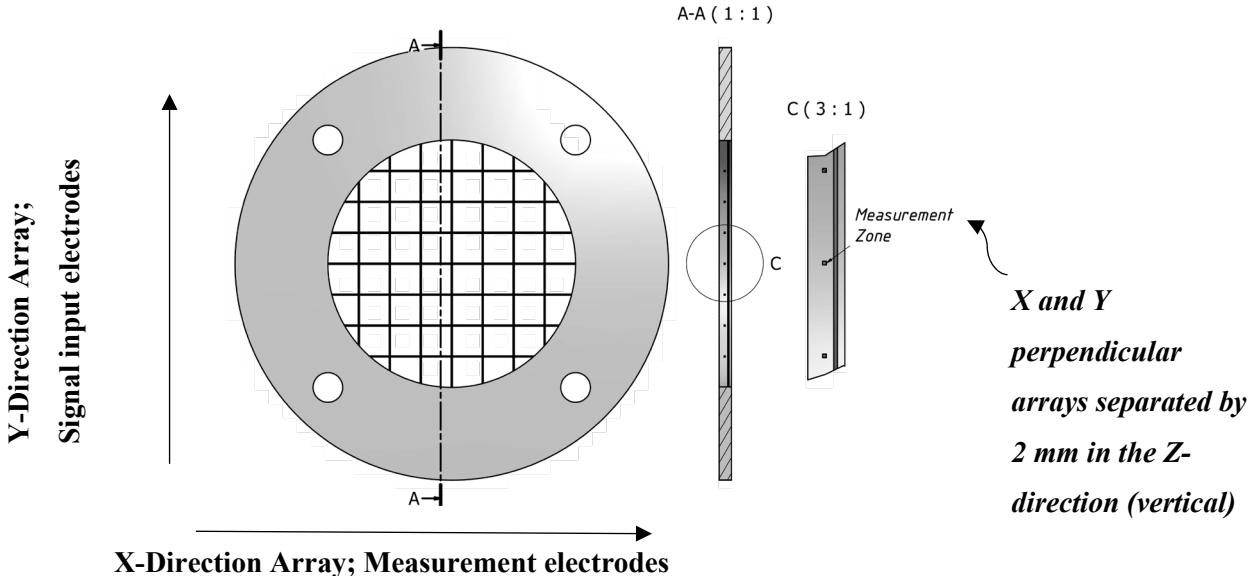

Figure 1.3: A schematic of a conventional wire-mesh sensor depicting two layers of perpendicular electrodes (X and Y), separated in the Z-direction. The wire-mesh sensor thereby provides measurement at each of the perpendicular points where the X and Y electrodes cross.

Against this background, wire-mesh EIT was selected for this study, based on cost, complexity resolution and safety, to characterize random packing through the associated inter-packing droplets and distributions.

1.3 The Link Between Kinetics, Hydrodynamics and Tomography

This work provides a brief overview of conventional characterisation methods, both hydrodynamic and kinetics in chapter 2, followed by a summary of the key findings in the relevant literature. The conclusions highlight the need for accurate droplet distribution data, for improved hydrodynamic and kinetic modelling. Based on this determination, a tomographic approach is developed. This approach

focusses on **e**lectric **i**mpedance **t**omography or EIT. A diagram linking the literature topics is presented in Figure 1.4.

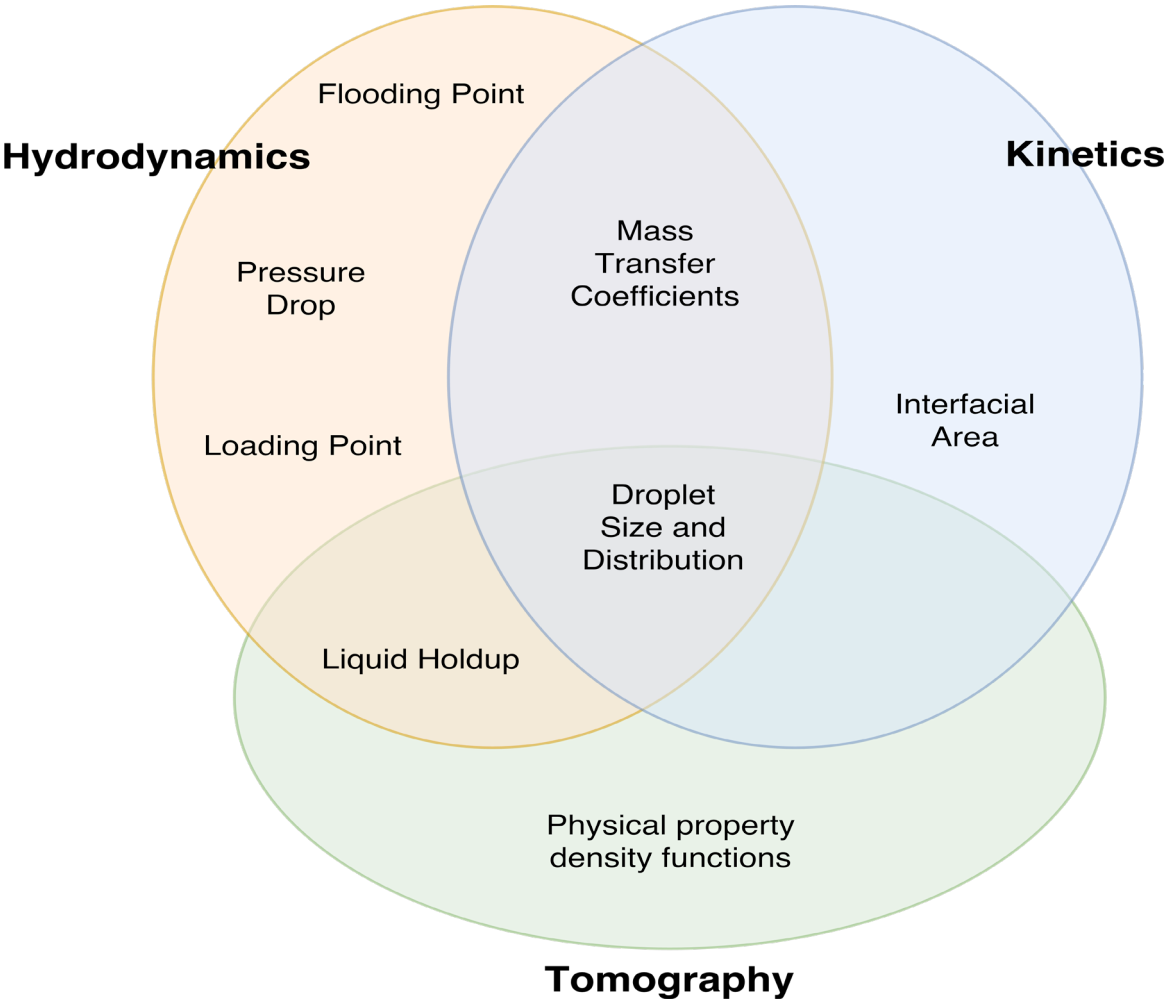

Figure 1.4: A schematic of the link between hydrodynamics, kinetics, and tomography within packed columns.

1.4 AIMS AND OBJECTIVES

The preceding problem statement illustrated the need for improved fundamentality in characterizing liquid element sizes and distributions between random packing pieces. This motivated the overarching aim of *improving the fundamental understanding of vapour - liquid interfacial distributions inside randomly packed columns* through tomography-based characterisation, assessing the effect of liquid properties on liquid element sizes and distributions.

To meet this aim and propose a novel means of packing characterisation, the following specific objectives were identified:

[1] Designing and building a cost-effective EIT system for:
   a. Conventional packed column tomography use, i.e., characterisation of liquid distribution and wall effects,
   b. the characterisation of inter-packing liquid distributions inside randomly packed columns.

[2] Quantifying the influence of random packing design on the development of liquid elements (droplets) in the inter- and intra-packing space. This entailed evaluating the distributions (based on volume and surface area) with Flexi® Rings and Intalox® Ultra Rings.

[3] Quantifying the effect of liquid physical properties on the liquid element and droplet creation in random packing.

1.5 Scope and Limitations

This study aimed to further the fundamental knowledge of liquid distribution and the formation of liquid droplets (considered as liquid elements). In accomplishing the objectives, a wire-mesh sensor was designed using a 37x37 sensing matrix, producing 1369 sampling points throughout a 400mm ID column. The wire-mesh array was placed 20mm below the packing (with a unique, low disturbance hold-up-up grid) at a packed height of 3m to approximate the inter-packing flow conditions.

The data collected from the EIT system were used in evaluating a variety of parameters through the combination of two- and three-dimensional image processing algorithms. The image processing was conducted in Matlab using the toolkits: *Regionprops*, *Regionsprops3* and *bwconnomp*. To limit confusion towards real properties and those generated from the image reconstructions, the term *element* is used. The disturbances imaged through reconstruction are consequently referred to as "*liquid-elements"* and not as droplets or streams.

The following **definitions** were consequently used:

- **Inter-packing liquid (IPL) element-volume(υ_e)** representing the liquid volume in the packing voids generated from the 3D image reconstruction (considering solid elements) algorithms and the 380 x 380 x ***M*** matrix.
- **Inter-packing liquid (IPL) element-surface area(æ) represents** the outer surface area of the liquid droplets in the packing voids based on the 3D image reconstruction algorithms 380 x 380 x ***M*** matrix.
- **Element liquid hold-up (hε),** referring to the time-averaged liquid area-fraction used to evaluate hold-up 380 x 380 x ***N*** matrix.

1.5.1 Random Packing Considered

- Flexi® Ring size 1.5” and 2”
- Intalox® Ultra Ring size A (1.5” equivalent), L (2” equivalent), O (2.5” equivalent)

1.5.2 Vapour-liquid Systems Considered

The following vapour-liquid combinations were considered, with physical properties in Table 5.3 on page 81. Both conductive (water) and non-conductive (ethylene glycol) systems were evaluated to highlight the ability of the proposed characterisation system in handling industrially relevant vapour-liquid combinations (low surface tensions are often limited to non-conductive hydrocarbon systems).

- Ethylene glycol / air
- Water / air

1.5.3 Range of Operation

Conventional operating ranges for packed columns were considered, hence:

- Vapour loadings up until flooding,
- Liquid loadings from 6 to 122 $m^3.m^{-2}.h^{-1}$

1.5.4 Limitations

Based on the fundamental premise, electrical impedance measurements consider a uniform liquid body. The quantitative evaluations are thereby limited in their capacity to account for dead zones, micro surface waves and surface renewal. The liquid-element areas from this study consequently represent the actual area within the packing space, and not the effective area of mass transfer. This differentiation and its implications are well-documented. Unfamiliar readers are referred to Du Preez et al. and Rejl et al. [15, 16].

Based on these restrictions, the project scope was limited to packed column hydrodynamics. Some comparative deductions were however made in section 8.3, based on the assumption of negatable variation in the interfacial effects (turbulence and surface renewal) within the inter-packing voids. The compared packings are therefore assumed to have the same level of surface interactions, in so far that these elements effectively resemble a falling liquid-element.

1.6 Novel Contributions

Several novel contributions are presented in this work. These are:

[1] The development of a characterisation methodology based on EIT for better understanding of inter-packing distributions.

[2] Novel experimental inter-packing distribution data for liquid element-volumes and -areas and their relation to:

i. Packing type.
ii. Liquid and vapour loadings
iii. Liquid physical properties

[3] Presenting the existence of a packing-specific transitional point, based on liquid and vapour loadings, where the mechanism of liquid hold-up changes. This point marks the cross-over between the conglomeration of inter-packing liquid elements into streams, and their break-up/ redistribution into smaller elements. This alludes to a possible increase in interfacial turbulence (decreasing liquid phase resistance to mass transfer) while adding to the understanding of the pressure drop mechanisms in packed columns.

[4] Presenting the total inter-packing liquid (IPL) element-surface area as a comparative kinetic characterisation parameter for use in prototyping. This is poised to assist the design of future packing's, in finding the optimum ratio of apparent-to-inter-packing area to minimize entrainment and maximize efficiency.

1.7 Foreword on Electronic Circuitry Development and Image Processing

The work presented in this dissertation, required specialised electronic circuitry development, automation as well as complex data and image processing. To not distract from the scope of column internal characterisation (towards specialised electronics) this document presents a discussion of these aspects in the subsequently defined "Block format". The complex components of the circuitry and data processing methodology were consequently divided into, and discussed in, logical blocks instead of shifting the focus towards the details. This was done in an attempt to keep the dissertation concise and focused while protecting the sensitive intellectual property contained within. The block definition was used in Chapter 4 and 6.

2. CHARACTERISATION OF COLUMN INTERNALS – AN OVERVIEW

Column-internals affect the capital investment and operating costs of phase contacting columns. Advances in their design and characterisation are therefore of critical importance to the field. The succeeding section will cover the background on both trays and packing.

2.1 COLUMN-INTERNALS

Column-internals are conventionally categorized into either trays or packing (excluding distributors and collectors), with both functioning as a promoter for phase contact and interfacial area [17]. Differences in column-internal performance are attributed to hydrodynamic variations intricately related to the design. A short description of the industrially available column-internals is presented in the following section.

2.1.1 TRAY COLUMNS

Tray columns facilitate vapour-liquid contact through an ascending vapour phase, bubbling through a laterally moving liquid. The ratio between vapour-liquid loadings and the physical properties culminates in four separately identifiable flow regimes, based on their relative phase density. According to Hofhuis and Zuiderweg [18], the regimes are distinctly denoted as:

[1] Free bubbling regime,
[2] Mixed froth regime,
[3] Emulsified regime,
[4] Spray regime.

Historically, the mixed froth regime is considered the most advantageous. Under these operating conditions, the rising vapour passes through the continuous liquid phase in a series of jets and bubbles, leading to increased hold-up and froth height [19]. Although outside the scope, the sensor developed for the succeeding packing study, is expected to have various future applications in tray column design. Examples include, but are not limited to:

- Simultaneous evaluation of the froth density across the whole active tray area. This is contrasted by the current norm of using a localized evaluation with a high-speed probe.
- Vapour entrainment evaluations within the downcomer, using phase density estimations.

2.1.2 Packed Columns

Packed column vapour-liquid contact is facilitated through a descending liquid phase, coating packing rivulets in the presence of a continuously upward travelling vapour phase. The resulting interactions create surface area through a combination of packing specific area and droplet formation.

Modern packings are categorized into three classifications [20], namely:

[1] Random Packing,

[2] Structured Packing,

[3] Grid Packing.

Random and structured packings are heavily susceptible to fouling and corrosion [2]. Consequently, applications limited by these parameters preferentially use grid packings (FlexiGrid® and GlitchGrid®) with enlarged flow channels for robustness [20]. Grid packing applications include heat transfer and wash-columns or crude oil fractionation [20]. The packings mentioned above are rarely evaluated from an academic perspective and are treated as a specialized sub-group of structured packings based on their geometrical similarities. This dissertation follows suit and only provides an overview of random and structured packing.

2.1.2.1 Random Packing

In randomly packed columns, specific geometrical elements are indiscriminately dumped, forming a randomized structure and variable flow paths [20, 15]. Both vapour and liquid flow paths are continuously disrupted, increasing their residence times and thereby their hold-up.

The historical progression of random packing was characterized by the progression from rings and saddles to hybrid- and sinusoidal wave-based geometries [2]. The first and second generations concentrated on rings and saddles and mostly considered the specific packing surface area for interfacial area creation [2]. Considerable pressure drops, therefore, hampered the subsequent designs and their enclosed geometries.

Third-generation packings combined the defining attributes of both rings and saddles, producing an effective “hybrid” [20]. The designs used free tips, focussing on drop generation to increase interfacial area between packing rivulets. However, these additional inter-packing droplets enhanced entrainment [21]. Furthermore, the third generation saw the design of rivulets with varying characteristic lengths depending on the viewing angle. One such example is the Koch-Glitsch IMTP® Ring. Its design presents a distinctly smaller diameter when comparing the top and side view. This shifts the centre of gravity of the packing and mechanically alters its packing arrangement when dumped into the column. This design feature combined the cost-effectiveness and organized nature of respective random and structured packings, producing a cost-effective decrease in pressure drop.

The fourth and latest generation of packing discarded the hybrid design in favour of a sinus wave-like geometry. This beneficial geometry offers optimized droplet formation with increased turbulent film flow and interfacial area [3]. A representation of modern packing progression is provided in Table 2.1, generated from Lamprecht [2] as well as Erasmus [20]. Both authors drew inspiration from Kister [22] and Schultes [23].

Table 2.1: Random packings according to generation (Lamprecht [2] and Erasmus [20]) [22, 23].

First Generation (1895-1950's)	Second Generation (1950-1970's)	Third Generation (1970-1990's)	Fourth Generation (1990's to present)
Raschig Ring	Super Intalox® packing	IMTP®	Sulzer NeXring™ (released 2016)
Berl Saddle	Intalox® Saddle	FlexiMac™	Raschig Super Ring®
Lessing Ring	Pall® Ring	Hiflow® Ring	Intalox® Ultra
	Hy-Pak®	Intalox® Snowflake®	
		Levapak	
		Cascade Mini-Ring (CMR®)	
		Nutter Ring™	

Randomly packed columns are industrially preferred for use in small to medium-sized applications, operated under both high pressures (>14 bar) and high liquid loadings (> 45 $m^{-3}m^{-2}h^{-1}$) [22]. However, applications favouring high purity and low volume (high-value) separations favour structured columns due to their high efficiencies and low pressure-drop.

2.1.2.2 Structured Packing

Structured packings were developed in response to the demand for high efficiency, low pressure-drop column internals for use in high-value separations. These packings employ modular corrugated sheets in creating two-phase flow, with the organized arrangement promoting decreased pressure drop.

Structured packings were also developed in four distinct generations in accordance with their random counterparts, evolving from metal gauze to folded sheet-metal packings. The first and second generations typically consisted of wire gauze as the primary phase contact promotor. The resulting designs offered notably decreased pressure-drops compared to random packing but at a higher cost.

The third generation trademarked the use of sheet-metal packing, promoting high efficiencies, low pressure-drops, and decreased solids sensitivity. However, the application of the third generation of structured packings remained limited to low liquid loadings, as sharp directional changes propagated localised flooding at high flow rates. The aforementioned deficiencies led to the development of the fourth generation of structured packing with larger flow channels and smooth directional changes [24].

A similar representation, as provided for random packings, is included in Table 2.2. This table was reproduced from both Erasmus [20] and Lamprecht [2] on inspiration from Kister [22] and Schultes [23].

Table 2.2: The evolution of structured packing from the 1940's to current day [2] [20] [22, 23].

First Generation (1940 -1950's)	Second Generation (1950-1970's)	Third Generation (1970-1990's)	Fourth Generation (1990's to present)
Panapak	Goodloe®	Gempak®	ProFlux®
	Hyperfil®	Koch Flexipac®	Flexipac®HC
	Sulzer, Koch BX and AX Wire Gauge Packing	Montzpak-B®	Intalox® High-Capacity Packing
		Sulzer MellapakTM®	Mellapak plus®
		SMVP Extraction Packing	Mellapak AYPlus DC Hybrid Packing
		Flexipac®S	Montz-PakM® Montz-PakA® Fabric
			Raschig Super-Pak
			Katamax®
			Mellagrid packing
			Rombopak
			Katapak-SP

The respective column internals, whether trays or packing, are suited to different applications based on their geometric and hydraulic differences. Therefore, thorough characterisation is required in order to utilize their advances fully. As per the scope, this dissertation focusses on random packing, with structured packing having been well researched using X-ray tomography.

2.2 Column-Internal Characterisation

The characterisation of column-internals is of interest for optimal design and the prediction of the performance of prospective installations. This dissertation considers both *kinetic* and *hydrodynamic* characterisation of random packing. This chapter highlighted the limitations of both characterisation methodologies and suggested improved fundamental understanding and modelling by developing a tomography-based characterisation system for packed columns. An outline of the literature evaluation of column-internal characterisation is presented in Figure 2.1.

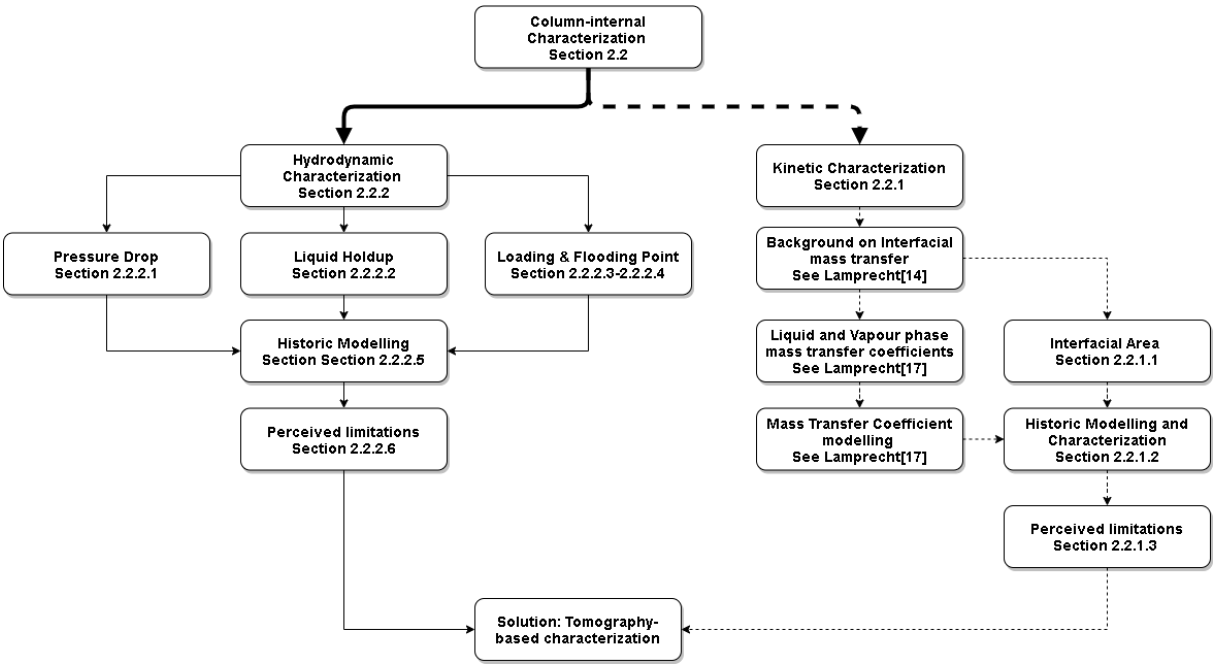

Figure 2.1: Roadmap of the column internal literature section of this dissertation.

The presented outline highlights the duality of the project motivation, as both hydrodynamic and kinetic characterisations are poised to benefit from the "inter-packing" tomography system. The benefits are summarized as follows:

- Hydrodynamic: Characterisation of the individual "size" distributions (IPL volume and surface area) that contribute to global parameters of hold-up and pressure drop are poised to add to the fundamental understanding of the relevant mechanisms. This is set to cascade into improved model fundamentals.

- Kinetic: Enhanced droplet creation is widely presented as the reasoning behind the kinetic improvements of the third and fourth-generation packings. However, these influences have not yet been evaluated independently of the overall effective interfacial area. Improved kinetic characterisation in that regard will consequently cascade into optimized droplet-promoting designs.

- Still, it should be noted that the tomography system is not expected to adequately assess stagnant mass transfer zones. The kinetic characterisation is therefore restricted to a comparative study as indicated by the dotted lines.

2.2.1 KINETIC CHARACTERISATION

A thorough body of work related to packed column kinetic characterisation has been presented in a previous publication (Lamprecht 2017 [17]). Readers are referred to this document for detail on the first principal derivations, conventional kinetic characterisation methodologies and mass transfer coefficient evaluations. These discussions are not repeated for the sake of brevity. Further discussion of the literature on kinetic characterisation will focus on the interfacial area and the considerations related to tomography.

2.2.1.1 INTERFACIAL AREA

Volumetric mass transfer coefficients ($K_{OL}a$ *or* $K_{OG}a$) are used to relate the net rate of molecule migration to an effective phase contact area (a_e) and diffusion related mass transfer coefficient (k_L and k_g), the relative weighting of the latter being specific to both species and operating condition (surface renewal).

The mass transfer coefficients (k_L and k_g) and interfacial areas (a_e) are conventionally evaluated independently due to the absence of fundamental models for the decomposition of the volumetric coefficients ($K_{OL}a$ *or* $K_{OG}a$).

Two methodologies are presented in the literature, namely:

[1] Physical absorption or desorption (wetted wall evaluation),

[2] Chemical absorption.

Physical absorption evaluations consider a thin liquid layer coated on the inside of a known diameter tube. Using an experimentally verified liquid or vapour phase mass transfer limiting system, a solute is either stripped or absorbed from the liquid with counter-current vapour [15]. Consequently, composition quantification at the inlet and outlet yields the volumetric mass transfer coefficient (K_La or K_Ga). The phase-specific mass transfer coefficient (k_L or k_g) is thereafter evaluated by division, as the interfacial contact area (a) is approximated by the inner area of the wall. The wetted wall mass transfer coefficients (k_L or k_g) are assumed constant and extrapolated to pilot columns. The use of these coefficients on pilot scale subsequently relies on an approximation of the interfacial area. [15].

This physical absorption approach was historically limited to evaluations of structured packing, as the smooth liquid flow paths hydrodynamically resemble the operation of structured packings. [20, 25]. However, the approximation of the effective interfacial area, as the area of phase contact, has since been criticised as it negates dead zones and liquid waves [20, 26]. Physical absorption using wetted wall data is, therefore, considered obsolete for the determination of the effective interfacial area of packing material. Instead, chemical absorption methods are advocated [20, 26].

Chemical absorption entails the measurement of liquid-side volumetric mass transfer coefficient through absorption, followed by a near-instantaneous chemical reaction in the liquid phase (historically preferable: carbon dioxide with a caustic solution (NaOH) [16, 20, 15, 4]). The absorption rate in the liquid phase is therefore considered rate-limiting due to the negligible vapour phase resistance. As a result, reaction rate measurements yield a liquid phase mass transfer coefficient (k_L), dependent solely on composition. Thus, the effective area is calculated by dividing the volumetric mass transfer coefficient and the experimental chemical reaction rate constant. The calculated effective interfacial area can consequently also be used to decompose volumetric mass transfer coefficients from other systems, given similar vapour and liquid physical properties.

2.2.1.2 Historic Modelling of Interfacial Area

Table 2.3 illustrates the available literature models for the estimation of the effective interfacial area. These models were regressed on both absorption/desorption and distillation data, and therefore offer a representative sample of the current knowledge. All the models use regressed constants (*C or d*) to differentiate between packing types. Such dependency on regressed constants makes these models ill-suited for general extrapolation and highlight the limitations of the existing quasi-fundamental knowledge.

The abundance of presented literature unilaterally fails to include parameters considering the inter-packing droplets. This presents a stark contrast between the models and the published data, where authors suggested droplet creation as the prevalent mechanism of phase contact area.

The effective interfacial area of fourth-generation packing is of particular interest, with publicly available evaluations remaining scarce. This is expected to be related to cost, complexity, and the large volumes of waste generated by the chemical absorption process. The available literature cites two papers on the effective interfacial area of the Intalox® Ultra [3] and Raschig Super Ring® [4] respectively. Their findings are summarized as previously presented in Figure 1.1, on the 3rd page of the introduction.

Both authors found that the total effective area greatly exceeded the packing surface area. This was attributed to the creation of droplets between the packing rivulets [3, 4]. The appropriate behaviour was most likely observed visually, as neither author provided validation methods. To the best of this authors knowledge, no characterisation of these inter-packing droplets currently exists.

Table 2.3:A summary of the predictive correlations for effective interfacial area found in literature [17].

Source	Effective Interfacial Area	Equation ID
Krevelen and Hoftjizer (1947) [27, 28]	$a_e = a_p \cdot (1 - \exp(5000.u_L))$	2.1
Semmelbauer (1967) [29]	$\frac{a_w}{a_p} = C_1 \cdot \left(u_L.\frac{d_p}{\upsilon}\right)^{C2} \cdot \left(\rho_L.\frac{dp^2}{\sigma_L}\right)^{0.5}$	2.2
Onda *et al.* (1967) [30, 31, 32]	$\frac{a_w}{a_p} = 1 - \exp\left(-1.45\left(\frac{\sigma_{crit}}{\sigma}\right)^{0.75} \cdot Re^{0.1} \cdot Fr^{-0.05} \cdot We^{0.2}\right)$	2.3
Bravo and Fair (1982) [33, 34]	$\frac{a_w}{a_p} = 19.76\left(Ca_L \cdot \frac{u_g.\rho_G}{a_p.\upsilon_G}\right)^{0.392} \cdot \sigma^{0.5} \cdot h^{-0.4}$ Note that his equation was translated into SI units.	
Kolev (1976) [35, 36]	$\frac{a_e}{a_p} = 0.583k_\sigma^{0.49}.Fr^{0.196}.(a_p.d_p)^{0.42}$	2.4
Zech and Mersmann (1979) [37]	$\frac{a_w}{a_p} = C_1.Re^{0.5}\left(\rho_L \cdot g \cdot \frac{d_p^2}{\sigma}\right)^{0.45} \cdot (a_p \cdot d_p)^{-0.5})$ Where C_1= 0.0222 for Berl saddles 0.0155 for Raschig Rings 0.0085 for spheres	2.5
Billet and Schultes (1993) [38, 39]	$\frac{a_w}{a_p} = 1.5 \cdot (a_p \cdot d_p)^{-0.5} \cdot \left(U_L \cdot \frac{d_h}{\mu_L}\right)^{-0.2} \cdot \left(\frac{u_L^2 \cdot \rho_L \cdot d_h}{\sigma}\right)^{0.75} \cdot \left(\frac{u_L^2}{g \cdot d_h}\right)^{-0.45}$ Where $dh = 4 \cdot \frac{\varepsilon}{d_p}$	2.6
Billet and Schultes (1999) [38]	Considering working above the loading point $h_L = h_{L,s} + (h_{FL} - h_{L,s})\left(\frac{u_v}{u_{v,FL}}\right)^{13}$ $h_{FL}^3(3.h_{FL} - \varepsilon) = \frac{6}{g} \cdot a_p^2 \cdot \varepsilon \cdot \frac{\mu_L}{\rho_L} \cdot \frac{L}{V} \cdot \frac{\rho_V}{\rho_L} \cdot u_{v,FL}$ $\frac{a_e}{a_p} = \frac{a_{e,s}}{a_p} + \left(a_{e_{FL}} - A_{e_{L,s}}\right)\left(\frac{u_v}{u_{v,FL}}\right)^{13}$ $\frac{a_{e,FL}}{a_e} = 10.5\left(\frac{\sigma_L}{\sigma_W}\right)^{0.56} \cdot (a_p \cdot d_h)^{-0.5} \cdot \left(\frac{u_L \cdot d_H}{v_l}\right)^{-0.2} \cdot \left(u_l \cdot \rho_L \cdot \frac{d_h}{\sigma_L}\right)^{0.75}\left(\frac{u_L^2}{g \cdot d_h}\right)^{-0.45}$	2.7
Kolov (2006) [4]	$\frac{a_e}{a_p} = K_0 + K_1 * \left(\frac{\rho_L \cdot g}{a_p \cdot \sigma_L}\right)^{K_2} \cdot Fr^{K_3} \cdot (a_p \cdot d)^{K_4}$ Where d is the nominal packing diameter in m $K_0 = 0.37$ $K_1 = 4.5$ $K_2 = 0.45$ $K_3 = 0.17$ $K_4 = -1.03$	2.8
Rejl et al. (2009) [16]	$a_e = 48.9 \cdot B^{0.0567 - 0.132logB}$ for Pall® Ring 25mm $a_e = 62.3 \cdot B^{0.187 - 0.0184logB}$ for Pall® Ring 50mm B = Liquid loading in $m^3.m^{-2}.h^{-1}$	2.9

2.2.1.3 Perceived Shortcomings in Kinetic Characterisation Literature

Following the discussions above, the literature provides an abundance of empirically regressed constants for effective interfacial area models, highlighting the need for more fundamental modelling approaches. Additionally, modern advances in internal design have placed renewed focus on inter-packing liquid droplets as a source of interfacial surface area [3]. To date, no attempts have been made to experimentally quantify and characterize these droplets in vapour-liquid contacting columns.

Therefore, this dissertation focuses on improving the fundamental understanding of the inter-packing liquid distribution by means of EIT measurements and mathematical manipulation of related data. Advances in this area should also aid future research in understanding the design parameters that affect the interfacial area.

2.2.1.4 Kinetic Characterisation using the EIT Method

Tomography methods are limited to the evaluation of the interfacial area (a) and not the effective area (a_e). For this reason, the proposed EIT method did not attempt to evaluate the effective interfacial area but rather the apparent interfacial area. The kinetic characterisation of the packing itself will consequently be limited to a comparative study, i.e., the difference in inter-packing droplet surface area between second and fourth generation random packing. Additionally, the increased fundamentally in clarifying the inter-packing droplet distributions and their variations with physical properties, is expected to provide future authors with tools to reduce the number of regressed constants.

The kinetic characterisation of random packing, and explicitly the interfacial area, establishes an interdependent relationship with the hydrodynamics. The increased interfacial area through droplet creation is likely accompanied by pressure drop and liquid hold-up. Section 2.2.2 therefore offers a systematic discussion on the concepts related to hydrodynamic characterisation.

2.2.2 Hydrodynamic Characterisation

The hydrodynamic capacity of column-internals is defined as the hydraulic region of operability and is based on the liquid and vapour loadings. Four parameters characterize the range of packed column operability:

[1] Pressure Drop,
[2] Liquid Hold-up,
[3] Flooding Point,
[4] Loading Point.

2.2.2.1 Pressure Drop

Phase contacting columns are designed to operate at optimum economic conditions. Therefore, the rationale for pressure drop reduction is self-explanatory, as it reduces reboiler duties and, subsequently, energy consumption (column pressures under 20 bar) [2].

Packed column pressure drop evaluations are subdivided into a dry bed- and irrigated bed pressure drop. The former referring to the inherent resistance of packing pieces to vapour flow, in the absence of liquid. The dry bed pressure drop is directly proportional to the squared superficial velocity (u_s^2) and is used as an integral parameter in various literature models to characterise packing (packing constants) [22].

The alternate irrigated bed pressure drop is evaluated under conditions of counter-current liquid and vapour flow. The descending liquid wets the packing, creating a combination of streams and droplets in the void spaces. The subsequent reduction in cross-sectional open area increases the vapour velocity and the accompanying frictional forces [40, 41]. Irrigated bed pressure drop is consequently used as a measure of hydrodynamic operability within packed columns, as an increase in the shear forces inevitably lead to inoperability through flooding. This phenomenon is discussed further in section 2.2.2.4.

A schematic of random packing pressure drop data is presented in Figure 2.2. The relevant graph illustrates the pressure drop behaviour of 1.5" FlexiRing® using an air / water system (obtained from Lamprecht [2]). The *A-A* and *B-B* lines are used in reference to the loading and flooding points, and are respectively discussed in sections 2.2.2.3 and 2.2.2.4. It should be noted that the presented estimation of flooding (*B-B* line) is based on the infinite pressure drop definition (see section 2.2.2.4). The exact flooding point consequently varies, where higher vapour loadings are expected for the definitions related to efficiency and complete hydraulic inoperability.

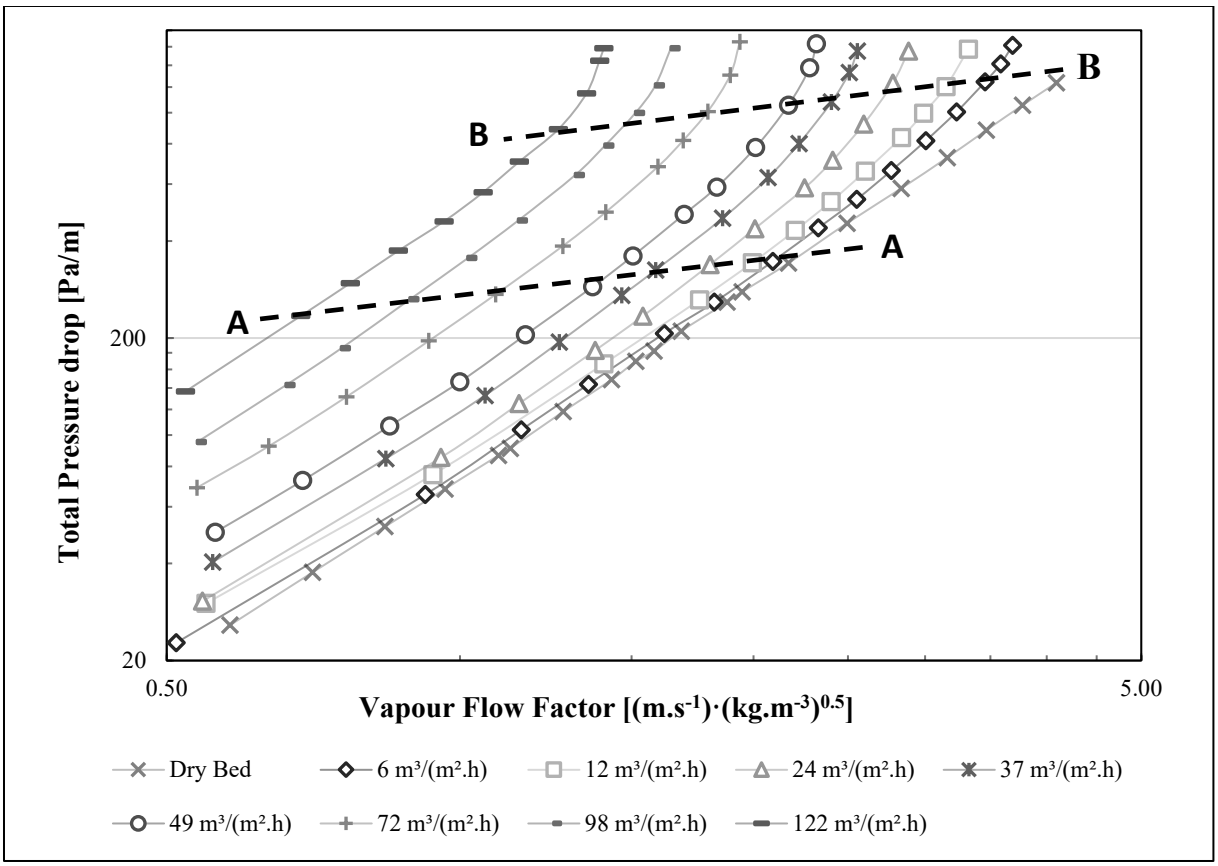

Figure 2.2: Pressure drop of 1.5" FlexiRing® using an air / water system as reference. The data have been obtained from Lamprecht [2] .

Figure 2.2 illustrates the explicit dependency between liquid and vapour loadings, and irrigated pressure drop. The dependence emanates from the decreased open area and increased vapour-liquid interactions (friction and shear forces). Inter-packing liquid behaviour and distribution are consequently expected to have a cascading effect on pressure drops.

2.2.2.2 LIQUID HOLD-UP

The liquid hold-up is defined as the liquid-occupied volume fraction (sans packing) for a set of operating conditions. The relative volume- fraction is distinctly related to pressure drop, with the shear forces of vapour-liquid contact affecting the momentum balance of the downward flowing liquid. The upward flowing vapour consequently counteracts the downward liquid momentum and increases the residence time. Liquid hold-up data are commonly used in rate-based column simulations for reaction residence times and heat transfer approximations. A graph illustrating the liquid hold-up behaviour of 1.5" FlexiRing® is presented in Figure 2.3. The data have been sourced from Lamprecht [2].

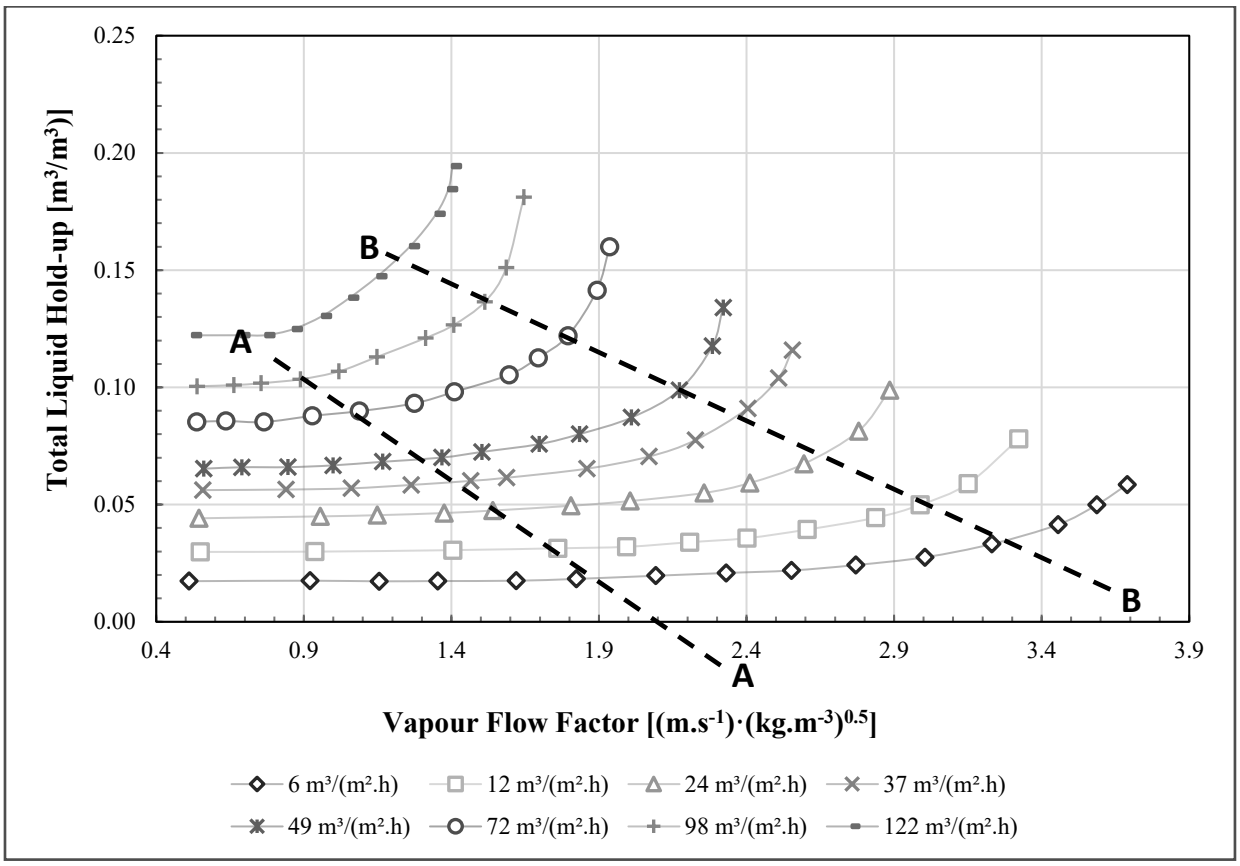

Figure 2.3: Liquid Hold-up data for 1.5" FlexiRing® using an air / water system as reference. The data were reproduced from Lamprecht [2].

Conventional measurement of liquid hold-up is based on the dropout- or collection methodologies, which consider the total liquid volume within the bed at steady-state, with quantifications performed through near-instantaneous shutdown and volume measurement. The measured values incorporate two hold-up constituents, namely static and dynamic. The dynamic element of liquid hold-up refers to the

fluid volume that is easily drained after shut-down, while the static component refers to the liquid that remains trapped in crevices between the packing.

The interdependence and trade-off between pressure drop and liquid hold-up are evident in Figure 2.2 and 2.3. However, as indicated before, these conventional strategies only offer an overall perspective without considering the mechanisms and distributions that produce increased liquid hold-up and pressure drop. This is presented as a shortcoming of conventional hydrodynamic characterisation.

Based on the premise of this dissertation, dynamic liquid hold-up is further be subdivided into:

[1] The volume fraction associated with liquid layers on (attached to) packing material/surface.
[2] The volume fraction associated with inter-packing "suspended" liquid droplets.

Thereby proposing:

$$h_{l,Total} = h_{l,surface} + h_{l,suspended} \quad 2.10$$

2.2.2.3 Loading Point

Packed column loading and flooding points are used to determine the minimum and maximum column operating conditions. The loading point is represented by the A-A lines in Figure 2.2 and 2.3. Below this point, the liquid hold-up is considered a sole function of liquid flow rate and liquid-vapour physical properties. Additionally, the pressure drop force transfer is considered sufficiently low to have a marginal effect on the liquid flow path [43]. The loading point is considered the lower limit for reasonable and economically viable operation, with HETP decreasing with an increase in vapour loadings beyond this point.

Dramatic increases in the liquid hold-up, however, can lead to a phenomenon called flooding. At this point, the excessive pressure drops from shear forces limit the descent of the liquid, leading to an increased HETP and ultimately to a non-functional column operation. The loading point is represented by the A-A lines in Figure 2.2 and 2.3.

2.2.2.4 Flooding Point

No universal definition exists for flooding, with 20 different literature sources citing different interpretations based on their research [22]. Typical descriptions, however, refer to:

[1] Visual observations of upward-moving liquid [2, 44],
[2] Pressure drop evaluations, where the pressure drop tends to infinity [2, 44],
[3] A percentage of entrainment specified as flooding [45, 38],
[4] A liquid level builds up above the packing [46],
[5] Reduction in separation efficiency, (HETP increase) [42]
[6] Complete Inoperability [22].

Regardless of the discrepancies in the exact definition of flooding, the literature is clear that a column should not be operated close to the flooding point (B-B lines). Therefore, the accurate characterisation of the hydraulic limits of operation is considered vital to ensure operations remains within the viable range between the loading and flooding points. The flooding point is represented by the B-B lines in Figure 2.2 and 2.3.

Hydrodynamic characterisation of packed columns is often considered intuitive when compared to the sophisticated methods of kinetic characterisation, detailed in Section 2.2.1. The presented dissertation therefore opted to stick to a brief overview of the hydrodynamic methodology and refer readers to the extensive work of Lamprecht [2] and Kister [22].

2.2.2.5 Historic Hydrodynamic Characterisation and Modelling

An abundance of literature sources have characterized and modelled the hydrodynamic behaviour of column-internals. The relevant models are divided between empirical charts and semi-theoretical models. Among the empirical models are those proposed by McNulty and Hsieh [47], Kister and Gill [22], Spiegel and Meier [48], and Robbins [49]. These models are simplistic but lack the ability to estimate liquid hold-up. They offer limited applicability for non-aqueous systems, producing absolute errors as significant as 60% [50].

Semi theoretical models were proposed by Texas University (SRPII) [33, 51], Delft [24], Billet [38, 52] and Maćkowiak [53]. These models represent packed columns as a series of inclined wetted wall columns, between which the liquid and vapour are continually split [2]. Pressure drop is considered through the summation of skin friction, drag friction and flow path changes [2]. The liquid hold-up is deemed to reduce the vapour flow area (voidage) through the thickening of the liquid film on the packing.

The presented work considers the Billet [38, 52] and Maćkowiak [53] models, as they form a representative sample of the available literature. Both models claim predicted pressure drop values to within an absolute error of 15%, with the Billet model asserting liquid hold-up predictions to within 6.7% [2, 42, 53, 52].

2.2.2.5.1 Billet: Pressure Drop

The Billet model considers pressure drop as a series of liquid streams passing vertically through the packing [38, 2, 52]. The available open area is equated to the packed bed voidage minus the liquid hold-up. The packed bed pressure drop is subsequently calculated by Equations 2.11 to 2.13

$$\frac{\Delta P}{H} = \Psi_L \left(\frac{a_p}{\varepsilon - h_L}\right) \cdot \left(\frac{F_v^2}{2}\right) \cdot \left(\frac{1}{K}\right) \quad 2.11$$

$$\Psi_L = C_{P,O} \left(\frac{64}{Re_V} + \frac{1.8}{Re_v}\right) \cdot \left(\frac{\varepsilon - h_L}{\varepsilon}\right)^{1.5} \cdot \left(\frac{h_L}{h_{L,s}}\right) \cdot \exp\left(C_1 \cdot \sqrt{Fr_L}\right) \quad 2.12$$

$$C_1 = \frac{13300}{a_p^{\frac{3}{2}}} \quad 2.13$$

Where:

$\boldsymbol{C_{P,O}}$ is a packing specific constant for the particle geometry

$\boldsymbol{Fr_L}$ is the liquid *Froude* number

The remaining parameters are presented in the glossary for reference.

2.2.2.5.2 Billet: Liquid Hold-up

Billet produced two different models for the prediction of the liquid hold-up in packed columns. The first in 1993 [52], suggested a fundamental relationship between flooding velocity and the hold-up at the flooding point. This approximation suggested that vapour loadings above the loading point increased the liquid hold-up by increasing the liquid film thickness [52]. The relevant liquid hold-up model is presented in Equations 2.14 to 2.18.

$$h_L = h_{L,s} + \left(h_{FL} - h_{L,s}\right) \cdot \left(\frac{u_v}{u_{v,FL}}\right)^{13} \quad 2.14$$

$$h_{FL}^3 (3.h_{FL} - \varepsilon) = \frac{6}{g}.a_p^2.\varepsilon.\frac{\mu_L}{\rho_L}.\frac{L}{V}.\frac{\rho_V}{\rho_L}.u_{v,FL} \qquad \text{for } \frac{\varepsilon}{3} \leq h_{F,FL} \leq \varepsilon \quad 2.15$$

$$\frac{a_e}{a_p} = \frac{a_{e,s}}{a_p} + \left(a_{e_{FL}} - a_{e_{L,s}}\right)\left(\frac{u_v}{u_{v,FL}}\right)^{13} \quad 2.16$$

$$\frac{a_{e,FL}}{a_e} = 10.5 \cdot \left(\frac{\sigma_L}{\sigma_W}\right)^{0.56} (a_p.d_h)^{-0.5} \left(\frac{u_L.d_H}{v_l}\right)^{-0.2} \left(u_l \cdot \rho_L.\frac{d_h}{\sigma_L}\right)^{0.75} \left(\frac{u_L^2}{g.d_h}\right)^{-0.45} \quad 2.17$$

$$h_{L,s} = \left(12 \cdot \frac{1}{g} \cdot \frac{n_L}{\rho_L} u_L \cdot a_P^2\right)^{\frac{1}{3}} \cdot (a_e)^{\frac{2}{3}} \quad 2.18$$

In later publications (1999) [42], the approximation of flooding hold-up was revised, citing that liquid flow channels undergo permanent flow changes and wet the packing partly. The revised hold-up model for “real” columns is presented in Equations 2.19 to 2.26.

$$\frac{a_e}{a_P} = C_h \left(\frac{u_L \cdot \rho_L}{a_P \cdot \eta_L}\right)^{0.15} \cdot \left(u_L^2 \cdot \frac{a_p}{g}\right)^{0.1} \text{ for } Re_L \leq 5 \quad 2.19$$

$$\frac{a_e}{a_P} = 0.85 \cdot C_h \cdot \left(\frac{u_L \cdot \rho_L}{a_P \cdot \eta_L}\right)^{0.255} * \left(u_L^2 \cdot \frac{a_p}{g}\right)^{0.1} \text{ for } Re_L > 5 \quad 2.20$$

$$h_{L,FL} = 2.2 \cdot h_L \cdot \left(\frac{\eta_L \cdot \rho_W}{\eta_V \cdot p_L}\right) \quad 2.21$$

$$u_{V,FL} = \sqrt{2} \cdot \sqrt{\frac{g}{\psi_{FL}} \left(\frac{(\varepsilon - h_{L,FL})^{\frac{1}{3}}}{\varepsilon^{0.5}}\right) \sqrt{\frac{h_{F,L}}{a_P} \cdot \frac{\rho_L}{\rho_V}}} \quad 2.22$$

$$\psi_{FL} = \left(\frac{g}{C_{FL}^2}\right) \cdot \left(\frac{L}{V} \cdot \sqrt{\frac{\rho_V}{\rho_L}} \cdot \left(\frac{\eta_L}{\eta_V}\right)\right)^{-2 \cdot n_{FL}} \quad 2.23$$

$$u_{L,FL} = \left(\frac{\rho_V}{\rho_L}\right) \cdot \left(\frac{L}{V}\right) \cdot u_{v,FL} \quad 2.24$$

Where:

$$n_{FL} = -0.194 \qquad \text{for } \frac{L}{V} \cdot \sqrt{\frac{\rho_V}{\rho_L}} \leq 0.4 \quad 2.25$$

$$n_{FL} = -0.708 \qquad \text{for } \frac{L}{V} \cdot \sqrt{\frac{\rho_V}{\rho_L}} > 0.4 \quad 2.26$$

$$C_{FL} = 0.6244 \cdot C_{FL} \cdot \left(\frac{\eta_L}{\eta_V}\right)^{0.1028} \quad 2.27$$

In summary, the Billet models offer acceptable fit and applicability to packing from the first two generations, with an absolute error of 6.7% for column hold-up and 9.1% for pressure drop [38, 52, 2]. However, limited data are available on modern packings. The billet models are expected to correlate trends inadequately in modern high open area packings based on the assumption of negligible liquid hold-up resulting from streams and spontaneous flow path changes. This was supported by the experimental data from Minne [5], presenting pressure drop (loading point) deviations between 68 and 285% (Absolute Average Relative Error - ARE) for the Intalox® Ultra size O (air / water) and 19-78% for the smaller size A.

2.2.2.5.3 Maćkowiak: Liquid Hold-up

The Maćkowiak multiphase models [54, 40, 55] use a simple calculation procedure, requiring no experimental data on the packing, except for a flooding point and packing constant. The aforementioned channel-based modelling approach was further extended to dry-bed (single-phase) approximations (2009 [41]), although this was considered outside the scope of this work.

The multiphase models (1990) [56, 40] are based on the characteristic capillary length approach (Equation 2.29), approximating the Sauter mean diameter of liquid droplets. The calculation procedure disregards the effect of gravity in the descending liquid droplets, as it is assumed to be cancelled by drag force (descending at terminal velocity). The aforementioned implies that the liquid droplet size is the sole function of liquid physical properties.

The liquid droplet sizes were experimentally evaluated by Maćkowiak [54, 56], in a 0.1m diameter column stacked with aligned Bialecki Rings (25mm and 50mm). The experimental evaluation was conducted on counter-current liquid extraction and considered loadings below 57 $m^3m^{-2}h^{-1}$.

The equations governing the liquid hold-up in the Maćkowiak model are presented in Equations 2.28 to 2.35.

$$u_{V,FL} = C_{FL} \cdot \varepsilon^{1.2} \cdot \left(\frac{d_h}{d_T}\right)^{\frac{1}{4}} \cdot \left(\frac{d_T \cdot \rho_L \cdot g}{\rho_V}\right)^{\frac{1}{2}} \cdot \left(1 - \frac{h_{L,FL}}{\varepsilon}\right)^{\frac{7}{2}} \quad 2.28$$

$$d_T = \sqrt{\frac{\sigma_L}{(\rho_L - \rho_V) \cdot g}} = Sauter\ mean\ diameter \quad 2.29$$

$$h_{L,FL} \cong \left(\frac{\varepsilon}{0.4(1-\lambda_0)}\right) \cdot [(1.44 \cdot \lambda_0^2 + 0.8 \cdot \lambda_0)(1 - \lambda_0^2)^{0.5}) - 1.2\lambda_0] \quad 2.30$$

$$h_{L,FL} \cong \left(\frac{\varepsilon}{0.24(1-\lambda_0)}\right) \cdot [(1.254 \cdot \lambda_0^2 + 0.48 \cdot \lambda_0)(1 - \lambda_0^2)^{0.5}) - 1.12\lambda_0] \quad 2.31$$

$$\lambda_0 = \frac{u_L}{u_{V,Fl}} \quad 2.32$$

$$h_L = h_{L,FL} - (h_{L,Fl} - h_{L,S}) * \left[1 - \frac{(F_V/F_{V,FL}) - 0.65}{0.35}\right]^{0.5} \quad 2.33$$

$$h_{L,S} = 2.2 \cdot \sqrt{B_L} \quad 2.34$$

$$B_L = \left(\frac{\mu_L}{\rho_L \cdot g^2}\right)^{1/3} \cdot \left(\frac{u_L}{\varepsilon^3}\right) \cdot \left(\frac{1-\varepsilon}{d_P}\right) \quad 2.35$$

2.2.2.5.4 Maćkowiak: Pressure Drop

The Maćkowiak pressure drop equations are depicted in Equations 2.36 to 2.37.

$$\frac{\Delta P}{H} = 3.8 \cdot \mu_L \cdot \left(\frac{1-\varepsilon}{\varepsilon^3}\right)\left(\frac{F_V^2}{d_p \cdot K}\right)\left(1 + \left(\frac{h_L}{1-\varepsilon}\right)\right)\left(1 - \frac{h_L}{\varepsilon}\right)^{-3} \quad 2.36$$

$$K = \left(1 + \frac{2}{3} \cdot \frac{1}{1-\varepsilon} \cdot \left(\frac{d_p}{d_S}\right)\right)^{-1} \quad 2.37$$

The Maćkowiak (1990) models attempted to improve the fundamental understanding of column hydrodynamics by using the Sauter mean diameter in Equation 2.29. This approach implies that the liquid body (liquid hold-up) is distributed into spherical droplets of a single size, which means that the liquid volume comprises droplets with a diameter of 2.6 mm for air / water evaluations. This simplification warrants further study.

2.2.2.6 Shortcomings of Current Hydrodynamic Characterisation Methods

Several shortcomings in the literature were identified in the evaluation of hydrodynamic characterisation.

These are provided in bullet point format.

[1] Only Maćkowiak [54, 56] attempted to evaluate the droplet sizes in packed columns, with the remaining literature using dimensionless models and regressed constants, to the best of this authors knowledge. The remaining models thereby fail to fundamentally correlate hydrodynamic performance differences with the design differences in the packing.

[2] The Maćkowiak model [54, 56] attempts to quantify the mean diameter of liquid droplets through a capillary length approach. This approach assumes terminal liquid velocity. The validity of the capillary length approach was experimentally evaluated in a small counter-current liquid-liquid setup. However, the experimental system experienced substantial wall effects due to the small diameter and evaluated the rising phase as the dispersed phase. This contrasts with the workings of regular columns, where normal operations use a continuous vapour phase.

[3] Further research into the fundamental effect of liquid and vapour physical properties on droplet sizes in packed columns is required to improve the understanding and enhance modelling.

Having provided an overview of the typical state-of-the-art characterisation models and their limitations, the next chapter proceeds to describe multiphase flow imaging techniques that can be used to improve our understanding of the fluid behaviour in columns.

3. MULTIPHASE FLOW IMAGING

Multiphase flow is broadly defined as the flow of two or more immiscible components with definable phase boundaries. Industrial examples include immiscible liquid transport, steam lines with condensate and vapour, as well as the transport of slurries and suspensions. Of primary interest to this study was the evaluations of vapour-liquid flow within randomly packed columns.

3.1 VAPOUR-LIQUID FLOW PATTERNS

An infinite number of vapour-liquid distribution patterns exist in phase contacting columns due to the presence of highly deformable interfaces [14]. The distributions, however, can be broadly categorised according to their flow regime. The parameters that govern the regimes include flow rates, direction, pipe geometry and fluid properties.

Counter-current columns are often modelled hydrodynamically through representation as a combination of vertical and horizontal wetted wall columns (See hydrodynamic characterisation section 2.2.2). For this reason, the widely used flow regimes for vertical and horizontal circular pipes are presented in Figure 3.1 [57].

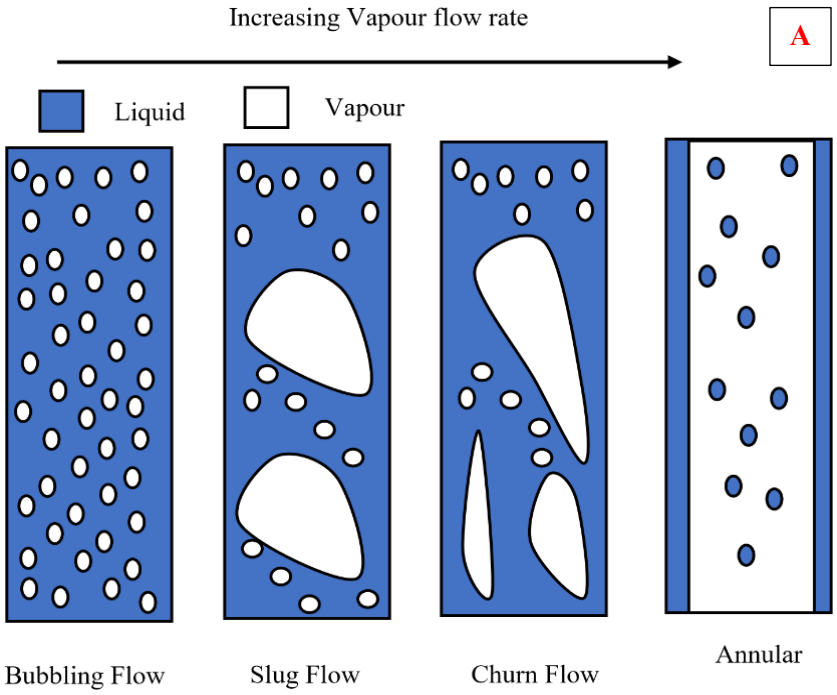

Figure 3.1A: Schematic of the multiphase flow regimes present in pipes. Vertical ; Redrawn from Da Silva [57]

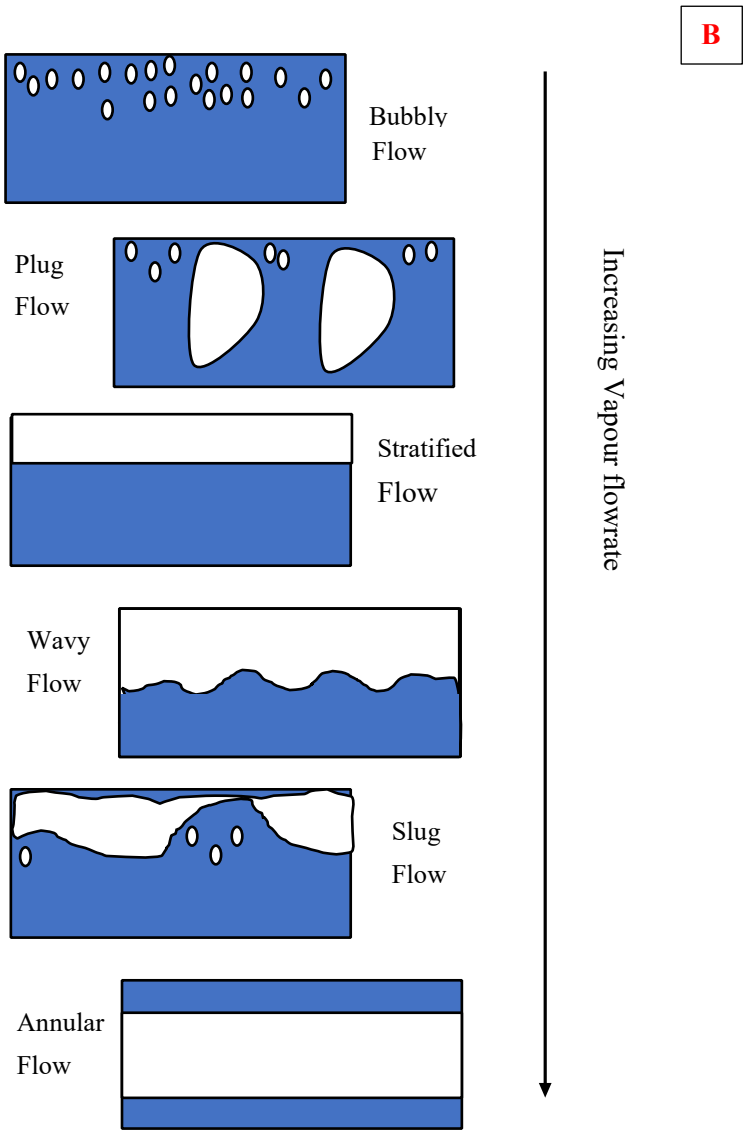

Figure 3.1B: Schematic of the multiphase flow regimes present in pipes. Horizontal.; Redrawn from Da Silva [57]

Counter-current columns are assessed and modelled through annular and wavy flow approximations (Figure 3.1). However, three-dimensional transient and fundamental modelling of counter-current columns are very sophisticated due to the multiple deformable and moving interfaces. This is further compounded by the difficulties in modelling micro-turbulence [14]. Fundamental analytical predictions for multiphase flow are therefore not readily achievable and outside the scope. Experimental multiphase measurement techniques are thus considered.

3.2 MULTIPHASE FLOW MEASUREMENT

Online measurement and evaluation of multiphase distributions is an essential measurement for various industrial applications. As a result, a variety of attempts have been made to develop multiphase measuring systems with two or more phases. The relevant techniques are discussed in the following sections.

3.2.1 PHASE FRACTION MEASUREMENT

Vapour-liquid phase factional measurements are commonly used to evaluate void fraction and liquid hold-up, depending on whether the liquid or vapour phase is of interest. Both quantities are interchangeable, as the liquid and void(vapour) fractions are required to sum to unity.

$$x_L + x_{Void} = 1 \tag{3.1}$$

The phase fractions are mathematically described using a phase density function ($\mathbf{P_k}$). A binary representation the phase density function is depicted in Equation 3.2 where $\boldsymbol{k}$ is the phase of interest, $\boldsymbol{x}$ is the given position and $\boldsymbol{t}$ a given time:

$$P_k(x,t) = \begin{cases} 1 & if\ x\ \in phase\ k \\ 0 & if\ x\ \notin phase\ k \end{cases} \tag{3.2}$$

The relative phase fractions are considered invaluable for the characterisation of multiphase flows as the values are used to evaluate mixture densities, viscosities, and averaged velocities. Averaging the density function ($\mathbf{P_k}$) over spatial and temporal domains consequently yields a time-averaged value.

Phase density functions can be considered through either local or cross-section measurement strategies. The local phase density function is typically measured using a needle-shaped probe, evaluating conductivity, capacitance, temperature, or electrochemical disturbances at the sensor's tip [58, 59]. The time-averaged function can, therefore, be written according to Equations 3.3 to 3.4. Where $\boldsymbol{T_k}$ is the cumulative residence time of the predetermined phase and $\boldsymbol{T_{\notin k}}$ the cumulative residence in its absence [58].

$$\alpha(x) = \lim_{T\to INF} \frac{1}{T} \int_0^T P_k(x,t)dt \tag{3.3}$$

$$\alpha(x) = \frac{T_K}{T} = \frac{T_k}{T_{\notin k} + T_k} \tag{3.4}$$

The local phase density function is translated to an averaged area or cross-sectional function using Equation 3.5. Where $\boldsymbol{A_k}$ is the cumulative area of the predetermined phase and $\boldsymbol{A_{\notin k}}$ the in its absence [58].

$$\alpha_{\text{cross-sectional fraction}} = \lim_{A\to INF} \frac{1}{A} \int_0^A P_k(x,t)dA = \frac{A_k}{A_{\notin k} + A_k} \tag{3.5}$$

Cross-sectional evaluations typically use radiation attenuation or electrical impedance as the physical measurement principle. Typical setups consist of a source (either Gamma, X-Ray, or an electrical signal) and a detector on the opposite side of the multiphase mixture. A schematic of a typical radiation attenuation setup is provided in Figure 3.2.

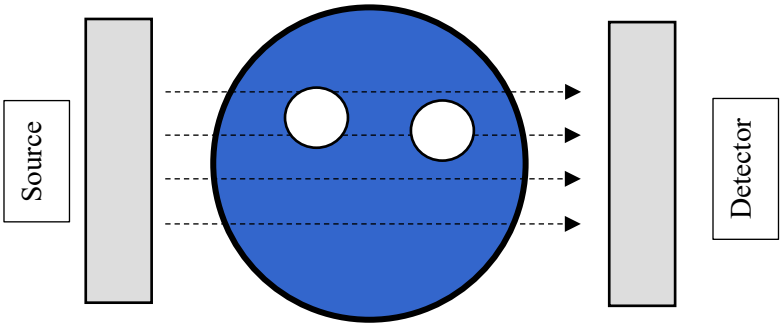

Figure 3.2:A radiation attenuation depiction showing cross-sectional phase area measurements.

The X-ray attenuation example was chosen for clarity as the rays conventionally follow a straight and parallel path. At the same time, electromagnetic waves form concentric circles of similar field density from the source. The phase density function for a homogeneous medium with paralleled, mono-energetic beams is presented in Equation 3.6.

$$I = I_0 . e^{-\mu d} \qquad 3.6$$

Where:

- I_0 represents the incident radiation,
- μ represents the absorption coefficient of the medium
- d represents the linear distance travelled through the medium.

Electrical impedance measurements are alternatively used in cross-sectional phase fraction evaluations, exploiting conductivity and relative permittivity differences. Impedance measurements offer a high-frequency response at reduced costs. The setups are conventionally comprised of electrodes placed at the perimeter of the multiphase medium across which differences in electrical impedance is calculated.

The local and cross-sectional phase fraction evaluations are further enhanced through incorporation into tomography systems. This entails using multiple samples across a vessel to provide an image of the flow distributions.

3.2.2 Tomographic Imaging of Multiphase Flow

Tomographic imagery refers to the generation of two-dimensional slices through an object or medium. Subsequently, computational tomography evaluates physical properties through an enclosed vessel and relates it to the phase fraction (as discussed in Section 3.2.1) using advanced algorithms. An illustrative schematic is provided in Figure 3.3.

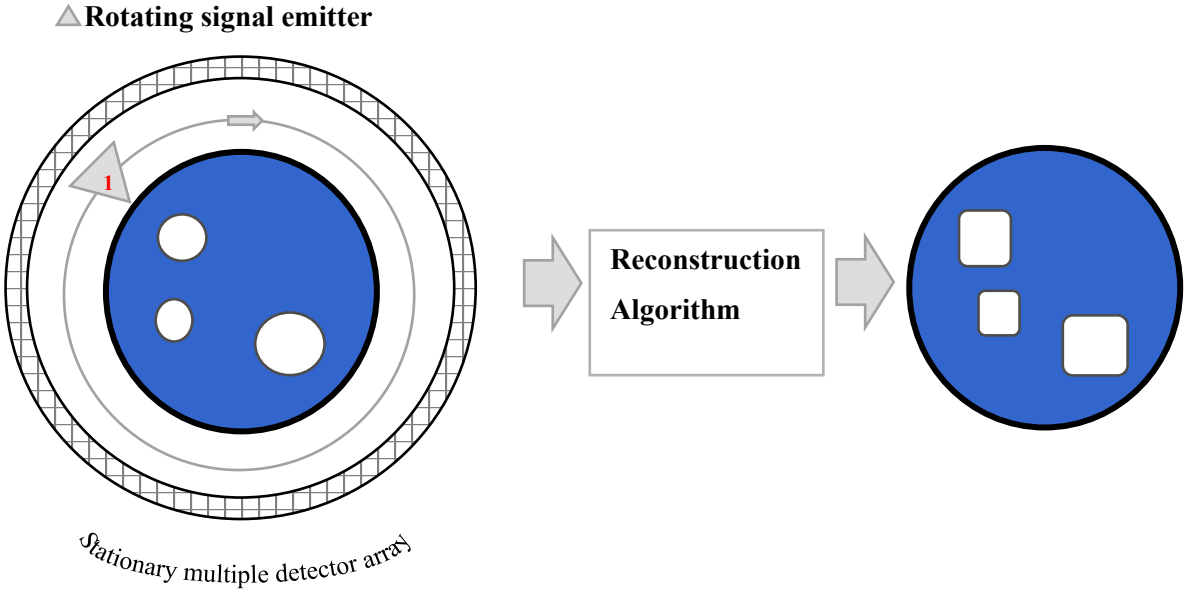

Figure 3.3: A schematic of conventionally computed tomography systems used in XT-scan and X-Ray systems [138, 11]. The signal emitter is shown rotating to evaluate the system from all angles. The data from the various angles are then combined into a single 2D image.

The process entails sequentially taking measurements from different sensors around the periphery, with either a single rotating emitter (Figure 3.3) or multiple discrete emitters (Figure 1.2). In so doing, measurements taken from different angles and reconstructed using a computer algorithm to provide a slice of the vessel phase properties. This process is similar to CT (Computed Tomography using X-rays) and MRI (Magnetic Resonance Imagery) scans used in medical diagnosis [60].

A variety of tomographic imaging techniques are used industrially for multiphase quantification. An illustration of the various techniques and their attributes is presented in Table 3.1, adapted from Da Silva [14].

Table 3.1: Comparison of tomography methods found in literature [14, 10, 11].

Technique	Description	Imaging Frequency	Spatial Resolution	Cost	Other Comments
X-Ray, Gamma-ray, and neutron tomography	Related to the cross-sectional phase measurements presented in Section 3.2.1. The projection sets are collected either from a rotating source and sensor or multiple sensor pairs arranged around the vessel or pipe.	Minutes	≈ 1mm 1% of Diameter	Very High	Bulky and complex apparatus. Safety concerns
Positron emission tomography (PET)	Uses gamma-ray emitting isotopes and radiation detectors to reconstruct tracer distributions. Therefore, multiphase systems can be reconstructed by labelling and tracking one of the phases through its radioactive trail.	Minutes	2-5mm	Very High	
Magnetic resonance imaging (MRI)	Exploits the phenomenon of hydrogen nuclei magnet resonance based on a specific radio frequency and therefore measures differences in hydrogen atoms. This provides excellent applicability to hydrogen-rich components such as water and hydrocarbons	Minutes	≈ 1mm	Very High	Not suitable for electrically conductive or magnetic vessels.
Ultrasound tomography	Based on evaluating changes in acoustic impedance properties between objects (Speed of sound through objects)	Milliseconds	2-5mm	Medium	Suitable for low void fractions
Optical tomography	It uses low energy light waves, either infrared (IR), visible or Ultraviolet (UV) and measures the excitation profiles through various media. The variations in excitation behaviour are exploited used to evaluate multiphase distributions.	Microseconds	2-5mm	Low	Requires visibility and transparent walls or fluids
Electrical tomography (ET).	Electrical impedance exploits differences in conductivity (ERT) and capacitance (ECT) to evaluate multiphase flow distributions. The method uses equally spaced electrodes within the vessel and measures variations in either capacitance or conductivity between them. A full two-dimensional image is collected by measuring the impedance differences between the electrodes. ET offers the advantage of evaluating either conductive and non-conductive systems with high imaging rates and at a relatively low cost compared to the other methods.	Milliseconds	5mm or 5% of Diameter	Low	
High-speed camera	Combination of high-speed imagery with image analyses software	Microseconds	≈ 1mm	Medium	Requires visibility

3.3 X-RAY IMAGING IN COLUMNS

The visual representation of column inner workings has been the centre of various studies since the 1950's. Evaluations have progressed from the use of coloured dies and floating balls toward X-ray and tracer imagery [6, 7, 10, 11]. However, radioactive computational tomography has been limited in its application due to the high equipment costs and inherent safety risks. Additionally, the available studies historically listed problems related to the slow rate of imaging frequency. Therefore, the literature leading up to 2010 predominantly reflected time-averaged rather than instantaneous imagery which is limited to perfect steady-state. This restricted the historical application of X-ray computed tomography to structured columns, as fluids were thought to flow smoothly across the packing interfaces with limited deviations expected over time.

Although limited, some literature evaluations were found considering X-ray computed tomography on randomly packed columns. Among these are the studies presented by Wang et al. [61] and Yin et al. [62] evaluating porosity and local liquid hold-up distributions in a 600mm column of 1" Pall® Ring. Their evaluations, however, were limited to a spatial resolution of 75mm. Additionally, Toye et al. [7] proposed a rotating experimental setup of similar size and evaluated Cascade Mini-Ring (1A) at a spatial resolution of 1.8mm. Unfortunately, due to the mass of the rotating setup, the system was limited to an imaging rate of 1 column image every 150 seconds. The shortcomings and complexity of the described experimental techniques consequently limited their use in random packing evaluations.

Recent advances in Ultrafast X-Ray computed tomography from Schubert et al. [63] , and Janzen et al. [11] increased sampling speeds to 2000 images/s with a spatial resolution of 1mm. The experimental setup used a ring-based detector around the whole structured column. Although having an excellent spatial resolution, the author reported difficulties in accurately resolving thin liquid films (for Montz B1-500MN structured packing), leading to liquid-hold-up underestimations in the order of 300% [11].

Motivated by the inherent safety risks, high costs, and inability to adequately weigh smaller particle effects, alternative tomography methods for randomly packed columns were evaluated. Electrical impedance tomography (EIT) was chosen based on various criteria, including cost, imaging frequency and spatial resolution. The basic concepts of impedance are discussed in the succeeding section for readers unfamiliar with electrical impedance. Readers familiar with the concept, including those of capacitors and inductors, are advised to advance to Section 3.4.3.

3.4 BASICS OF ELECTRICAL IMPEDANCE

Electrodynamics define electrical impedance as the non-steady-state relationship between voltage and current. Impedance is therefore similar to the widely known electrical resistance, defined by Ohm's law in Table 3.2. The predominant difference is that the electrical impedance considers time-variant electrical properties [64]. Alternating current (AC-current) is exemplary of this, with the magnitude and

direction of the voltage and current in continual flux. A comparison of resistance and impedance is given in Table 3.2.

Table 3.2: Comparison: Impedance vs. Resistance.

Resistance (R)	**Impedance (Z)**
$\mathbf{R} = \frac{\mathbf{V}}{\mathbf{I}}$	$\mathbf{Z} = \frac{\mathbf{V}}{\mathbf{I}}$
Where:	Where:
$V = V$ $I = I$	$V(t) = \lvert V_m \rvert * \mathrm{Cos}(\omega t + \theta_V)$ $I(t) = \lvert I_M \rvert * \mathrm{Cos}(\omega t + \theta_L)$
	Moreover, $\mathbf{V_m}$ and $\mathbf{I_m}$ are the magnitudes
	In exponential form:
	$\mathbf{V} = \lvert V_M \rvert * e^{j(\omega t + \theta_V)}$
	$\mathbf{I} = \lvert I_M \rvert * e^{j(\omega t + \theta_I)}$
	$j = \sqrt{-1}$

The electrical impedance of a sinusoidal wave, therefore, translates to Equation 3.7. This form is further simplified using Euler's identity ($e^{j\theta} = \cos(\theta) + j\sin(\theta)$) to obtain the Cartesian vectors values of impedance [64].

$$\mathbf{Z} = \frac{\mathbf{V}}{\mathbf{I}} = \frac{\lvert V_M \rvert * e^{j(\omega t + \theta_V)}}{\lvert I_M \rvert * e^{j(\omega t + \theta_I)}} = \frac{\lvert V_M \rvert}{\lvert I_M \rvert} * e^{j(\theta_V - \theta_L)} \quad 3.7$$

$$\mathbf{Z} = \frac{\lvert V_M \rvert}{\lvert I_M \rvert} * e^{j(\theta_V - \theta_L)} = \frac{\lvert V_M \rvert}{\lvert I_M \rvert} * \mathrm{Cos}(\theta_V - \theta_L) + j\mathrm{Sin}(\theta_V - \theta_L) = R + jX \quad 3.8$$

Where the values of **R** and **X** are the respective real and complex components, determined using geometry found in Figure 3.4 [64].

$$\frac{\lvert V_M \rvert}{\lvert I_M \rvert} = Z_M = \sqrt{X^2 + R^2} \quad 3.9$$

$$\theta = \arctan\left(\frac{X}{R}\right) \quad 3.10$$

Electrical impedance is consequently considered a complex quantity (Figure 3.4) due to the use of the imaginary number system. Its value can therefore be broken down into real and complex components. The real and complex elements are respectively related to resistance(***R***) and reactance(***X***), where reactance refers to the non-resistive losses in an AC circuit due to capacitors and inductors. From this reasoning, electrical impedance is set to equate pure resistance if the phase angle ***(θ)*** is equal to zero or

180° (direct current circuits) and capacitance or inductance when the phase angle ($\boldsymbol{\theta}$) is respectively equal to ±90°.

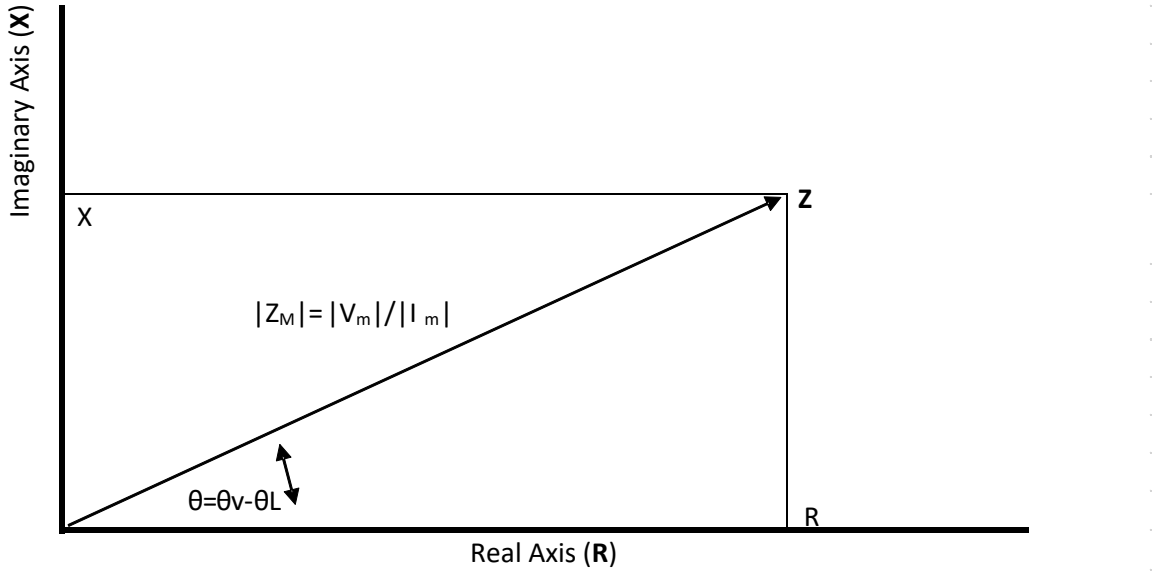

Figure 3.4 Electrical Impedance vector diagram [64] showing the contributions of both the real and imaginary constituents of electrical flow. The real component is analogous to conventional electrical resistance and the imaginary to the contribution of capacitance and inductance.

Resistance and reactance can consequently be evaluated independently using impedance, given a phase angle ($\boldsymbol{\theta}$) on any multiple 90 degrees [64]. A short discussion on the importance of resistance and reactance is given in Section 3.4.1 and 3.4.2. Pure electrical resistances conventionally have a phase angle of 0° or 180° while capacitors have 90° or 270° [65].

3.4.1 Electrical Resistance

The electrical conductivity of aqueous solutions is widely used throughout chemical engineering in evaluating water quality through the dissolved ion content [66]. The measurement principle and theoretical background are consequently well understood [67]. The ability of a solution to pass an electrical current is measured through conductance (**G**), i.e., the inverse of resistance (**R**). Where Ohm's law defines the resistance as:

$$G = \frac{1}{R} = \frac{I}{V} \qquad 3.11$$

The evaluated conductance is dependent on both the solution properties and the physical shape of the measurement cell.

A cell constant (K, Equation 3.13), is used in relating the dimensions of the measurement setup to the evaluated electrical conductivity (***κ*** in µS/cm), displayed by the analytical equipment (Equation 3.12).

$$\kappa = G \cdot K \qquad 3.12$$

$$K = \frac{L}{A} \qquad 3.13$$

where

- ***L*** represents Distance between electrodes (cm)
- ***A*** represents the area of the electrodes in the measurement cell that is in contact with the conductive fluid (cm^2)

The relationship presented in the preceding equations suggests a proportional response toward the area of the electrode exposed to the fluid. The implication is that for specific fluid (with constant ***κ***) and constant electrodes distance, the relationship simplifies to Equation 3.14. The aforementioned (proportionally) is consequently used in this study to evaluate the area of each droplet between the sampling points.

$$A = \frac{C_1}{R} \qquad i.e \qquad A\ \alpha\ \frac{1}{R}\ \alpha\ G \qquad 3.14$$

A graphical illustration is presented in Figure 3.5 to aid in the understanding of this concept, depicting two identical conductivity cells with square electrodes. Both cells are filled with the same fluid (water with a conductivity of 10µS/cm), but with differing amounts. The resistance measured in each cell is thereby inversely proportional to the two-dimensional area of the fluid within

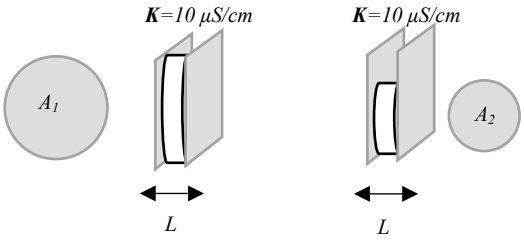

Figure 3.5: The graphical illustration of a conductivity measurement cell where the evaluated resistance is a function of the area of the fluid contacting the electrodes.

3.4.2 Electrical Reactance

Electrical reactance fundamentally refers to the inertia of electrons and their opposition to changes in their flow and/or direction [64]. For this reason, the complex reactance (***X***) in Equation 3.9 is only present in alternating current circuits. The degree to which these circuits oppose electron flow is related to whether the reactance is considered capacitive (X_c) or inductive (X_L), differing mainly in their principal method of energy storage.

3.4.2.1 CAPACITORS

Capacitors (See Figure 3.6) are comprised of two conductors divided by an insulating dielectric [68]. An applied potential difference generates an electrical field between the conductors and stores current to neutralise the potential difference. The electrical field consequently opposes changes in electron motion by either building charge or discharging depending on potential difference.

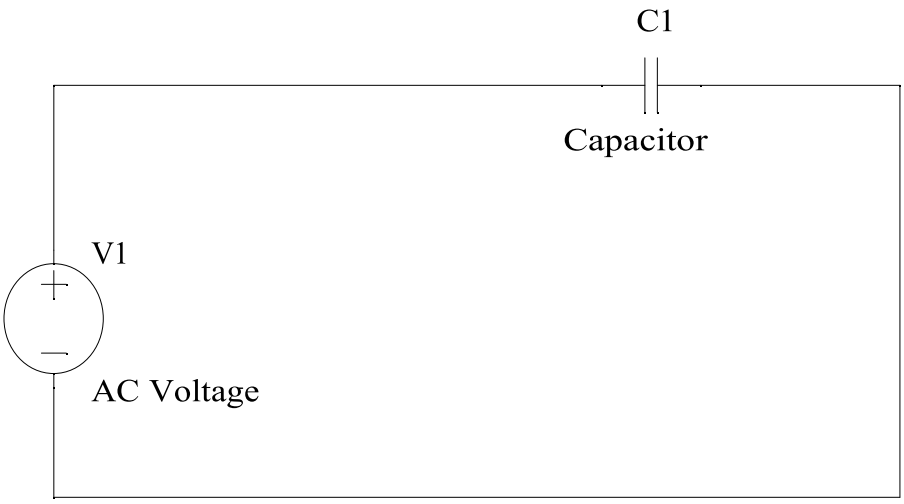

Figure 3.6:An electrical circuit depicted a capacitor [14].

The amount of stored charge is measured in *Farad*. A mathematical depiction of the stored charge storage for paralleled plate capacitors is depicted in Equation 3.15.

$$C = \frac{\varepsilon_i \varepsilon_0 . A}{d} \qquad 3.15$$

Where

- $\boldsymbol{C}$ is the capacitance in Farad,
- $\boldsymbol{\varepsilon_0} = 8.854 \cdot 10^{-12}$ and the permittivity of vacuum (F/m),
- $\boldsymbol{\varepsilon_i}$ is the relative permittivity of the dielectric, compared to vacuum,
- **A** is the area of the plates in m^2,
- **D** distance between the plates in m.

Equation 3.15 depicts the direct proportionality of capacitance to the electrical permittivity ($\boldsymbol{\varepsilon_i}$) of the dielectric insulator. Capacitors of equal area and dielectric width are therefore differentiated based on the electrical permittivity of the insulator. This forms the foundation for the adaptation of capacitance in measuring interfacial area. A system with widely varying permittivity (such as vapour and liquid) and a specified dielectric width will consequently produce a linear and measurable capacitance trend based on the area. For example, given a water droplet ($\boldsymbol{\varepsilon_i}$=80) evaluated between two wires spaced 1mm apart (Equation 3.16).

The measured capacitance is consequently directly proportional to the area.

$$C = \frac{8.854 \cdot 10^{-12} \cdot 80 \cdot A}{0.001} \quad 3.16$$

3.4.2.2 INDUCTORS

Alternatively, inductors store energy in the form of magnetic flux. The inductive magnetic flux is generated through conductive windings around a dielectric in the presence of a potential difference [69]. The magnetic field consequently opposes changes in electron flow by either increasing the field strength of discharging electrons back into the circuit. The latter is the basis for modern electricity generation.

Figure 3.7: An electrical circuit depicted an inductor [14].

$$L = \mu_i \cdot \mu_0 \cdot (A) \cdot \frac{N^2}{l} \quad 3.17$$

Where

- L is the inductance measured in Henries,
- $\mu_0 = 4\pi \cdot 10^{-7}$ and the permeability of vacuum,
- μ_i is the relative permeability medium, compared to vacuum,
- **A** is the area of the inner core of the inductor (area within the windings) in m^2,
- **l** is the length of the inductor in m,
- **N** is the number of windings.

3.4.3 SIGNIFICANCE OF IMPEDANCE MEASUREMENTS

The relevance of impedance as the principal method of tomography resides in the ability to independently evaluating both resistance and reactance, where resistance and reactance are respectively directly proportional to conductivity and electrical permittivity.

For the purposes of this document, electrical permeability and inductors will not be considered. This results from the chosen design (Section 5.1) as it experiences limited inductive forces due to the absence of spools or coils [14].

Impedance measurements are consequently able to determine both the electrical permittivity and conductivity of an object between the conductors. This is of great interest as this measurement principle applies to conductive systems through conductivity and non-conductive systems through relative permittivity. Three-phase systems can consequently be quantified using Table 3.3.

Table 3.3: Impedance decomposition table, showing the implications of the respective conductivity and capacitance measurements.

Component	High Conductivity	High Reactance
Vapour phase	No	No
Conductive aqueous phase	Yes	Yes
Non-conducting organic liquid	No	Yes

Table 3.4 presents an array of components and their literature conductivity and relative permittivity values. The listed components were evaluated using an impedance probe by Da Silva et al. with applicable accuracy [14]. These components are therefore also reasoned to be suitable for electrical impedance phase tomography.

Table 3.4: Literature conductivity and electrical Permittivity, as measured for various liquids.

Component	Conductivity (µS/cm)	Relative permittivity(ε_i)
Air	0 [70]	1 [71]
Isopropanol	0.1 [70]	19.74 [71]
Glycol	1.5 [70]	40.56 [71]
Deionized water	2-10 **	79.86 [71]
Tap water	10-60 **	79.86 [71]
Silicone Oil	0 [70]	2.78 [71]
Diethyl ether	0 [70]	4.27 [71]

* Measured in this work with an RS-Pro conductivity meter

3.5 Electrical Impedance Tomography (EIT) in Chemical Engineering

Tomography based on electrical field and matter interactions has become a prevalent part of multiphase evaluation. As a result, a variety of studies have focussed on either ERT [72] (Electrical resistance tomography) or ECT [73, 74] (Electrical capacitance tomography). To date, the adaptation of this technology into chemical engineering has been mostly confined to ERT on vertical and horizontal pipe

flows, with a handful of studies focussing on mixing [75, 76, 72, 77]. The presented studies concentrated on the axial flow variations for CFD model verification [72]. Alternatives used perimeter mounted sensors that provide a cross-sectional phase density function (see Section 3.2.1) [78]. The resulting density function lacks spatial resolution but offers applicable property averages.

A study, by Da Silva [79], was found evaluating radial pipe distributions using a dual-modality (ECT+ERT or EIT) wire mesh sensor array. The sensor offered high-speed measurements and imaging but requires expensive oscilloscope sensing capabilities.

3.6 Electrical Tomography Imaging in Columns

X-Ray tomography's inherent safety risks and high costs led authors to incorporate electrical capacitance- (ECT) and electrical resistance tomography (ERT) in structured columns. The evaluations [10, 80, 63] were primarily based on conventional electrical tomography (without a mesh-grid as depicted in Figure 3.3) and column diameters ranging from 40mm to 190mm (which is less than the minimum of 400mm recommended for evaluation of column hydrodynamics). The relevant electrical tomography systems used eight electrodes outside of the column to generate an electromagnetic field for imaging. This presented a substantial restriction in the material of construction of the column wall and packing. Metallic packing is expected to have a shielding effect (similar to a faraday cage), limiting imaging within the packing. Additionally, conventional electrical tomography is hampered by its relatively low spatial resolution of 5% of the column diameter. This spatial resolution restriction is thought to be a physical restriction of the measurement technique [81, 82].

In the case of random packing tomography, only two studies were found reported in the literature. Both studies on 25mm Pall® Ring by Grünewald et al. [8, 9] focussed on finding the critical column diameter (smallest industrially relevant diameter for pilot scale evaluations) for packed experimental setups using a wire-mesh electrical tomography (ECT) system to characterize wall effects and the radial distributions. The grid sensor itself consisted of two a 32x 32 electrode matrix (similar to the schematic in Figure 1.2) at a 1.5mm spacing. Grünewald [8] used a phase density function similar to Equation 3.2 to evaluate the liquid hold-up along the perimeter (9mm ring along the column wall) and validated the results with the conventional draining method (See section 2.2.2.2). Grünewald's liquid hold-up validations were limited to the perimeter with no consideration of the overall hold-up.

3.7 Improving Multiphase Measurements for Column-Internals

The currently available ET sensors either offer limited spatial resolution or have high costs due to the high sampling rate requirements. Therefore, this project proposed a new EIT sensor based on Da Silva's

[79] dual-modality wire-mesh design. The new design proposed a trade-off between sampling speeds and data collection costs, while remaining applicable to randomly packed columns.

Additionally, the following restrictions to current tomography systems were noted, to be improved upon in this study:

- Random packing wire-mesh electrical tomography evaluations were found limited to Grünewald et al. [8, 9]. The available studies focussed on the liquid hold-up along the column wall and validated their findings with a specialized wall collection draining setup [8]. Limited consideration was given to the global liquid hold-up. This was likely due to the small diameter of the column (ID = 288mm) and the presence of notable wall effects (3x the hold-up compared to the centre of the column).

  Tomography based liquid hold-up evaluations assume constant downward liquid velocity across the bed. The presence of extreme wall effects, as presented by Grünewald et al. [8], contradicts this assumption as the no-slip boundary condition creates varying velocity profiles. Scaling up to the industrially relevant 400mm ID in this study is expected to address this limitation.

- Conventional wire-mesh sensors increase spatial resolutions by increasing the number of parallel electrodes (Figure 1.3). Measurements produce a simple 1 or 0 at each crossing point, reflecting the presence or absence of a specific phase. However, the decreased mesh size creates additional obstructions to flow and can affect both the natural liquid flow paths and the accompanying pressure drop.

  The commercially available options are also designed for liquid-continuous operations (e.g. pipe flow and bubble columns) and perceive the disturbances as a void , i.e., a zero. As a result, the fundamental governing equations of conductivity and capacitance cannot be used to provide additional information regarding the disturbance area. The spatial resolution of the available offerings are therefore limited by the electrode spacing.

  Distillation columns, however, are operated under vapour-continuous conditions. The mesh-grid subsequently measures the presence of the liquid as the disturbance. This allows for the use of the definition of both capacitance and conductivity to be incorporated to refine the resulting disturbance (measurement $\neq 0$). The presented study thereby developed an electrical circuit that accurately measures conductivity and capacitance (linear response) rather than relying solely on the grid for sizing. Each crossing point is calibrated using the definitions of capacitance and conductivity to estimate the projected area (2D see Figure 3.5) of the passing

liquid, increasing the spatial resolution down to 2mm, while limiting the adverse effect on the column flow.

- Conventional tomography systems are designed to evaluate local liquid hold-up, radial distribution, and liquid maldistribution at steady-state conditions. Based on steady-state assumptions, experimental evaluation times are kept short, as limited variability is expected. Times vary from 0.2s (100 images) for Janzen et al. [11] to 10 seconds (4000 images) for Grünewald et al. [8, 9] and Wu et al. [10]. Although sufficient for their purpose, the short evaluation times cannot evaluate time-dependent distributions such as the formation of droplets between random packing.

  As this is of particular interest in modern packings, this study developed an EIT wire-mesh sensor for the express purpose of adding this functionality. In addition, 3D image processing techniques were used to characterise the dynamic distribution of liquid (and liquid elements) over a period of 2 minutes (120 seconds).

Against this background, Chapters 4 to 6 provide a systematic description of the development of the equipment and the data-processing methods, as indicated in Figure 3.7.

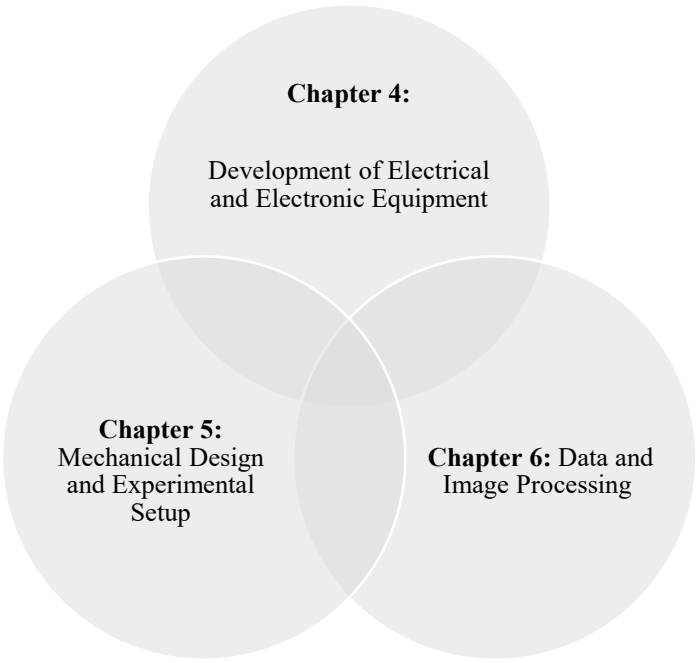

Figure 3.8: Categories of description and discussion in this work related to the development of the EIT sensor and data-processing systems

4. DEVELOPMENT OF ELECTRICAL AND ELECTRONIC EQUIPMENT

This chapter covers a variety of topics related to electronic circuitry and their design. Readers are referred to "Lessons in Electronic Circuits" by R.T. Kuphaldt for additional background if required (volumes I,II and III) [83, 84, 65].

A broad overview of the methodology of this chapter is presented in Table 4.1. This was included to introduce key concepts and clarify their importance.

Table 4.1: Outline of this chapter and the reasoning behind each development section.

Concept	Outline	Significance
Method of impedance measurement	Based on literature and feasibility screening, an auto balancing bridge method was chosen to measure electrical impedance.	This method provides the means of both measuring and splitting electrical impedance into resistance and capacitance.
Electromagnetic field modelling	The fundamental principles of physics were used to predict the capacitance and resistances for various fluids and droplet sizes EM force interferences from other sources were also evaluated in this section.	The EMF models were used in both feasibility evaluations and for choosing the initial circuitry for the prototype.
Transient circuitry modelling	This involved selecting and simulating the electronic circuitry with Laplace transfer functions (obtained from the manufactures of each component resistors, capacitors amplifiers etc.).	The mathematical models were used choose the specific electronic components and their sizes for prototyping.
Single channel circuitry development	A single channel prototype was constructed (based on the transient modelling) and tested with various liquid combinations.	The point circuitry was used for initial proof of concept and to refine the electrical circuitry and layout.
Small scale evaluations	Printed circuit boards (PCB) were designed and constructed to house multiple channels of auto balancing bridges. A sampling and storage methodology was also developed using Arduino microprocessors.	A small-scale prototype with working mesh-grid was used for refining and validation, prior to the final prototyping.
Final Prototype	The small-scale circuitry was adapted and combined with a Master-Slave control methodology using multiple Arduino micro controllers.	Final prototype for use in the experimental evaluation of liquid distributions.

The previous chapters established the need for an improved packed column tomography system and highlighted wire-mesh electrical impedance tomography as the proposed solution. An auto-balancing bridge was chosen as the preferred impedance measurement method for its simplicity and wide measurement range. This simplified circuit has been successfully used in similar ECT and EIT systems, citing high signal to noise ratios and fast sampling speeds [14, 74]. The preferred method has also been found to illustrate valuable stray capacitance immunity [14]. This is a significant advantage over other measurement techniques, as the presence of the packing within the column is expected to produce sizable stray capacitance.

4.1 Method of Impedance Measurement: Auto Balancing Bridge

A schematic of an auto-balancing bridge is presented in Figure 4.1. In the schematic, V_{in} represents the excitation voltage and V_{out} the output voltages. The complex impedance Z_x refers to an unknown impedance, where Z_f represents a known impedance. Zx, therefore, represents the "sensor" section.

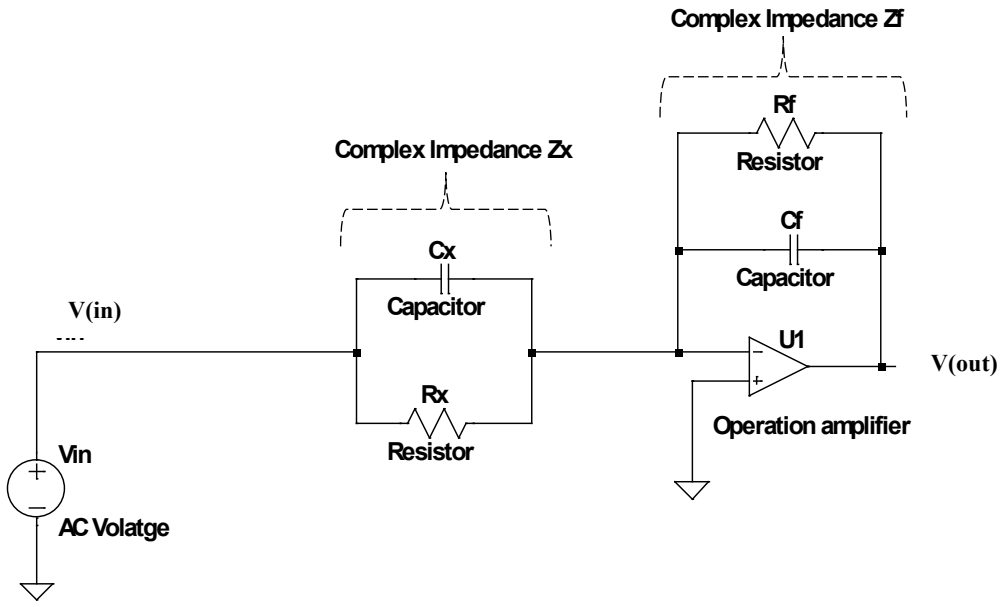

Figure 4.1: An electrical drawing depicting impedance measurement using an auto-balancing bridge.

Mathematically solving an auto-balancing bridge yields Equation 4.1. $\mathbf{R_x}$, $\mathbf{R_f}$ and $\mathbf{C_x}$ represent the various resistors and capacitors, and $\boldsymbol{f}$ represents the input wave frequency [14].

$$\frac{V_{in}}{V_{\text{out}}} = \left(\frac{Z_f}{Z_x}\right) = \left(\frac{R_f + j\omega C_f}{R_x + j\omega C_x}\right) = \left(\frac{R_f + j(2\pi f)C_f}{R_x + j(2\pi f)C_x}\right) \qquad 4.1$$

The significance of auto-balancing bridge impedance measurements, however, lay in the frequency response of the circuit. Thereby taking the mathematical limits of the frequency(***f***) to zero and infinity yields a measurable voltage relationship between known and unknown parameters. The decomposition of the respective limits by the Taylor and Laurent series are presented in Equations 4.2 to 4.5.

Limit to infinity via Laurent series expansion

$$\lim_{f\to\infty}\left(\frac{R_f+j(2\pi f)C_f}{R_x+j(2\pi f)C_x}\right)=\frac{C_f}{C_x}+\frac{j(C_fR_x-R_fC_x)}{2\pi f{C_x}^2}+\left(\frac{{R_x}^1(R_fC_x-C_fR_x)}{4\pi^2f^2{C_x}^3}\right)-\frac{j*{R_x}^2(R_xC_f-R_fC_x)}{8\pi^3f^3{C_x}^4}+\frac{{R_x}^3(C_fR_x-R_fC_x)}{16\pi^4f^4{C_x}^5}+0*\left(\frac{1}{f}\right)^5 \quad 4.2$$

$$\lim_{f\to\infty}\left(\frac{R_f+j(2\pi f)C_f}{R_x+j(2\pi f)C_x}\right)=\frac{V_i}{V_0}=\left(\frac{Z_f}{Z_x}\right)=\frac{C_f}{C_x} \quad 4.3$$

Limit to zero via Taylor series expansion

$$\lim_{f\to 0}\left(\frac{R_f+j(2\pi f)C_f}{R_x+j(2\pi f)C_x}\right)=\frac{V_i}{V_0}=\left(\frac{Z_f}{Z_x}\right)=\frac{R_f}{R_x}+\frac{2j\pi f(C_fR_x-R_fC_x)}{R_x}+\frac{2^2\pi^2f^2C_x(C_fR_x-R_fC_x)}{{R_x}^3}-\frac{2^3\pi^3f^3j{C_x}^2(C_fR_x-R_fC_x)}{{R_x}^4}-\frac{2^4\pi^4f^4{C_x}^3(C_fR_x-R_fC_x)}{{R_x}^5}+\frac{2^5\pi^5f^5j{C_x}^4(C_fR_x-R_fC_x)}{{R_x}^6}+f^6 \quad 4.4$$

$$\lim_{f\to 0}\left(\frac{R_f+j(2\pi f)C_f}{R_x+j(2\pi f)C_x}\right)=\frac{V_i}{V_0}=\left(\frac{Z_f}{Z_x}\right)=\frac{R_f}{R_x} \quad 4.5$$

Equations 4.2 to 4.5 illustrate the ability of an auto-balancing bridge to independently measure resistance and capacitance, depending on the frequency of the excitation signal.

- $f\to 0$ measures ***Resistance*** and,
- $f\to\infty$ measures ***Capacitance***.

Dual excitation signals can therefore be used to evaluate both impedance sub-parameters (resistance and capacitance) simultaneously.

Figure 4.2 and 4.3 are provided, depicting the frequency response of an ideal auto-balancing bridge, with variations in both the unknown resistance **(R_x)** and capacitance (**C_x**). Both figures affirm the results of equations 4.2 and 4.5 and illustrate a plateau formation at both the upper and lower frequency ranges. Any frequency within the identified plateaus can subsequently be used to evaluate an unknown capacitance or resistance. The zero gradients on the plateaus also provide added flexibility in selecting excitation frequency and mitigating the possible effects of standing waves and natural harmonics.

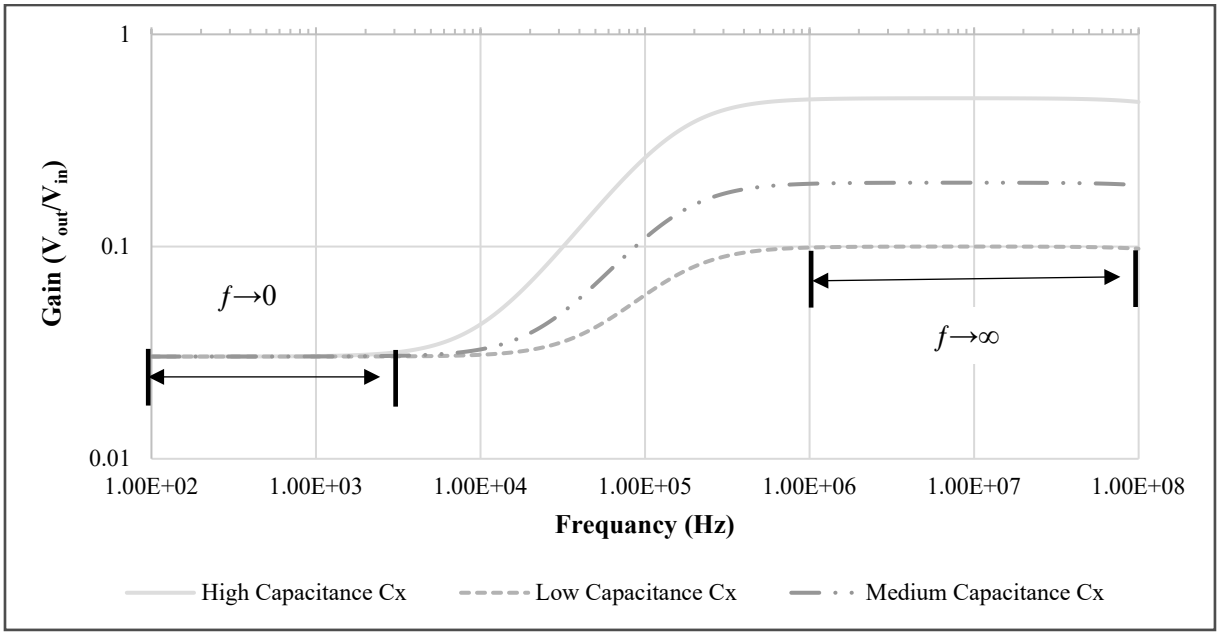

Figure 4.2: Effect of changes in capacitance on the frequency response of an auto-balancing bridge.

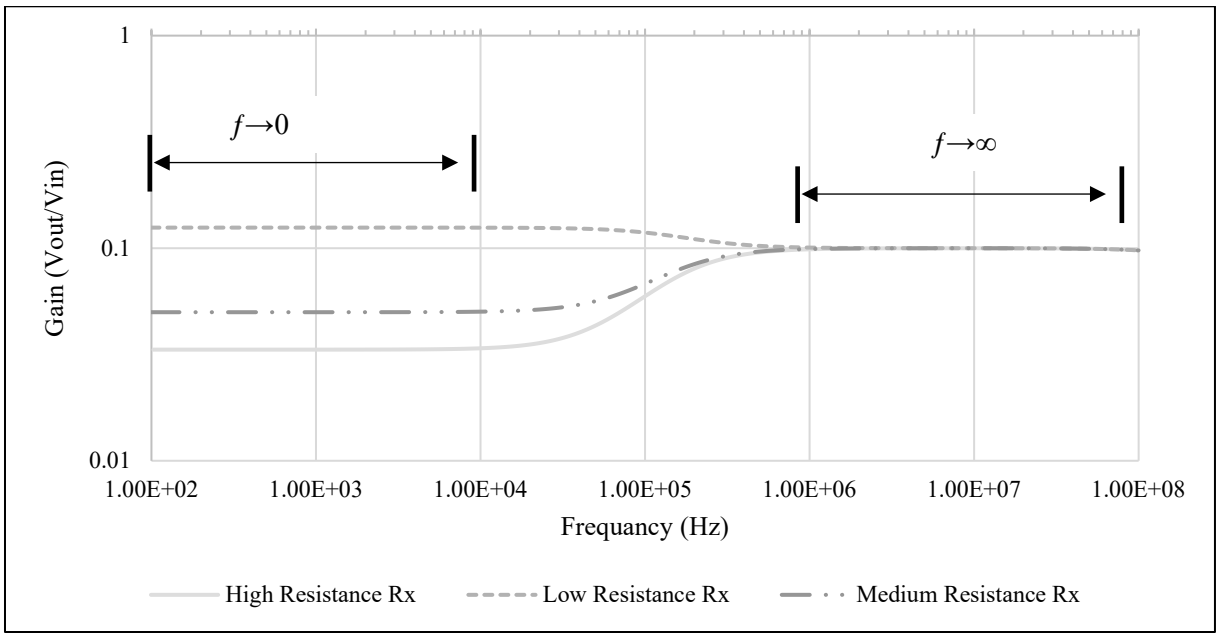

Figure 4.3: Effect of changes in resistance on the frequency response of an auto-balancing bridge.

Therefore, the EIT design methodology opted to superimpose both high and low-frequency signals (on either plateau) to yield simultaneous resistance **(R_x)** and capacitance **(C_x)** measurements. The combination of parameters allows multiphase quantification of up to three phases (Organic-aqueous - vapour, see Table 3.3).

4.2 Circuitry Description and Design

A summary of the circuit development strategy is provided in Figure 4.4. The development mirrored the chronological design progression and was therefore used in logical representation of the final design.

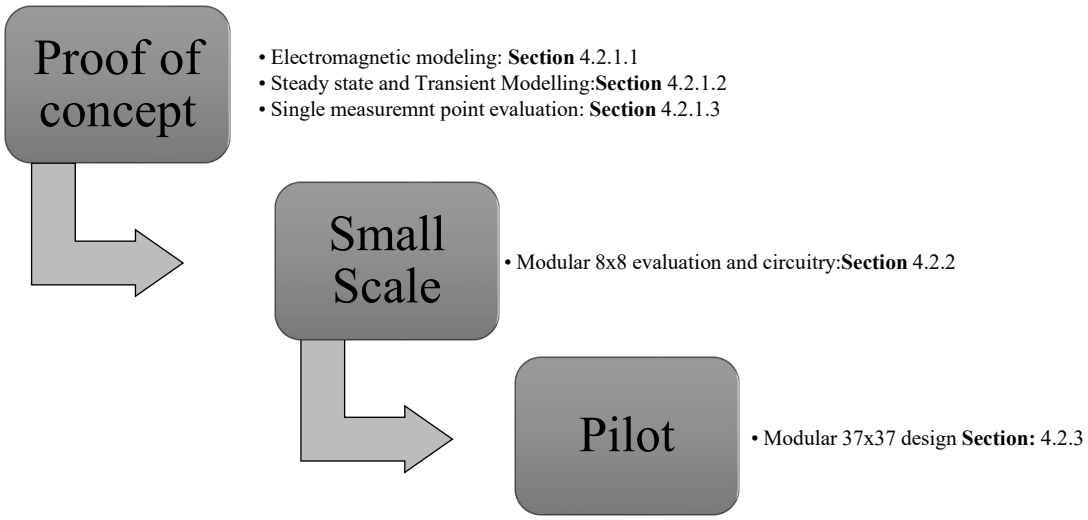

Figure 4.4: A summary for the electrical development methodology. This methodology progresses from first principal basic engineering to the design and implantation.

4.2.1 Proof of Concept

The concept of impedance-based tomography, foreign to chemical engineers, was initially evaluated using electromagnetic steady-state modelling. These models were developed to provide answers to the following questions:

[1] What are typical ranges and values for electrical conductivity and capacitance?

[2] How do the expected values change based on changes in **a)** wire diameter, **b)** electrode spacing, and **c)** the size of the disturbance itself?

[3] What do the induced electromagnetic fields look like, and how do they change based on other objects?

A finite-element model (FEM**)** was constructed in the Electromatic field solver package OpenEMS, to visualize the effect of electromagnetic fields and answer these preliminary questions. The model combined **a)** OpenEMS FEM, **b)** 3D constructions from Autodesk Inventor, and **c)** iso-surface plotting with MatLab.

4.2.1.1 ELECTROMAGNETIC FIELD MODELLING

The model was based on an electrostatic evaluation and assessed the possible ranges of capacitance and conductivity values within a wire mesh array. A simplified array was created using staggered electrodes within a 100mm x 20mm x 20mm cuboid and was solved using the Poisson equation presented in Equation 4.6; assuming a zero charge on the cuboid perimeter

$$\nabla\, \varepsilon_0\, \varepsilon\, (\mathrm{r})\, \nabla V(r) \;=\; 0 \qquad 4.6$$

Additionally, all wires were modelled as grounded (V=0), except for a single excitation electrode (V_{in}= 1V). The inside of the cuboid was modelled as air ε_i=1, with the relative permittivity of the disturbance varied between air ($\boldsymbol{\varepsilon_i}$=1) and water ($\boldsymbol{\varepsilon_i}$=80). An illustration of the potential difference across a 1mm diameter disturbance, with 5mm electrode spacing and a wire diameter of 0.1mm is presented in Figure 4.5.

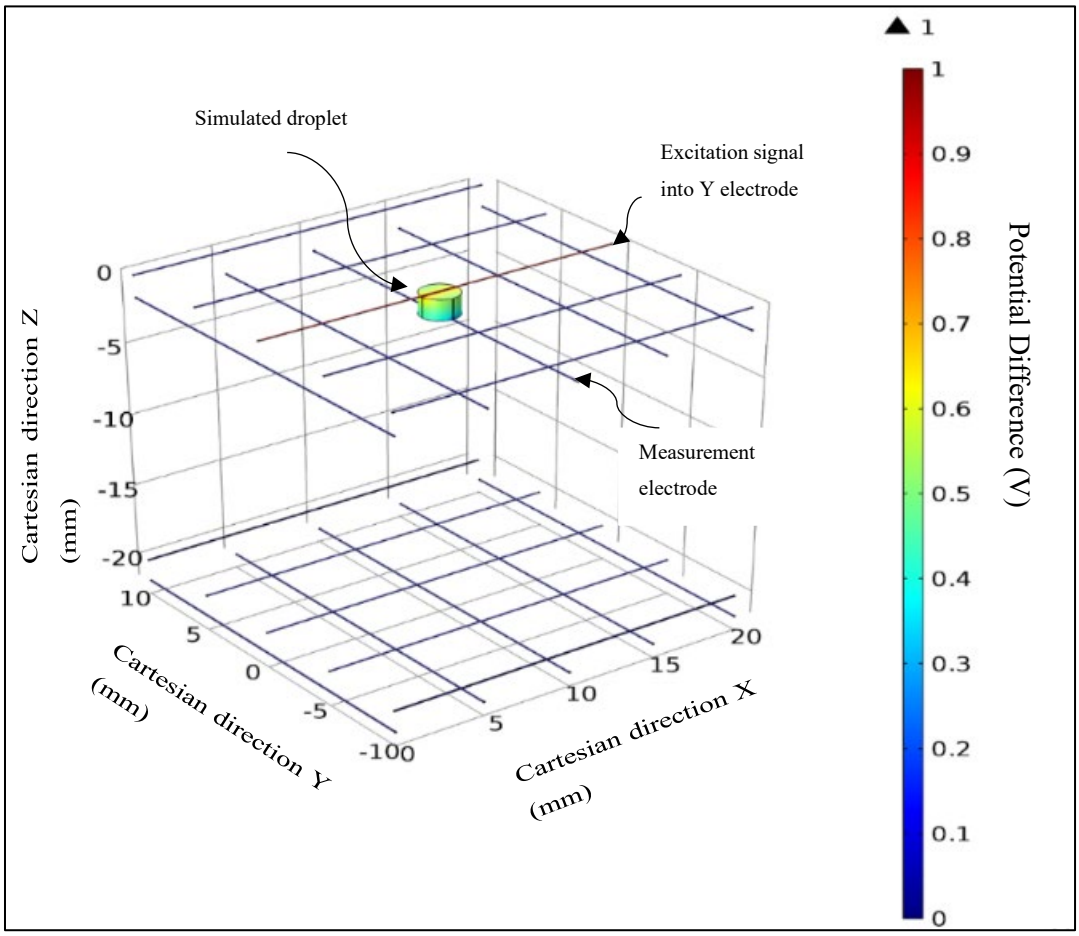

Figure 4.5: OpenEMS model showing the expected voltage across a liquid element (water droplet). The voltage measured by the measurement electrode was used to evaluate the feasible ranges of capacitance and resistance that the sensor was likely to encounter.

The wire-mesh design and its corresponding operating window were evaluated varying the following parameters. The chosen parameters were guided by literature [79, 14]

- electrode spacing (2-10mm),
- electrode diameter (0.1-1mm),
- disturbance diameter (1-10mm),
- the relative permittivity of the disturbance (ε_i=1 to 80),
- the influences of other objects, i.e., the packing.

The chosen mesh orientation for the continuation of the study was based on practical factors (wire strength and rigidity) and material considerations, with specifications of:

- Electrode spacing 10 mm.
- Wire diameter = 0.625 mm.
- Electrode separation 2mm.
- Electrode material, 304SS

A sample of the simulated capacitance values for this design based on varying droplet permittivity is presented in Figure 4.6, using air as the cuboid medium. The simulated capacitance ($\boldsymbol{C_{sim}}$) values were calculated in post-processing by integrating the induced charge density across the wire boundaries. This is expressed mathematically in Equation 4.7. The equation was derived by combining the definition of capacitance (Charge/Voltage) with the Maxwell's magnetic field volume integral and Gauss' Law [85].

$$C_{sim} = \frac{1}{V} \oiiint_{1}^{Volume} \rho\,(x, y, z)dv \qquad 4.7$$

Where

- V represents the induced potential difference
- ρ represents the charge density in C/m^2
- dv represents an infinitesimally small element volume

The results highlighted the expected range of operability for capacitance; between 0.12 pF and 5.43 pF. These values were used for continued steady-state and transient modelling in Section 4.2.1.2. The presented linearity across the spectrum of relative permittivity suggested the applicability of capacitance across a wide range of fluids.

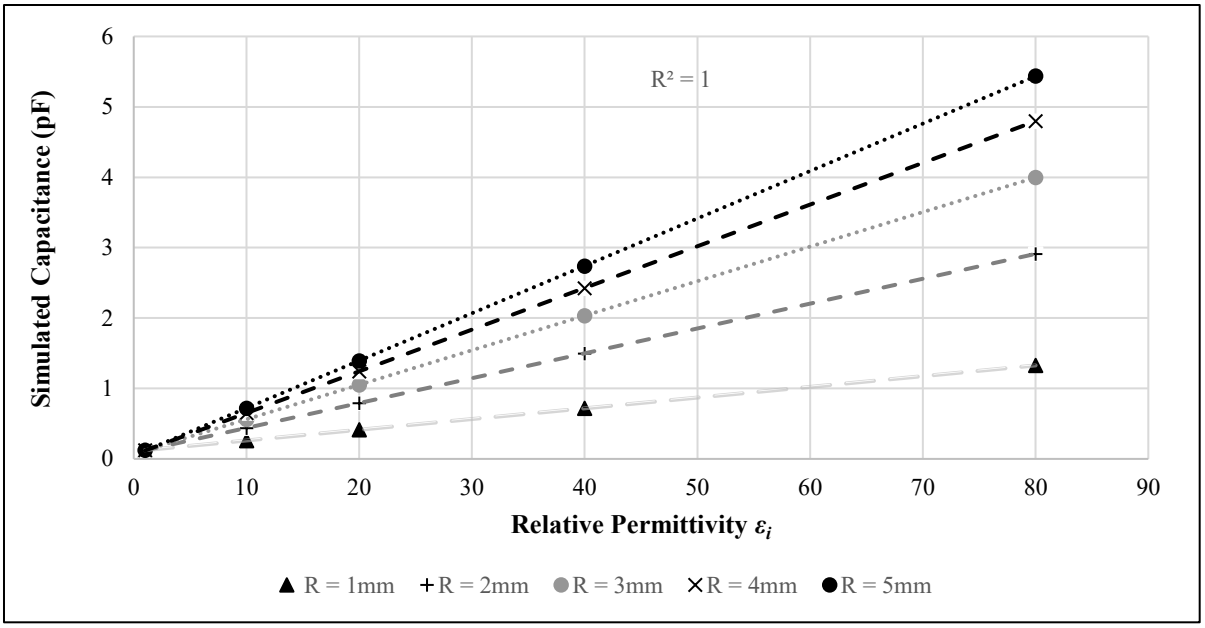

Figure 4.6: OpenEMS model predicting capacitance based on both relative permittivity and the cross-sectional radius of a liquid droplet.

The concept of cross-sectional area approximation in a wire-mesh grid, through capacitance (See section 3.4.2.1), was further evaluated with the simulation. The presented results in Figure 4.7 illustrated sufficient linearity with changing disturbance cross-sectional radius and area. Deviations from linearity across the smaller particle sizes were attributed to the meshing processes of the FEM model, with OpenEMS. The results consequently motivated the use of capacitance for estimation of the droplet sizes in the wire-mesh EIT sensor.

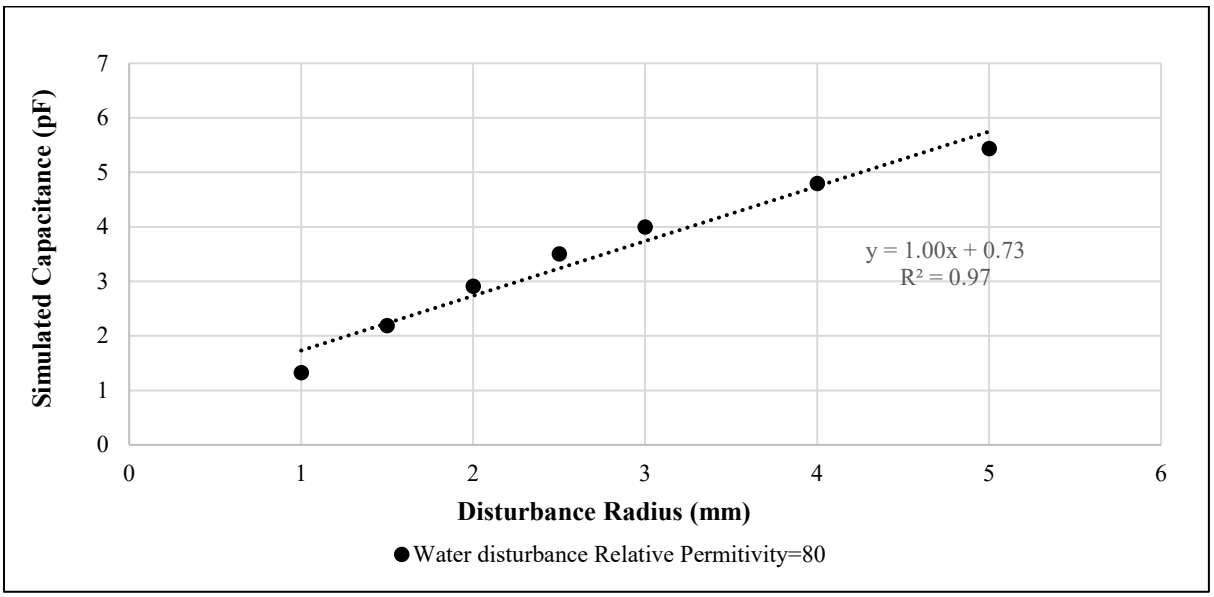

Figure 4.7: Response of disturbance cross-sectional diameter on capacitance. The graph depicts a linear tend thereby suggesting that the liquid cross-section can be correlated based on a capacitance reading.

The additional effects of other electrically conductive objects were evaluated through simulation, with the result presented in Figure 4.8 for a secondary grid. The results showed a negligible induced voltage difference (consequently negligible induced EMF) and stray-capacitance at a distance of 10mm from the excitation node. Allowing for a margin of error led this study in placing the proposed mesh-grid 20mm below the packing to limit EMF interference.

Figure 4.8 was also used to evaluate the possibility of future resolution improvements by adding and additional mesh-grid. The results showed limited stray capacitance at a distance of 20mm, even when both grids were activated. The result shows great promise for future works and improvements.

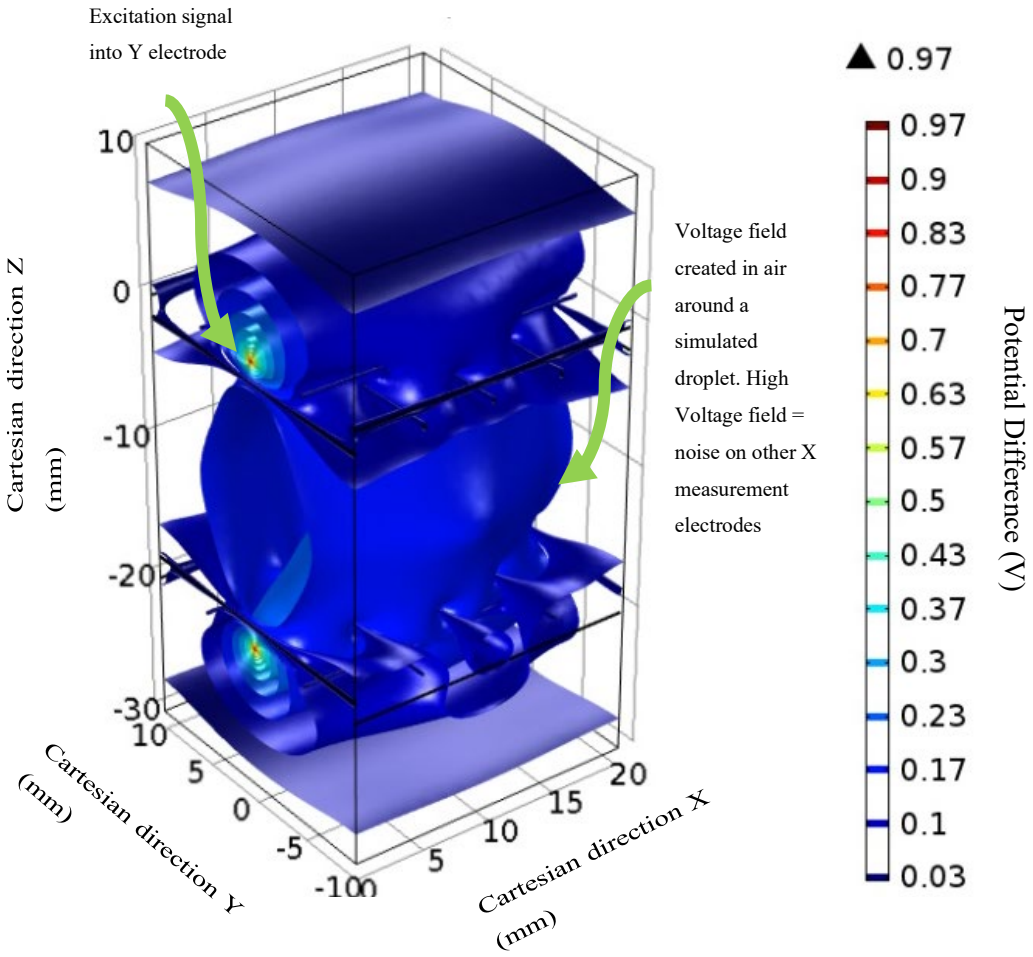

Figure 4.8: Voltage distribution model from OpenEMS considering the voltages experienced by other electrodes not in contact with the liquid droplet.

The conclusions drawn from the electromagnetic analysis are summarised as:

- An expected capacitance range between 0.12 pF and 5.4 pF,
- negligible EMF disturbance at distances 20mm and further from the grid,
- linear capacitance trends with electrical permittivity at a constant disturbance radius,
- linear capacitance trend with disturbance cross-sectional area given a constant electrical permittivity, and
- a proposed mesh-grid design of:
    - 10 mm electrode spacing,
    - 0.625 mm wire diameter,
    - 2 mm electrode separation and,
    - 304 stainless-steel.

4.2.1.2 Steady State and Transient Modelling

The steady-state and transient circuitry simulation was performed to considered choice of electrical components based on the suggested operating ranges from section 4.2.1.1.

The initial circuitry design was performed on the LTspice® XVII package from Analog instruments. This software package incorporates manufacturer and third-party Laplace domain transfer functions for individual electrical components and offers transient and steady-state simulations. The simplified circuitry is provided in Figure 4.9, with each component having a transfer function obtained from the manufacture websites.

The technical discussion regarding the individual component selection was deemed outside the scope of this report. The circuitry is consequently only discussed in blocks (1.1-1.8) in layman's terms. The reasoning behind this approach is presented in Section1.7. The LTspice® XVII model was used to evaluate the components, their sizes, and tolerances. Additionally, the simulations were used to estimate the signal response time of the circuit, i.e., how long the sensor takes to reflect the presence of a disturbance.

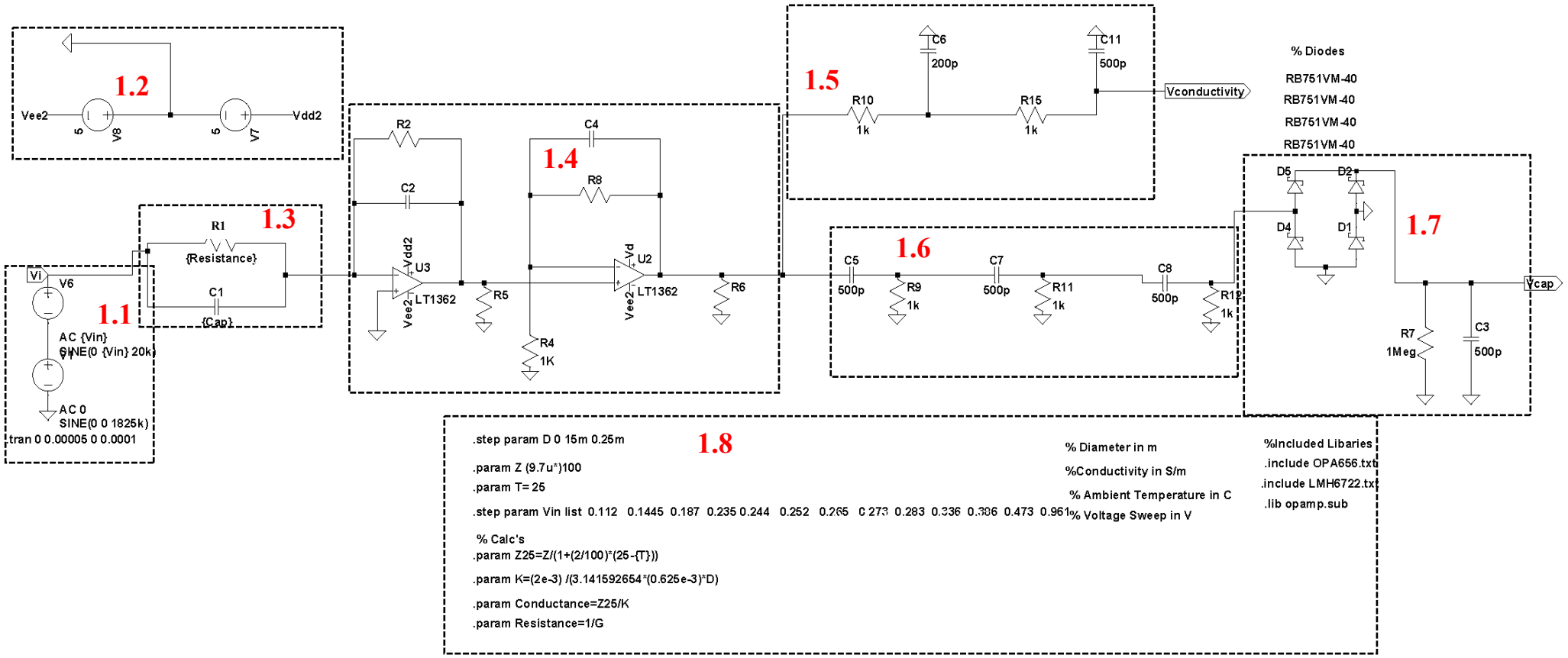

Legend	
R-x	Resistor
C-x	Capacitor
D-x	Diode

Figure 4.9 : Schematic of the LTspice XVII model, with various blocks numbered to guide discussions in this section of the thesis. The model was solved in the Laplace domain.

4.2.1.2.1 Block 1 1: Input signal

This block shows a signal generator (direct digital synthesiser or DDS), producing an analog waveform at a specified frequency and amplitude. For the purpose of this study, a sinewave at 20kHz and 10MHz. A sinewave was chosen as the alternating voltage gives rise to both a real and imaginary component (as discussed in section 3.4). The relevance of the specific frequencies is presented in section 4.1.

4.2.1.2.2 Block 1.2: Power

Block 1.2 represents the constant voltage (Dc) power rails used to power the amplifiers and the auto-balancing bridge. Two independent DC power supplies were used to produce both +5V and -5V. Both positive and negative voltages were required as sinewaves are centred around zero and consequently have a positive and negative component.

4.2.1.2.3 Block 1.3: The Disturbance

This block represents the disturbance in the wire mesh-grid, containing both a *Real* and *Complex* component through the represented parallel resistance and capacitance (See section 3.4). The design window for the expected resistance and capacitance was projected from the EMF field modelling (0.12pF and 5.4pf) and through tests with an existing conductivity probe (RS-pro calibrated conductivity probe).

4.2.1.2.4 Block 1.4: Measurement

The fourth block (1.4) is comprised of the auto-balancing bridge and a secondary amplifier. The purpose of the second amplifier was to increase the voltage to within the span of 0-3.3V for sampling. The exact values of the resistors and capacitors are no provided to protect intellectual property. Dual LT1362 operational amplifiers were used in the circuitry. These (LT1362) were chosen for their bandwidth of 50MHz. In layman's terms, this reflects applicability for signals up to 50MHz.

4.2.1.2.5 Blocks 1.5 and 1.6: Filters

These blocks acted as high- and low pass filters to separate the signals into conductivity and capacitance. Block five subsequently allowed only low frequency (below 100kHz) signals to pass, producing conductivity for measurement. The opposite was true for Block 1.6, operating as a high-pass filter, for capacitance evaluations.

4.2.1.2.6 Block 1.7: Sample and Hold

Block 1.7 represented a half-wave rectifier circuit to reduce sampling costs. In nonspecific terms, the circuitry converted an AC-wave to DC to reduce the need for fast sampling. Comparative circuits are often referred to as sample and hold circuits. The sampling and specifically the sample-and-hold circuitry is discussed further in section 4.2.2.1.5

4.2.1.2.7 BLOCKS 1.8: USER PARAMETERS

This block contained the mathematical code translating conductivity measurements (µS/cm) into electrical resistance with the required temperature compensation. Additional LtSpice directive coding was placed in this area, among which the automation of input parameters and solver specifications.

4.2.1.3 SINGLE CHANNEL EVALUATIONS

A single-channel measurement circuit was constructed based on the modelling in LTspice® XVII, with a picture of the prototype presented in Figure 4.10. The setup used external power rails (Block 1.2) and logged (output of Block 1.4) using an Analog [1]Discovery 2 oscilloscope and considered the measured voltage on the red clip.

The constructed circuitry was evaluated by submerging the grid (excitation and measurement electrodes separated at 2 mm increments) in various liquids with varying conductivity and relative permittivity. The baseline conductivity was measured using a calibrated RS-pro conductivity probe, and the relative permittivity's were obtained from the literature.

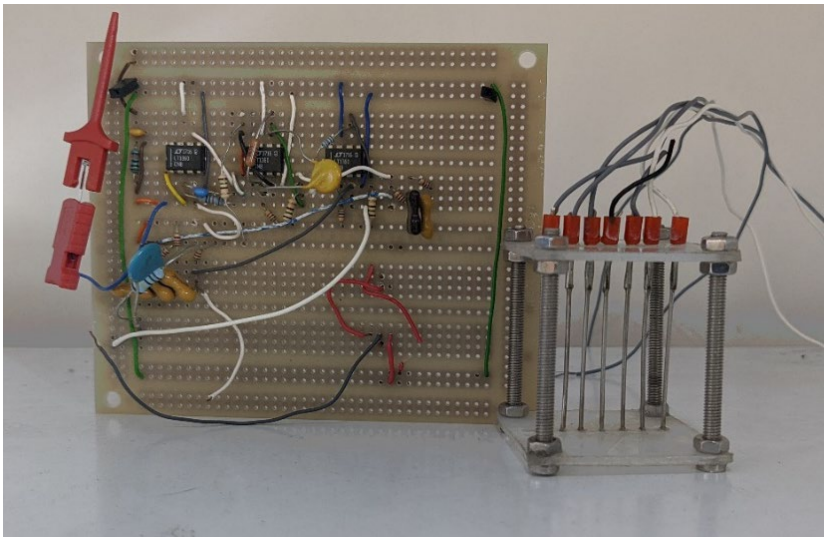

Figure 4.10: The single-channel experimental circuitry used to evaluate the components and pre-feasibility of the method

Two sinewaves were evaluated, with the results presented in Figures 4.11 and 4.12 for a 2mm electrode spacing and a 0.625mm diameter wire.

- ***Conductivity:*** 0.1V at 20kHz
- ***Capacitance:*** 0.1V at 10MHz

[1] . The Analog Discovery 2 (SN:210321A68718) allows for 100 million samples per second.

Evaluated liquids (See Table 3.4 for relative permittivity values):

- Water
- 99% Isopropanol
- Silicone Oil
- Ethylene Glycol

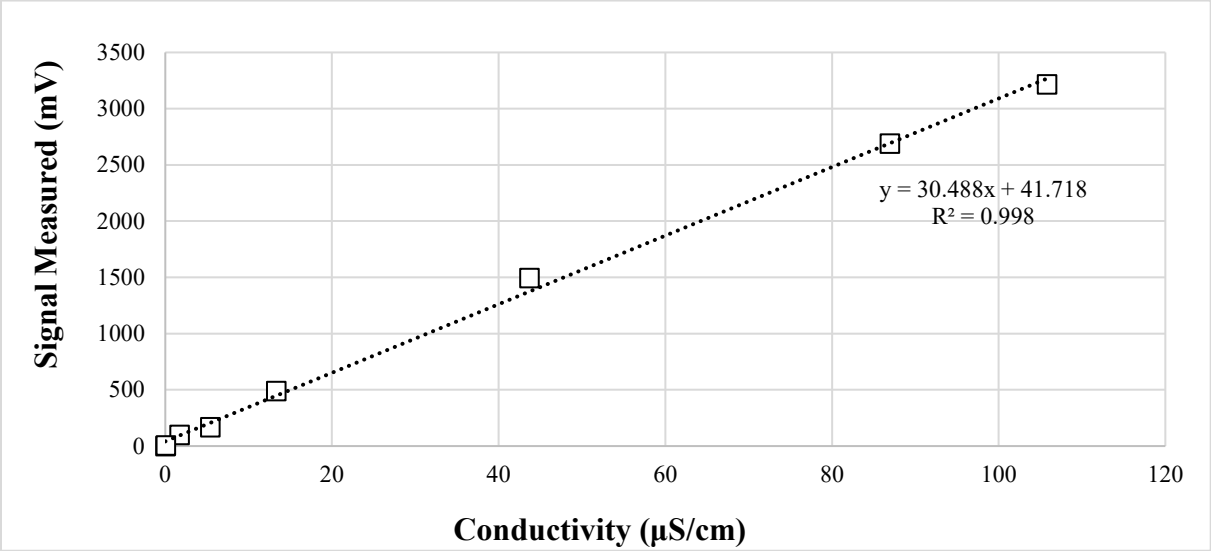

Figure 4.11: Conductivity readings from prototype sensor based on the measured voltage output.

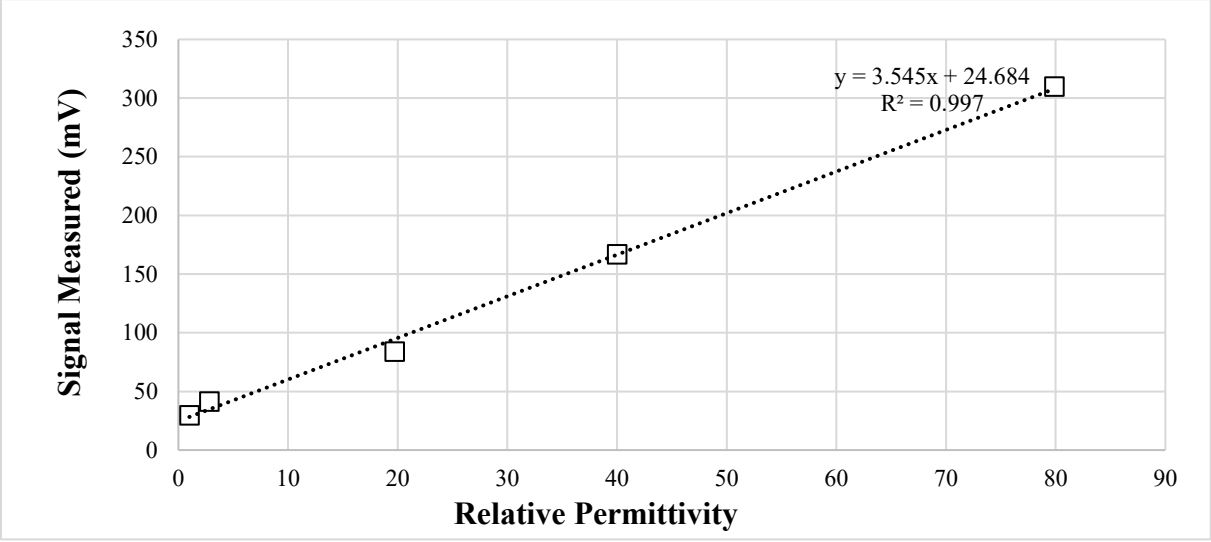

Figure 4.12 Capacitance readings from prototype sensor based on the measured voltage output.

The experimental evaluation of the circuitry yielded the following:

- It validated the electrical impedance measurement circuitry, as designed, and modelled in LTspice® XVII.
- It showed sufficient linearity (experimental proven) for both conductivity and capacitance measurements in terms of a millivolt reading and,
- Proved capable of differentiating between water, ethylene glycol, silicone oil and isopropanol based on the principal of electrical impedance.

Figures 4.11 and 4.12 present excellent linearity across the evaluated fluid property ranges and validated the EMF and steady-state modelling. The results underscore linearity based on both conductivity and capacitance when considering a set disturbance. The presented results were consequently seen as sufficient proof of concept, with the study progressing to small scale modular designs.

4.2.2 Small Scale Modular Design (8x8 Modular Design)

The successful point-measurement circuitry was adapted to tomography with a wire-mesh grid. Figure 4.13 is presented, illustrating a schematic of the small-scale modular design. For the sake of clarity, the schematic is reduced to show 4x4 channels instead of the 8x8 used in the design. Similar to the previous section, the design will be discussed in blocks using the descriptors 2.1 to 2.5. The simplified block definition is discussed in section 1.7.

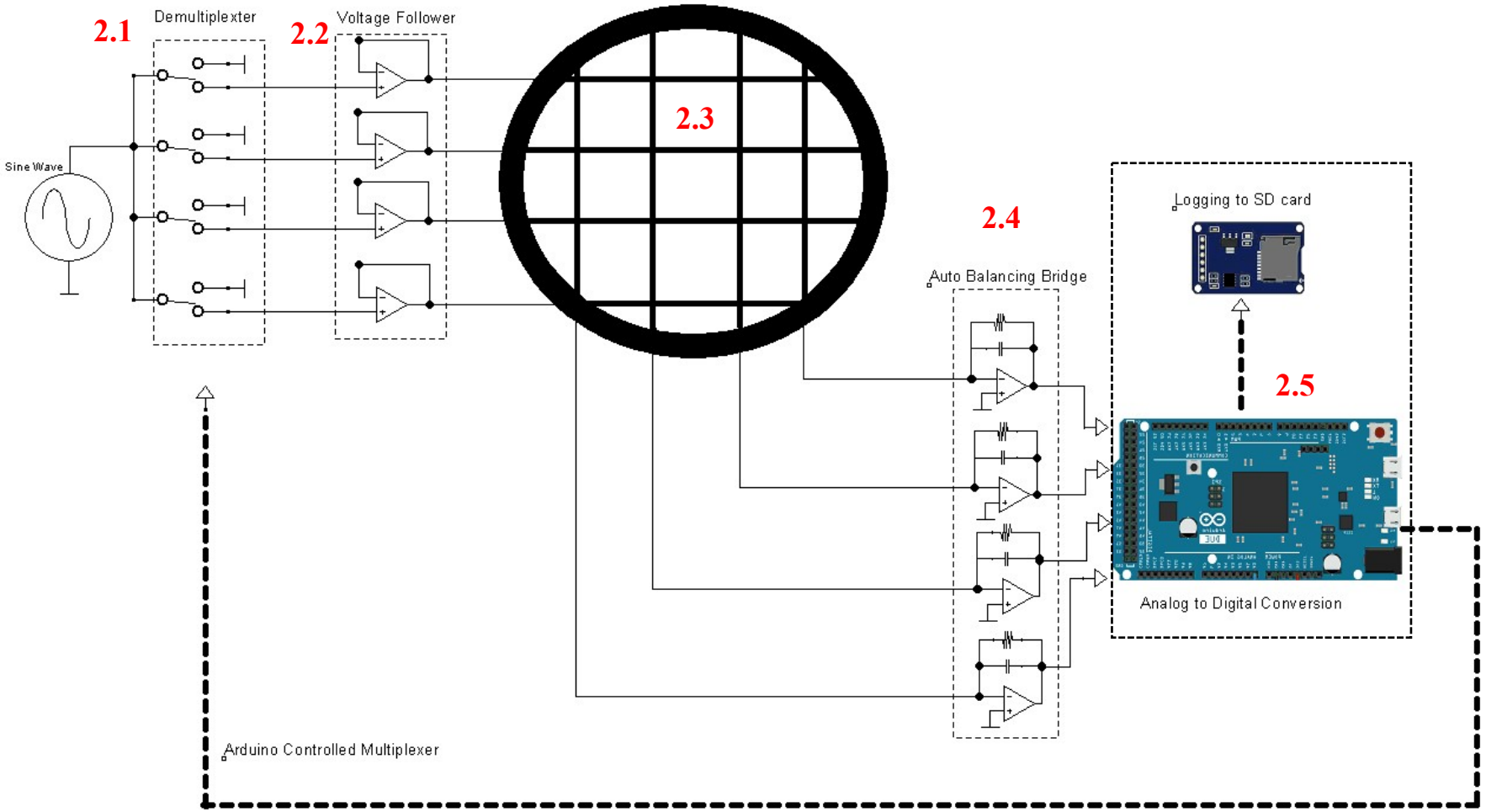

Figure 4.13 : Small scale schematic of the wire-mesh EIT system. Block 2.4 refers to the circuitry developed in section 4.2.1.2, while the other blocks depict the peripherals used to log the data and control the various sensing channels.

4.2.2.1.1 Block 2.1: De-Multiplexer

In layman's terms, multiplexers (Mux) and demultiplexers (De-Mux) are high-speed switches designed for data selection. These switches transition between various inputs signals and connect them to a single output and vice versa. The presented design used a 74HC4067 analog demultiplexer to split a single incoming sinewave into one of 8 possible channels within a typical switching time of 1.39ns. The de-mux was controlled using the digital pins of the Arduino microprocessor.

4.2.2.1.2 Block 2.2: Buffer Amplifier

Voltage followers (unity gain amplifiers) were added to the output of each de-mux channel to buffer the incoming signal before the mesh grid—this mitigated feedback from the mesh grid into the de-mux and consequently into the other channels. LT1362 amplifiers from Analog were used as buffer amplifiers for the circuit.

4.2.2.1.3 Block 2.3: Sensor Grid

The wire-mesh grid is depicted in this section, referring to two perpendicular layers of electrodes, separated at a set distance. Figure 4.15**(c)** is provided as an illustration of the initial prototype. Using the de-mux in block 2.1, the sine-wave signal was sent to a single electrode at a time (horizontal) while constantly measuring along all the vertical electrodes. This cycle rapidly repeated, activating each vertical channel and creating effective measuring sites at the crossings. A complete image was obtained when each horizontal electrode was activated at least once. Further clarification on the grid itself is provided in section 5.1.

4.2.2.1.4 Block 2.4: Auto Balancing Bridge

Block 2.4 represented the circuitry discussed in Section 4.2.1.2. Negligible changes were made, with modifications limited to changes in the component mountings, from through-hole to surface-mounted. The aforementioned was preferred as it lent itself towards a simplistic scale-up and a smaller footprint PCB.

4.2.2.1.5 Block 2.5. Sampling and Logging

An Analog Discovery 2 oscilloscope was used for measurement and logging in the proof-of-concept, single-channel evaluations (Section 4.2.1.3). The oscilloscope, however, is only capable of measuring two channels concurrently and is therefore inadequate for tomography. Various high-speed measuring systems were evaluated but ruled out due to the sizable costs of commercially available high-speed multi-channel sampling.

However, the implications of the sampling speed required addressing, as is presented in Figure 4.14. The illustrations present the inability of slow sampling to evaluate the *real* amplitude of the wave. The Nyquist sampling theorem consequently limits the lowest effective sampling rate to twice that of the waveform [14].

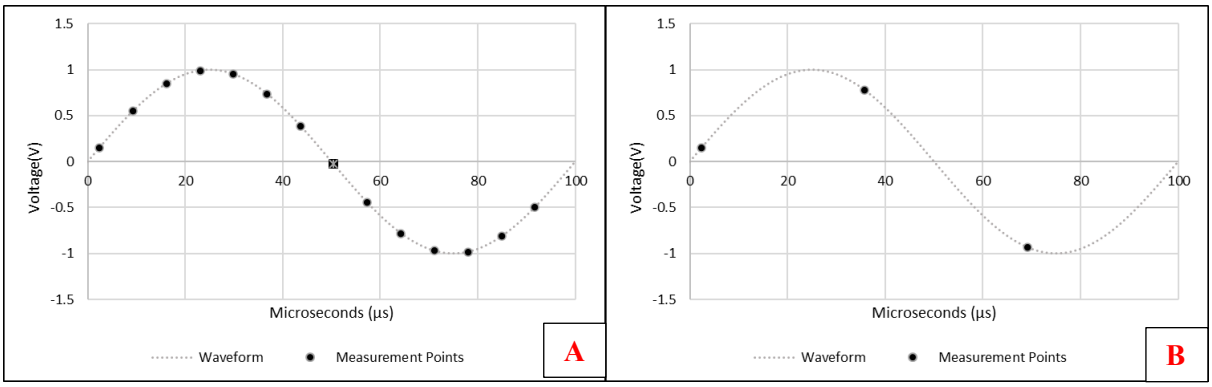

Figure 4.14: Effect of Sampling speed on the accurate sampling a wave; A) sample rate = 10kHz with wave at 148kHz; B) sample rate = 10Khz wave at 30kHz

Cost-effective, commercially available multichannel sampling systems were consequently ruled out, given the operating frequency of the circuitry (20kHz for conductivity and 10Mhz for capacitance). Instead, sampling speeds were addressed by including a half-wave rectifier on the capacitance side to convert the high-frequency signal into constant DC voltage (Block 7 in Section 4.2.1.2). The result is a straightforward signal to measure but at a slight expense to the overall sampling speed (charge storage in capacitors). A similar strategy was used by Prasser et al. [86] in 1998 to simply the sampling of conductivity ERT with a wire-mesh grid.

A cost-effective sampling and logging solution was consequently developed using Arduino DUE microprocessors. The DUE offered 12 separate ADC's (Analog to digital converters) capable of measuring voltages between 0 and 3.3V (12 bit, i.e., resolution of 0.8mV). The conventionally slow sampling speed of 10kHz in the DUE (single channel) was boosted to 2MHz by disabling all the Arduino interrupts and coding directly onto the Atmel SAM3X8E ARM Cortex-M3 CPU. A stable sampling speed of 148kHz (Standard deviation of 1kHz) was achieved, measuring eight channels concurrently.

Data collection and sampling spanned 120 seconds, intermittently writing the results to a text file on an SD card. The intermittent data storage was incorporated to limit memory bottlenecking and ADC conversion slow-down. The Arduino library "SDFatEX" was adapted to minimize internal housekeeping functions on the SD cards for storage. These ROM based functions created sporadic slow-downs in the logging speeds and were mitigated by packing the written data in increments of 512kB (buffer size). The coding strategy is further elaborated upon in section 4.2.3.2.

4.2.2.2 PRINTED CIRCUIT BOARDS (PCB'S)

The circuitry was miniaturized and integrated into modular printed circuit boards (PCB) with Autodesk Eagle [2]. The PCBs were designed in accordance with the considerations presented by Montrose [87]. Additional resources, including online courses and the Eagle helpfiles, were also incorporated [88].

The technical considerations related to the PCB layout were adjudged to be outside the scope of this report, and consequently, only a short strategy description is provided.

The design aimed to produce a modular setup that could easily be scaled. For this purpose, a "motherboard" was created to host the various modular add-ons. These add-ons included **a)** the sensor PCB (Block 2.4), **b)** the sampling PCB with incorporated de-mux (Block 2.5), and **c)** the connectors sending signals to and from the wire-mesh grid. The "motherboard" itself was created to support modular linking to other motherboards (referred to as "slave-boards"), share power utilities and allow microprocessor cross-communication.

Some detailed PCB specifications:

- Dual-Layer,1.6mm PCB's with 0.035mm of copper plating on each side.
- Ground planes on both sides to reduce noise.
- Minimum trace clearance of 0.3mm to limit crosstalk noise (traces = printed wires connecting components).
- Trace widths of **a)** 0.3mm for signal wires, and **b)** 0.5mm for power rails.

The PCB layouts are presented in the Appendix (Section12). The assembly was done in-house, using an SMD workstation from RS components. Figure 4.15 is provided, showing the fabricated and assembled modular PCB's along with the small-scale grid used to evaluate them.

[2] Autodesk Eagle version 9.6.2.

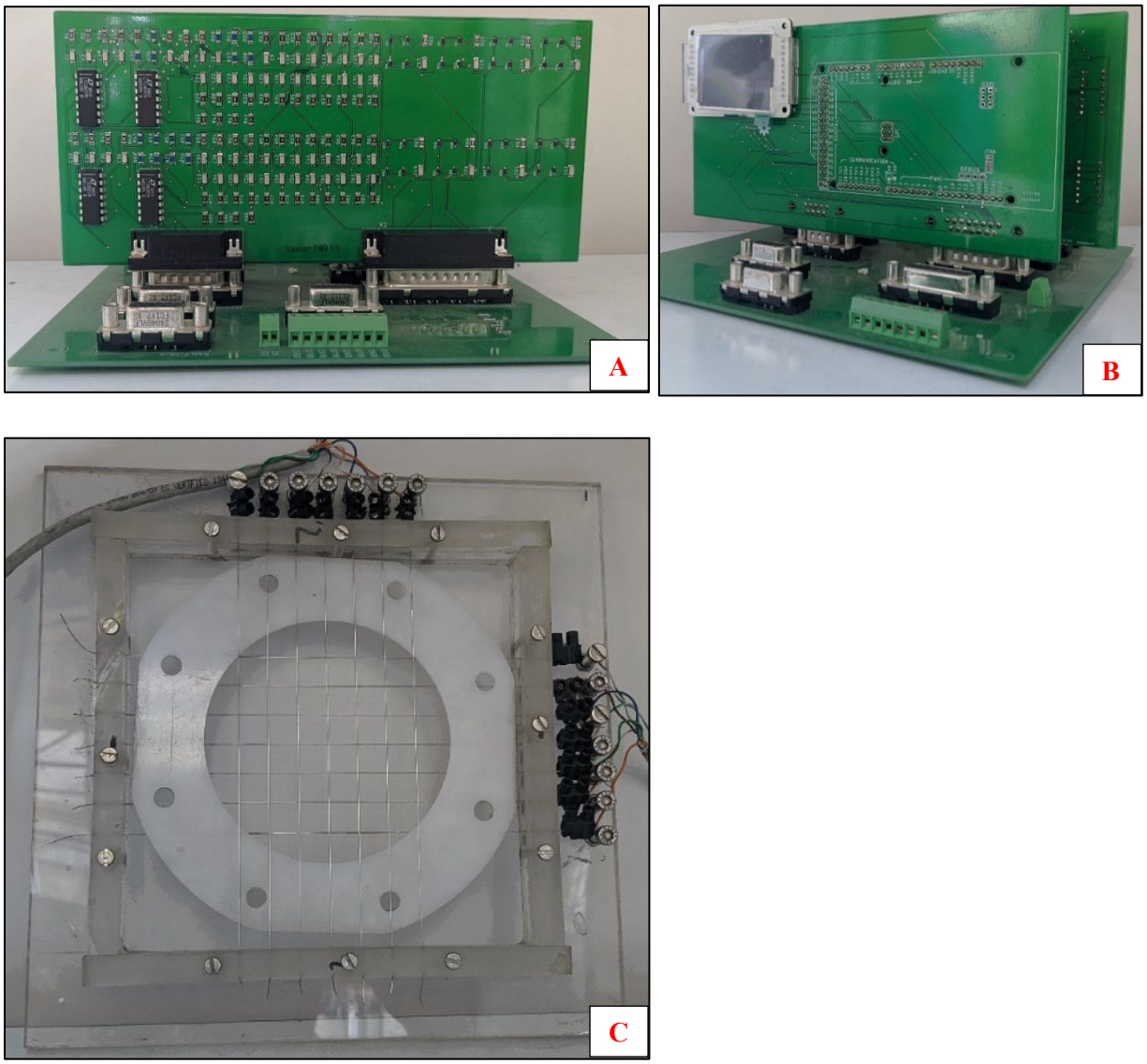

Figure 4.15: A) Auto-balancing bridge PCB, and B) Logging PCB, C) Small-scale wire mesh grid; Electrode spacing =10mm; Wire diameter 0.625mm. Gap between electrode planes 2mm

4.2.2.3 MODULAR CIRCUITRY TESTING AND VERIFICATION

A small-scale grid (8x8) was used for preliminary testing of the modular design. The grid presented in Figure 4.15 **c)** was tested as follows:

[1] Air-testing: The signal response of the circuitry was evaluated on each of the channels using the small-scale grid. The results are presented in Figure 4.16**b)**. Of the eight channels evaluated, the mean, minimum and maximum are presented to illustrate the consistency of the measurements. The presented results show the logical trend of no-conductivity (low frequency) and yet measurable capacitance (high frequency) for air. The noise in the evaluation was attributed to the scale of the measurements (very low voltages).

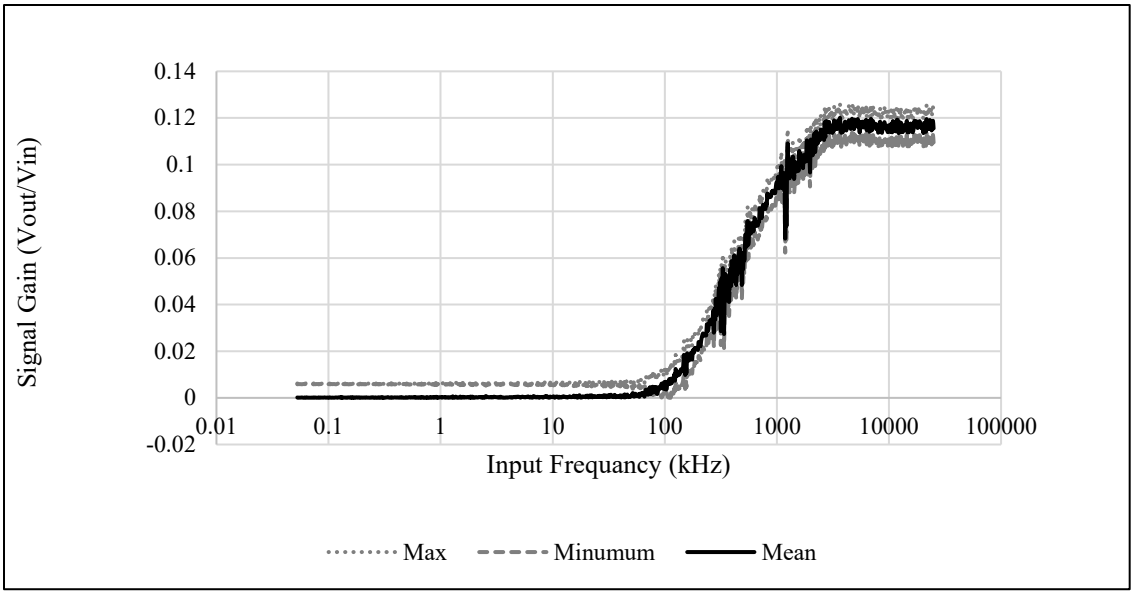

Figure 4.16: Signal response of air, i.e., no liquid on the grid. On the small-scale wire mesh grid; Electrode spacing =10mm; Wire diameter 0.625mm. Gap between electrode planes 2mm.

[2] Capacitance and resistance testing: Each crossing point of the grid was evaluated with an electrical resistor and capacitor in parallel to simulate a disturbance. The evaluations were conducted using a 100kΩ resistor and a 1pF capacitor. The results presented in Figure 4.17 illustrate measurable values for both resistance and capacitance, with negatable variation between the 64 crossing points.

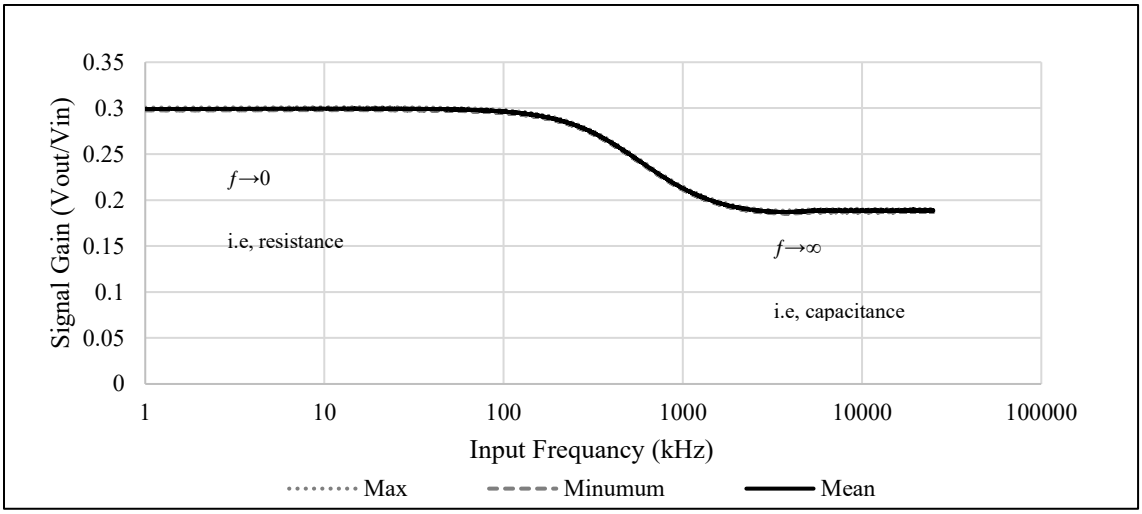

Figure 4.17: Signal response 100k resistance and 1pF capacitor in parallel. The response shows little variation in the readings and depicts long plateaus, which are key for stability.

[3] Water testing: Further testing was conducted using a 3/8" acrylic pipe, gasketed across individual wire mesh "crossing points". The signal response was evaluated using tap water as a disturbance (± 10mm). The response shows little variation in the readings and depicts long plateaus which are key for stability.

Figure 4.18 presents the results evaluated on both the capacitance(B) and resistance(A) channels (see labels on Figure 4.9 – *Vcap* and *Vconductivity*) of the circuitry. The figures highlight the measurement plateaus of both the capacitance and resistance circuits. The deviation of the plateau at frequencies lower than 500 Hz are attributed to insufficient settling times during the frequency sweep.

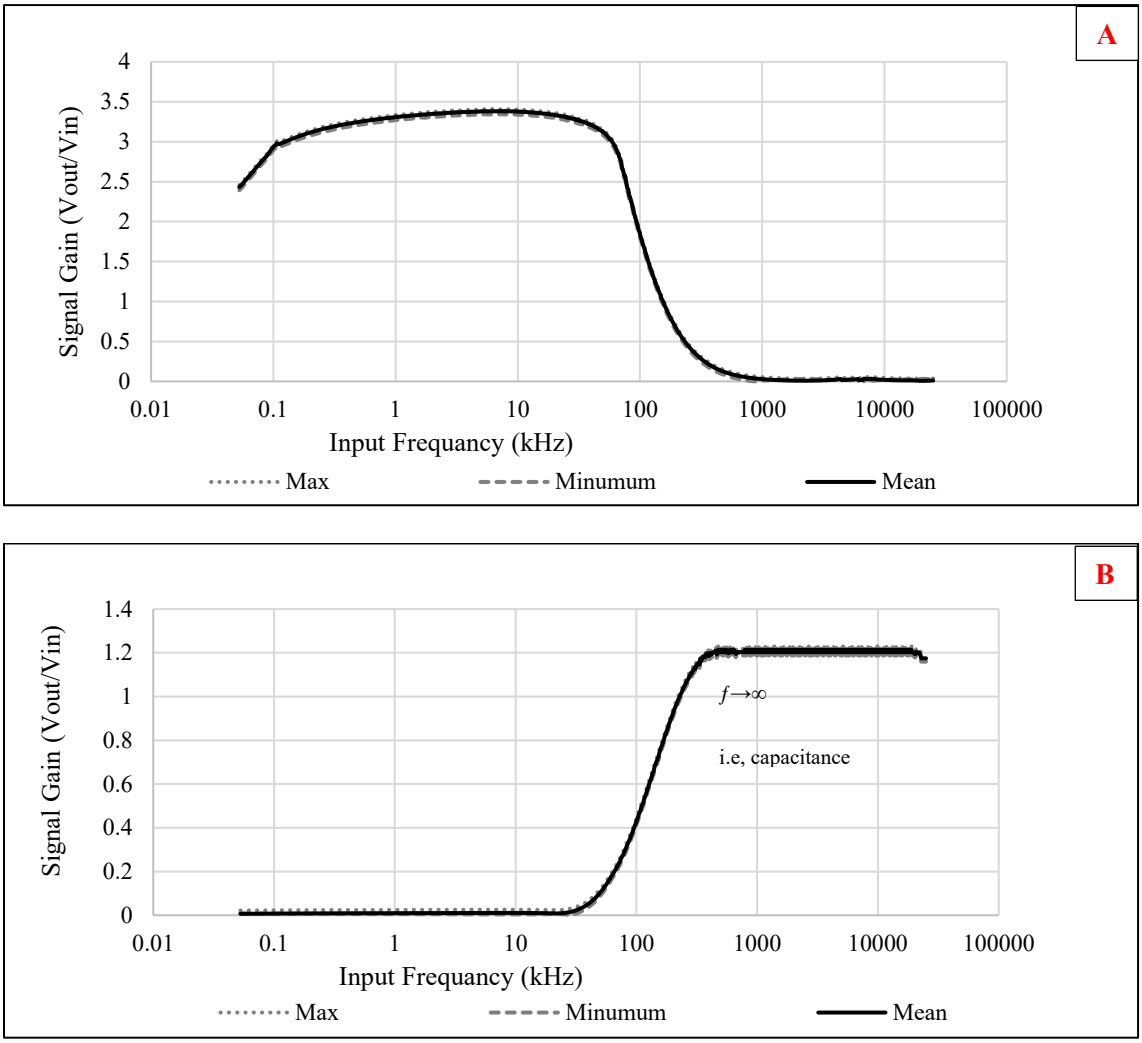

Figure 4.18: Signal response of water using A) conductivity; B) capacitance. The respective measurements were taken high and low pass filters and consequently only depict the values for capacitance and resistance.

[4] De-mux testing. The scheduling and wave splitting was tested on the small-scale grid to evaluate the switch-over times, capacitor loading times and the effective imaging speed. The results are presented in section 12.1 of the Appendix.

4.2.2.3.1 Conclusions from Modular design:

The following key aspects were highlighted in summary of the experimental evaluation of the small-scale prototype.

- The modular design used an adapted sample-and-hold circuitry to minimise high sample costs.
- Experimental evaluations validated the circuitry signal response, i.e. low frequencies measure conductivity, and high frequencies measure capacitance.
- 20 kHz was chosen for low-frequency conductivity evaluations and 10 MHz for high-frequency capacitance measurements.

Figures 4.18 A and B present excellent stability and long plateaus for both capacitance (Frequency approaches infinity) and conductivity (frequency approaches zero). This is advantageous as it offers a wide range of experimental input frequencies, offering additional flexibility in the presence of natural harmonics. The plateaus also affirm the fundamental requirements of a functional auto-balancing bridge.

4.2.3 Pilot-scale Circuitry

The pilot-scale sensor system was constructed from 5 separate modular blocks in a master-and-slave configuration, creating a 40 x 40 setup. A master node (M1) was used in a regulatory capacity to oversee the operations of the slave nodes (S1-S4). During sampling, the master node controlled the cycling of the excitation signal and storage times through communication with the slave nodes and their accompanied de-multiplexers. This ensured system integrity and that only one electrode could be activated at any instance. The ID of the activated electrode and data from the eight concurrently sampled channels were stored in separate text files based on the sampling Arduino (M1; S1-S4). An external signal generator (KKmoon 0-25MHz) was used to provide the sinusoidal signal to the circuitry.

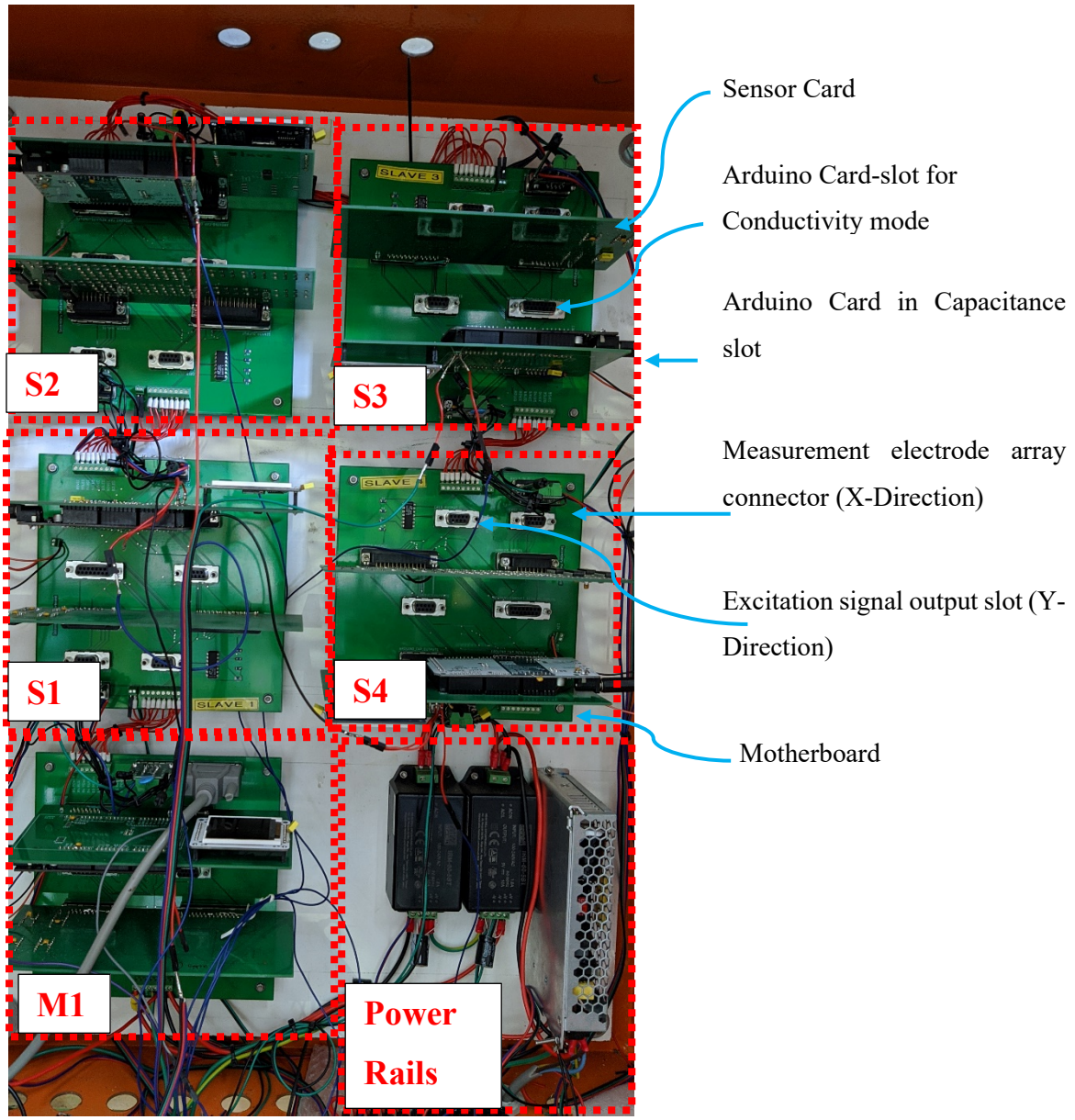

Figure 4.19: Pilot-scale sensor circuitry where M1 refers to the "master node" that controls the cycle times of the other nodes i.e., "slave nodes" (S1-S4)

4.2.3.1 Pilot Circuitry Testing and Verification

Preliminary evaluations were conducted on the pilot circuitry, based on single-channel performance with the methods set out in section 4.2.2.3. Any deviations from the expected tolerances were assessed and addressed. Deviations were mainly attributed to solder joint failures and were corrected.

Additional testing in the piloting phase included size calibrations using pseudo-droplets block/moulds. These pseudo-droplet blocks were created using a milling machine to drill incremental diameter holes into 12mm PVC and installing a single electrode crossing point (2mm separation in the Z- direction i.e., between the perpendicular electrodes) in the cavity. This allowed for the diameter-based calibration of the circuitry. A simplistic illustration of the blocks is provided in Figure 4.20, showing the variation in

simulated diameter. Additional experiments were conducted evaluating the influence of streams using holes drilled into PVC sheets up to 45 mm thick. The results showed little variation based on the liquid height outside the measurement zone (2 mm). The 12 mm thick calibration blocks were consequently used throughout.

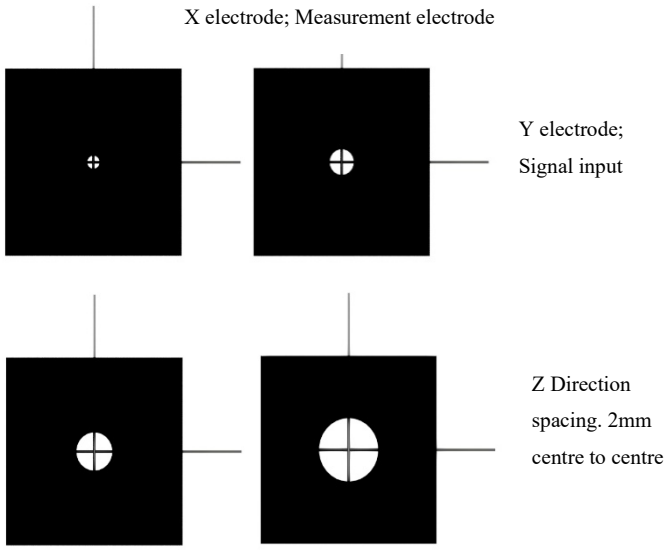

Figure 4.20: Pseudo droplet calibration blocks showing point evaluations for a variety of simulated droplet sizes.

Triplicate calibrations were conducted on both conductivity and capacitance using water and ethylene glycol. Figure 4.21**a)** presents the evaluations of capacitance; water, and ethylene glycol at 1.9 V and 10 MHz. The results showed excellent linearity and the ability to evaluate the disturbance's diameter based on the capacitance. The circuitry also produced excellent linearity across a range of input voltages, adding to the flexibility of the design. An example of such an evaluation is presented in the Appendix, Section 12.2

Comparison of the EMF model (0.12-5.4 pf) and the pilot-scale capacitance (1.1-10.5 pf) illustrated a sizable underestimation. The deviations were thought to be attributed to the numerous solder joints, connections, traces, and wires present in the pilot circuitry, as broken wires and insufficient joints approximate capacitors in the presence of high-frequency signals. Nonetheless, the sensor is still considered applicable, owing to the linearity across a variety of input voltages,

Figure 4.21**b)** shows the conductivity calibrations. The solutions were made up by diluting demineralized water with tap water, to obtain the required conductivity. Results are presented for water at 0.2V and 20kHz. Once again, excellent linearity was illustrated, highlighting the ability to evaluate the diameter of the disturbance based on the electrical circuitry, given known fluid conductivity. Following suit with the capacitance evaluations, the calibrations presented excellent linearity at a variety of input voltages (Appendix, section 12.2).

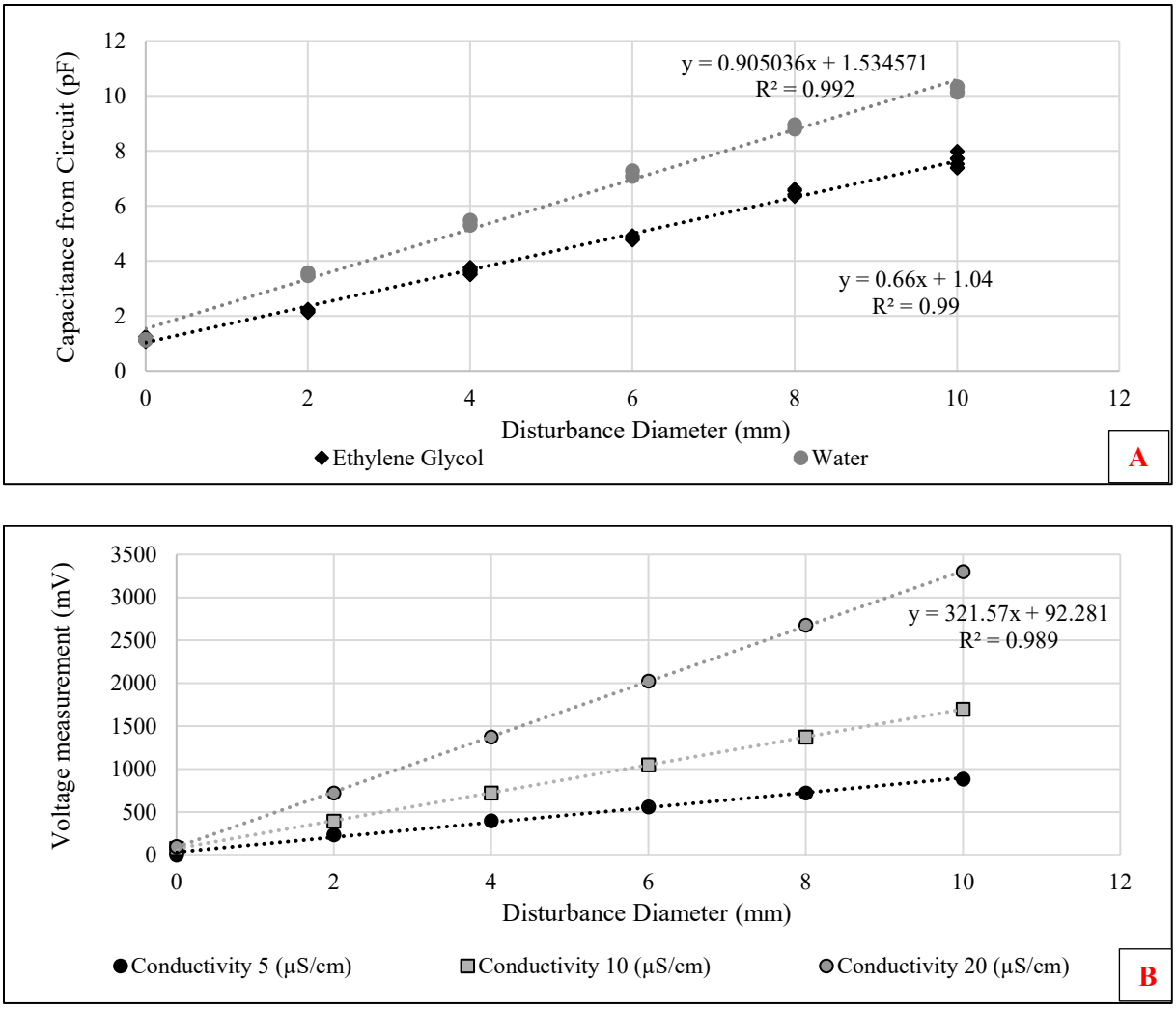

Figure 4.21: Cross sectional diameter-based calibrations using the millivolts recorded on the sensor for A) the capacitance circuitry and B) the conductivity circuitry.

4.2.3.2 Arduino Sampling and Measurement Code

A flow diagram of the Arduino coding strategy is provided in Figure 4.22. The code itself was omitted from the appendix due to the large volumes (10 000 lines of code) but is available from the department of process engineering, Stellenbosch University.

Based on the provided strategy, each electrode was activated for a minimum of 100 µs to allow for at least two complete waves at 20kHz to be sampled. The excitation times were extended to 1 ms for capacitance to mitigate the loading and discharge effects of the sample-and-hold circuitry.

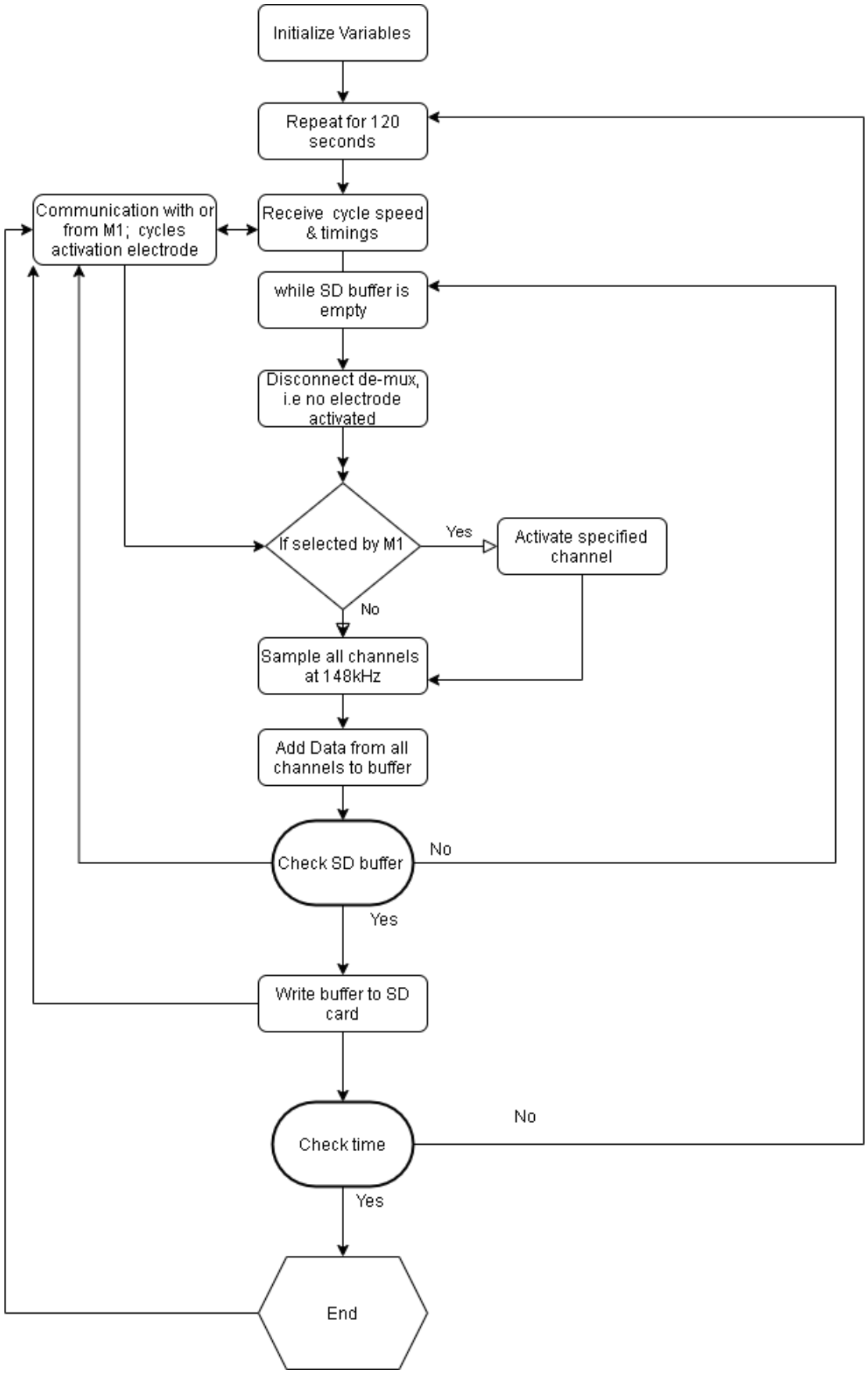

Figure 4.22: Arduino code flow diagram presenting the sampling logic.

4.2.3.3 SENSOR PRECISION

The experimental calibration curve measurements (Figure 4.21) used an entire modular block (8x8 Sensor PCB+ Motherboard + Arduino Sampling board), as discussed in section 4.2.2. Six separate channels were used and connected to the pseudo-droplet calibration blocks presented in Figure 4.20 (diameters of 2,4,6,8 and 10mm). The incremental blocks were filled with relevant liquid, and an additional 10mm block was left empty to reflect the vapour phase (Air). The calibrations considered 120s of measurements at each diameter. Each diameter was subsequently evaluated a respective 7659 and 777 independent times for conductivity and capacitance.

The diameter-based standard deviations are provided in Table 4.2 for water at 5µS/cm (Input: 0.2V) and Ethylene glycol (Input: 1.9V). These were chosen as they are at the low end of the feasibility window and would likely illustrate the exaggerated effects of noise.

Table 4.2: Standard deviations of calibration curves for both capacitance and resistance channels.

Diameter (mm)	Conductivity (mV)	Capacitance (mV)
0	1	0.8
2	1.72	0.89
4	1.68	1.01
6	1.9	0.95
8	1.81	0.76
10	2	0.82

The relative magnitude of the deviations compared to the measurement resolution (0.8mV) suggested excellent repeatability and circuitry stability. A minimum signal-to-noise ratio of 125 was consequently reported at 2mm diameters. This was deemed sufficient for diameter evaluations down to 2mm using either capacitance or conductivity.

4.2.3.3.1 Conclusions Drawn after Evaluation of Pilot Circuitry

As outlined in this chapter, the EIT circuitry development progressed from idea generation to full scale prototyping. In so doing, the following key conclusions were drawn from the final prototype:

- The presented circuitry was experimentally validated to produce a linear response to diameter based on both capacitance and conductivity.
- Therefore, the circuitry improves the spatial resolution of the wire-mesh grid by evaluating the diameter of the disturbance as measured.
- A linear voltage response was recorded for droplet diameters between 2 and 10 mm using both capacitance and resistance. Droplet diameters down to 2mm are thereby accurately detected.
- Given the chosen frequencies, the circuitry and sampling speeds were adapted to provide 207 full images of column (37x37 channels) per second on conductivity and 21 on capacitance. The reduction in speed on the capacitance side is attributed to the discharge rate of the half-wave rectifier (oscilloscope images in 12.1.1.1). Additional settling time was consequently incorporated as mitigation.
- A minimum signal-to-noise ratio of 125 is expected, with excellent repeatability.
- Due to the nature of the auto balancing bridge, any frequency below 50kHz and above 10MHz can be respectively used to evaluate resistance and capacitance. This provides added flexibility.
- The chosen design is very cost-effective, amounting to a total circuitry and sampling cost of R45000 or $3200 at the time of development.

5. MECHANICAL DESIGN AND EXPERIMENTAL SETUP

The EIT wire-mesh grid, discussed in this chapter, was built into an existing pilot column with a 400m diameter at the Department of Process Engineering of Stellenbosch University. The pilot plant installation is discussed in detail in work of Uys [89] and was previously used by Lamprecht [2] and Minne [5] in their hydrodynamic characterisations of random packing.

5.1 WIRE-MESH GRID DESIGN FOR EIT SENSING

The wire-mesh grid was used alongside the auto-balancing bridge quantification system, discussed in Chapter 4. The mesh array efficiently created measuring points at every wire crossing (Figure 5.1), providing a pixelated cross-sectional area plot of impedance values. These values are grouped into resistance and capacitance measurements. The pixelated plot was refined using the parallel plate capacitive theory and the diameter-based calibrations in the previous section. The aforementioned increased the spatial resolution and provided the ability to distinguish between two adjacent droplets and one large stream.

The adapted wire-mesh methodology is widely used in electrical engineering, most notably in the capacitive touch screens found in modern smartphones. In essence, it entails:

- Cyclic activation of the signal input electrodes (Y-direction, Y1 to Y37), i.e., only one input electrode is active at any time instance, with
- Continuous measurement of **all** of the measurement electrodes (X1 to X37).

This method produces the cartesian vector coordinates of the disturbance. In the examined case, the red droplet. The data, therefore, have the cartesian form:

$$(x : y) = (Measured\ electrode\ or\ column; Active\ electrode\ or\ row\ ) \quad 5.1$$

The pilot-scale wire-mesh grid comprised two layers of 37 electrodes per plane (parallel distance of 10mm), spaced perpendicularly at a distance of 2mm (See Figure 5.2). The 37 x 37 grid created 1369 measuring points across the bed diameter of 396mm. Aeronautical grade 302 stainless steel locking wire (0.625mm diameter) was used for its resistance to elongation when tensioned.

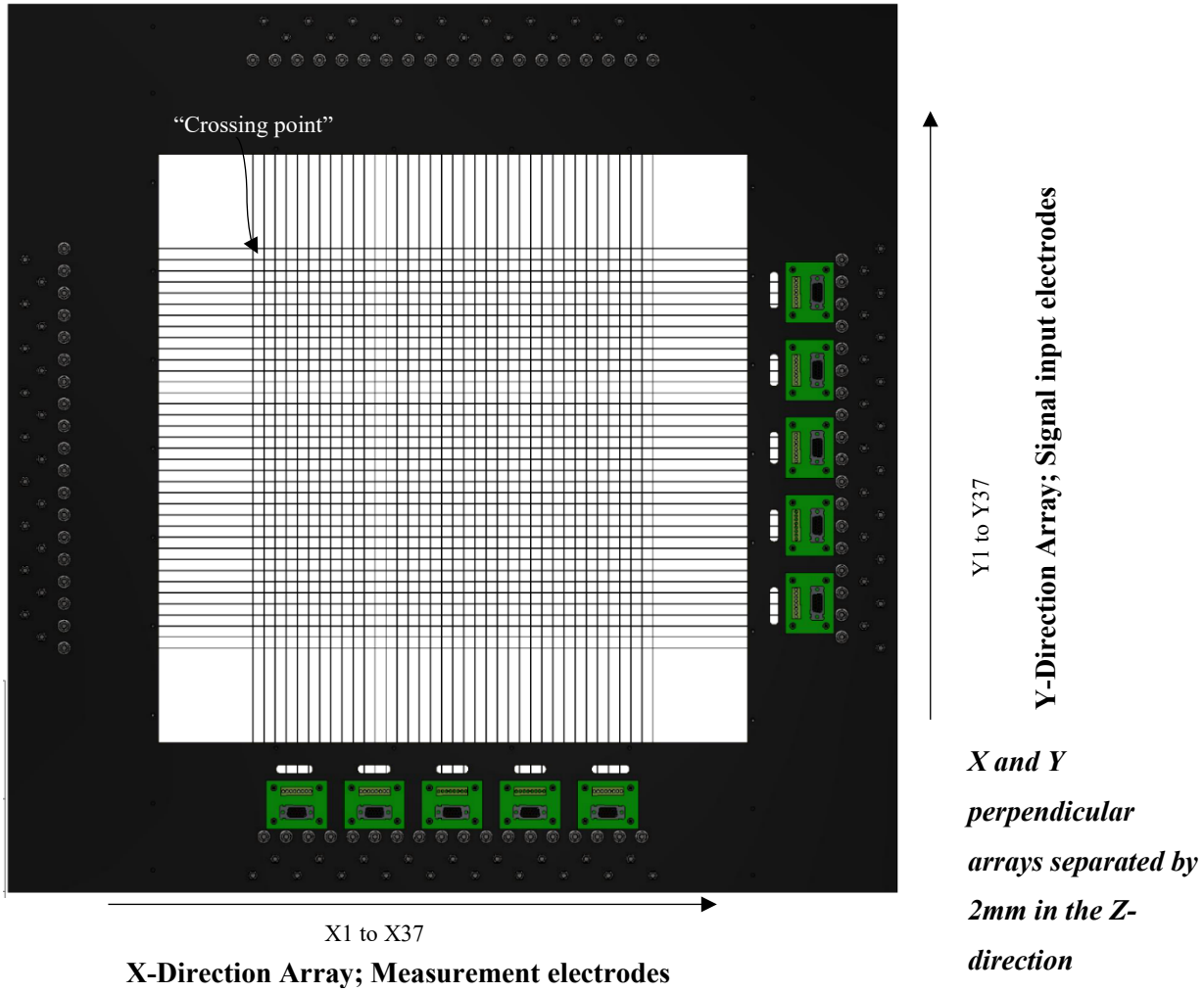

Figure 5.1: Schematic of Wire-mesh grid developed in this chapter. The schematic shows toe perpendicular planes of electrodes (Y&X). The separate planes are kept from touching by separating them by 2mm. The "gap" at the crossing points creates the effective sampling zone.

All electrode wires were cut to 490mm prior to in stallion and tensioning to limit variation between channels. The individual electrodes(wires) were attached with a locknut system and tensioned with tension springs to 105N (±5N). The tension springs:

[1] Limited sagging and tightening from temperature fluctuations,
[2] Assured that the electrodes would not deform and short-circuit,
[3] Enabled tensioning and fault checking without disassembly.

The exact tightening strength was determined as the minimum tension that **a)** insured rigidity and **b)** limited natural harmonics on the wires when exposed to falling droplets and vapour. This was evaluated using the oscilloscope measuring the induced signal from the column at F_s =1.83 $(m.s^{-1})\cdot(kg.m^{-3})^{0.5}$ and liquid loading of 98 $m^3.m^{-2}.h^{-1}$.

The induced voltage was limited to below 5mV (measured at block four based on the previous analogy) and deemed sufficiently low (See Figure 12.11 in section 12.3 of the appendix).

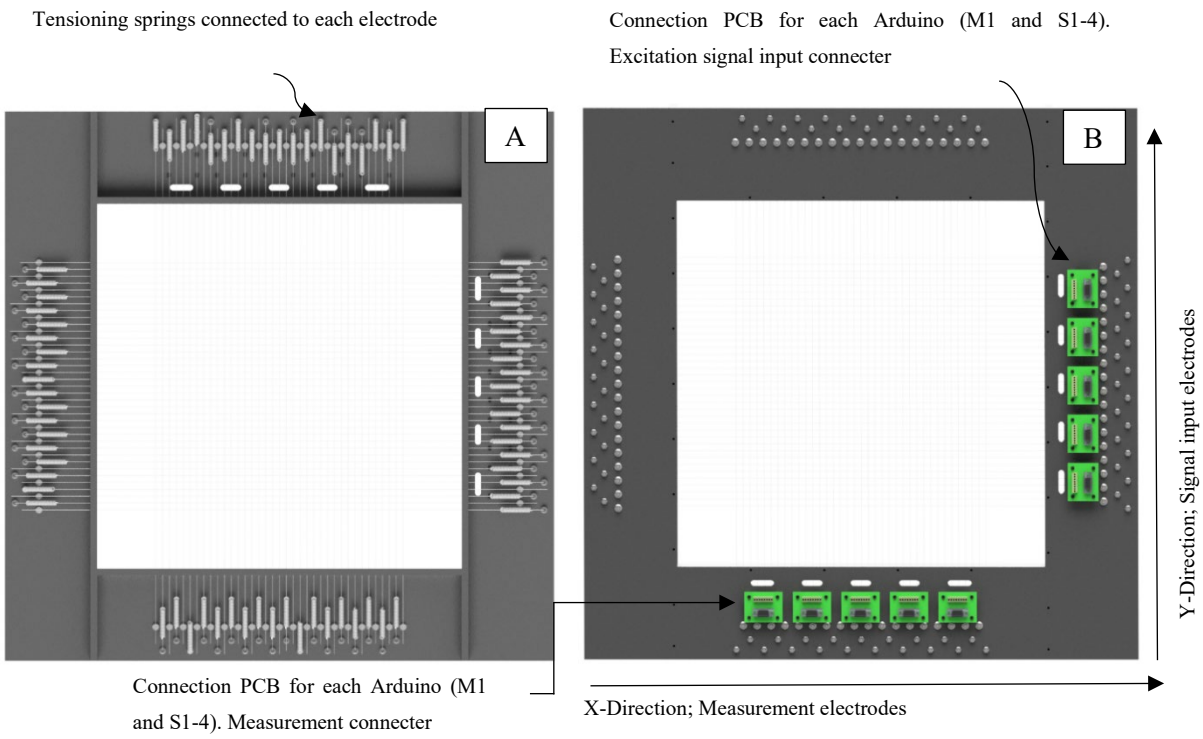

Figure 5.2: Wire mesh grid design: A) Bottom view, and B) Top view. The schematic depicts the tensioning system and PCB's for simplified connections.

A finite element deformation model was constructed to ensure that the grid-frame could handle the tensioning forces. The evaluation was performed in the Autodesk Inventor statics package. The model evaluated PVC, POM and PET as possibilities based on their electrical stability (isolator), cost and structural properties. The evaluation for the 10mm POM design is provided in Figure 5.3. The relevant deformation data are summarized in Table 5.1.

Table 5.1: FEM deformation analysis.

	Weight [kg]	Max Displacement[mm]
PET (Polyethylene terephthalate) 8mm	5.59	0.08
PET (Polyethylene terephthalate) 10mm	6.88	0.037
POM-C (Acetal Copolymer) 8mm	5.17	0.68
POM-C (Acetal Copolymer) 10mm	6.37	0.357
PVC 8 mm	4.68	2.78
PVC 10 mm	5.76	1.46

The evaluated materials all presented elastic deformation, with PET outperforming POM-C and PVC. However, PET was ruled out as the standard sheet sizes were insufficient (620mm x 1000mm). The frame was subsequently constructed from 10mm POM-C, with the holes and grooves being precision cut via waterjet.

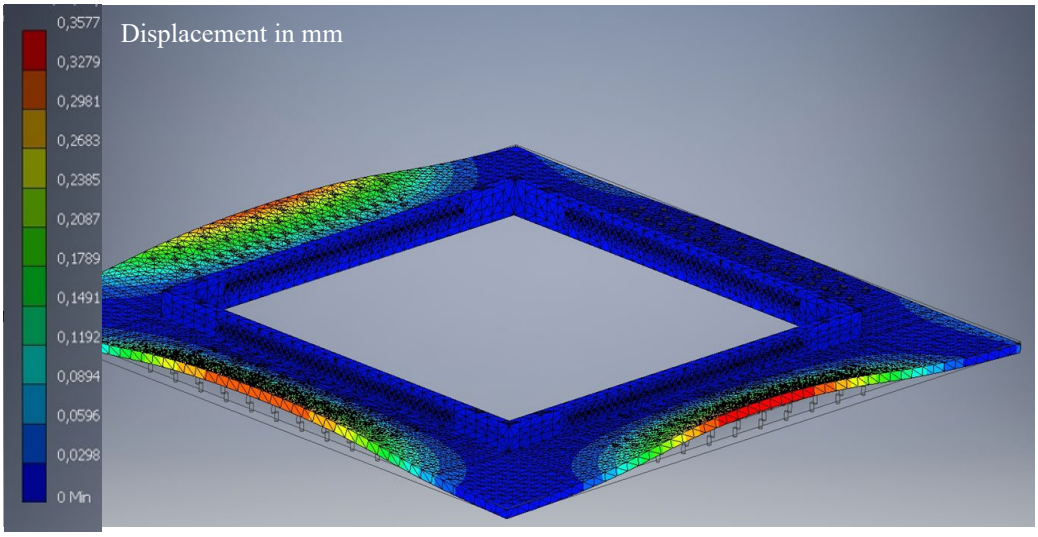

Figure 5.3: POM 10mm deformation model as projected by Autodesk Inventor. The Red indicating areas of maximum deformation under tensioning stress.

A spacer and gaskets were used to seal between the two electrode layers, totalling 1.4mm after compression (Centre-to-centre electrode distance of 2mm). Additional gaskets and POM-C dummy flanges were installed on either side to ensure that no electrically conductive parts were within the 20mm of the excitation or measurement electrode (as suggested by the EMF model). The setup was sealed with the combined weight of the column and 4 G-clamps hand-tightened to prevent leaks. Figure 5.4 to 5.6 are presented to illustrate the mesh-grid design and final implementation.

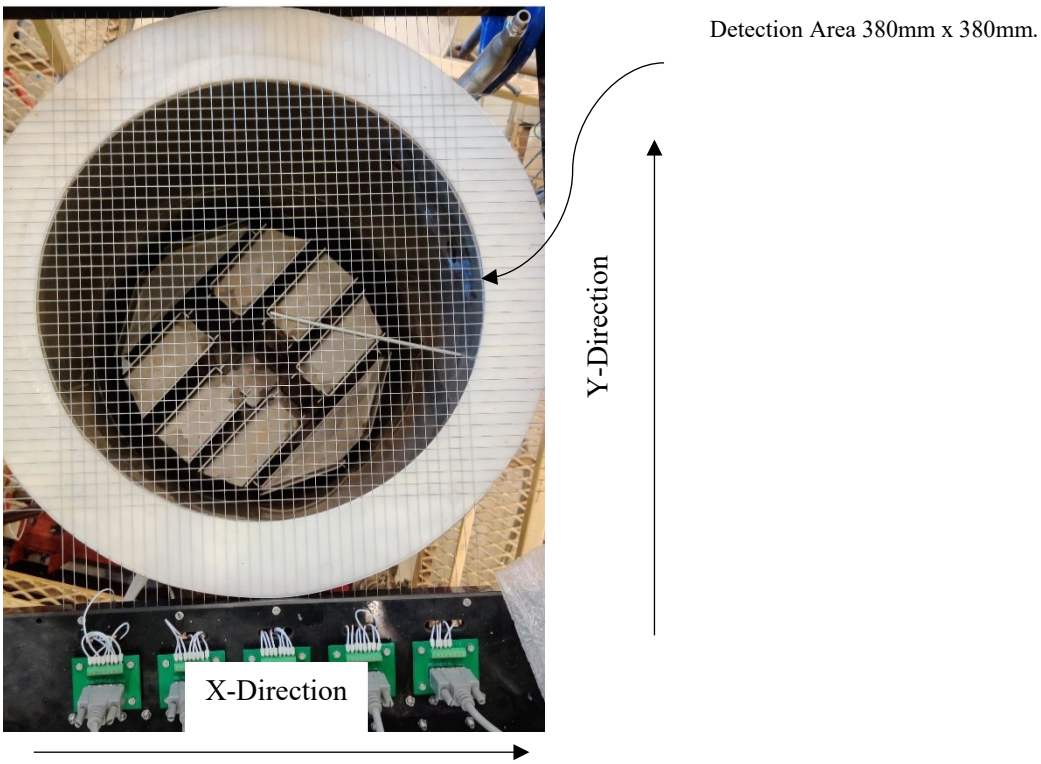

Figure 5.4: Mesh-grid spacing at the bottom of the distillation column showing the detection area.

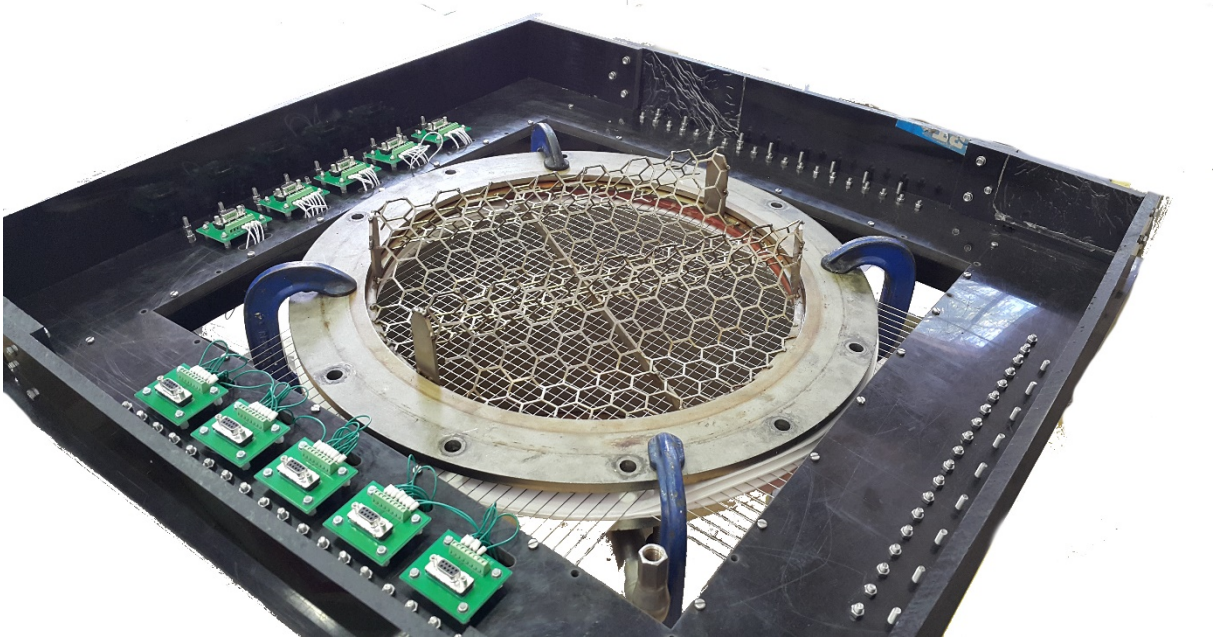

Figure 5.5: Image of sensor grid installation with the sinusoidal packing support grid used by Lamprecht [2] and Minne [5]. This support grid was later replaced with a woven support grid.

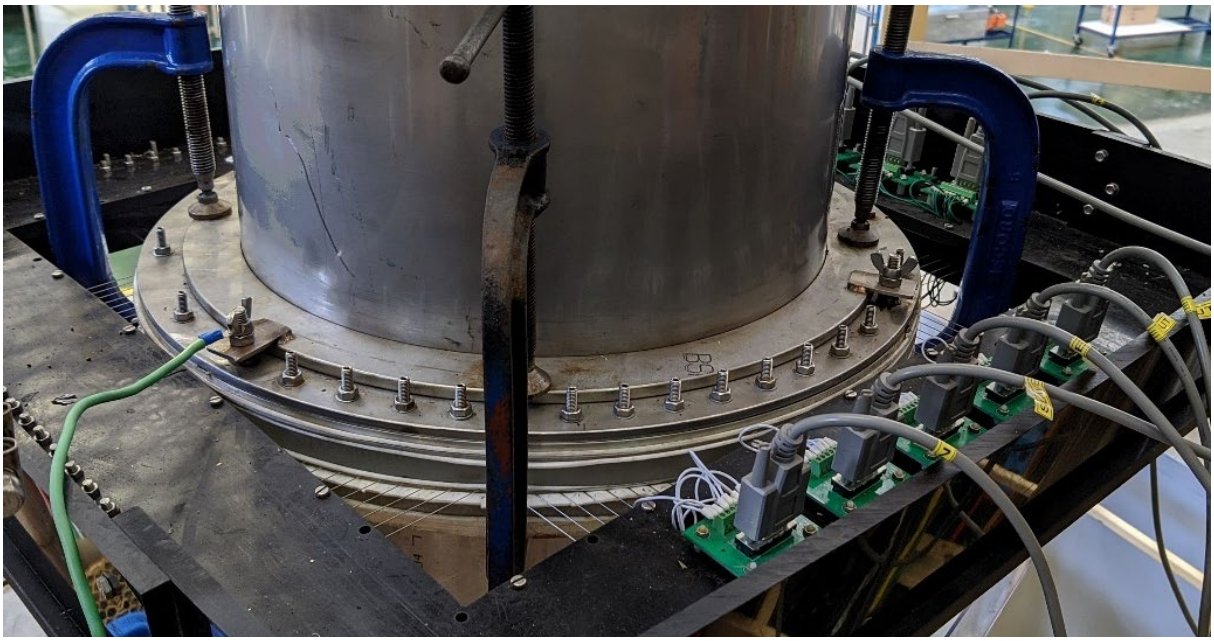

Figure 5.6: Image of sensor grid installation at the bottom of the distillation column. The electrodes are illustrated moving through the flange and onto the PCB's. The G-claps are sued to seal the column with compression force.

Additional measures were taken to ensure that all wires connecting the grid and the PCBs were of identical lengths to mitigate channels differences. The wires connected the grid (mini-PCB in Figure 5.6), and sensor PCB (Figure 4.19) were standardized at 1m to mitigate crosstalk.

The design parameters and the reasoning behind them are tabulated in Table 5.2

Table 5.2: Summary of the design parameters and their reasoning related to the mesh grid

Parameter	Value/Specification	Reasoning
Number of electrodes in each perpendicular array (X and Y Directions)	37, spaced 10mm apart	Chosen imaging size for maximum resolution and minimum flow interference
Electrode spacing in the Z Direction	Centre to centre: 2mm	Choice based on chapter 4 and the modelling within
Electrode description	0.625mm wire diameter made from 302 stainless steel.	The reasoning was to use a small enough wire diameter to inhibit droplet accumulation between the perpendicular electrodes (surface tension forces keeping the droplets in). There is however a trade-off between diameter and strength, hence the choice.
Effective area of sampling	380mm x 380 mm within a 396mm diameter column	Detection area, therefore, comprised 99.5% of the column area. Graphical representation in Figure 6.4.
Electrode tensioning	Each of the electrodes was tensioned to 105N.	Mitigation step to reduce sag and natural harmonics through vibration. Any sag in the electrodes will decrease the Z-direction electrode spacing.
Material of construction of frame housing the electrodes	10mm POM-C	Combination of rigidity, machinability, and availability.
Housing frame size	External square 800x800mm. Internal square 530x530mm	Physical restraints of column and surrounding scaffolding.
Individual electrode lengths	490mm	Standardised length to ensure negligible variation in baseline resistance and capacitance to each measurement channel.
Connecting wires.	All wires, connecting the Grid to the mini-PCB on the frame and from the frame PCB to the sensors, were standardized to within 5mm.	This was to ensure minimum variation in the baseline measurement of each channel and simplify the calibration procedures.

5.2 Pilot Plant Layout and Operation

The hydrodynamic characterisation setup from Lamprecht [2] and liquid the liquid distributor from Minne [5], was used for the experimental characterisations with the EIT sensor. The characterisation setup was modified, replacing the glass sections with 396mm (ID) stainless steel to closer resemble industrial EMF conditions. A schematic of the setup is provided in Figure 5.7, redrawn from the Minne [5]. The EIT sensor grid was installed under 3m of packing to allow sufficient distribution. A brief description of the setup will be provided, with further details available in Lamprecht [2] and Minne [5].

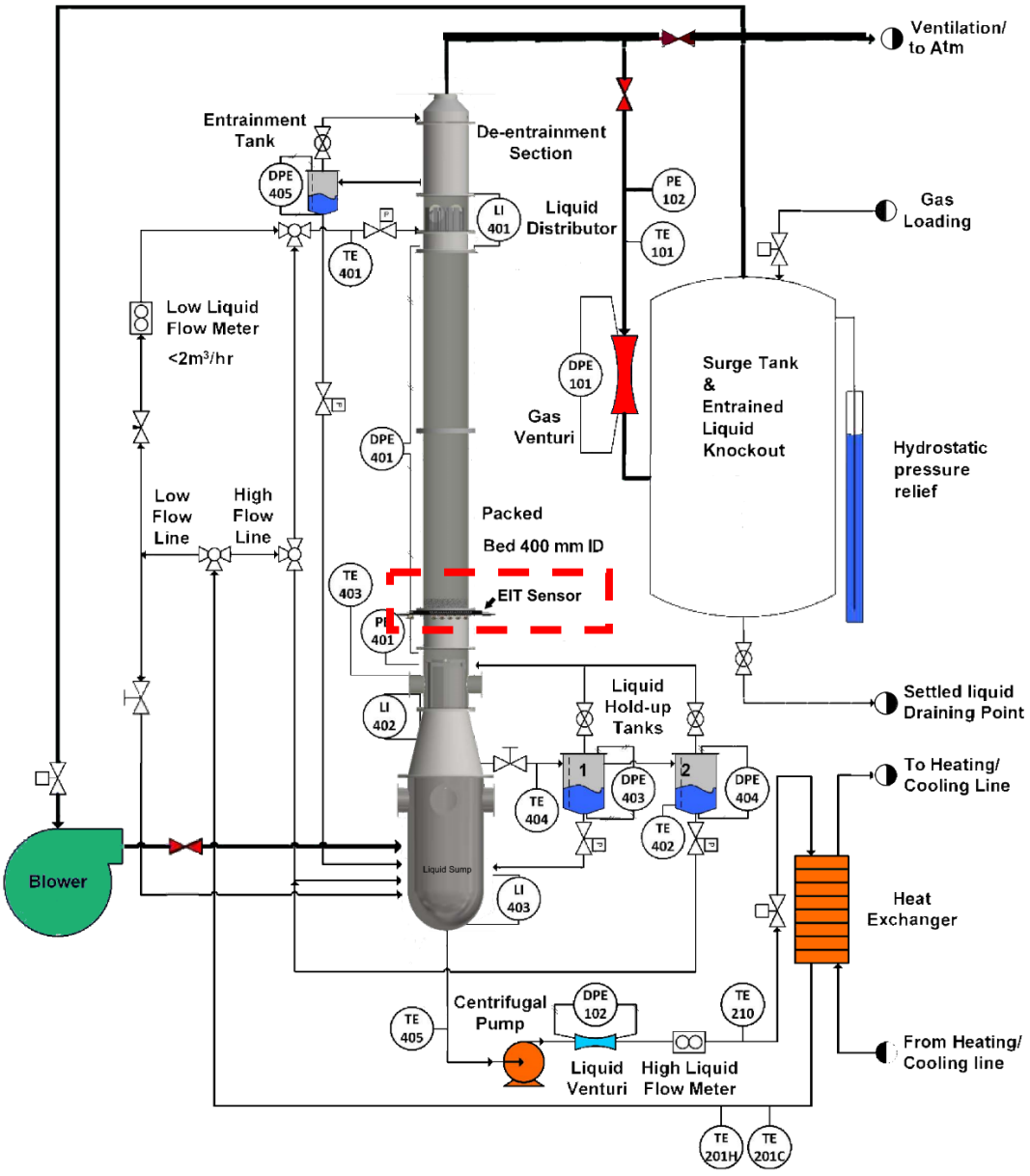

Figure 5.7: Packed column experimental setup at Stellenbosch University.

The experimental setup was designed and validated to operate with liquid loadings ranging from 0 – 122 $m^3.m^{-2}.h^{-1}$ and vapour flow factors from F_s =0-6 $(m.s^{-1})\cdot(kg.m^{-3})^{0.5}$. It offered a 3m packed height and used the liquid drop-out method of liquid hold-up estimation. The setup was equipped with a channel-type liquid distributor comprised of 19 drip points for a drip point density of 157 per m^2. A de-entrainer using centrifugal force (supplied by Koch-Glitsch) was used to remove the entrained liquid above the liquid distributor. The collected liquid was drained and measured in the de-entrainment tank. Uniform gas distribution was achieved at the bottom of the column through with a chimney design vapour distributor. Interested readers can further consider the experimental setup with the interactive 3D model of the packed column in Appendix 14.8.2 . The model can rotate, zoom, measure and the components can be rendered transparent for interrogation of the column design.

5.2.1 Process Flow

The experimental setup aimed to evaluate packed column hydrodynamics in the absence of mass transfer. It consequently recycled both the liquid and favour in a closed system. This ensured negligible mass transfer effects after sufficient phase exposure. The process flow was split into separate phase loops to aid discussion. Subsequently:

5.2.1.1 Liquid Loop

The liquid loop for the experimental setup was split into high- (>2$m^3.m^{-2}.h^{-1}$) and low flow (>2$m^3.m^{-2}.h^{-1}$) using a 2” and 1” line, respectively. This allowed for greater measurement accuracy across the whole range. The liquid was collected from the sump and pumped through both a 2” gear-flowmeter and calibrated liquid venturi (redundancy), whereafter it was sent through a plate-and-frame heat exchanger. The heat exchanger was connected to both cooling water and a heating line to regulate the liquid temperature to 25 ℃.

The resulting liquid was split into either the low or high flow lines, depending on the required flowrate. The low-flow line was equipped with an additional 1” gear-flowmeter for accurate quantitation between 6-20 $m^3.m^{-2}.h^{-1}$. Both high- and low liquid lines combined before the column, where the liquid was introduced via the channel-type liquid distributor. The distributed liquid flowed down the 3m packed-bed before reaching the wire-mesh grid 20mm below the packing. The sinusoidal packing support-grid (30mm hexagonal openings with 86.5% open area supplied by Koch-Glitsch) from Lamprecht [2] was exchanged for a flat woven design with 96.2% open area. The grid was made from 1.1mm diameter braided stainless wire and woven to produce 30mm openings. The purpose of the design was to reduce the influence of the support grid and measure the droplet behaviour directly under (20mm) the packing. Given the packing sizes, 38mm to 62mm, this was thought to be sufficient to approximate inter-packing distributions.

5.2.1.2 VAPOUR LOOP

Vapour was introduced onto the column through a centrifugal blower and quantified with a calibrated venturi. The venturi was designed according to ISO 5167-1:1991 specifications. More detail is provided in Lamprecht [2].

A chimney vapour distributor (static mixer) was used to ensure uniform vapour distribution at the bottom of the column. Upon entering, the vapour passed through the whole bed and collected in the knock-out/surge drum. This allowed small, entrained droplets that escaped the de-entrainer, to settle out before gas recirculation. Indirect temperature control was used on the vapour line (heating through the liquid), motivated by the ratio of heat capacities (water/air = 6).

Pressure drop readings were continually taken across the bed for use in hydrodynamic verification. Additional details regarding the relevant sensors and their tolerances are available in Lamprecht [2] and Minne [5]. For reference, the experimental setup measurement ranges and maximum errors are presented in Table 11.1of the appendix

5.2.2 COMPONENT CHOICES

A testing regime similar to that of Lamprecht [2] and Minne [5] was chosen to ensure comparative applicability with their published data on pressure drop and liquid hold-up. Both studies were conducted on the same experimental setup and showed comparative results. The study from Lamprecht [2] focussed on the air / water evaluation of 1.5" Pall® Ring, 38mm IMTP® and Intalox® Ultra size A. The alternate study from Minne [5] used Intalox® Ultra (size A and O) and evaluated various combinations of physical properties, among which the ethylene glycol / air.

The conductive and capacitive nature of the EIT sensor was consequently evaluated, using the following systems:

- **Conductive principal**: Air / water.
- **Capacitive principal**: Air / ethylene glycol.

The liquid combinations were chosen to illustrate EIT characterisation applicability on:

- Conventional air / water hydrodynamic characterisation systems, and
- high viscosity and low surface tension alternative (more industrially applicable to distillation).

The liquid flowrates were chosen at specific increments between 6 and 122 $m^3.m^{-2}.h^{-1}$. These choices were influenced by distribution efficiency (based on the standpipe design by Minne [5]) and to correlate with literature sources in Minne [5] and Lamprecht [2].

The loadings are as follows:

- $6 m^3.m^{-2}.h^{-1}$
- $37\ m^3.m^{-2}.h^{-1}$
- $73\ m^3.m^{-2}.h^{-1}$
- $98\ m^3.m^{-2}.h^{-1}$
- $122\ m^3.m^{-2}.h^{-1}$

The liquid-vapour pairings (Table 5.3) and their physical properties are distinctly related to the hydrodynamic behaviour of the column. The relevant physical properties were measured and logged after each loading, with their averages represented accordingly.

Table 5.3: Vapour and liquid physical properties.

		Molecular weight [g/mol]	Density [kg/m^3]	Dynamic Viscosity [mPa.s]	Surface Tension [mN/m]	Boiling Point@1 atm [°C]	Kinematic Viscosity [m^2/s]
Liquid	**Water**	18	997	0.89	70	100	-
Liquid	**Ethylene Glycol**[3]	62	1095	11	34	198	-
							-
Gas	**Air**	29	1.18	1.84E-02	-	-	1.54E-05

Analytical measurements.

- Liquid Density: SIGMA 702 Tensiometer with a resolution of $0.1 kg/m^3$
- Liquid surface tension: SIGMA 702 Du Noüy Ring Tensiometer with a resolution of 0.01 mN/m.
- Liquid Viscosity: Paar Physica MCR501 Rheometer of with a resolution 0.01 mPa.s.

5.2.3 Random Packing

The progression across the packing generations was evaluated using Pall® Ring and Intalox® Ultra variants. Packing availability limited the study to 1.5",2" Pall® Ring and Intalox® Ultra sizes A, L and O. The progressive trend across the generations has been to increase packing open area for decreased pressure drop. The Intalox® Ultra are consequently more reliant on droplet formation than on the packing's specific/geometric surface area [21]. This provided functional differentiation between packings.

[3] The hygroscopic nature of ethylene-glycol is well document. The specific reagents were used by Minne [50] and subsequently hygroscopic equilibrium was assumed. This assumption was validated through the stability of the physical properties across all of the experimental runs.

5.2.4 Testing Procedure

The hydrodynamic testing procedure from Lamprecht [2] was emulated with the addition of the EIT system. The procedure entailed loading liquid and vapour within a closed-loop packed column and allowing the counter-current system to reach steady-state (both temperature and pressure stability) at 25°C. At steady state, the various physical properties were analytically evaluated, as set out in Table 5.3. Additional conductivity measurements were taken using and calibrated RS-pro conductivity meter.

5.2.4.1 Calibration of the Wire-Mesh EIT Sensor

The EIT circuitry presented excellent linearity to the disturbance diameter, at a range of input voltages. The specific input voltage of the excitation signal was selected to maximize the Arduino's 0- 3.3V measurement span. Consequently, it was chosen to produce a 2.8V (85% of max range) response to a 10mm diameter disturbance. A representative sample was taken from the sump, and calibration curves were generated using the pseudo droplets discussed in Section 4.2.3.1.

The calibrations were performed in triplicate with the five incremental (diameter of 2,4,6,8,10mm) blocks containing liquid, and one 10mm block kept empty to approximate air (0 mm). The calibrations were performed on a spare modular block and sampled with the Arduino PCB (As stated in section 4.2.3.1) for a complete cycle of 120s. This produced triplicate calibration curves with 7659 and 777 independent conductivity and capacitance measurements each. The averaged data were used as the final calibration curves.

Initial estimates of the input voltages were chosen using by incorporating the measured conductivity and capacitance into the LTspice XVII model and solving for a signal output of 2.8V.

These estimates were considered sufficient for lower conductivities (>15µS/cm) and produced a maximum under-prediction of 0.4V in solutions above 30µS/cm. This was likely as a result of the exaggeration of the error in approximating linear temperature compensation for conductivity (coded into LTspice XVII).

5.2.4.2 SAMPLING

After a minimum of 15 min at steady state, the EIT system was activated and allowed to sample for 120s. Upon completion, all relevant pressure drops, and flow measurements were taken, averaged over the 120s. The stored data were transferred to computers for post- and image processing.

Additional aspects:

[1] Liquid hold-up- and entrainment data were not measured in this study, opting to rather compare with the available literature from Lamprecht [2] and Minne [5].

[2] Low liquid flow evaluations were preceded by a packing wetting stage of 20 min at $98 m^3.m^{-2}.h^{-1}$.

[3] Conductivity measurements were taken twice daily to compensate for potential changes in ion content of the liquid.

The detailed operating and start-up procedures are elaborated upon in section 11 of the Appendix.

6. DATA AND IMAGE PROCESSING

A flow diagram (Figure 6.1) show the sequence of steps in the complex post-processing algorithms. The raw code is not presented in the Appendix due to the volume (+-6000 lines) and the nature of the intellectual property held within. The code is available at Stellenbosch University, Department of Process Engineering.

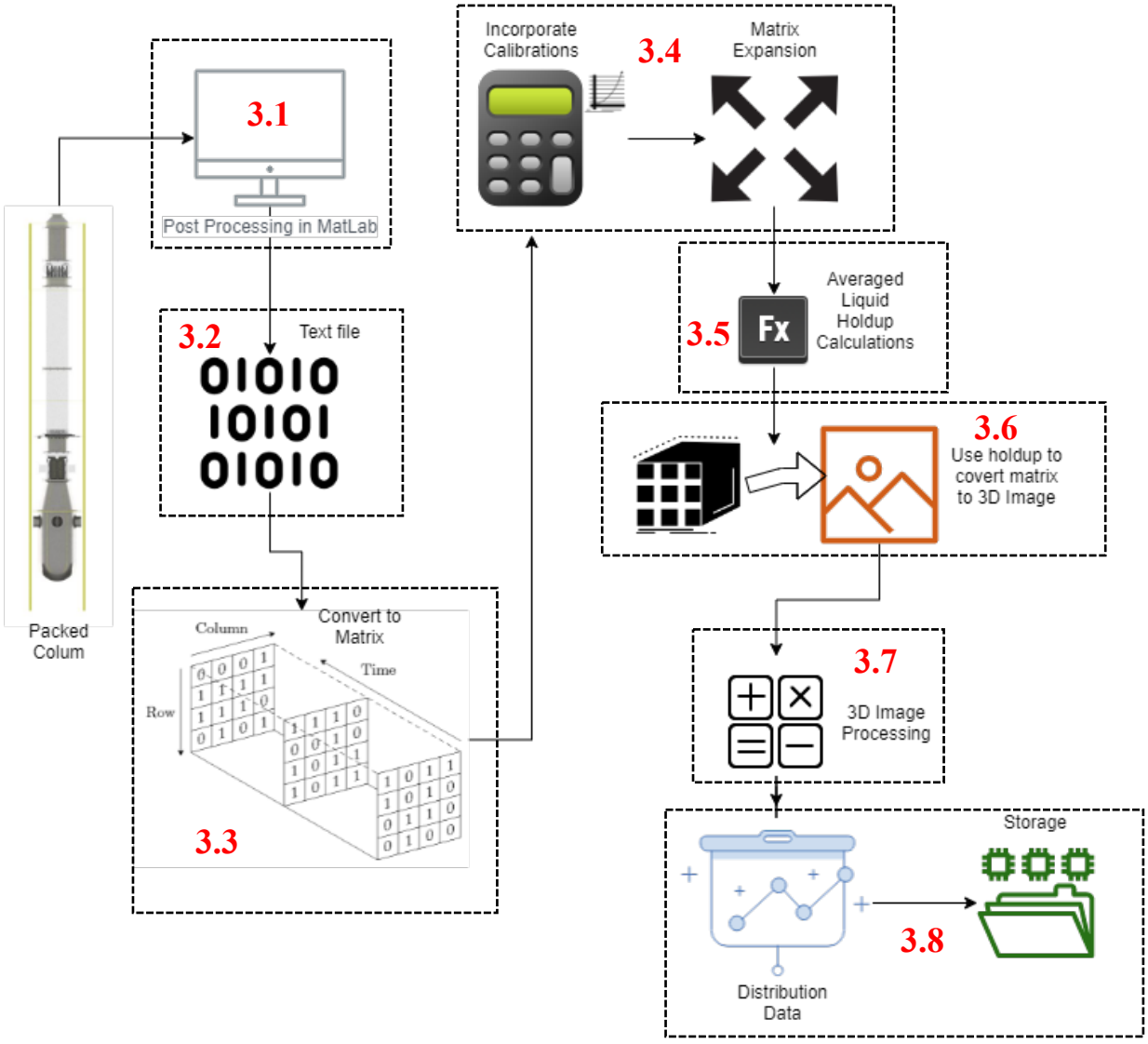

Figure 6.1: Flow diagram of post-processing and imaging. The diagram is explaining using the block approach suggested in Section 1.7.

6.1 IMAGE PROCESSING METHODOLOGY

The presented diagram (Figure 6.1) was used to clarify the post-processing methodology used in this document, continuing with the block-based description strategy. Post-processing was very time-consuming, taking between 4-10 hours per run (560 experimental runs were considered).

6.1.1 Block 3.1: Import to PC

Post- and image processing were done in Matlab. The package version and complete list of included toolboxes are presented in the appendix in section 13. The alternative use of Python was evaluated using 10000 iterations of a set of vector-volume calculations. The freeware package (without specialized vectorization algorithms) offered an order of magnitude slower processing speeds than Matlab, and the latter was subsequently chosen. The specificity of the computers used in the study are presented in Section 13.2 of the Appendix.

6.1.2 Block 3.2: Combining Text files

The individual modular blocks compiled 120s worth of data into a single text file per run, which contained:

- The activated electrode; Y1 to Y37 and,
- 12Bit values from each measurement (X1 to X37) electrode. Each used eight measured channels except for Slave #4, which only used 5.

This translated into four text files of nine columns and one of six (Slave#4), for each experimental run. The data from the separate modules were synced and combined into a 38-column matrix. This was possible as the sampling speeds and activated electrodes were regulated via the Master Arduino M1. The newly created "combined" text file contained 38 columns with multiple rows, each row being responsible for $1/37^{th}$ of the total imaging speed. The conductivity imaging speed was regulated to 207 images per second and capacitance to 21. Each row consequently symbolized an elapsed time of 0.131ms and 1.29ms for conductivity and capacitance, respectively.

6.1.3 Block 3.3: Matrix Creation

The first column in the 38-column matrix was used to indicate the excitation electrode ranging from 1 to 37. Each multiple of 37 rows consequently presented a full column image. A new matrix was created by discarding the first column and creating a 3D matrix of 37x37x*N,* with ***N*** depicting the number of images collected in the allowed 120s. A simplified schematic of this conversion (4 channels) is provided in Figure 6.2.

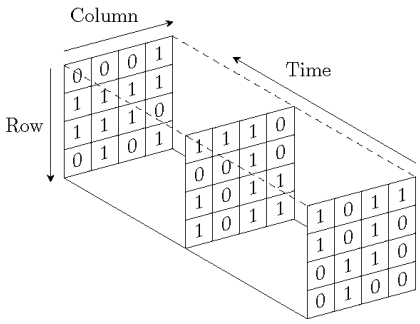

Figure 6.2: Three-dimensional binary matrix depicting a matrix of voltage values over time.

6.1.4 BLOCK 3.4: MATRIX MANIPULATION

In this section, each 12-bit analog signal from the Arduino ADC was combined with the diameter-based calibration curves (Figure 4.20 and Section 4.2.3.1) to expand each measurement "crossing-point" into 10 x 10 binary submatrices. This matrix was used to construct round liquid elements based on the calibrated cross-sectional diameter. The assumption of round liquid-elements was assumed sufficient based on surface tension and the fast-sampling speeds. Subsequently, the 37 x 37 x ***N*** matrix was expanded into a 370 x 370 x ***N*** matrix. A mathematical depiction of the cartesian transformation is provided in Figure 6.3 for an 8 x 8 x ***N*** Matrix.

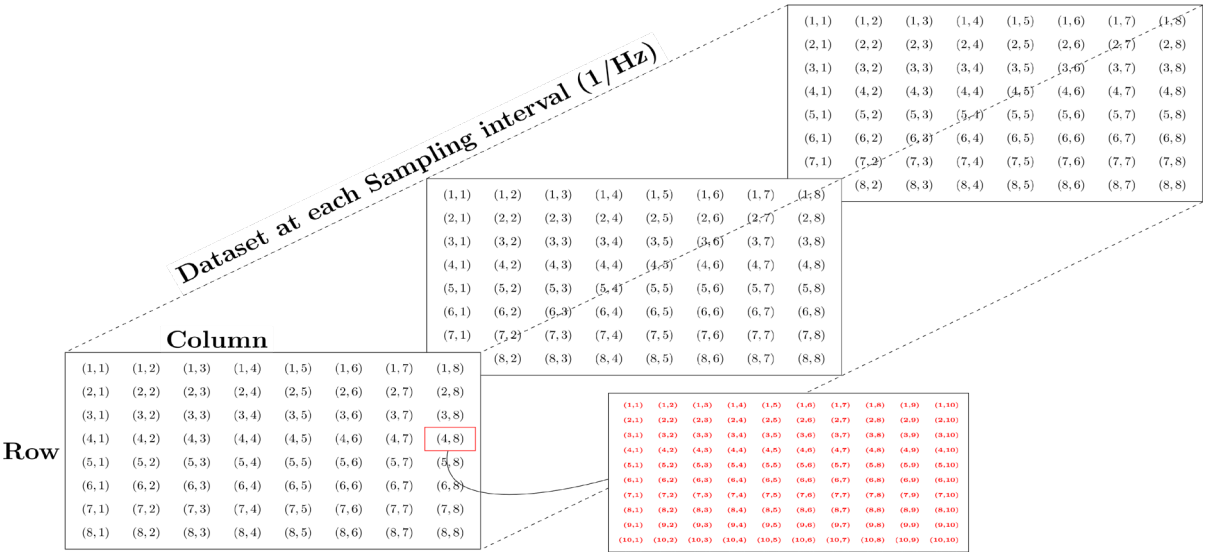

Figure 6.3: Expanded 3D matrix. The matrix depicts the cross-sectional liquid comprised area over time.

The available computational memory limited the resolution of the submatrices. The selected 10x10 submatrices varied between 45-110GB of memory usage. The 370 x 370 x *N* matrix was inserted into a 380 x 380 x N matrix to account for the area around the outer electrodes (#1; #37 5mm on each side). The aforementioned matrix yielded a ***(x;y)*** cartesian detection range equivalent to 380mm x 380 mm. Figure 6.4 is provided for clarification. The detection range was deemed sufficient as the support grid

used a 5mm radial lip to avoid vapour short circuiting along the column walls. The detection area, therefore, comprised 99.5% of the experimental column area.

Mitigation of this 0.5% loss was not considered, as it would require separate specialised calibration curves for the 148 crossing points along the edges.

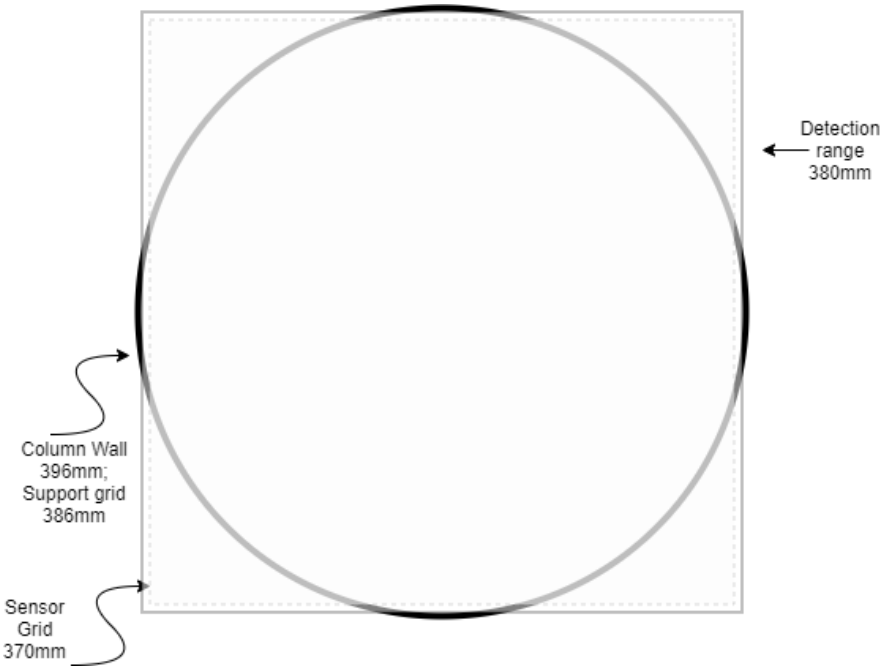

Figure 6.4: Detection range of the of the mesh-matrix within the column. The detection area is 380 x 380mm square block within a 396mm internal diameter column.

6.1.5 Block 3.5: Phase Distribution to Evaluate Liquid Hold-up

The constructed binary 380 x 380 x ***N*** matrix was used to consider the local cross-sectional area phase distribution, as stipulated in Equation 3.5. Binary two-dimensional imaging (*bwconncomp* and *region prop*s) was used to evaluate the ratio between the liquid- and total area and subsequently a liquid comprised cross-sectional area-ratio distribution over time. The presented liquid cross-sectional area-fraction was further related to the liquid volume-fraction through equation 6.1 and the assumption of constant liquid velocity across the whole cross-sectional area.

$$\textbf{Overall Holdup} = \frac{\mathrm{V_L}}{V_{Tot}} = \frac{A_L \cdot h}{A_{Tot} \cdot h} = \frac{A_L \cdot \bar{v} \cdot t}{A_{Tot} \cdot h_{max}} \qquad 6.1$$

Overall liquid hold-up evaluation using equation 6.1 is consequently only valid when the average velocity ($\bar{v}$) and time(t) product, is equal to the maximum vertical displacement of the liquid(h_{max}). The aforementioned mathematical relationship thereby highlights the crucial requirement of uniform liquid velocity and by implication, negligible wall effects.

A tomography equivalent to liquid hold-up (Volume of liquid / Total Volume) is proposed in this work, based on equation 6.2. This time-averaged liquid hold-up was used for validation in Section 7.2.

$$\mathbf{h\varepsilon, i} = \frac{\sum_{i=1}^{n}\left(\lim_{A\to INFA}\frac{1}{A}\int_0^A P_k(x,t)dA=\frac{A_k}{A_{\notin k}+A_k}\right)}{n} \qquad 6.2$$

6.1.6 Block 3.6: 3D Image Processing

The 380 x 380 x ***N*** matrix was resized to 380 x 380 x ***M*** (M =Actual displacement [mm]). This was done using the superficial liquid loading (from the liquid flowmeters [$m^3.m^{-2}.h^{-1}$]), column cross-sectional area and the measured liquid area fraction ($\alpha_{cross-sectional\ fraction}$) to consider the average downward velocity of the droplets. The resized 3D matrix was thereby reconstructed as solid voxels (3D pixels) representing 1 mm^3. Solid bodies were created using linear interpolation between z-vector (**M** dimension) slices. Linear interpolation was adjudged sufficient due to the high rate of sampling.

In non-technical terms, this processing step created a matrix to scale (resolution of $1mm^3$), where the individual liquid elements-disturbances were constructed and viewable in 3D, as they passed through the EIT sensor grid (see Figure 6.5). The 3D matrix only considers and reconstructs the liquid elements as the pass a specific point and does not provide an image of the full column at a specific point in time. This gives rise to one of the key assumptions of the EIT mesh-grid analysis, in that the measurements taken at the packed height of 3m are representative of the whole column. This assumption is discussed in detail in section 6.3.

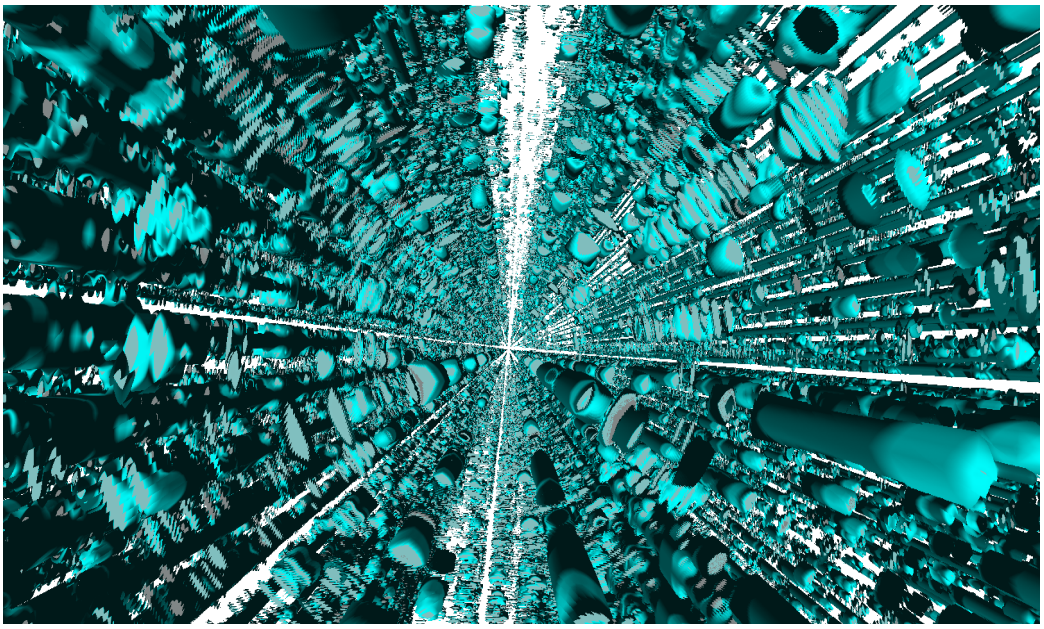

Figure 6.5:Graphical representation of the 3D matrix of inter-packing liquid elements. Top isometric view. The elongated elements depicted stream-like behaviour and the "shorter" elements depicting droplets.

Based in this assumption, the 3D matrix allows for intuitive interpretation and scrutiny of results. An example is provided in Figure 6.5, where the liquid distribution and individual elements were reconstructed as the passed the sensing grid. The image shows an isometric view of the detected inter-intersection. This view allows for the intuitive viewing of elongated liquid elements (presumed to be more stream-like) and smaller and "shorter" liquid elements (droplets). Aside from the intuitive evaluations, the 3D matrix also allowed the use of advanced 3D image-processing algorithms.

6.1.7 Block 3.7 & 3.8: Distribution Plots

Three-dimensional binary image processing (*Regionprops3*) was implemented on the matrix mentioned above (380 x 380 x ***M)*** to evaluate each disturbance element's volume, surface area, and sphericity. The data were represented via number, volume, and probability distributions. This novel evaluation was possible due to the extended sampling times, which allowed between 500k and 2500k individual liquid elements to pass in the allotted 120s. An example of the cumulative distribution of IPL element-volume and surface area are presented Figure 6.6 based on water without vapour and the Intalox® Ultra size A.

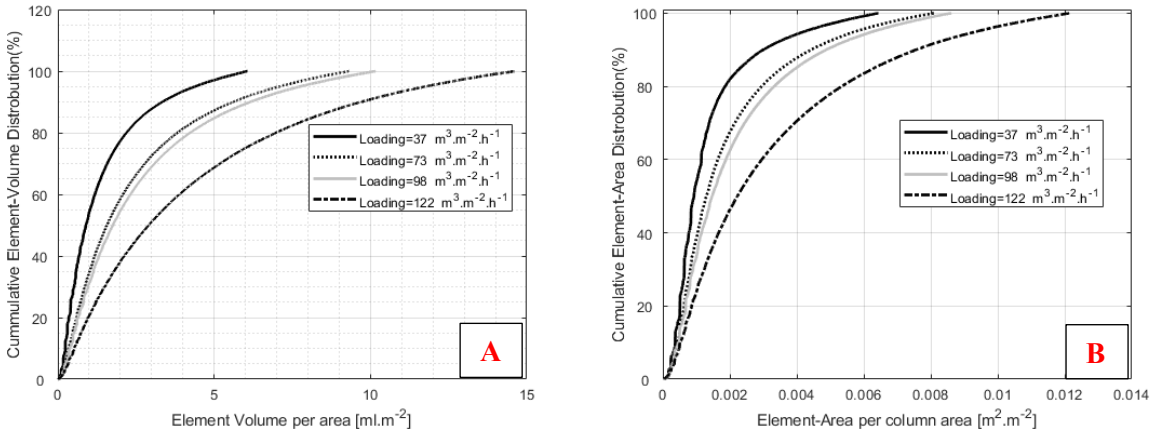

Figure 6.6: A) Cumulative IPL element-volume distributions using air / water at zero vapour loading on Intalox® Ultra size A; B) Cumulative element-surface area distributions using air / water at zero vapour loading on Intalox® Ultra size A.

6.2 Generated Outputs and Definitions

A variety of liquid-element characteristics were generated through the combination of the two- and three-dimensional image processing algorithms. A prefix of *element* is suggested to limit confusion towards real properties and those generated from the image reconstructions. The disturbances imaged through **reconstruction** are consequently referred to as *elements* and not as droplets or streams.

The following **definitions** were consequently used:

- **Inter-packing liquid (IPL) element-volume(υ_e)** representing the liquid volume in the packing voids generated from the 3D image reconstruction (considering solid elements) algorithms and the 380 x 380 x ***M*** matrix.
- **Inter-packing liquid (IPL) element-surface area(æ) represents** the outer surface area of the liquid droplets in the packing voids based on the 3D image reconstruction algorithms 380 x 380 x ***M*** matrix.
- **Element liquid hold-up (hε),** referring to the time-averaged liquid area-fraction used to evaluate hold-up 380 x 380 x ***N*** matrix.

The following outputs were generated through image processing and reconstruction, based on the afore-mentioned definitions

- Inter-packing element-volume distributions based on their number and volume contribution.
- Inter-packing element interfacial area distributions, based on their number and area contribution
- Total-column element liquid hold-up.
- Liquid radial distributions based on the fraction the of total IPL element-volume evaluated along selected sections
- Element interfacial area to element-volume ratio's

6.3 Assumptions & Limitations

The data processing and imaging strategy was based on several of critical assumptions, listed below:

- Uniform liquid velocity across the whole bed. Excessive wall effects and the accompanied velocity profiles were consequently assumed to be negligible. This assumption was based on literature [2] and evaluated using the radial distribution analysis.
- A closed system where all the liquid fed to the column passes over the sensor grid downward. This subsequently ruled out evaluations above or near flooding.
- All liquid elements interact with the "crossing points" of the electrode planes.
- The negligible influence of the mesh- and woven support grid on column hydrodynamics.
- Adequate sensor placement to evaluate the inter-packing behaviour.
- The behaviour measured at the mesh grid is assumed representative of the whole packed bed.

The following limitations were identified, based on both the nature of the EIT principal and the mechanical construction of the setup.

- The evaluations are inapplicable to conditions where packed columns are considered hydrodynamically inoperable (flooding), owing to the assumptions above.
- Additional physical limitations were noted when evaluating low liquid flow rates. The liquid physical properties (surface tension and viscosity), delayed liquid-elements on the mesh grid, contradicting the assumption of negligible interaction. This effect was further compounded at elevated vapour loadings with shear forces exaggerating this effect. For that reason, liquid loadings below 37 $m^3.m^{-2}.h^{-1}$ were considered on a case-by-case basis and limited to zero vapour loading.
- The evaluated cross-sectional area only considers 99.5% of the experimental area. This simplification was adopted for calibration simplicity.

7. VERIFICATION OF EQUIPMENT AND METHODS

Verification of the experimental setup and EIT sensor was considered within the context of packed columns. Pressure drops, both dry bed and irrigated, and liquid hold-up were consequently used for both validation of the EIT sensor and mesh-grid. The pressure drop evaluations were further used for verification of the experimental hydrodynamic setup. A short reference diagram is provided showing the focus and implication of each verification step (See Figure 7.1).

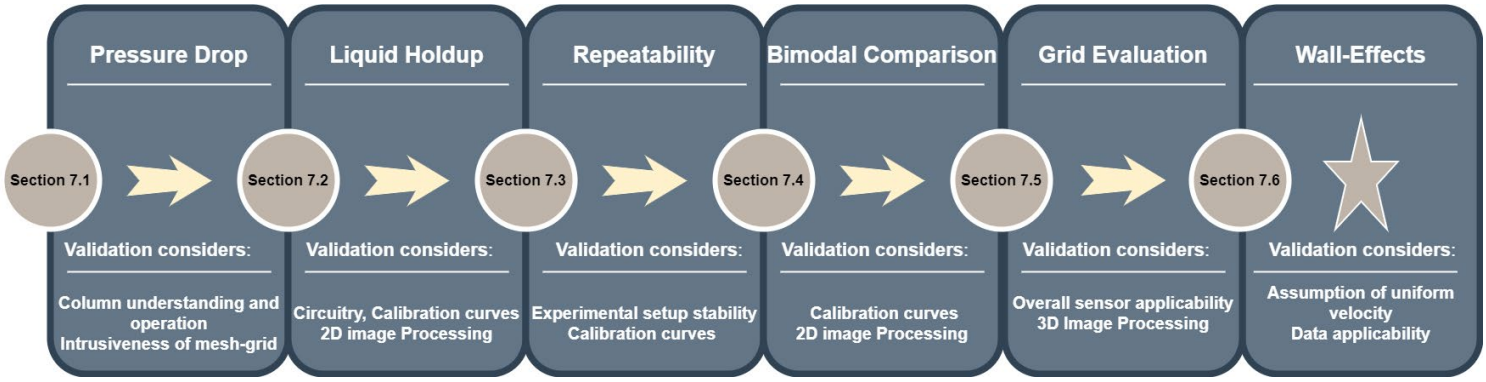

Figure 7.1 : Validation and verification roadmap for the succeeding section, illustrating the respective sections and their focus.

Additionally, this chapter considered the relevant assumptions of Section 6.3, and so doing:

- experimentally verified the assumption of limited grid-intrusiveness,
- experimentally verified negligible wall-effects and consequently the assumption of a uniform liquid velocity, and
- experimentally considered the effectively liquid interaction with the grid.

7.1 METHOD VERIFICATION AND MESH-GRID VALIDATION USING PRESSURE DROP

The intrusiveness of wire-mesh sensors i.e., the effect of the grid itself on fluid flow, was evaluated in literature using concurrent multiphase flow (Wangjiraniran et al [90], Prasser et al. [91]) and found to be negligible (liquid continuous system). The relative effect on counter-current columns, however, required experimental validation.

Both the dry- and irrigated bed pressure drops were evaluated using 1.5” FlexiRing® for the validation of the mesh-grid and verification of the experimental method. The dry bed pressure-drop, presented in Figure 7.2, negatively deviated from Lamprecht [2] to the order of 10 Pa. This decrease in pressure drop was attributed to the increased open area of the woven support grid (96.2%) when compared to the sinusoidal grid hex-grid (86.5%) used by Lamprecht [2]. The Billet model for 2” Pall® Ring was

included for additional reference to confirm feasibility. The presented comparison suggested that the lower pressure drop was still within feasible ranges for the 1.5" packing.

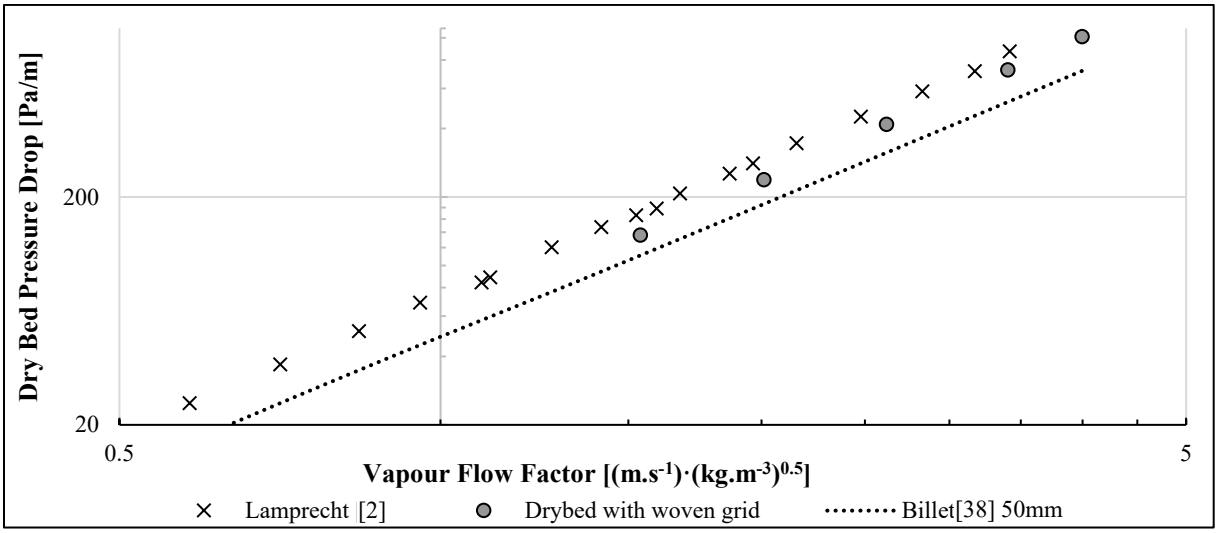

Figure 7.2: Comparison between the dry-bed pressure drop data from this study, and that of Lamprecht [2].The data were collected on 1.5" FlexiRing® and compared to 50mm Rings using the Billet model [38] .

Having conformed to the expected dry bed trends, the irrigated pressure drop was evaluated on the 1.5" FlexiRing®, the results of which are presented in Figure 7.3. The shorthand ***L*** was used to represent the liquid loadings in $m^3.m^{-2}.h^{-1}$., for clarity in the figure. The experimentally measured data were compared to the KG-Tower software package models from Koch-Glitsch. The software was preferred to the experimental data from Lamprecht [2], which were validated against KG-Tower with good agreement, as the Lamprecht [2] focussed exclusively on low liquid flow rates (<73 $m^3.m^{-2}.h^{-1}$).

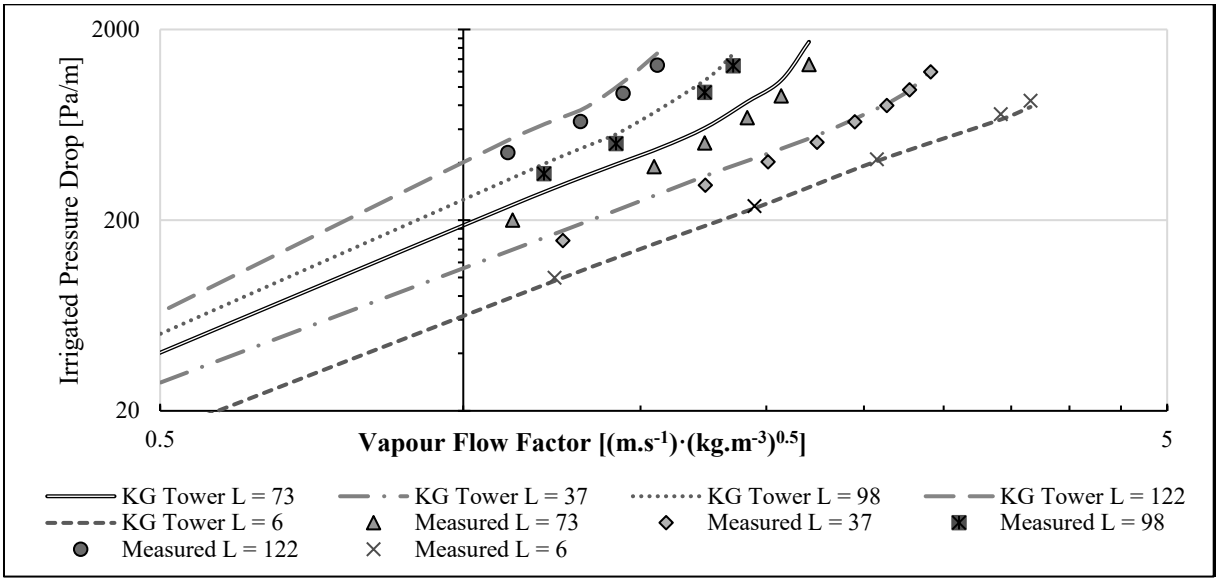

Figure 7.3 : Comparison between the irrigated pressure drop data from this study, and that of Lamprecht [2]. The data were collected on 1.5" FlexiRing® All loadings in $m^3/m^2/h$.

Figure 7.3 presented similar trends between the experimentally measured values in this work and those predicted by the KG-Tower software. The lower experimental values were attributed to the differences between industrial support grids and the woven variant used in this study. Industrial packed column support-grids conventionally use a sinusoidal design to channel the flow (liquid into valleys and vapour to peaks) and mitigate localized flooding. The absence of such modification limited this work to vapour loadings below flooding. The findings, however, remain applicable as columns are conventionally designed to operate at loadings up to 80% of flooding.

The similarities between dry bed and irrigated pressure drop, and the available literature were deemed sufficient to validate the grid, noting limited hydrodynamic influences.

7.2 Liquid Hold-up vs Element Liquid Hold-up

Element liquid hold-up**(hε)**, based on time-averaged liquid area-fraction, combines the influence of circuitry, pseudo-droplet calibrations and image processing algorithms. It was consequently seen as an adequate tool to validate the measurements.

The element liquid hold-up**(hε)** was evaluated using both the air / water and air / ethylene glycol systems, with the results presented in Figure 7.4 and 7.5. The results are presented for the evaluated liquid loadings, incrementally increasing the vapour velocities until flooding. Two independent sources were used for validation as historical hold-up measurements were found to vary significantly between authors (+20%) [2].

The data collected using only capacitance on the Intalox® Ultra size O on the Air / ethylene glycol system, is compared against Minne [5] in Figure 7.4. The presented results illustrate acceptable agreement between the data from Minne [5] and the measured element liquid hold-up (time-averaged liquid area-fraction). Minimal deviations were recorded in the liquid loadings above 37 $m^3.m^{-2}.h^{-1}$. This was adjudged especially noteworthy as tomography techniques rarely produce comparable results at higher vapour loadings [11, 8]. The success of the EIT sensor in relating the influence of vapour loading was thought to be a function of the column size rather than the sensor itself. The lack of wall effects in this study was evaluated experimentally and will be discussed in Section 7.6.

The overpredictions at low liquid loadings seen in Figure 7.4 were attributed to liquid droplet interactions with the wire-mesh grid. Low-velocity liquid droplets, having less momentum, were considered more likely to be slowed down in their interactions with the grid. This slow down due to the combined effect of the no-slip boundary, viscous forces, and surface tension likely lead to overestimation as the liquid spent more time on the grid.

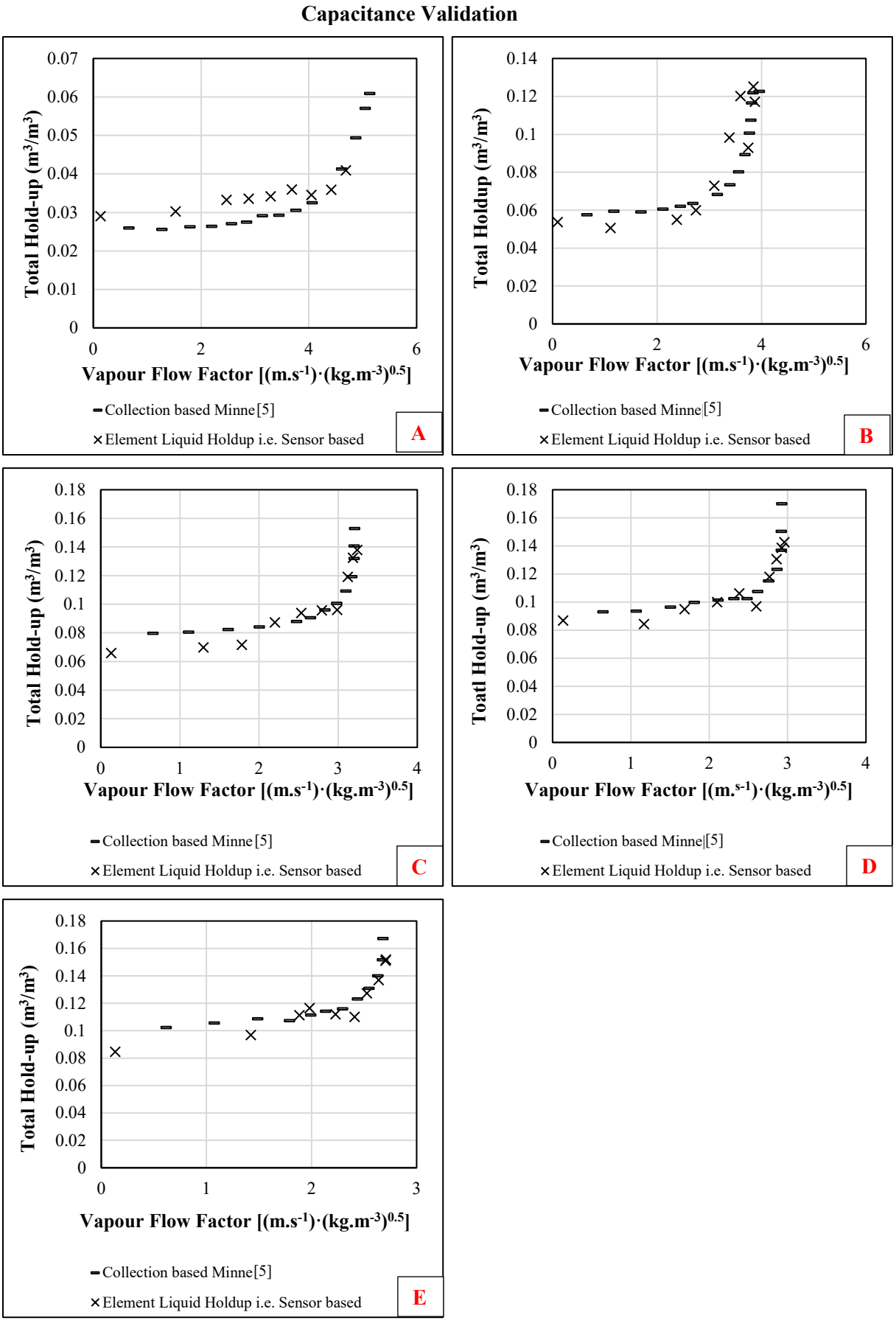

Figure 7.4: Intalox® Ultra size O , literature liquid hold-up vs element-liquid hold-up from this study; air / ethylene glycol; A) 6 $m^3.m^{-2}.h^{-1}$; B) 37 $m^3.m^{-2}.h^{-1}$; C) 73 $m^3.m^{-2}.h^{-1}$; D) 98 $m^3.m^{-2}.h^{-1}$; E) 122 $m^3.m^{-2}.h^{-1}$.

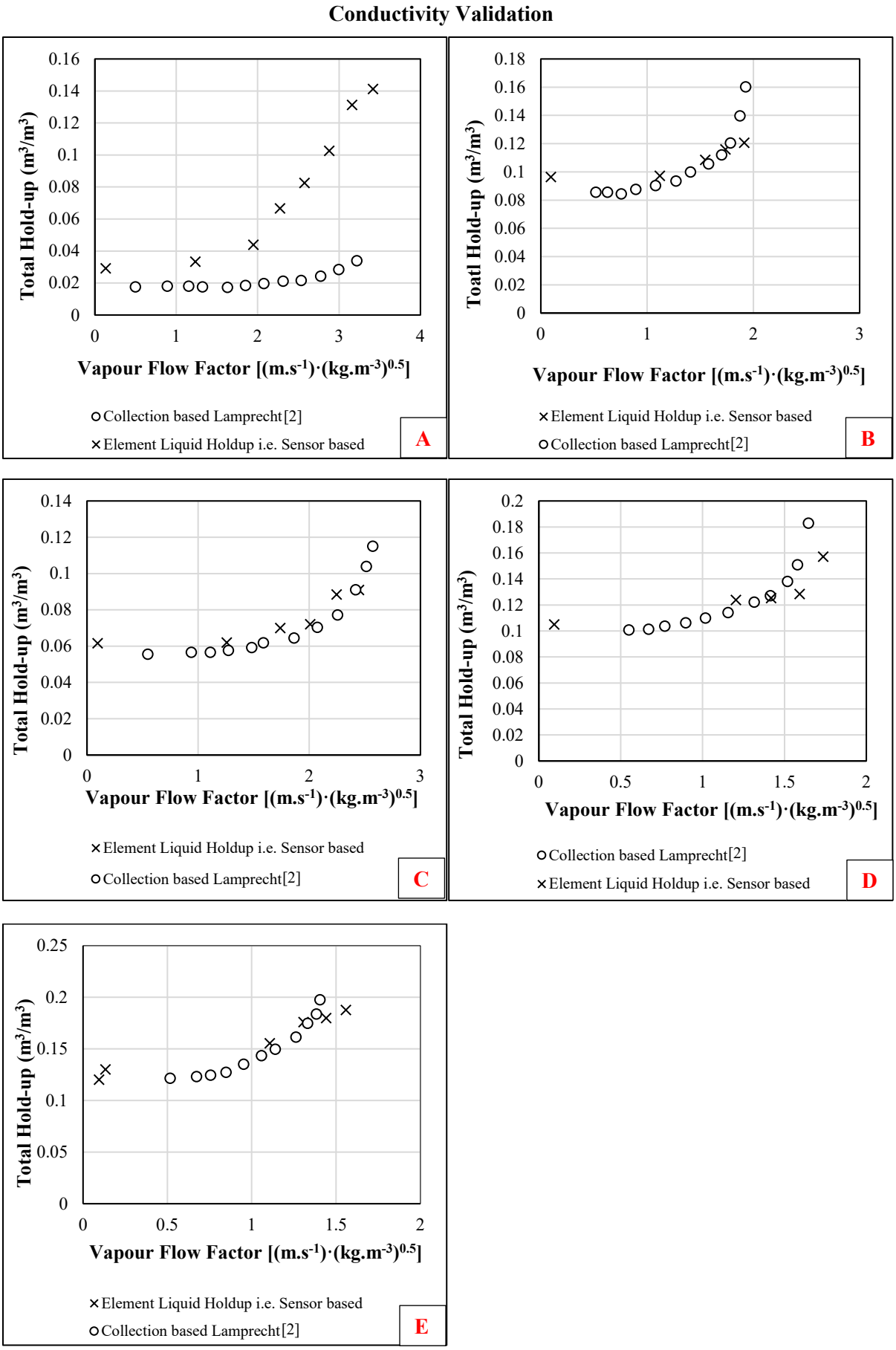

Figure 7.5 : Comparison of 1.5" FlexiRing®, literature liquid hold-up vs element-liquid hold-up from this study; water/air; A) 6 $m^3.m^{-2}.h^{-1}$; B) 37 $m^3.m^{-2}.h^{-1}$; C) 73 $m^3.m^{-2}.h^{-1}$; D) 98 $m^3.m^{-2}.h^{-1}$; E) 122 $m^3.m^{-2}.h^{-1}$.

For the conductivity-based validation, 1.5" FlexiRing® were considered with the air / water system and compared to the collection-method results from Lamprecht [2]. The results presented in Figure 7.5 showed similar trends, with the main deviation between the element liquid hold-up and the data from Lamprecht [2] occurring at the lowest liquid loading. This was likely due to surface tension forces creating an unfavourable force balance, where the water elements are trapped between the "crossing points" of the grid. The detrimental effect of increased vapour loadings subsequently did little but worsen the unfavourable force balance, exaggerating the errors.

Additional minor deviations were recorded at or near flooding for both 98 and 122$m^3.m^{-2}.h^{-1}$, Figure 7.5 d) and Figure 7.5 e).In both cases, however, the data from Lamprecht [2] illustrated premature flooding when compared to the KG-Tower software. The software recommended flooding at F_s =1.8 and F_s = 1.68 $(m.s^{-1})\cdot(kg.m^{-3})^{0.5}$ while Lamprecht recorded these values at 1.46 and 1.25 $(m.s^{-1})\cdot(kg.m^{-3})^{0.5}$ respectively. The element liquid hold-up results were consequently deemed more applicable in this case.

7.2.1 Conclusion on Hold-up Validation

The measured element liquid hold-up was proven to adequately emulate the results from the collection method. This was sufficient to validate the sensor and 2D-image processing, as tomography systems rarely evaluate global liquid hold-up accurately. However, the author is of the opinion that this is related to the size of the experimental setups and their impact on the required assumptions.

Grünewald et al. [8] was the only other author found considering electrical tomography in packed columns and evaluated a 288mm column. This study did not consider overall liquid hold-up, instead opting to evaluate wall effects. Deviations upward of 300% were recorded between the liquid hold-up in the middle and the perimeter of the column. The subsequent excessive wall-effect behaviour contradicted one of the critical assumptions of tomography-based hold-up evaluations in assuming that all liquid elements have the same downward velocity. Similar wall effects likely hampered the study from Janzen et al. [11] , who used ultrafast X-Ray tomography on structured packings in an 80mm ID column. Janzen et al. [10] noted errors ranging between 100-300% of the global liquid hold-up and their element liquid hold-up equivalent. The success of the presented sensor in this work in estimating global liquid hold-up is consequently partly attributed to the absence of wall effects.

However, application limitations were identified based on the results of the 6 $m^3.m^{-2}.h^{-1}$ liquid loadings for both water / air and ethylene glycol / air systems. Significant inferences on the data are consequently not advised below liquid loadings of 37 $m^3.m^{-2}.h^{-1}$ and vapour loadings exceeding 95% of flooding.

7.3 REPEATABILITY

Element liquid hold-up **(hε)** was considered for the air / water system on Intalox® Ultra size O, to prove experimental repeatability. A liquid loading of 122 $m^3.m^{-2}.h^{-1}$ was chosen for its likeliness to highlight variability and errors. For comparison, the data were plotted in Figure 7.6, against the collection-method results from Minne [5].

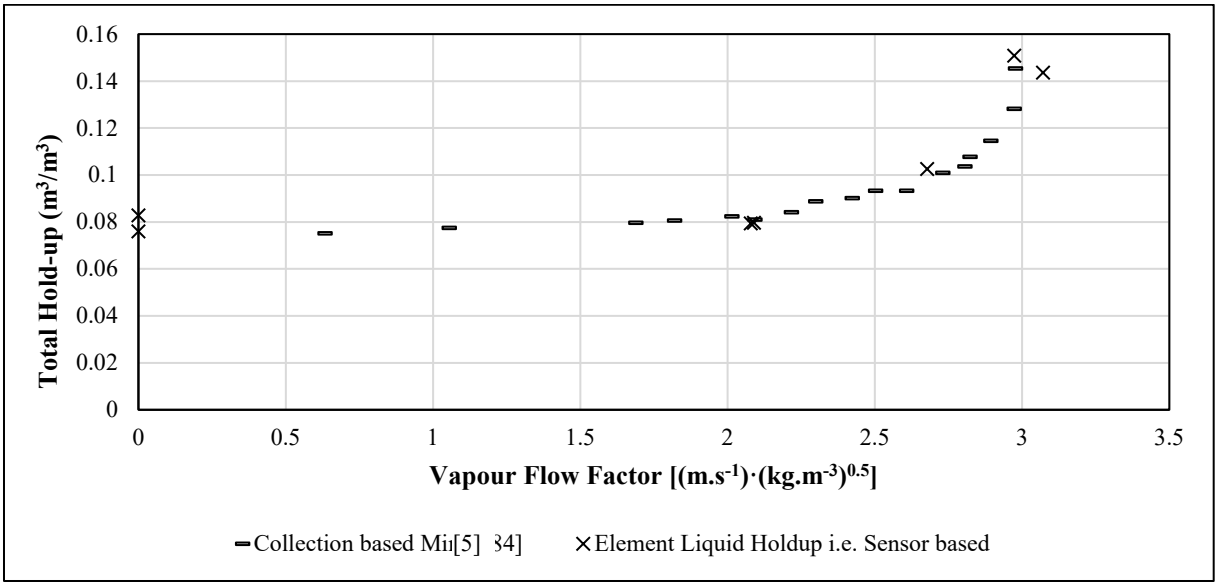

Figure 7.6: Intalox® Ultra size O liquid hold-up vs element liquid hold-up; water/air; 122 $m^3.m^{-2}.h^{-1}$.

The system was evaluated in duplicate on consecutive days. The representative vapour loadings were chosen according to the trends in Minne [5]. The conductivity of the liquid was measured at the onset of each run and found to be 24µS/cm. The system was evaluated with a 20kHz sinusoidal signal at 0.2V.

The chosen loadings were:

- No Vapour Loading,
- Vapour Loading of 2.1 $(m.s^{-1})\cdot(kg.m^{-3})^{0.5}$ representing the start of the loading phase ,
- Vapour Loading of 2.6 $(m.s^{-1})\cdot(kg.m^{-3})^{0.5}$ representing the middle of the loading phase, and
- Flooding.

Minimal variation was found between the results, with the tomography-based flooding points evaluated at vapour loadings of 2.97 and 3.07 $(m.s^{-1})\cdot(kg.m^{-3})^{0.5}$, respectively. The results were deemed sufficient to prove repeatability.

Additional 3D-imaging repeatability was evaluated on the Intalox® Ultra size O at 37 $m^3.m^{-2}.h^{-1}$ and no vapour loading (air / water). The evaluation was aimed at proving sufficient stability for the tomography-based characterisation, presented in section 8.2.

Three separate experiments were considered, with varied conductivity to consider the flexibility and range of the EIT characterisation method. The liquid volume was drained between each run and replaced with a combination of tap- and demineralized water. The individually measured liquid elements were created in a 3D matrix and evaluated with the image processing software. An average of 2.5 million elements was considered and sorted according to volume. The results are presented in Figure 7.7 as a function of the column diameter through a cumulative volume-based distribution.

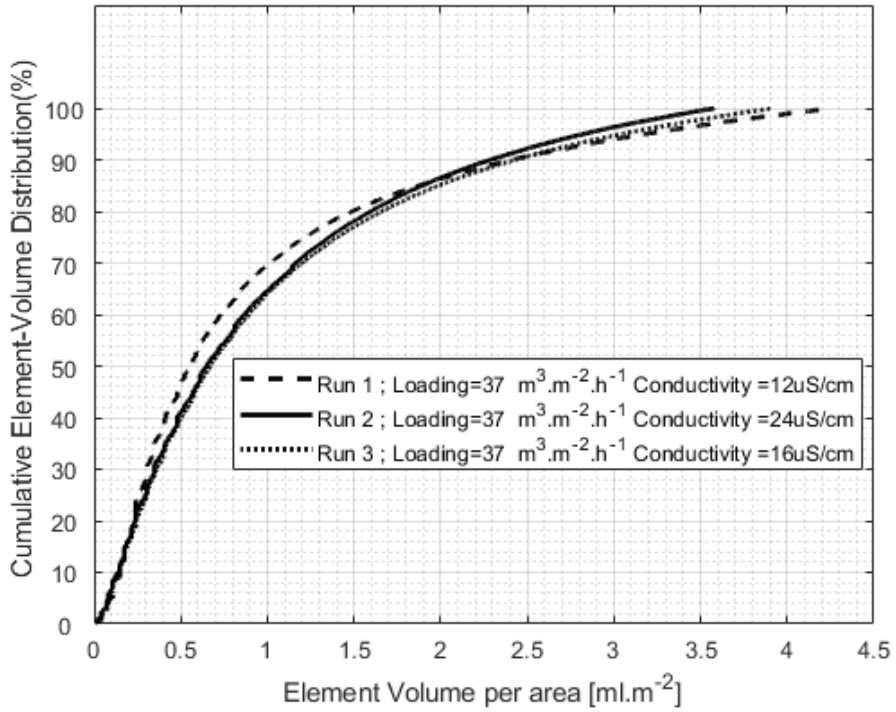

Figure 7.7: Repeatability of 3D- image processing using a cumulative IPL element-volume analysis; air / water

The results showed excellent repeatability and provided the needed validation for the measurement of element distributions between packings.

7.4 BIMODAL COMPARISON

Using both capacitance and resistance, the nature of the EIT circuitry presented the means for additional comparative validation. An element liquid hold-up comparison is consequently presented for water / air (water having both capacitance and electrical conductivity), evaluating said parameter using the individual influences of conductivity and capacitance. Figure 7.8 is presented as an illustration, with ***L*** used to indicate liquid loadings in $m^3.m^{-2}.h^{-1}$.

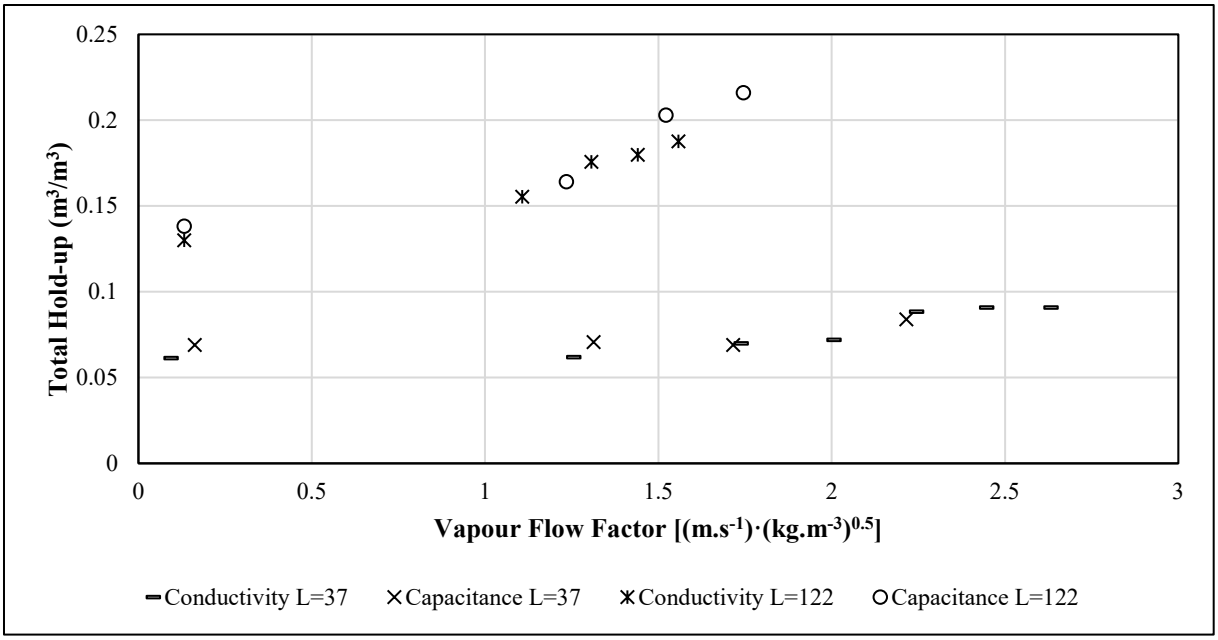

Figure 7.8: Comparison of the element liquid hold-up from capacitance and conductivity of Intalox® Ultra size O using the air / water system. The liquid loading L is depicted in $m^3/m^2/hr$.

The presented results were collected from consecutive and separate experimental runs, evaluating element liquid hold-up using conductivity and capacitance independently. Although the comparison included minor variations due to random errors, the data nonetheless proved in line with the experimental repeatability results discussed previously in Section 7.3. This provided the needed validation and verification of the circuitry and setup in comparing behaviour irrespective of measurement principle.

7.5 Grid Evaluation and Validation

The tomography study was based on the assumption of effective liquid interaction with the wire-mesh grid. Any liquid missing the 1369-point grid and passing through the openings subsequently contributed to imaging errors.

As a measure of validation, the 3D image software was used to reconstruct all the evaluated elements and total their volumes. This volume was compared with the known volume introduced into the columns in the evaluated 120s. A ratio of element- to actual volume was subsequently calculated based on Equation 7.1 , where $\boldsymbol{L}$ denotes the liquid loading in $m^3.m^{-2}.h^{-1}$ and the area is given in square meters.

$$Ratio = \frac{\sum_{i=1}^{n} Element\ volume_i}{L * A_{column} * \frac{1}{30}} \qquad 7.1$$

The evaluation results are summarised in Figures 7.9 and 7.10, depicting all the water / air and air / ethylene glycol systems experiments, respectively. Vapour loadings up to 80% of the flooding velocity

were considered. The experiments conducted on the 6 $m^3.m^{-2}.h^{-1}$ were omitted as stagnant liquid droplets contradict the assumptions of the 3D-image processing in assuming a constant liquid velocity.

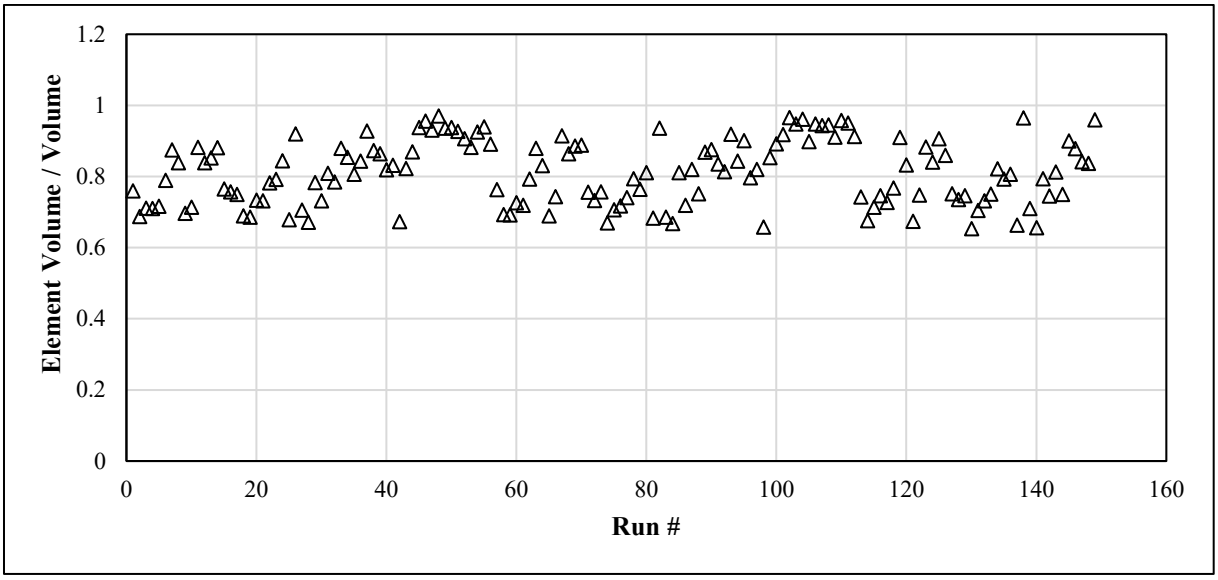

Figure 7.9: IPL element-volume recreation: water / air

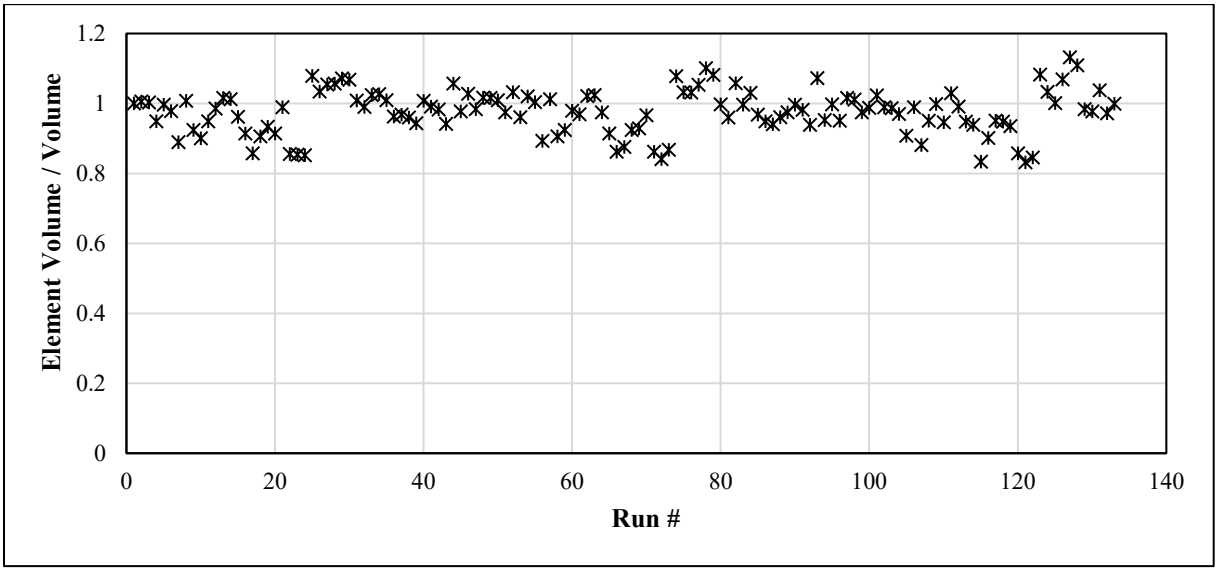

Figure 7.10: IPL element-volume recreation: ethylene glycol / air

The presented results illustrate an average of 80% and 97% volume pickup and recreation, respectively, for the air / water and air / ethylene glycol systems. Differences between the two systems were attributed to the competing effects of liquid viscosity and surface tension.

In summary, the findings of this section showed the presence of smaller liquid elements in the air / water system. These elements are statistically more likely to miss the electrodes and pass through the column unevaluated. However, their impact on the characterisations was deemed mitigated by the sheer number of elements evaluated in the 120s. In many cases, the number exceeded 500k-2500k, and subsequently,

normally distributed errors were assumed. However, limited applicability is anticipated for lower surface tension paraffinic liquids, as even smaller liquid elements are expected. Consequently, an additional staggered mesh grid is recommended for future work, installed 20mm below the current installation.

7.6 Hydrodynamic Characterisation of Wall-Effects

Although less prevalent on an industrial scale, wall-effect based liquid maldistribution is thought to hamper academic and pilot-scale evaluations. The EIT system was consequently used to characterize the wall effects present in the experimental 396mm column. This characterisation is imperative for the overall liquid hold-up requisite of uniform liquid velocity across the whole bed.

The characterisation considered the column inner diameter, divided into eight concentric circles, with the element liquid hold-up calculated independently for each. A visual representation is provided for clarification; see Figure 7.11

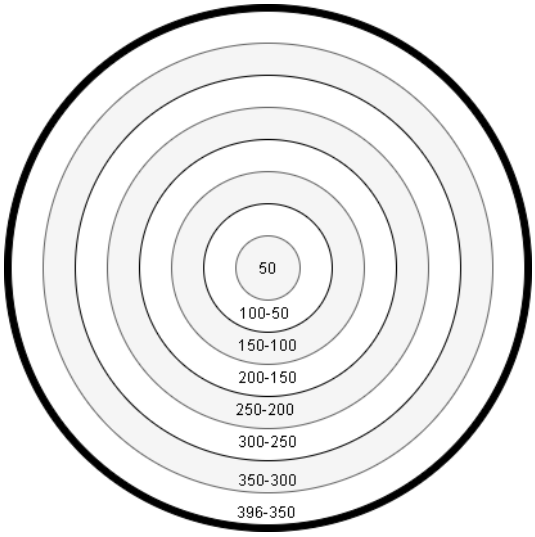

Figure 7.11: Wall-effect evaluated by grouping the total IPL liquid volume collected in concentric circles throughout the column.

An illustration of the results for Intalox® Ultra size L is presented in Figure 7.12. The graphical representation considers the effect of liquid loading on radial hold-up distributions. The increase in element liquid hold-up along the perimeter was deemed notable yet sufficiently low to allow the assumption of uniform velocity. This was motivated by the lack of exponential liquid hold-up increase conventionally reported in the presence of wall effects. For scale, the 288mm evaluation from Grünewald et al. [8] showed a 300% increase between the average and perimeter hold-up.

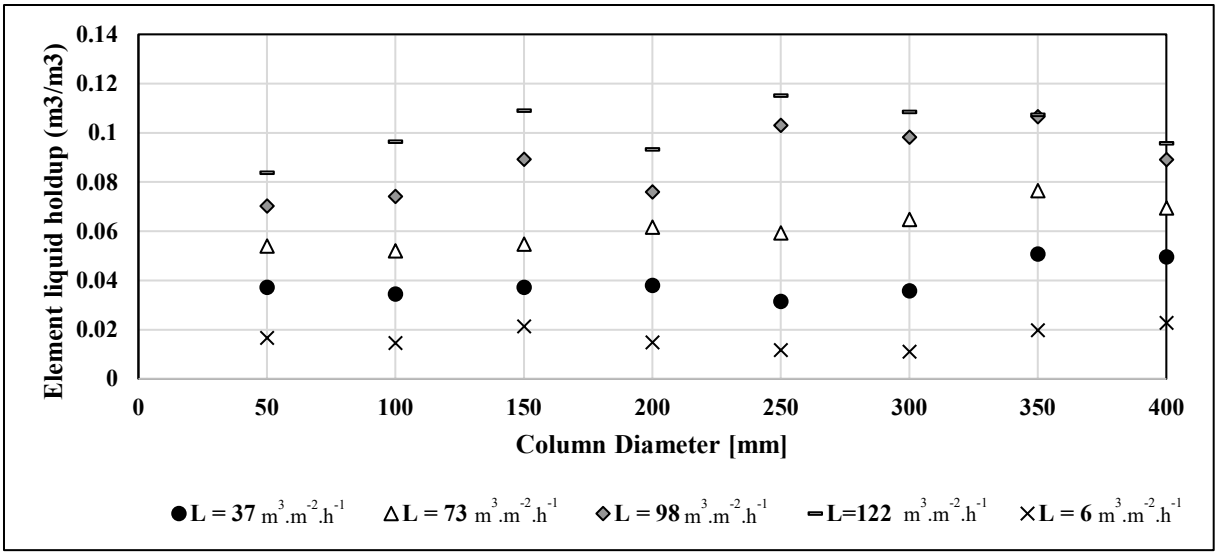

Figure 7.12: Wall-effect evaluation using element liquid hold-up; Intalox® Ultra size L with water at F_s = 0 $(m.s^{-1})\cdot(kg.m^{-3})^{0.5}$.

A comparative evaluation is provided in Figure 7.13, showing the ratio between the perimeter and average element hold-up for all the air / water experiments. The evaluation presented an average ratio of 1.16, with the ratios above 1.3 limited to vapour loadings above 90% of the flooding velocity. Ratio's above 1.5 were only reported for experiments beyond flooding. This was adjudged sufficient to motivate the negligible influence of wall effects on the characterisation to follow. This was adjudged sufficient to motivate the negligible influence of wall effects on the characterisation to follow.

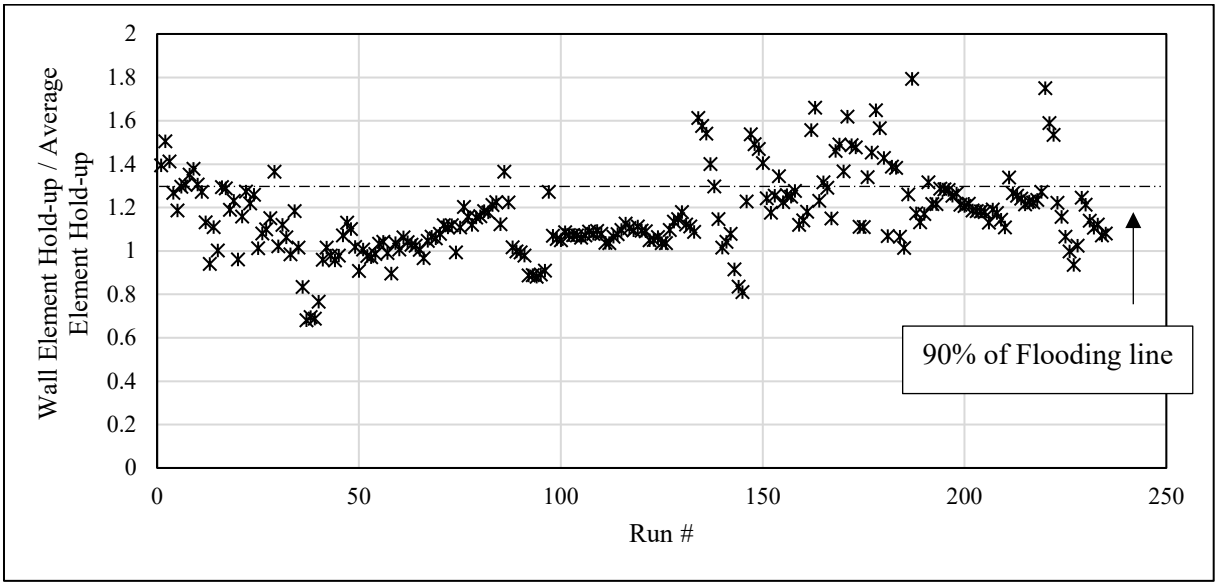

Figure 7.13: Ratio of average- to perimeter element liquid hold-up

7.7 MALDISTRIBUTION EVALUATION

Distribution evaluations were conducted through a combination of the EIT data and 3D image processing. These evaluations entailed calculating the total IPL element-volume passing along each of the 1369 crossing points with the allotted 120s, at a packed height of 3m. The data were normalised to illustrate effective "*hot(1)*" and "*cold(0)*" spots of high and low irrigation volumes. The resulting plots show the combined effects of the liquid distributor and the distributing effects of the random packing rivulets.

Maldistribution effects were evaluated with both the air / water and air / ethylene glycol systems with similar results. For the sake of brevity, the full study is presented in section 14.7 of the appendix, with only an example presented in the main body.

The channel-type liquid distributor from Minne [5] was used in this work. It comprised 19 drip points for a drip point density of 157 per m^2 and offered a turndown-ratio of 20:1. The applicability of the high turndown ratio design was evaluated on the Intalox® Ultra size O. This evaluation contradicts the conventional design norm of a minimum column diameter-to-packing ratio of 8 [2] (396/63=6.3). It was thereby expected to highlight maldistribution and the ability of the EIT sensor to help in the characterisation thereof.

Evaluating the liquid loading at 6 $m^3.m^{-2}.h^{-1}$ without vapour presented an interesting distribution pattern, as seen in Figure 7.14B. This case was evaluated at zero vapour loading to mitigate the unfavourable drag forces and liquid trapping between the electrode planes (Section 7.2).

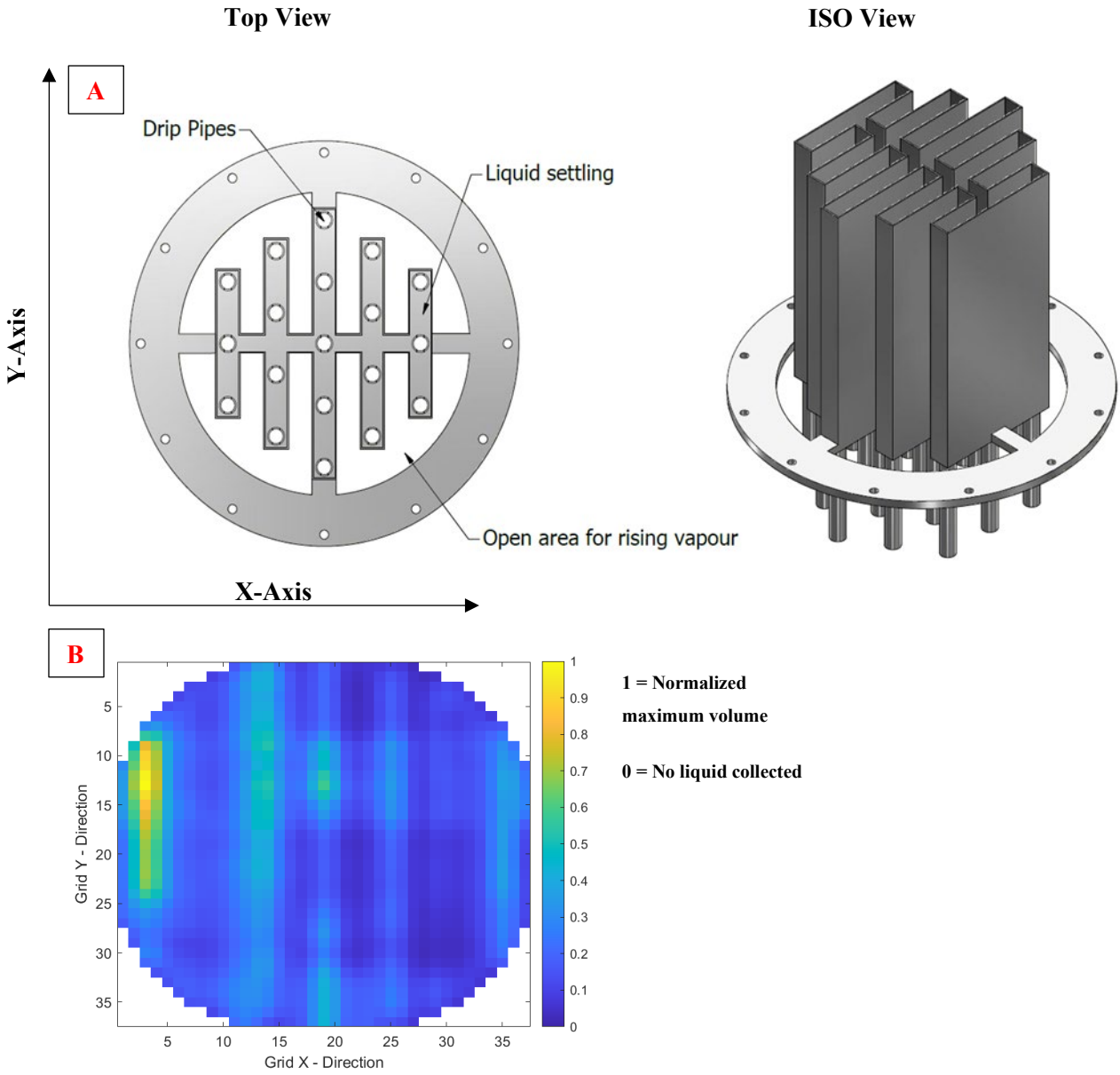

Figure 7.14: Maldistribution at 6 $m^3.m^{-2}.h^{-1}$ compared to the liquid distributor; Normalized liquid flow; Maximum total flow =1.

The evaluated distribution seemingly emulated the Y-axis of the drip points (pattern of the distributor downpipes), suggesting minimum interaction with the packing throughout the bed. This is likely due to the larger open area Intalox® Ultra size O offering limited restriction and interaction with the downward flowing liquid. This inefficiently wetted and underexploited the packing rivulets.

7.7.1 Liquid and Vapour Loadings

The maldistribution effects were also evaluated on liquid loadings of 37 $m^3.m^{-2}.h^{-1}$ and 98 $m^3.m^{-2}.h^{-1}$, incrementally increasing vapour $A<B<C<D$. These evaluations considered increased liquid and vapour distribution effects and are presented in Figures 7.15 and 7.17.

Figure 7.15 illustrated the advantageous distribution effects of both increased liquid and vapour loadings, compared to 6 $m^3.m^{-2}.h^{-1}$. In so doing, the presented trend emulated conventional tomography literature [10]. The initial resemblance between the pattern presented in Figure 7.14 subsequently faded with increased vapour loadings at 37 $m^3.m^{-2}.h^{-1}$, and was almost unrecognizable in Figure 7.17 for all the 98$m^3.m^{-2}.h^{-1}$ experiments.

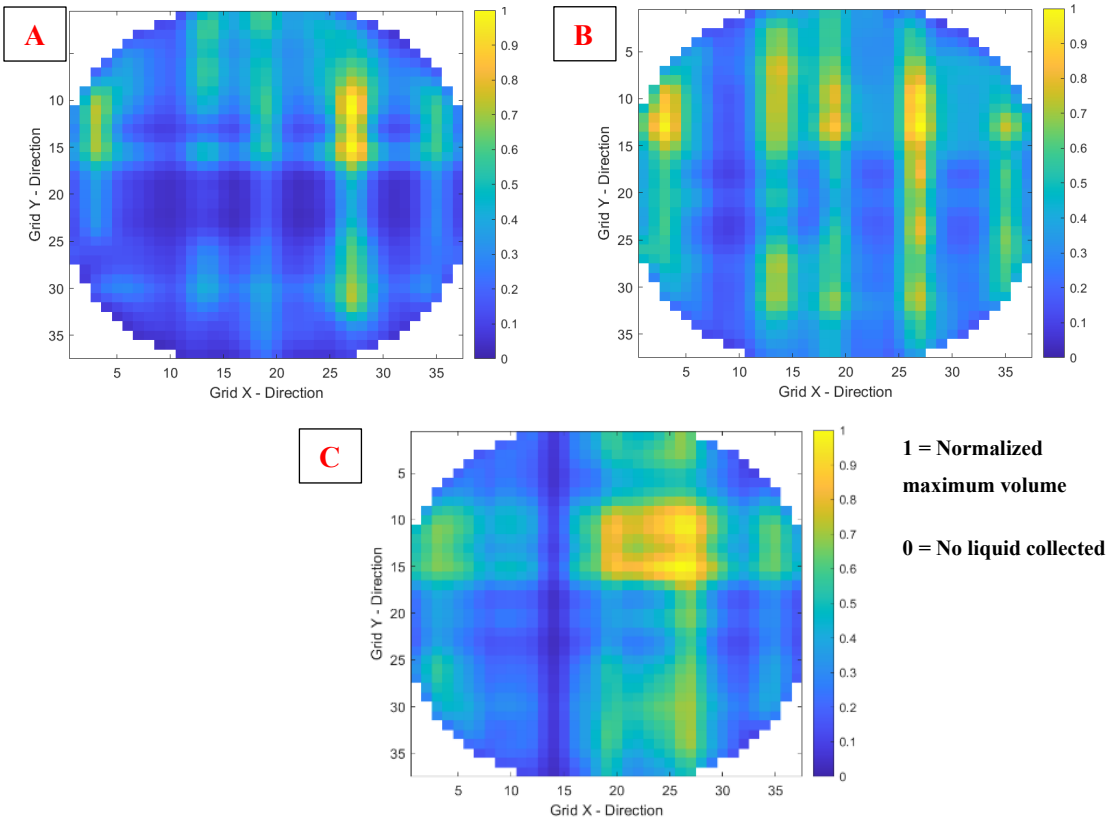

Figure 7.15: Normalized volume distribution of Intalox® Ultra size O evaluated with air / water at 37 $m^3.m^{-2}.h^{-1}$. A) F_s =0 $(m.s^{-1})\cdot(kg.m^{-3})^{0.5}$; B) F_s = 2.4$(m.s^{-1})\cdot(kg.m^{-3})^{0.5}$; C) F_s =3.1 $(m.s^{-1})\cdot(kg.m^{-3})^{0.5}$

The change is distribution performance at low liquid loadings with increased vapour, correlated with previous study (from Lamprecht [17]) on liquid phase mass transfer. The aforementioned evaluated liquid phase mass transfer in a 400mm ID column with a similar liquid distributor [2] at a drip point density of 157 per m^2. The study noted a discontinuous increase in the Intalox® Ultra size O performance at low liquid loadings (<73 $m^3.m^{-2}.h^{-1}$) while still below the loading point. This was deemed unconventional as vapour velocities are not known to affect liquid distribution in the preloading range. The sudden performance increase was speculated to be related to inadequate liquid distribution being corrected through vapour loading. The discontinuity is presented in Figure 7.16, redrawn from Lamprecht [17].

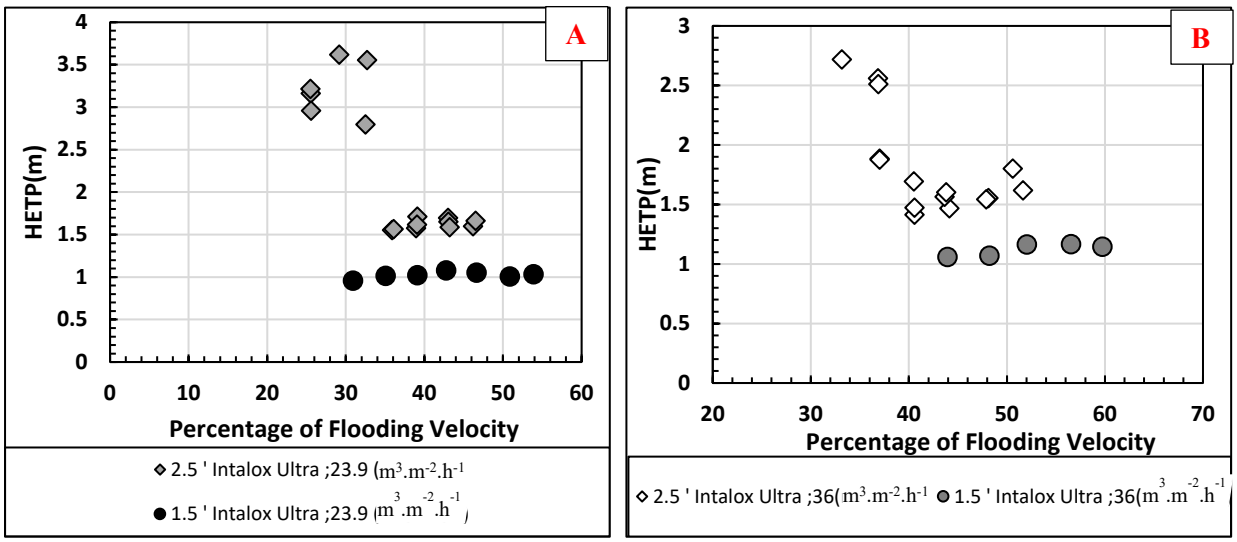

Figure 7.16 : HETP comparison of 1.5" and 2.5" Intalox® Ultra on a liquid phase mass transfer limited system – The Aqueous desorption of isobutyl acetate into air; Recreated from Lamprecht [17] . A) 23 m3/m2/hr B) 36 m3/m2/hr

The tomographs in Figure 7.15 showed increased distribution efficiency with increased vapour loadings in the preloading range (Figure 7.15 **a→b**), consequently validating our previous study's suspicions (Lamprecht [17].). These results call attention to the increased importance of distributor design with larger and high open area packings

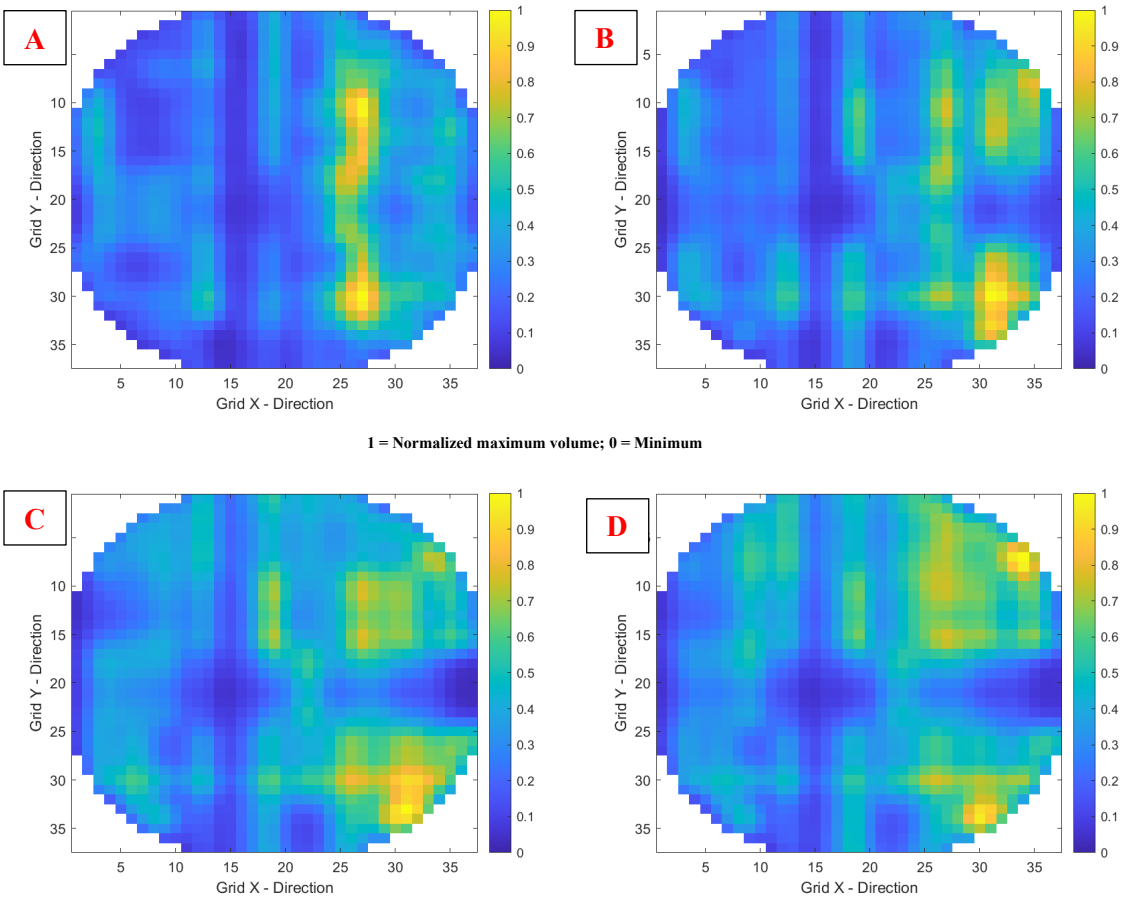

Figure 7.17: Normalized Distribution of Intalox® Ultra size O evaluated with air / water at 98 $m^3.m^{-2}.h^{-1}$: A) F_s =0 $(m.s^{-1})\cdot(kg.m^{-3})^{0.5}$; B) F_s = 2.1 $(m.s^{-1})\cdot(kg.m^{-3})^{0.5}$; C) F_s =3.7 $(m.s^{-1})\cdot(kg.m^{-3})^{0.5}$; D) F_s =3.2 $(m.s^{-1})\cdot(kg.m^{-3})^{0.5}$.

In summary, the distribution evaluations highlighted the intricate relationship between maldistribution, the liquid distributor and chosen liquid flowrates. The data showed intuitively increased distribution performance with increased liquid flow in comparing the tomographs from 6 - 98 $m^3.m^{-2}.h^{-1}$. This trend followed suit with the available literature [10]. However, it should be noted that industrial liquid distributors are conventionally designed with a turndown of 4:1 and that the ambitious 20:1 design likely suffers from error intensification at the lower operating limits. The author, therefore, recommends using an alternative low flow liquid distributor for future evaluations below 37 $m^3.m^{-2}.h^{-1}$.

7.7.2 PACKING TYPE

The additional distribution variation of different packings was considered and presented in Figure 7.18. This was based on the notion that obstructive designs and geometrically smaller packings would present differing levels of distribution based on their intrinsic geometry and consequently distributor influence. The large Intalox® Ultra size O geometry was expected to offer little physical obstruction to the fluid flow path and was therefore hypothesised to be less forgiving of liquid distributors.

This was confirmed in Figure 7.18, through comparison of 2" FlexiRing® and Intalox® Ultra size L. Both packings were considered at a liquid loading of 37 $m^3.m^{-2}.h^{-1}$ and zero vapour flow. The results presented the clear absence in the distributor pattern found on the Intalox® Ultra size O, Figure 7.17. This was thought to be related to the increased interactions between the liquid and the packing.

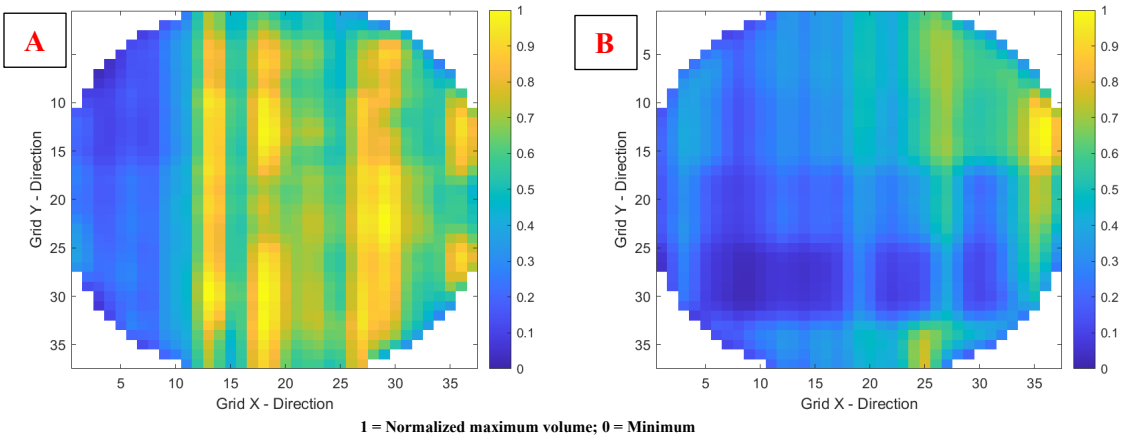

Figure 7.18: Normalized distribution of air / water at 37 $m^3.m^{-2}.h^{-1}$. F_s =0 $(m.s^{-1})\cdot(kg.m^{-3})^{0.5}$; A) 2" FlexiRing® ; B) Intalox® Ultra size L.

The results Figure 7.18 illustrate the differences between the distribution of the Intalox® Ultra size L and 2" FlexiRing® under 3m of packing. The IPL element-volume evaluations show a significant "hotspot" area for the latter. However, being based on a normalized IPL element-volume, the results often fail to represent the complete picture. The percentage of the total IPL element-volume collected along each of the 1369 crossing points was consequently presented (See Figure 7.19) for clarification. The illustration shows that bar the localized high flow, the volume distribution of the Intalox® Ultra size L was still comparable to that of the 2" FlexiRing®.

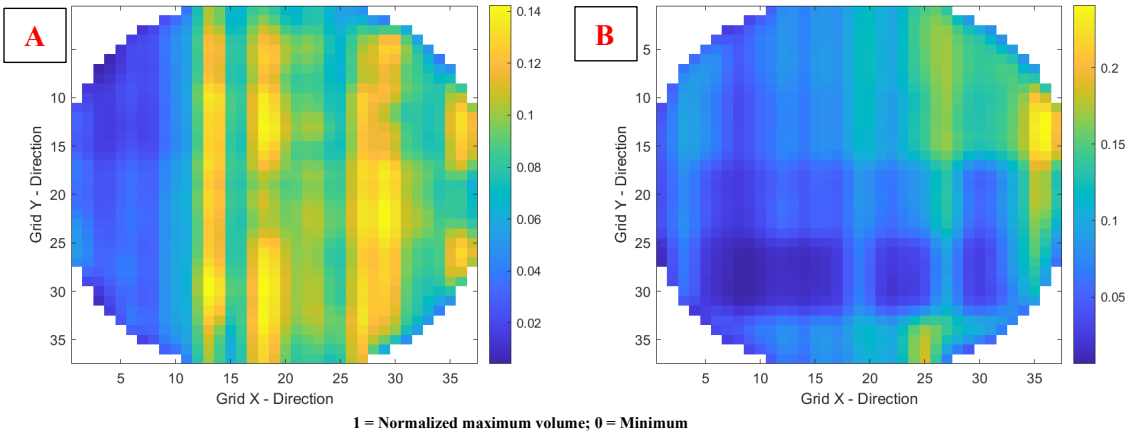

Figure 7.19: Parentage distribution of air / water at 37 $m^3.m^{-2}.h^{-1}$. F_s =0 $(m.s^{-1})\cdot(kg.m^{-3})^{0.5}$; A) 2" FlexiRing® ; B) Intalox® Ultra size L.

The increased distribution uniformity of for the Intalox® Ultra over the 2" FlexiRing ®, is likely due to the:

- enclosed geometrical design of the FlexiRing®, offering less available open area, thereby
- Increasing the presence of continuous liquid elements and preferential flow (presumed to be streams).

7.8 Discussion of Additional Assumptions

All the assumptions in section 6.3, bar two, were experimentally evaluated. The remaining assumptions namely:

- sufficient mesh-grid placement to evaluate inter-packing distributions, and
- that the mesh-grid results were assumed representative of the whole packed bed,

were considered through a combination of literature and intuitive reasoning.

The assumption of sufficient grid placement was intuitively validated in considering the packing sizes. The 20mm separation between the electrodes and the packing ranged from 32% to 53% of the nominal packing diameters. This was adjudged to be sufficiently small, noting that the packing is randomly dumped into a column and often leave inclusions based on their orientation.

The assumption of pseudo-constant parameters across the packed height is widely used throughout the mass transfer and hydrodynamic characterisation, with steady-state operations considering equilibrium distributions. The respective parameters are consequently presented as a scalable function of the packed height or packing volume. To mitigate the initial distribution effects and their impact, columns are sized to a minimum packed height where deviations are assumed to be averaged out.

Hoffmann et al. [92] suggested a standardized approach to evaluating mass transfer in a packed column and used a packed height of 820mm (ID 400mm). The approach recommended a liquid distributor with a drip point density of 100-200m^{-2} and considered 25mm Pall® Ring. The results from the study indirectly highlight the applicability of the 820mm packed height (noting the combination of the liquid distributor and packing). This suggested that equilibrium liquid distribution was attained quickly enough to consider negatable entrance effects at the 820mm packed height.

The effect of the liquid distributor, however, cannot be disregarded. Ibrahim [93] evaluated the effect of packed height on liquid distribution based on a drip point density of 45 m^{-2} (ID 300mm and 25mm Pall® Ring). The results indicated equilibrium liquid distribution at height-to-diameter ratios of 2.5 and above.

The 3m packed height experimental setup used in this study was consequently considered sufficient to evaluate the distribution effects at distribution-equilibrium, noting both the ideal case in Hoffmann [92], and the worst-case scenario in Ibrahim [93].

The future applications of the EIT sensor can be extended to include the experimental evaluation of packed heights and, in so doing, experimentally motivate the afore-mentioned assumption. This was, however, deemed beyond the scope of this work.

8. FINAL EXPERIMENTAL RESULTS

Perceived shortcomings in the presented literature illustrated the need for improved fundamentality in evaluating IPL element sizes and their distributions. This motivated the overarching aim of *improving the fundamental understanding of inter-packing interfacial distributions inside randomly packed columns* through tomography-based characterisation.

To accomplish this goal, an EIT system was developed and validated. The relevant aspects are discussed in Chapters 4 to 6. The constructed EIT system offers column imaging speeds of 207Hz and 21Hz, respectively, for conductivity and capacitance. This was surmised as sufficient for hydrodynamic evaluations in packed columns, as illustrated in the validations in chapter 7.

EIT characterisation allows for the effective calculation the following characterisations in a single experimental run of 120s

- Conventional hydrodynamic characterisation: pressure drop and liquid hold-up -Section 7.2;
- Conventional tomography:
    - Liquid distribution below the packing (***Hot*** and ***Cold*** spots of irrigation) - Section 7.7;
    - Wall-effects - Section 7.6.

These parameters were evaluated at a fraction of the cost of conventional radiation tomography and without the inherent safety risks. The results were believed sufficient to prove the applicability of the developed EIT system for packed column conventional tomography and characterisation.

However, the scope of the project was to provide insight as to the inter-packing droplet behaviour in randomly packed columns. The EIT-based characterisation system subsequently presents additional functionality for the characterisation of interfacial distributions between packing rivulets. This was evaluated using the *element* distributions of volume, surface area and the area-ratios.

The presented work attempted to address the following questions.

[1] Can random packing be evaluated and characterized based on their inter-packing distribution behaviour?

[2] What is the effect of the vapour on said distributions?

[3] Is there a correlatability between the distributions and the kinetic performance of the packing?

8.1 FOREWORD

Packed column interfacial distributions cannot be considered in a vacuum. This is owed to the fact that, aside from the packing, other column internals are known to have a considerable effect. The specific interfacial distributions are consequently thought to be a function of

[1] the liquid and vapour distributors,
[2] the support-grid and,
[3] the packing itself.

This study opted to standardize and mitigate the effect of the distributor and support grid, by using a single design throughout. However, their implicit effect on characterisation through aspects including maldistribution and wall-effects, required evaluation. The validations were done through conventional tomography with the EIT system and are presented in Chapter 7.

8.2 HYDRAULIC CHARACTERISATION THROUGH TOMOGRAPHY

Packing characterisation through inter-packing distributions was evaluated based on element-distributions (volume and surface area), using air / water and air / ethylene glycol systems. The distributions were initially evaluated at negligible vapour loadings as a comparative measure. This was done in an attempt to evaluate packing performance sans vapour influences. The influences of vapour loading were considered a later stage in section 8.2.2.

The evaluation was based on the scale version of the 3D matrix (380 x 380 x **M**) and considered the volume / surface area of each of the distinct liquid elements. These elements were subsequently categorized and grouped in order of size. The data are presented as cumulative density functions (CDF) on a weighted basis (volume: $dV/d\upsilon_E$; surface area: $dA/d\text{æ}$). The weighted-base (volume or surface area) distributions were chosen for the main body, as arithmetic differential number distributions ($dN/d\upsilon_E$; $dN/d\text{æ}$) add an unrealistic weighting to small elements when considered within the scope of packed columns. Although numerous, these small elements contribute very little to the overall liquid body, and subsequently, their influence should be taken within context. The cumulative differential number and probability distributions are, however, used in CFD (computational fluid dynamic) validations and modelling, and are consequently provided in the Appendix, Sections 14.5 and 14.6.

Table 8.1 is provided to better understanding and interpretation of the distributions to follow in Section 8.2. The table aimed to highlight key aspects that can and cannot be evaluated or assumed from the EIT data.

Table 8.1: Hydrodynamic characterisation limitation summary.

Can	Cannot	Reasoning
Presented IPL element-volume distributions can be used to consider the "Size-fraction" contribution to the total volume.		$\dot{V}_{total} = \dot{L} * A_{colum} \approx \sum \upsilon_E = Constant$ eqn:8.1 Where V_{Total} represents the total liquid m^3h^{-1} L represents the liquid loading in $m^3.m^{-2}.h^{-1}$ A represents the column area in m^{-2}. **Assumptions:** Constant densities, No mass transfer
Cumulative IPL element-volume distributions can be applied intuitively. **Cumulative IPL element-volume ≈ Liquid loading*Area**		Equation eqn:8.1 Validation of the mesh-grid in Section 7.5
	IPL element-volume distributions ≠ overall kinetic performance	Volumes vary in shape and area
	IPL element-surface area distribution curves ≠ overall kinetic performance	$\sum Area \neq Constant$ Curves only consider the individual contributions and not the total
Evaluate the volume-weighted average $\upsilon_{E,50}$. area-weighted average $æ_{,50}$.		Parameters that represent the cumulative *size* below value makes up 50% of the total. Expected better applicability than the arithmetic mean.
	Consider the root cause of hydrodynamic variations.	Point measurements

8.2.1 CUMULATIVE IPL ELEMENT-VOLUME COMPARISON WITHOUT VAPOUR

A summary of the structure of the IPL element-volume results is provided in Figure 8.1.

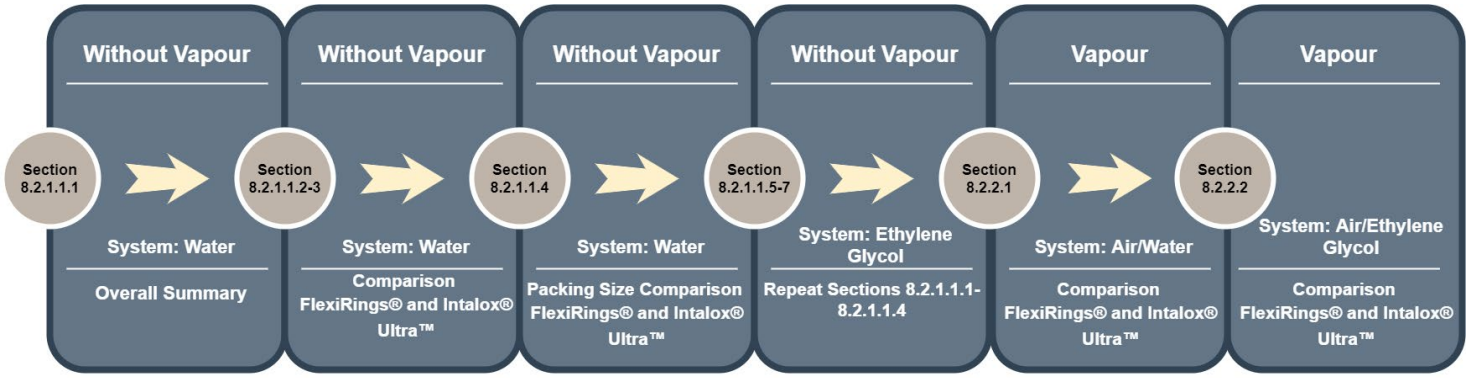

Figure 8.1: Summary of the structure for IPL element-volume results presented within this chapter

8.2.1.1.1 VOLUME-BASED CDF IPL ELEMENT-VOLUME: WATER

The IPL element-volume results present an array of distributions distinctly related to the **a)** packing **b)** liquid physical properties, and **c)** the liquid distributor. A general increase in inter-packing element-volumes with increased liquid loadings was recorded throughout (Figure 8.2). This was deemed intuitive as higher liquid loadings exhibit higher liquid hold-ups, through increased interactions. However, the benefits of the tomography-based characterisation are found in the distributions that make up these parameters and, consequently, the shape of the curves.

The slope of the presented graphs is suggested for consideration during packing development, as uniform IPL element-volumes are surmised as advantageous. A larger slope and consequently "narrower" distribution illustrates greater uniformity and likely translates into better performance through **a)** uniform velocities and residence times and **b)** uniform mass transfer areas and diffusion resistances. A narrower distribution is consequently proposed as a measure of liquid-to-packing interaction uniformity.

Of equal importance is the consideration that shifts towards smaller elements at set liquid loadings presents an increase in individual elements and consequently a droplet-creation favouring design. The droplet-creation mentioned above is conventionally used to motivate increased kinetic performance through the increased interfacial area (See Figure 1.1 on page 3). However, the focus of the hydrodynamic section is centred around the contribution of individual element sizes, rather than the total area consideration. The kinetic aspects are consequently addressed in Section 8.3. Readers are advised to take note that the x-axis of the presented graphs were not standardised, as it hides the finer details on low liquid loads.

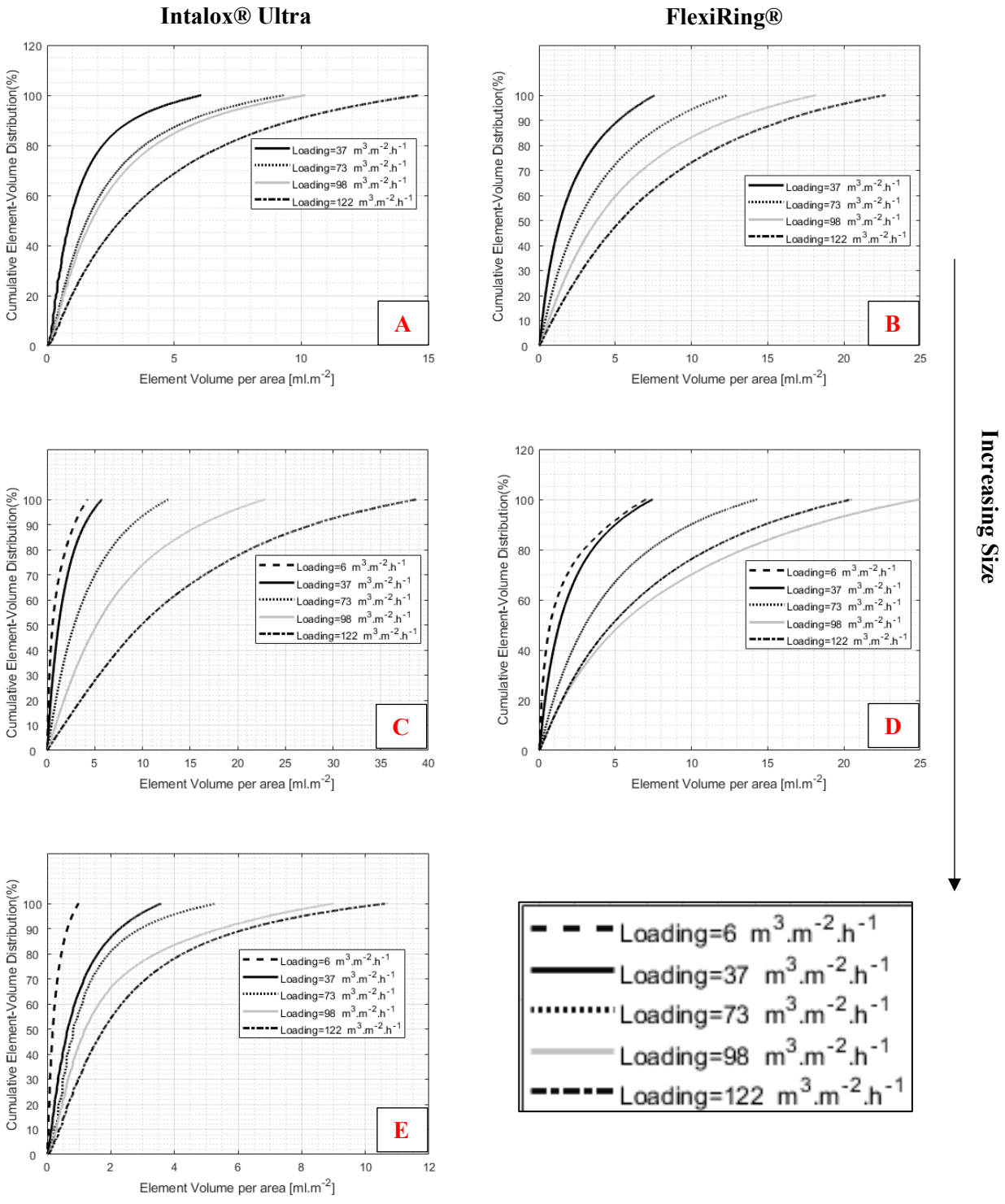

Figure 8.2: Cumulative IPL element-volume distributions using air / water at zero vapour loading A) Intalox® Ultra size A; B) 1.5" FlexiRing®; C) Intalox® Ultra size L; D) 2" FlexiRing® ; E) Intalox® Ultra size O.

8.2.1.1.2 WATER: 1.5" FLEXIRING® AND INTALOX® ULTRA A

The tomography-based characterisation allows for differentiation between packing based on geometrical design, as illustrated in the 1.5" and 2" comparisons of FlexiRing® and Intalox® Ultra (Figure 8.3-8.4). The latter showed increased IPL element-volume uniformity and smaller volume distributions throughout. This was based on both a higher slope and lower volume-weighted average $\upsilon_{E,50}$.

The 1.5 and 2" comparisons of FlexiRing® and Intalox® Ultra consequently present the noteworthy trend in which the design of the latter illustrates increased IPL element creation. This was adjudged to be related to the geometrical design, with the Intalox® Ultra providing a larger open area within which stream elongate and form droplets (given the surface conditions influenced by the liquid surface tension and viscosity).

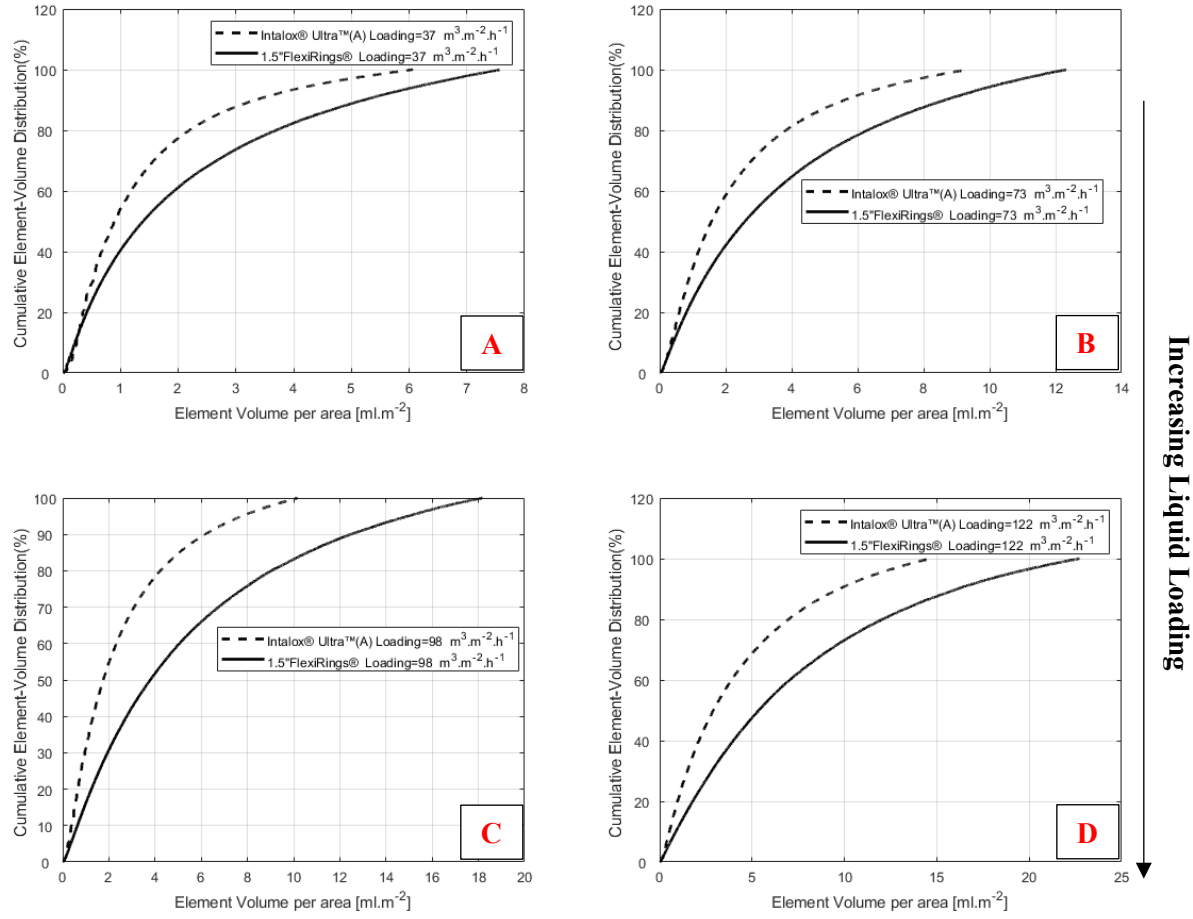

Figure 8.3: Cumulative IPL element-volume distributions using air / water at zero vapour loading considering Intalox® Ultra size A vs. 1.5" FlexiRing® @ A) 37 $m^3.m^{-2}.h^{-1}$; B) 73$m^3.m^{-2}.h^{-1}$; C) 98$m^3.m^{-2}.h^{-1}$; D) 122$m^3.m^{-2}.h^{-1}$;

8.2.1.1.3 WATER: 2" FLEXIRING® AND INTALOX® ULTRA L

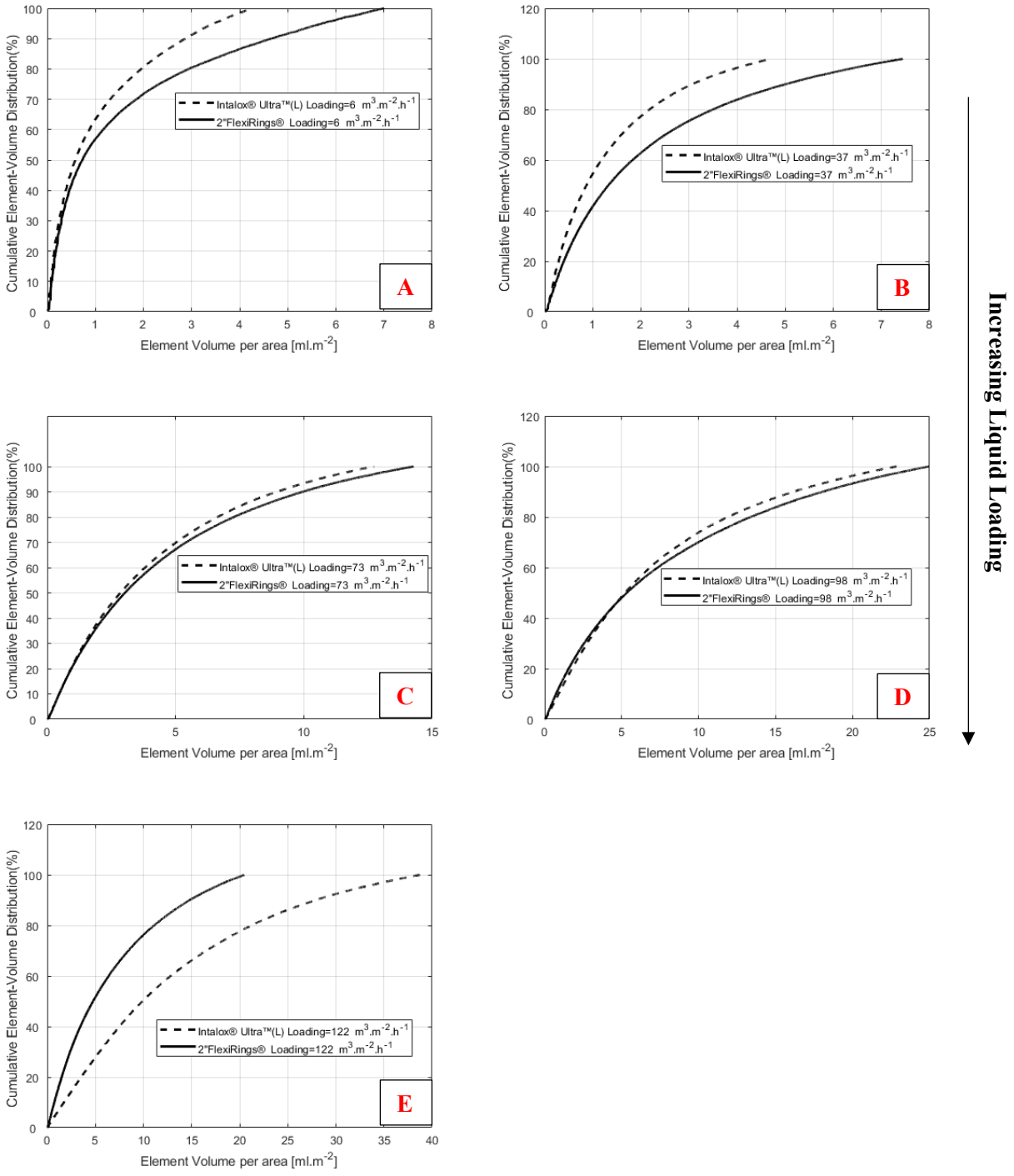

Figure 8.4: Cumulative IPL element-volume distributions using air / water at zero vapour loading considering Intalox® Ultra size L vs. 2" FlexiRing® @ A) 6m^3.m^{-2}.h^{-1}; B) 37 m^3.m^{-2}.h^{-1}; C) 73m^3.m^{-2}.h^{-1}; D) 98m^3.m^{-2}.h^{-1}; E) 122m^3.m^{-2}.h^{-1};

The notable deviation from the expected trend of increased IPL element-volume (Intalox® Ultra >FlexiRing®) with liquid loading for the 2" FlexiRing® at 122m^3.m^{-2}.h^{-1} (Figure 8.2**d**) and the consequent implications on the 2" geometrical comparison (Figure 8.3**e**), were further evaluated using the differential number distribution as presented in Figure 8.5**a**.

The presented Figure 8.5**a** illustrates an almost identical number distribution when comparing the 2" FlexiRing® at 98 and 122 $m^3.m^{-2}.h^{-1}$. Differentiation only occurred above a cumulative distribution of 85%. The probability density function (PDF) was used to illustrate the different behaviour between the liquid loadings (Figure 8.5**b**) and presented a lower maximum IPL element-volume for 122 $m^3.m^{-2}.h^{-1}$.

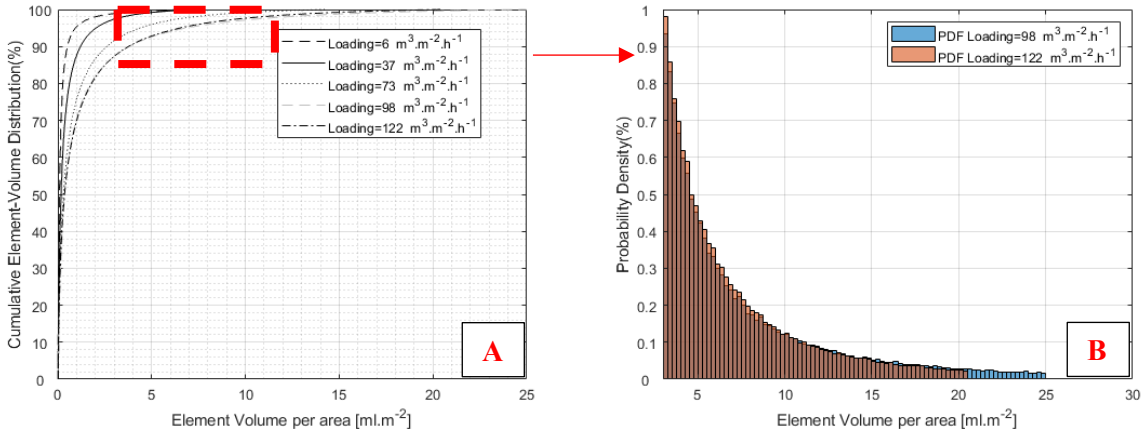

Figure 8.5 : Cumulative element-volume distributions using water at zero vapour loading; Intalox® Ultra size L; differential number-based; A) CDF; B) PDF

The IPL element-volume breakup and redistribution at 122 $m^3.m^{-2}.h^{-1}$ was thought to be related to the packing geometry. However, the presented EIT characterisation system only considers the implications and not the root cause of hydrodynamic variations. For this reason, conclusive justification cannot be provided, and further experimentation is required.

Nevertheless, this behaviour is theorized to be related to the shrouding effect of the FlexiRing® at orientations other than vertical. The "perceived" voidage of both liquid and vapour consequently varies depending on the orientation of the ring. The accompanying areas of preferential flow are speculated to create increased liquid velocities and shear, leading to element break-up.

8.2.1.1.4 Water: Characterisation based on varying packing size

Evaluation of IPL element-volume distributions across different packing sizes were limited due to the complex relationship between the packing and the liquid physical properties. Both the 1.5" and 2" evaluations of the respective FlexiRing® and Intalox® Ultra, presented an increase in the IPL element-volumes with increased packing sizes at high liquid loadings. At the low end, both packing variants illustrated negligible size dependence. The cumulative volume depiction of these results is presented in Figure 8.6**a-d**. The results suggested negligible size dependence at low liquid loadings and consequently the dominating influence of the liquid physical properties (viscosity and interfacial tension). However, the impact of different packing sizes was found accentuated at higher liquid loadings, where the friction and momentum forces outweigh the influence of the water properties. The suggested physical property dominance at low liquid loadings(<37$m^3/m^2/hr$) was further motivated with the Intalox® Ultra size O

(Figure 8.6**e**). The Slight deviations between the size O and the sizes A and L, are likely attributed to the maldistribution discussed in section 7.7. However, significant conclusions could not be drawn with regards to the Intalox® Ultra size O at high liquid loadings (Figure 8.6**f**) due to the combined effects of its large voidage and physical properties. The increased voidage is theorized to have given prominence to individual droplet freefall and physical property-dominated effects.

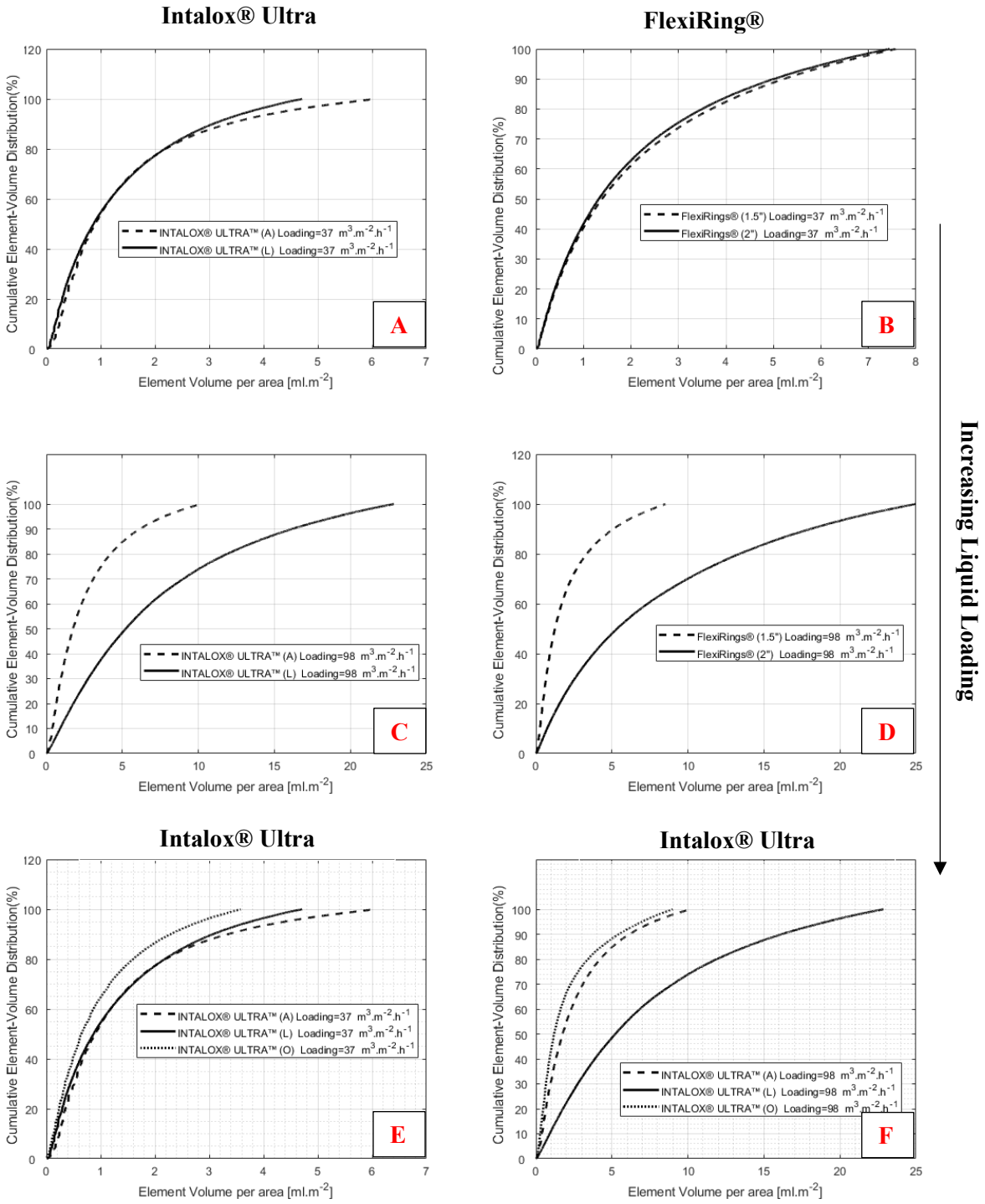

Figure 8.6: Cumulative IPL element-volume distributions using water at zero vapour loading : A) Intalox® Ultra size A and L @ 37 $m^3.m^{-2}.h^{-1}$; B) 1.5" &2" FlexiRing® @ 37 $m^3.m^{-2}.h^{-1}$; C) Intalox® Ultra size A and L @ 98 $m^3.m^{-2}.h^{-1}$; D) 1.5" &2" FlexiRing® @ 98 $m^3.m^{-2}.h^{-1}$; E) Intalox® Ultra sizes A, L and O @ 37 $m^3.m^{-2}.h^{-1}$; F) Intalox® Ultra sizes A, L and O @ 98 $m^3.m^{-2}.h^{-1}$;

The presented results are equivalent to pre-loading and consequently support the assumption of the Maćkowiak (section 2.2.2.5.3) liquid hold-up model, in assuming that physical properties dominate droplet sizes and their behaviour at low liquid loadings. The experimental data from this section, however, deviated from this assumption at higher liquid loadings. The aforementioned is hypothesised as the reasoning behind the non-normal (ARE crossover between positive and negative) error distribution presented by Minne [5], evaluating the preloading liquid hold-up and the Maćkowiak model on Intalox® Ultra size A. Minne [5] regressed the packing constants form the Intalox® Ultra size A and found that the regressed model overpredicted the preloading hold-up at low liquid loadings and underpredicted at high liquid loadings. This trend indicates that parameters (either one or many) are still left unaccounted in this model.

8.2.1.1.5 Ethylene Glycol: Volume-based CDF IPL Element-volume

The cumulative volume distributions for the ethylene glycol system are presented in Figure 8.7**a-c** for the 2” packing equivalents. The study considered the additional 1.5” evaluations for both FlexiRing® and Intalox® Ultra (A). However, the data on these systems were discarded due to power limitations on the signal generator (DDS). The 5W power delivery of the DDS was not enough to provide the required voltage stability throughout these evaluations. The discussion was relegated to section 12.5 of the appendix to not distract from the scope. The normalized liquid distribution plot for the Intalox® Ultra size O at 6 $m^3.m^{-2}.h^{-1}$ is provided in Figure 8.7**d** as motivation towards the negligible maldistribution effects in the ethylene glycol characterisations.

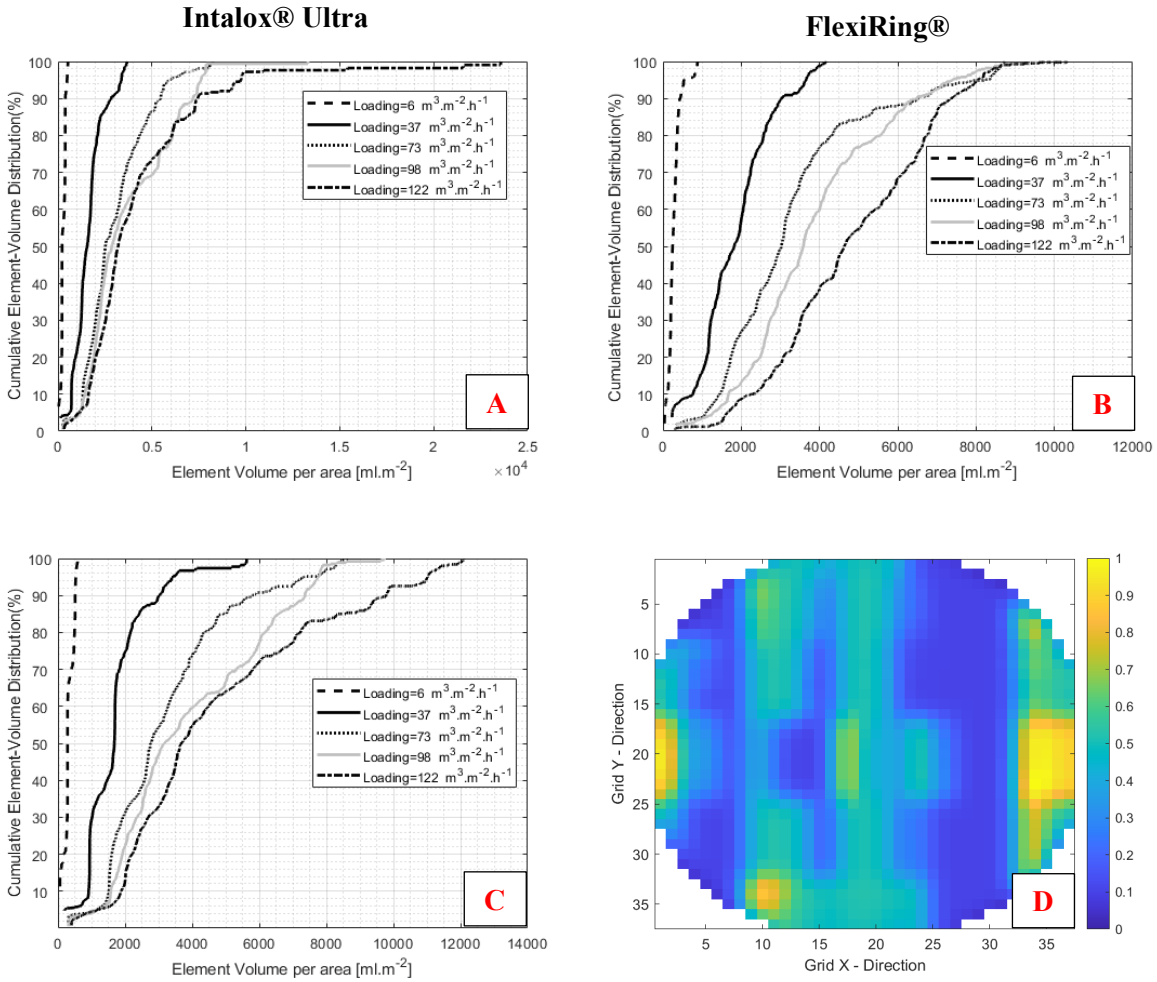

Figure 8.7 : Cumulative IPL element-volume distributions using air / ethylene glycol at zero vapour loading; A) Intalox® Ultra size L; B) 2” FlexiRing®; C) Intalox® Ultra size O; D) liquid distribution @ 6$m^3.m^{-2}.h^{-1}$.

The presented results illustrate an order of magnitude increase in the IPL element-volume compared to the water system. This is likely due to the dominating viscosity effect, creating long stream-like elements as opposed to the small elements evaluated for water. This stream-like behaviour was also noted by Minne [5] in visual observations.

The total liquid volume of ethylene-glycol consequently comprised far fewer distinct elements than that of water. These large continuous liquid elements provide possible clarification as to the increased hold-up of ethylene glycol compared to water.

8.2.1.1.6 Ethylene Glycol: 2" FlexiRing® and Intalox® Ultra L

The 2" equivalent geometrical comparison between FlexiRing® and Intalox® Ultra is provided in Figure 8.8**a-d**. The results confirm the proficiency of the tomography characterisation in highlighting variations in hydrodynamic behaviour.

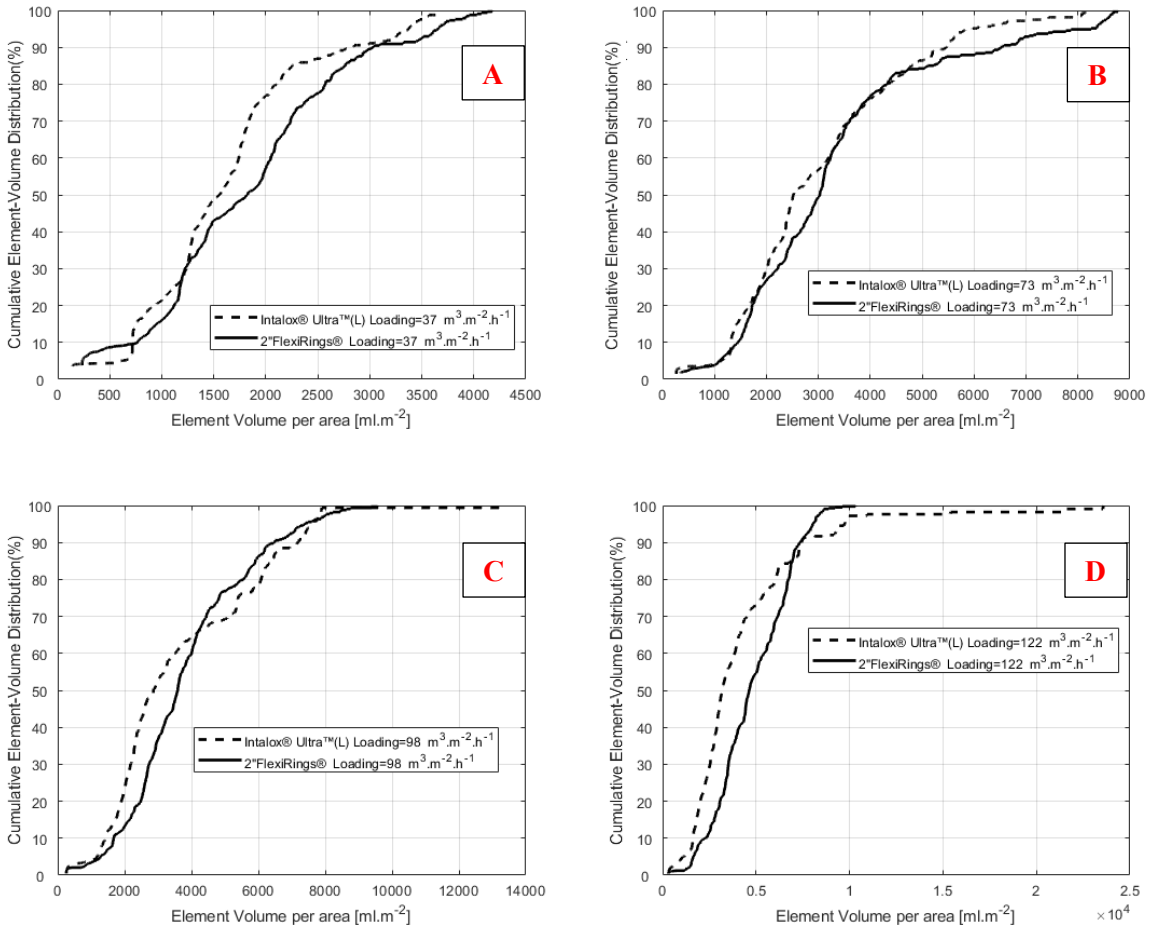

Figure 8.8 : Cumulative IPL element-volume distributions using air / ethylene glycol at zero vapour loading considering Intalox® Ultra size L vs. 2" FlexiRing® @ A) 37 $m^3.m^{-2}.h^{-1}$; B) 73$m^3.m^{-2}.h^{-1}$; C) 98$m^3.m^{-2}.h^{-1}$; D) 122$m^3.m^{-2}.h^{-1}$;

Increased IPL element-volume uniformity is presented in favour of the Intalox® Ultra throughout, noting the lower IPL element volume and narrower distribution. The Intalox® Ultra again proved superior in droplet creation, following suit with the water-based evaluations. However, the graphical comparison in Figure 8.7d presents the additional notion of unfavourable conditions for the high open area Intalox® Ultra, with the existence of a handful of very large liquid elements. These elements are hypothesised to likely present diffusion limitations for liquid phase mass transfer limiting systems due to their perceived negative impact on bulk diffusion rates (Eddie and penetration theory).

8.2.1.1.7 CHARACTERISATION BASED ON VARYING PACKING SIZE: ETHYLENE GLYCOL

Related results to that of water were reported for the size-based comparison of Intalox® Ultra sizes L and O. The comparison presented in Figure 8.9 again highlighted limited differentiation at low liquid loadings and consequently liquid physical property dominated effects. The effects above were reported up until 98$m^3.m^{-2}.h^{-1}$, with slight differentiation at the highest liquid loading of 122$m^3.m^{-2}.h^{-1}$. This suggests an extension of the physical property dominated regime to higher liquid loadings, based on the increased viscosity for the ethylene glycol.

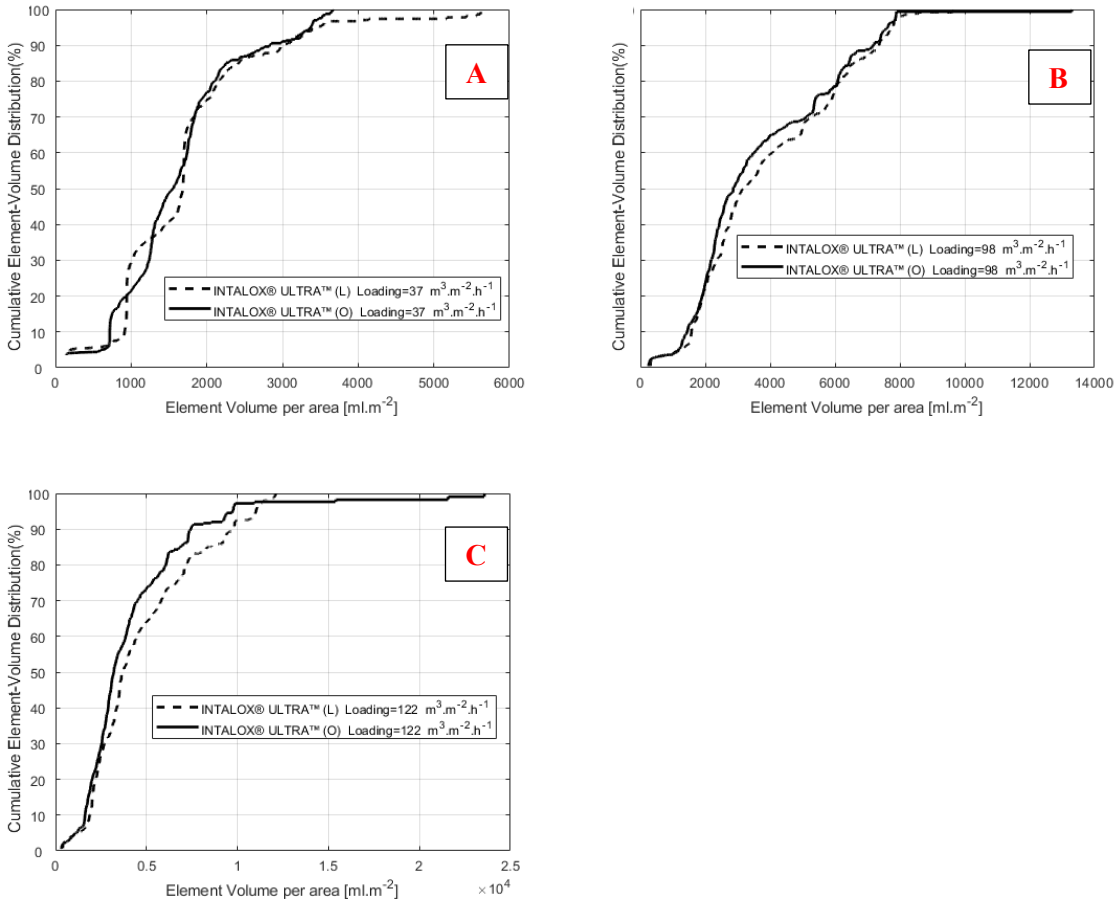

Figure 8.9: Cumulative IPL element-volume distributions using ethylene-glycol at zero vapour loading A) Intalox® Ultra size L and O @ 37 $m^3.m^{-2}.h^{-1}$; B) Intalox® Ultra size L and O @ 98 $m^3.m^{-2}.h^{-1}$; C) Intalox® Ultra size L and O @ 122$m^3.m^{-2}.h^{-1}$;

The extended physical property dominance is presented as likely justification to the Minne [50] findings, and that the Maćkowiak pre-loading liquid hold-up models presented a better correlation for ethylene glycol than water. In this Minne [5] considered both Intalox® Ultra size A and O. The results highlight the intricate dependence of "droplet creation" on the physical properties and related voidage. The latter, however, likely diminishes with increased viscosity.

8.2.2 Effect of Vapour Loading on Cumulative IPL element-volume

The study further considered the effect of vapour loading on inter-packing element-volumes and subsequently droplet creation. The results were again split into air / water and air / ethylene glycol. As a comparative measure, the vapour loadings were based on the percentage of flooding velocity provided in KG-Tower.

8.2.2.1 Air/Water

The effect of vapour loading on the IPL element-volume distributions was evaluated independently for the 1.5" and 2" equivalent packings. The results are presented in Figure 8.10-8.11 and figures 8.12-8.13 respectively. Coloured arrows are included for clarification, showing the effect of increased vapour loadings on the distribution results. Accordingly:

- **Red arrows**, pointing along the X-axis from left to right are indicative of increased IPL volumes with increased vapour loadings,
- **Blue arrows**, pointing along the X-axis from right to left are indicative of decreasing IPL volumes with increased vapour loadings, and
- **Green arrows,** depict the transition zone.

8.2.2.1.1 Vapour loading: 2" FlexiRing® and Intalox® Ultra L

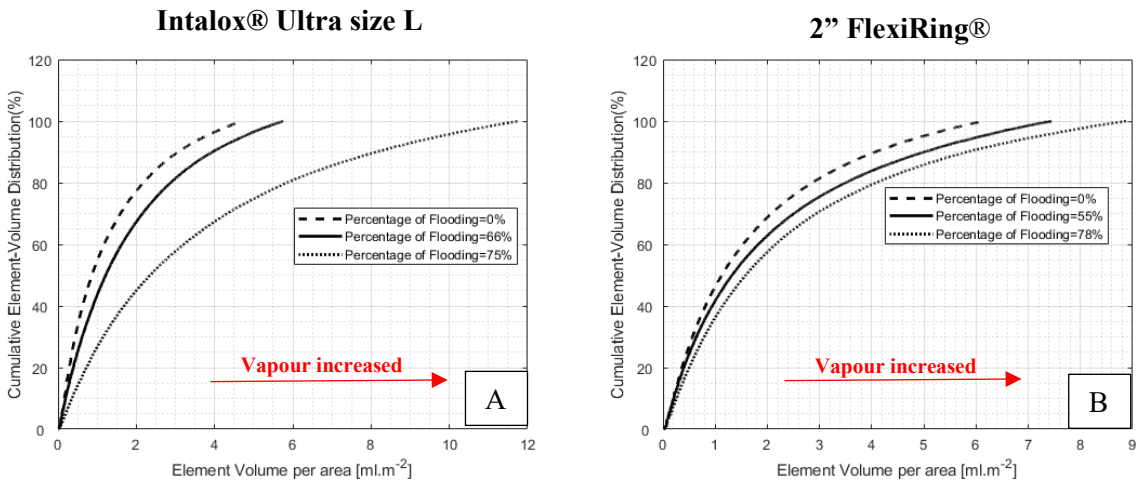

Figure 8.10 : Cumulative IPL element-volume distributions for air water; A) Intalox® Ultra size L @ 37 $m^3.m^{-2}.h^{-1}$; B) 2" FlexiRing® @ 37 $m^3.m^{-2}.h^{-1}$.

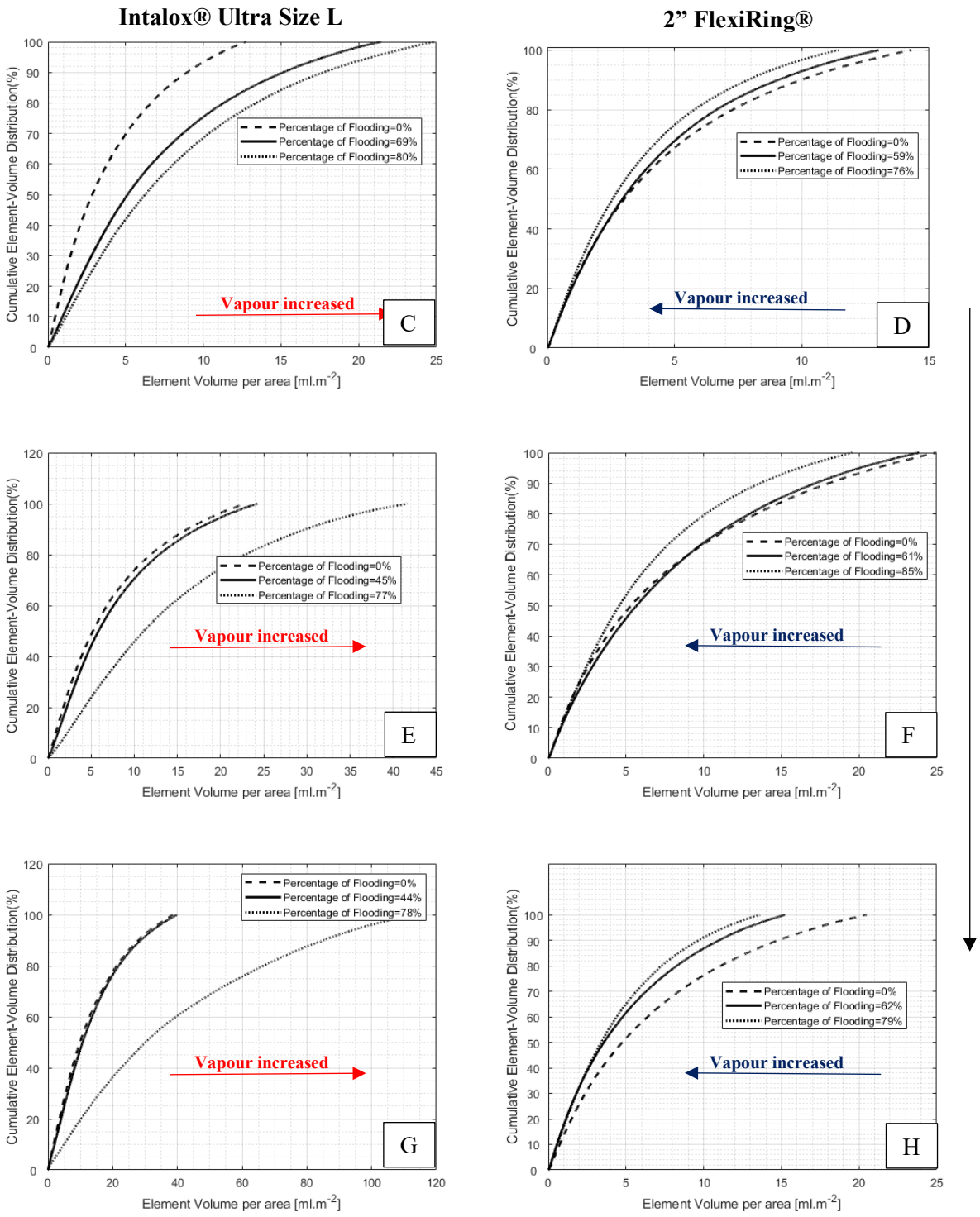

Figure 8.11: Figure 8.10 continues ; C) Intalox® Ultra L @ 73 $m^3.m^{-2}.h^{-1}$; D) 2" FlexiRing® @ 73 $m^3.m^{-2}.h^{-1}$; E) Intalox® Ultra L @ 98 $m^3.m^{-2}.h^{-1}$; F) 2" FlexiRing® @ 98 $m^3.m^{-2}.h^{-1}$; G) Intalox® Ultra size L @ 122 $m^3.m^{-2}.h^{-1}$; H) 2" FlexiRing® @ 122 $m^3.m^{-2}.h^{-1}$;

8.2.2.1.2 VAPOUR LOADING: 1.5" FLEXIRING® AND INTALOX® ULTRA A

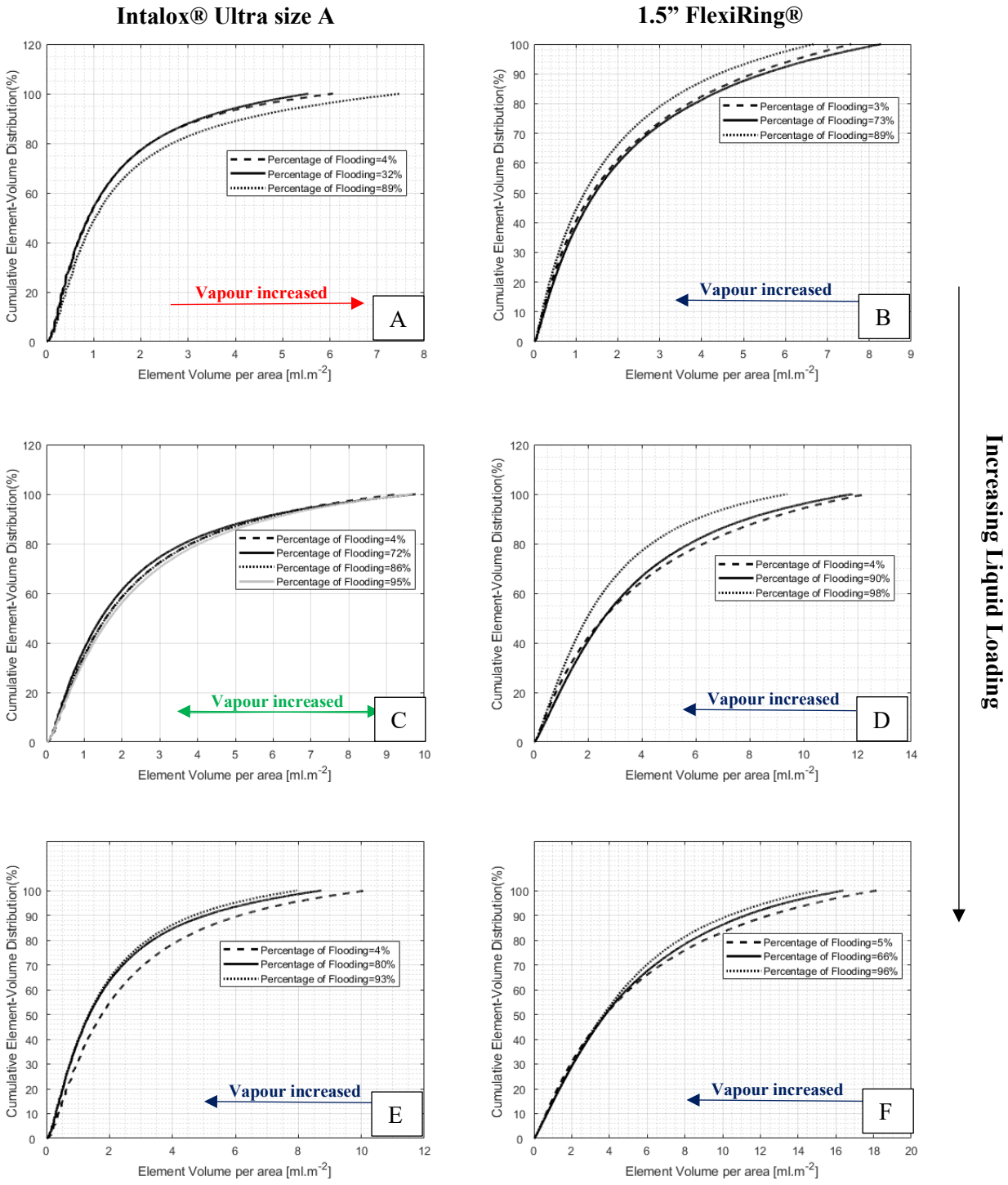

Figure 8.12 : Cumulative IPL element-volume distributions for air / water; A) Intalox® Ultra A @ 37 $m^3.m^{-2}.h^{-1}$; B) 1.5" FlexiRing® @ 37 $m^3.m^{-2}.h^{-1}$; C) Intalox® Ultra A@ 73 $m^3.m^{-2}.h^{-1}$; D) 1.5" FlexiRing® @ 73 $m^3.m^{-2}.h^{-1}$; E) Intalox® Ultra A@ 98 $m^3.m^{-2}.h^{-1}$; F) 1.5" FlexiRing® @ 98$m^3.m^{-2}.h^{-1}$

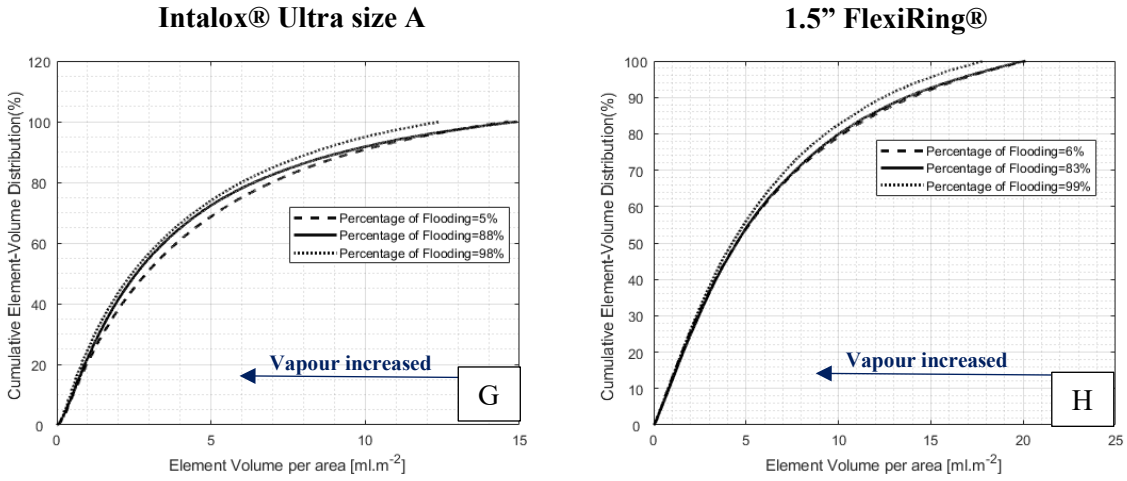

Figure 8.13 : Figure 8.12 Continues; G) Intalox® Ultra size A @ 122 $m^3.m^{-2}.h^{-1}$; H) 1.5" FlexiRing® @ 122$m^3.m^{-2}.h^{-1}$.

The presented results illustrate the presence of two distinct "droplet-based" operating zones, namely:

[1] **Z1:** Where increased vapour loading propagates IPL element-volume breakup & redistribution and (additional droplets are created),

[2] **Z2:** Where increased vapour enlarges the inter-packing elements.

These distinct zones are intricately related to the physical properties and their interactions with the packing and the accompanied forces. The transition zones were reported at different sizes for the respective FlexiRing® and Intalox® Ultra. Subsequently, between 37 and 73 $m^3.m^{-2}.h^{-1}$ for the 2" FlexiRing® and at 73 $m^3.m^{-2}.h^{-1}$ for the 1.5" equivalent Intalox® Ultra(A).

The Z2→Z1-transition consequently represents instances where the combined interactions between the packing and relative vapour velocity induced shear forces are sufficient to overcome the fluid phase physical properties and redistribute or reshape the liquid elements. The size differentiation of the transition point was theorized stemming from the effects of "perceived" voidage (see section 8.2.1.1.3) and its relative impact on velocity profiles and friction forces. The Intalox® Ultra's transition point at the lower 1.5" size range, as opposed to the 2" of the FlexiRing®, was consequently thought related to its mitigation of excessive velocity profiles through geometrical design.

8.2.2.2 AIR/ETHYLENE GLYCOL

The effect of vapour loading on ethylene glycol IPL element-volume distributions was evaluated for the 2" equivalent packings. The results are presented respectively in Figure 8.14 and 8.15. Transitions in the droplet "zones" were again noted, in the case of the 2" of the FlexiRing®.

8.2.2.2.1 VAPOUR LOADING: 2" FLEXIRING® AND INTALOX® ULTRA L

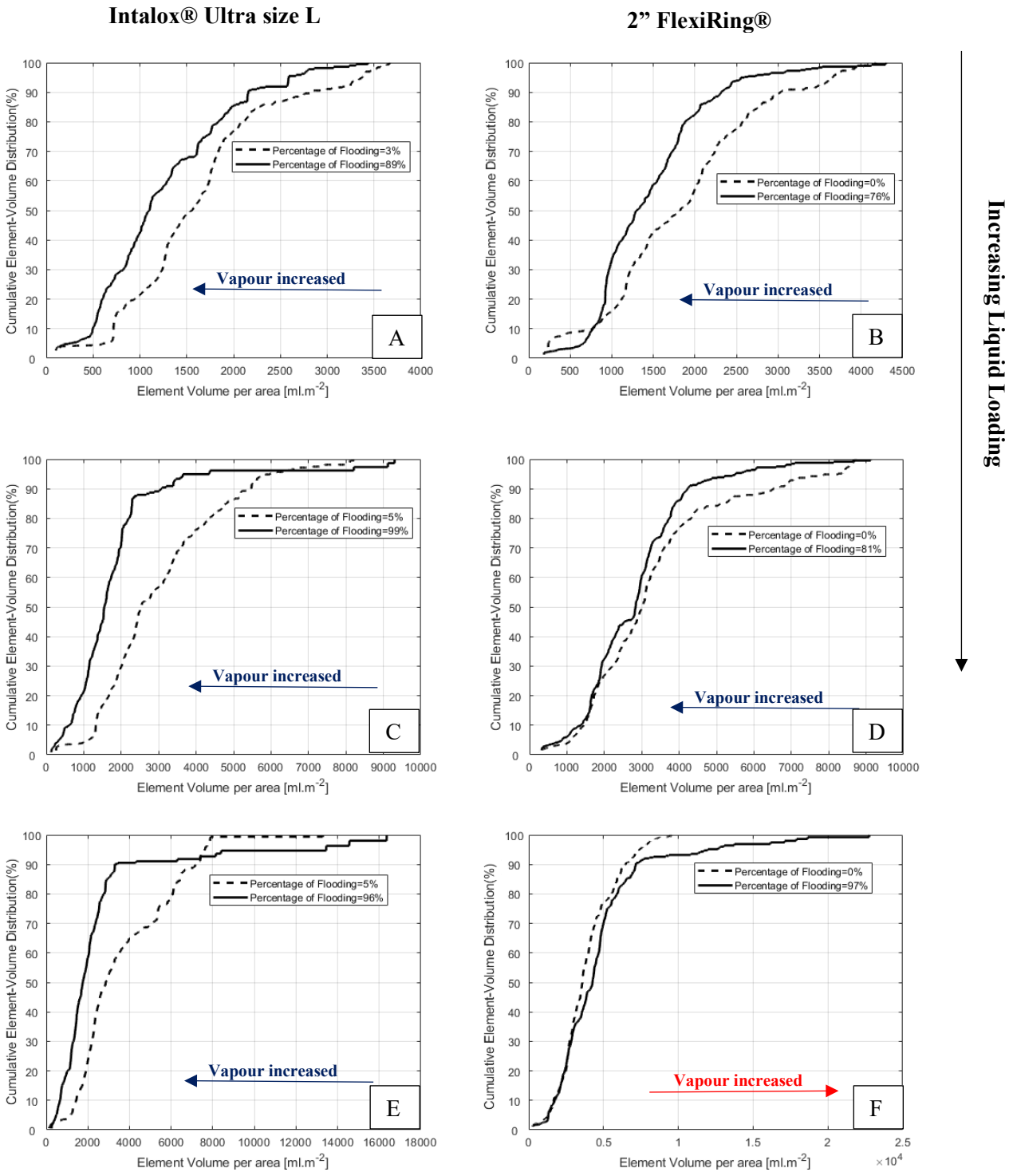

Figure 8.14: Cumulative IPL element-volume distributions for air / ethylene glycol; A) Intalox® Ultra size L @ 37 $m^3.m^{-2}.h^{-1}$; B) 2" FlexiRing® @ 37 $m^3.m^{-2}.h^{-1}$; C) Intalox® Ultra size L@ 73 $m^3.m^{-2}.h^{-1}$; D) 2" FlexiRing® @ 73 $m^3.m^{-2}.h^{-1}$; E) Intalox® Ultra size L@ 98 $m^3.m^{-2}.h^{-1}$; F) 2" FlexiRing® @ 98$m^3.m^{-2}.h^{-1}$;

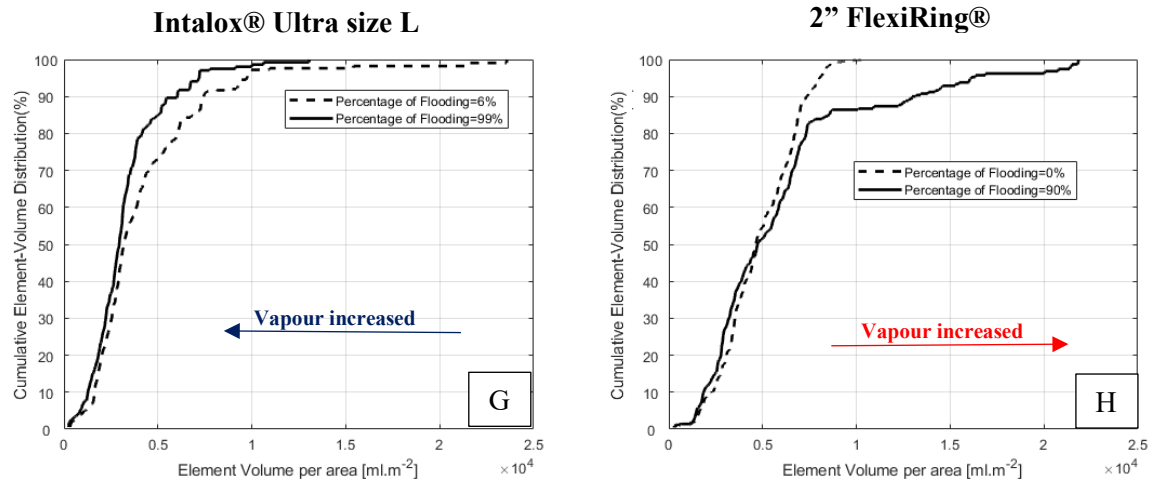

Figure 8.15 : Figure 8.14 Continues; G) Intalox® Ultra size L@ 122 $m^3.m^{-2}.h^{-1}$; H) 2" FlexiRing® @ 122$m^3.m^{-2}.h^{-1}$.

The seemingly contradictory influence on vapour on the IPL element-volumes for 2" FlexiRing®, evaluating water and ethylene glycol respectively, draws focus to the complexity of the interactions between the packing and physical properties. Due to its point measurement nature, the presented tomography technique is unable to consider the root cause of the variations. However, the behaviour is speculated to again be related to the geometrical design of the FlexiRing®.

In the case of the high liquid loadings of ethylene glycol (high viscosity), the intermolecular friction from the viscosity was suspected of dominating distributions, accentuating short-circuiting through preferential liquid and vapour flow channels. This presumably reduced the liquid and vapour interactions and the subsequent element breakup. More experimental work is, however, still required to prove this hypothesis.

It should be noted that FlexiRing® are rarely operated at liquid loadings exceeding 100 $m^3.m^{-2}.h^{-1}$ and that the evaluations are likely on or beyond the cusp of feasibility. Nonetheless, phenomena outside the feasibility range may still be insightful as it highlights the mechanisms and physical property influences.

8.2.3 Cumulative IPL Element-surface Area Comparison

An approach similar to the IPL element-volume characterisation (Section 8.2.1) was used to compare IPL element-surface area on an area-weighted base. The accompanied differential number and probability functions are once again presented in the appendix (See Section 14.3-14.5). Readers are advised against overall-kinetic deductions based on the area-distribution curves, as the total (cumulative surface area) is variable. The included differential curves are consequently only valid for hydrodynamic interpretations and insight into how the inter-packing area distributions.

The study replicated the parameters of Sections 8.2.1-8.2.2 and considered the IPL element-surface area. For the sake of brevity, this is provided in full within the appendix. Table 8.2 is included to link the previous IPL element-volume sections to their element area counterparts.

Table 8.2: Table providing the corresponding IPL element-surface area within the Appendix, to the equivalent IPL element-volume sections in this section.

Description	IPL element-volume	Page	IPL element-surface area Section	Page
CDF summary: Water without vapour loading	8.2.1.1.1	115	14.3.1	14-171
Water without vapour: 1.5” FlexiRing® and Intalox® Ultra A	8.2.1.1.2	117	14.3.2	14-173
Water without vapour: 2” FlexiRing® and Intalox® Ultra L	8.2.1.1.3	118	14.3.3	14-173
Water without vapour: Size comparison	8.2.1.1.4	119	14.3.4	14-174
CDF summary: Ethylene glycol without vapour loading	8.2.1.1.5	122	14.3.5	14-175
Ethylene glycol without vapour: Size comparison	8.2.1.1.6	123	14.3.6	14-176
Water with vapour loading: 2” FlexiRing® and Intalox® Ultra L	8.2.2.1.1	126	14.4.1	14-177
Water with vapour loading: 1.5” FlexiRing® and Intalox® Ultra A	8.2.2.1.2	127	14.4.2	14-179
Ethylene glycol with vapour loading: 2” FlexiRing® and Intalox® Ultra L	8.2.2.2.1	129	14.4.4	14-181
Additional				
Water with vapour loading: Intalox® Ultra O	14.2.1	14-170	14.4.3	14-181

The IPL element-surface area considerations presented similar results to IPL element-volume in differentiating between packing types. The Intalox® Ultra subsequently presented increased uniformity of both IPL element-surface area and IPL element-volume across the evaluated sizes using both water and ethylene glycol.

The vapour loading considerations additionally highlighted the intricate relationship between surface area and volume in packed columns. The transition zones were subsequently noted at the same liquid-vapour-packing combination. Therefore, between 37 and 73 $m^3.m^{-2}.h^{-1}$ for the 2” FlexiRing® and at 73 $m^3.m^{-2}.h^{-1}$ for the 1.5” equivalent Intalox® Ultra (A).

8.2.3.1 SIGNIFICANCE: Z1:Z2 ZONES

The presented variations in vapour loading illustrated distinct zones of either droplet creation (via breakup) or reduction (accumulation into streams), as noted in the IPL element-volume discussion (Section 8.2.2.2.1). These mechanisms are complexly related to the force balances, shear forces, physical properties, and the geometrical design of the packing. The results illustrate that neither design offers blanket-droplet creation across all parameters of liquid and vapour loadings.

The implications of the transitions relate to the improved understanding of hydrodynamic mechanisms within the packing. An increase in liquid-hold-up, in either case, is consequently based on either the creation of additional small volumes or the slowdown/accumulation of liquid. The transitions, therefore, represent a change in the mechanism of liquid hold-up propagation with vapour .

The small volumes present a lower area-weighted average for element area and vice versa for the larger volumes. The aforementioned, however, cannot be correlated directly towards overall-kinetic performance, as the total area is not considered constant within the distributions. Nevertheless, the zones and their implications are theorized to include the relative influence of the respective ratio of gas-to-liquid mass transfer resistances.

The breakup zone, in particular, will likely offer benefits towards gas-side mass transfer limiting systems (conventionally distillation) as the finer particle distributions aid diffusion through and into the bulk vapour phase. The extent of the benefit, however, remains undetermined and requires further research.

8.2.3.2 SIGNIFICANCE: DATA

A combination of the volume and area-based data are poised to aid the mathematical and CFD modelling of packed-column flow. The data can also be transposed to surface-to-volume ratios for simplified use in CFD validations. The data present added fundamentality to packed column modelling through droplet size distributions and, more specifically, improvements in considering individual element Reynolds numbers.

The data also presents a means of evaluating the assumption related to hydrodynamic modelling. Examples are presented in section 8.2.1.1.4, where the assumptions related to the Maćkowiak model on liquid distribution physical property dependence was considered.

8.3 MASS TRANSFER IMPLICATION

The preceding sections focussed on hydrodynamic characterisation and determining the individual element contributions towards factors such as liquid-hold-up. These evaluations considered distribution behaviour but were limited in their kinetic applicability. This stems from its focus on contributing components and not the total IPL element-surface area. The cumulative IPL element-surface area presented in Section 8.2 is not constant for a given liquid loading, owing to the additional variations in

liquid-hold-up (downward velocity). Therefore, meaningful kinetic deductions from the distribution analysis in section 8.2, were adjudged impractical. Mathematically,

$$\sum a_E \neq Constant;\ \sum \boldsymbol{\upsilon_E} = Constant \qquad 8.2$$

The study accordingly used the scaled 3D matrices (380 x 380 x **M**) to evaluate total inter-packing element-surface area (apparent surface area of droplets) as a comparative measure of kinetic performance. Results are consequently presented through comparison and not as absolutes. The limitations and their implications are highlighted in Table 8.3.

Table 8.3: Kinetic characterisation can/cannot table.

Can	Cannot	Reasoning
	IPL element-surface area ≠ effective interfacial area	• It does not account for the area on packing itself • It does not account for dead zones • It does not consider surface renewal or penetration effects.
Correlate IPL element-surface area between different packings		Standardized • Sensor • Liquid Distributor • Support grid
Mitigate the effect of surface waves and turbulence		Considering low vapour loadings

The aqueous inter-packing element-surface area comparison of the 1.5" and 2" equivalents is presented in Figure 8.16. The ratio of the effective interfacial area between the Intalox® Ultra(L) and 2" FlexiRing® (based on Nieuwoudt [3]) was added for scale. The original publication, however, presents the data using the effective-to-specific surface area (a_e/a_p) ratio, with unpublished packing surface areas (a_p) (Equation 8.3)

$$\frac{a_{\text{e Intalox® Ultra Size L}}}{a_{\text{e 2" FlexiRing®}}} * \frac{a_{p\ \text{2" FlexiRing®}}}{a_{p\ \text{Intalox® Ultra Size L}}} = f(x) \qquad 8.3$$

Where

- a_e is the effective interfacial area
- a_p is the outer surface area of the packing

The curve consequently requires offset by the ratio of $a_{p\ Intalox®\ Ultra(L)}/\ a_{p\ 2"\ FlexiRing®}$ for direct comparison. The direct comparison, however, remains impossible, owing to the limitations of the available literature.

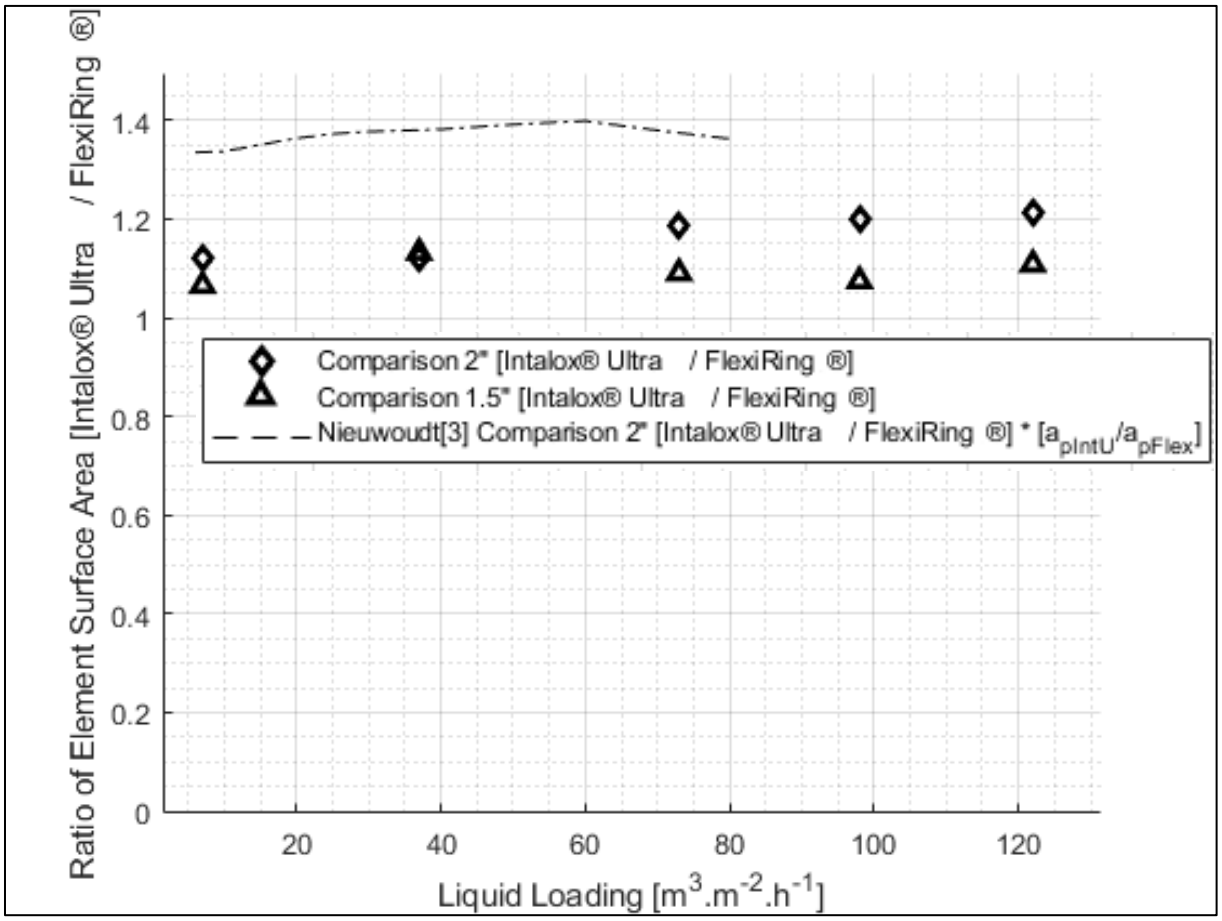

Figure 8.16:Total IPL element-surface area ratio for air / water: Intalox® Ultra size L and 2" FlexiRing® @ F_s =1.8 $(m.s^{-1})\cdot(kg.m^{-3})^{0.5}$; Intalox® Ultra size A and 1.5" FlexiRing® at F_s =1 $(m.s^{-1})\cdot(kg.m^{-3})^{0.5}$;

As a basic logic test, the specific surface area of conventional 50mm Pall® Ring (112.6 $m^2.m^{-3}$ [42, 38]) was compared with IMTP50 (vary from 90.1 [94] to 100 [95] ; based on manufacturer). The IMPT packing variant was chosen based on geometrical similarity to the Intalox® Ultra, while also presenting similar voidage percentages. The results presented a plausible and constant offset-ratio of between 0.8-0.9. The constant offset and the values thereof suggest that this works adequately agrees with that of Nieuwoudt [3]. This was deemed sufficient to motivate the use of the overall IPL element-surface area as a measure of kinetic performance.

Aqueous evaluation of the total inter-packing "droplet" or element-surface area consequently suggests an average improvement of *ca* 17% and 9.4% for the 2" and 1.5" evaluations respectively. Additional comparison of the inter-packing area also presented near equal areas when comparing the Intalox® Ultra size O with the 2" FlexiRing® (see Figure 8.17). This is considered in line with the manufacturer claims

The IPL element-surface area ratios were further evaluated using the air / ethylene glycol system and considered the Intalox® Ultra size L versus 2" FlexiRing® (See Figure 8.18). The results present similar trends to the aqueous and highlight an 18% average IPL element-surface area increase of the Intalox® Ultra size L over the 2" FlexiRing® .

Figure 8.18 presented the maximum deviation between the air / water and air / ethylene glycol systems at low liquid loadings. This is theorized to be related to the increased influence of droplet creation, based on the orders of magnitude difference between the relative IPL element-volumes and -surface areas of the ethylene glycol and water. A combination of the aforementioned with the results of section 8.2.1.1.4 (liquid physical property domination at low liquid loadings) therefore likely led to the deviations.

It should be noted that the effect of the different droplet zones (Z1; Z2) was negated in these evaluations, as it considered low vapour loadings to mitigate the effect of interfacial turbulence variations between the 2nd and 4th packing generations.

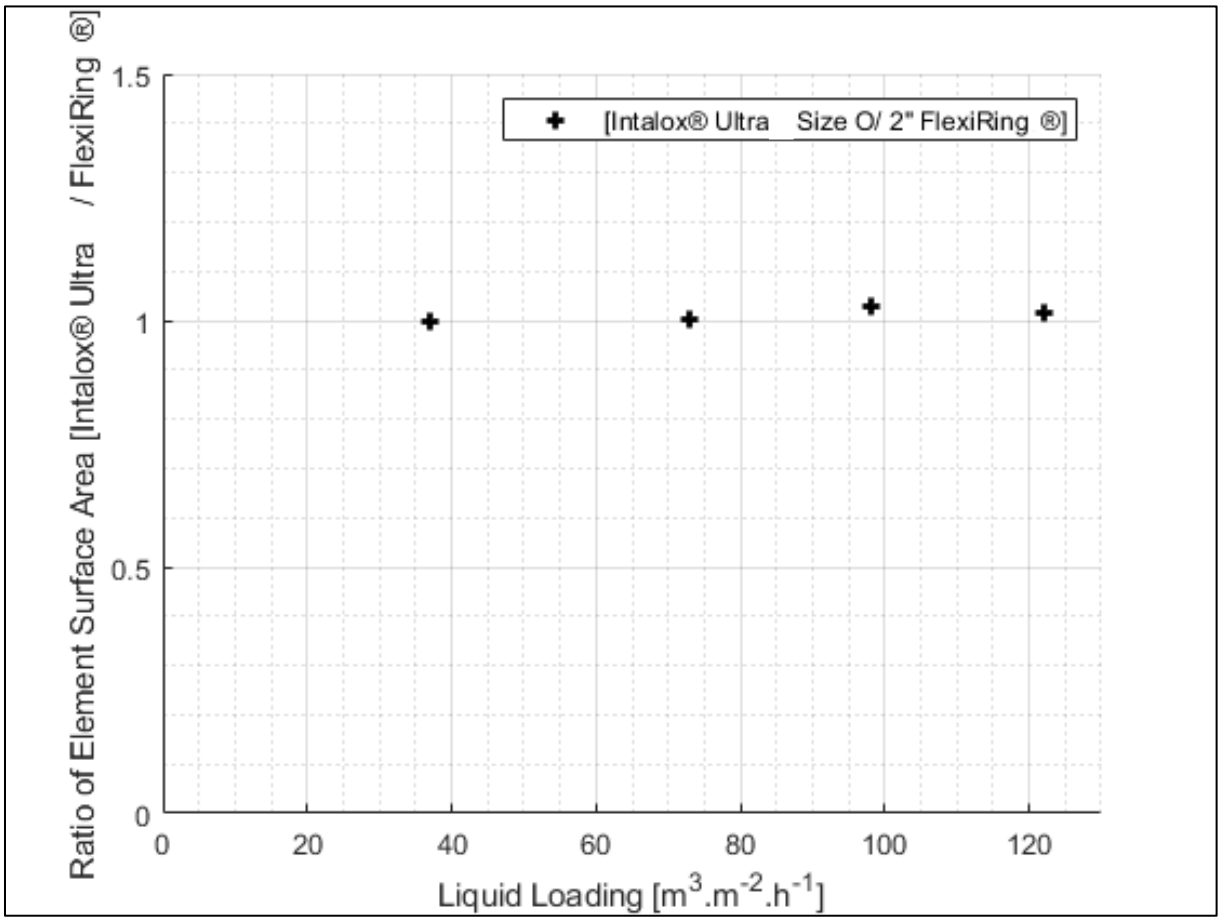

Figure 8.17: Total IPL element-surface area ratio for water: Intalox® Ultra size O and 2" FlexiRing® at F_s =1.8 $(m.s^{-1})\cdot(kg.m^{-3})^{0.5}$.

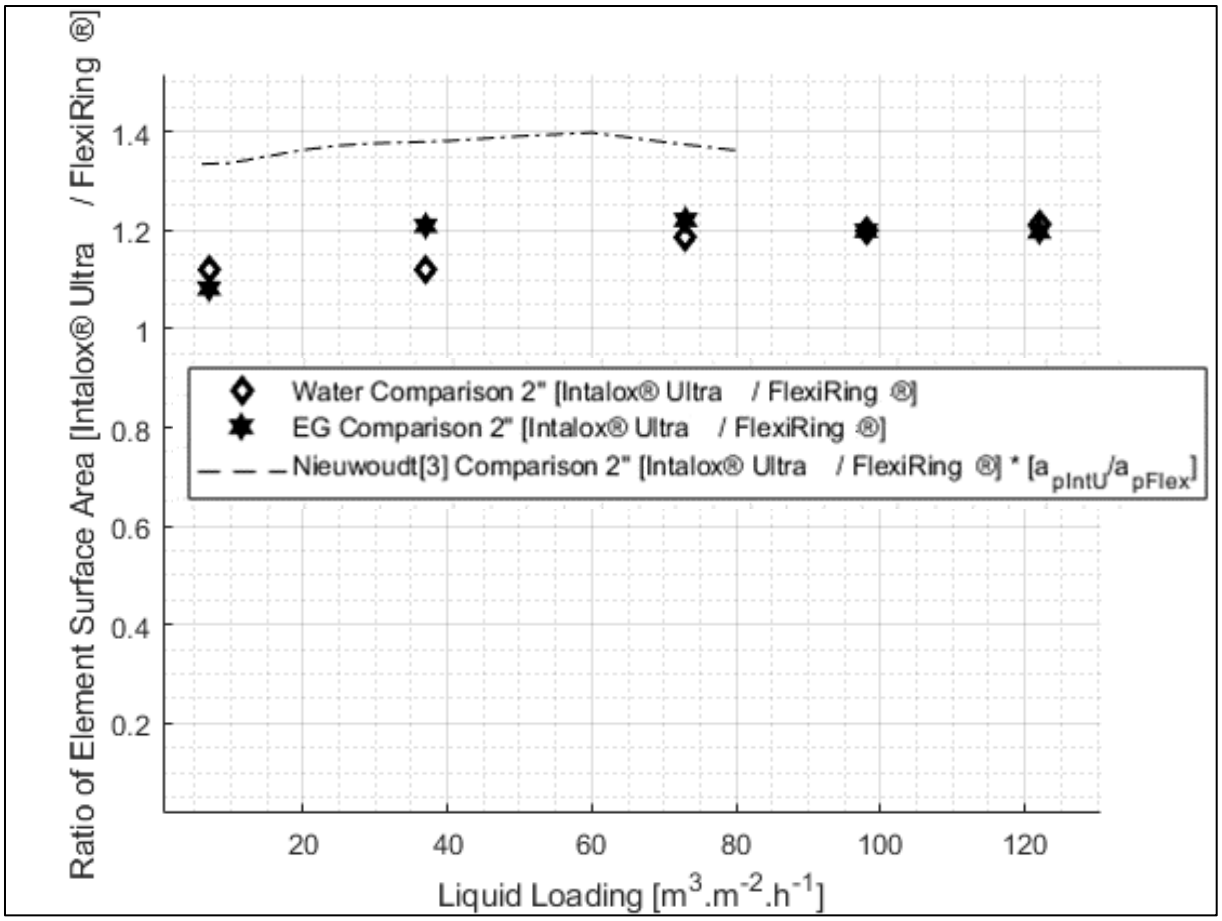

Figure 8.18: Total IPL element-surface area comparison; air / water Intalox® Ultra L and 2" FlexiRing® @ F_s =1.8 $(m.s^{-1})\cdot(kg.m^{-3})^{0.5}$; ethylene glycol Intalox® Ultra L and 2" FlexiRing® at F_s =0.8 $(m.s^{-1})\cdot(kg.m^{-3})^{0.5}$

8.4 INDUSTRIAL SIGNIFICANCE

The significance of the presented results is proposed to reside in the prototyping phase of column internals. The tomography-based characterisation approach offers all the benefits of conventional tomography with the addition of:

[1] Evaluation of total liquid hold-up through element-hold-up.

[2] Characterisation of the

a. Distribution uniformity and droplet-creation capabilities,
b. Break up and accumulation zones,
c. Contributing components IPL element-volumes and areas.

[3] Kinetic performance estimations through total IPL element-surface area.

The aforementioned data is collected in a single experiment comprising 120 seconds. Future mitigation of the computational bottleneck is also expected, with continual innovation in the sector. The presented EIT characterisation is subsequently poised to expedite prototyping by offering both high-speed kinetic and hydrodynamic characterisation.

9. CONCLUSION

Evaluating the parameters limiting the progression of packed column characterisation, this project identified ample room for improvement related to inter-packing droplets and distributions. At the time of publication, the afore-mentioned was still experimentally unevaluated in packed columns, and an electronic impedance tomography (EIT) characterisation system was developed for this purpose.

The cost-effective wire-mesh EIT system was designed and constructed in this work for a fraction of the cost of conventional tomography (X-Ray). The system offered applicability to both conductive and non-conductive liquids through the use of an auto-balancing bridge for electrical impedance measurements. It comprised 1369 independent measurement points throughout the 400mm column and was capable of imaging speeds of 207Hz and 21Hz (number of full column images per second) for conductivity and capacitance, respectively. The measurement resolution was further increased, through size-based calibrations, at each of 1369 measurement points – incorporation of the aforementioned increased resolution without excessive flow intrusiveness.

Tomography-based characterisations were performed on the collected data, with 2D and 3D image processing in MATLAB. The combination of imaging speed and extended evaluation times (120s) allowed sufficient liquid displacement to present between 500k and 2500k individual liquid elements. The processing allowed each liquid element to be evaluated and visualized individually, based on volume and surface-area.

The EIT characterisation was validated by comparing liquid hold-up data with data generated through conventional methods by both Lamprecht [2] and Minne [5]. The validation included both air / water and air / ethylene glycol systems. In addition to the accurate measurement of overall liquid hold-up, the technique also proved effective from a classical tomography perspective (measuring and visualising areas of high and low liquid velocities), through:

- Experimentally considering the presence of wall effects in the experimental setup and offering the ability to calculate the extent thereof.
- Experimentally considering liquid distribution efficiencies and maldistribution effects.

The tomography-based characterizing system was used for hydrodynamic and kinetic evaluation and considered:

- Intalox® Ultra (sizes A,L,O) and FlexiRing® (1.5” and 2) with
- air / water and air / ethylene glycol, and
- variable vapour and liquid loadings.

Hydrodynamic characterisation was conducted through weighted-, number- and probability distributions of both the inter-packing liquid element-volume and surface area. The results presented more uniform droplet behaviour across the board when evaluating the Intalox® Ultra compared to the older FlexiRing® at negligible vapour loadings. This held true for both water and ethylene glycol, with air in the vapour phase. The Intalox® Ultra packings were subsequently found to produce smaller liquid elements between the packing pieces than the FlexiRing® equivalent. This is advantageous as the "narrower" distributions suggest less variance in vapour/liquid interactions and subsequently less variance in parameters such as liquid interfacial turbulence, shear force and pressure drop.

Variations in the vapour loadings produced two perceivable regimes within the inter-packing distributions, namely:

[1] Where increased vapour flow produces smaller distinct liquid elements.
[2] Where increased vapour flow produces larger liquid conglomerates.

The transitions between these distinct zones were recorded in the case of the air / water system:

- between 37 and 73 $m^3.m^{-2}.h^{-1}$ for the air / water system of 2" FlexiRing®;
- 73 $m^3.m^{-2}.h^{-1}$ for the 1.5" equivalent Intalox® Ultra(A) also air / water;
- Additionally, at 98 $m^3.m^{-2}.h^{-1}$ for the 2" FlexiRing® with ethylene glycol and air.

The size variations between the transitions and the liquid physical properties led the author to theorize that the transition was intricately related to the physical properties, shear forces acting on the liquid interface (velocities due to perceived voidage) and the liquid distributor. The transition thereby eluded to a change in the liquid hold-up mechanism, from film thickening (on the packing itself) towards IPL liquid redistribution.

For overall kinetic characterisation, the focus was shifted from the individual contributions towards the total surface area attributed to inter-packing elements. Via comparison, the Intalox® Ultra was found producing on average *ca* 17% and 9.4% more surface area within the packing voids (apparent or non-effective area) through droplets than the comparative FlexiRing® (2" and 1.5") using the air / water. A negligible variation was noted based on liquid properties, with the air / ethylene glycol system showing an average increase o*f ca* 18% between the Intalox® Ultra L and 2" FlexiRing®.

In conclusion, the produced body of work presented a novel approach for random packing characterisation based on the liquid elements between packing pieces. Using the presented EIT characterisation, both hydrodynamic and kinetic parameters were evaluated for a fraction of the cost and time. This system is likely best suited for prototyping, where various prospective designs are compared and evaluated.

Additional uses of the EIT characterisation include:

- Mounted atop the de-entrainer to consider the breakthrough point. While conventionally evaluated through visual observation, the aforementioned breakthrough-point evaluations present sizable experimental difficulties for low surface tension liquids
- Liquid distributor evaluations.
- Froth density evaluations across the whole active tray area.
- Continuous measurement of vapour entrainment in downcomers.

9.1 Novel Contributions

Several novel contributions are presented in this work. These are:

[1] The development of a characterisation methodology based on EIT for better understanding of IPL distributions.

[2] Novel experimental inter-packing distribution data for liquid IPL element-volumes and surface-areas and their relation to:

i. Packing type
ii. Liquid and vapour loadings
iii. Liquid physical properties

[3] Presenting the existence of a packing-specific transitional point, based on liquid and vapour loadings, where the mechanism of liquid hold-up changes. This point marks the cross-over between the conglomeration of IPL elements into streams, and their break-up/ redistribution into smaller elements. This alludes to a possible increase in interfacial turbulence (decreasing liquid phase resistance to mass transfer) while adding to the understanding of the pressure drop mechanisms in packed columns.

[4] Presenting the total IPL element-surface area as a comparative kinetic characterisation parameter for use in prototyping. This is poised to assist the design of future packing's, in finding the optimum ratio of apparent-to-inter-packing surface area to minimize entrainment and maximize efficiency.

9.2 Recommendation for Improvements to the EIT System:

The following recommendations are proposed to extend the functionality of the EIT sensor system:

[1] Installation of an additional staggered grid below the current installation to increase the measurement points to 5474.

[2] Use of a higher power (max wattage) signal generator to extend the capacitance applicability to smaller packing sizes.

[3] Developing an advanced temperature dependence model in LtSpice to simplify calibrations.

10. REFERENCES

[1] F. Zhu, R. Hoehn, V. Thakkar and E. Yuh, Hydroprocessing for Clean Energy: Design, Operation, and Optimization, John Wiley & Sons, 2017, pp. 250-254.

[2] S. Lamprecht, "Establishing a Facility to Measure Packed Column Hydrodynamics," Stellenbosch: MSc Dissertation: University Stellenbosch, 2010.

[3] I. Nieuwoudt, P. Quotson, J. Juarez and N. Yeh, "Improving the Performance of Towers with Random Packing," *Chemical Engineering Transactions,* vol. 69, 2018.

[4] N. Kolev, S. Nakov, L. Ljutzkanov and D. Kolev, "Effective area of a highly efficient random packing," *Chemical Engineering and Processing: Process Intensification,* vol. 45, no. 6, pp. 429-436, 2006.

[5] U. L. Minne, "Effect of liquid and gas physical properties on hydrodynamics of packed columns," Stellenbosch University, Stellenbosch, 2017.

[6] P. Marchot, D. Toye, A. Pelsser, M. Crine, Z. Olujic and G. L'Homme, "Liquid distribution images on structured packing by X-ray computed tomography," *AICHE,* vol. 47, no. 6, pp. 1471-1476, 2001.

[7] D. Toye, M. Crine and P. Marchot, "Imaging of liquid distribution in reactive distillation packings with a new high-energy x-ray tomograph," *Measurement Science and Technology,* vol. 16, p. 22136, 2005.

[8] M. Grünewald, G. Zheng and M. Kopatschek, "New Challenges for a well-known task," *Ingenieur Technik,* vol. 83, pp. 1026-1035, 2011.

[9] M. Grünewald, J. H. Brinkmann, M. Hapke and F. van Holt, "Improved and Innovative Methods for the Characterisation of Random and Structured Packings," *Chemical Engineering Transactions,* vol. 69, pp. 103-108, 2018.

[10] H. Wu, B. Buschle, Y. Yang, C. T. Tan, F. Dong and J. Jiabin, "Liquid distribution and hold-up measurement in counter current flow packed column by electrical capacitance tomography," *Chemical Engineering Journal,* vol. 353, pp. 519-532, 2018.

[11] A. Janzen, M. Schubert, F. Barthel, U. Hampel and E. Keniga, "Investigation of dynamic liquid distribution and hold-up in structured packings using ultrafast electron beam X-ray tomography," *Chemical Engineering and Processing: Process Intensification,* vol. 66, pp. 20-26, 2013.

[12] M. Hamood-Ur-Rehman, Y. Dahman and F. Ein-Mozaffari, "Investigation of mixing characteristics in a packed-bed external loop airlift bioreactor using tomography images," *Chemical Engineering Journal,* vol. 213, pp. 50-61, 2012.

[13] T. Eda, A. Sapkota, J. Haruta, M. Nishio and M. Takei, "Experimental study on liquid spread and maldistribution in the trickle bed reactor using electrical resistance tomography," *Journal of Power Engineering Systems,* vol. 7, pp. 94-105, 2013.

[14] M. da Silva, "Impedance Sensors for Fast Multiphase Flow Measurement and Imaging," Technischen Universität Dresden, Technischen Universität Dresden, 2008.

[15] L. Du Preez, J. Knoetze and L. Callanan, "Reactive Absorption Kinetics of CO2 in Alcoholic Solutions of MEA: Fundamental Knowledge for Determining Effective Interfacial Mass Transfer Area," Stellenbosch University South Africa, Stellenbosch, 2014.

[16] J. Rejl, V. Linek, T. Moucha and L. Valenz, "Methods standardization in the measurement of mass-transfer charactaristics in packed absorption columns," *Chemical Engineering research and Design,* vol. 87, pp. 695-704, 2009.

[17] J. Lamprecht, "The development of simplistic and cost-effective methods for the evaluation of tray and packed column efficiencies," Stellenbosch University MEng, 2017.

[18] P. Hofhuis and F. Zuiderweg, "Distillation," *Institute of chemical engineering Symposium 56,* vol. 2.1, no. 1, 1979.

[19] Henly, Seader and Roper, Seperation Process Principles, T. Edition, Ed., John Wiley and Son's Inc., 2011.

[20] A. Erasmus, "Doctoral Disseration: Mass transfer in structured packing," Stellenbosch University Department Chemical Engineering, Stellenbosch, 2004.

[21] T. Moucha, V. Linek and E. Prokopova, "Effect of Packing Geometrical Details: Influence of Free Tips on Volumetric Mass Transfer," *Transactions of the Institution of Chemical Engineers,* vol. 83, no. A, pp. 88-92, 2005.

[22] H. Z. Kister, Distillation Design, New Tork: McGraw Hill, 1992.

[23] M. Schultes, "Research on Mass Transfer Columns: Old Hat or Still Relevant," in *Presentation at D&A Conference*, Eindhoven, 2010.

[24] Z. Olujic´, A. Kamerbeek and J. d. Graauw, "A corrugation geometry-based model for efficiency of structured distillation packing," *Chemical Engineering and Processing: Process Intensification,* vol. 38, pp. 683-695, 1999.

[25] R. Tsai, "Mass Transfer Area of Structured Packing," The University of Texas at Austin, Texas at Austin , 2010.

[26] G. Wang, X. Yuan and K. Yu, "A method for calculating effective interfacial area of structured packed distillation columns under elevated pressures," *Chemical Engineering and Processing,* vol. 45, pp. 691-697, 2006.

[27] D. Van Krevelen and P. Hoftijer, "Kinetics of gas liquid reactions Part I- General theory," *Recueil: Journal of the Royal Netherlands Chemical Society,* vol. 67, pp. 563-586, 1947 a.

[28] D. Van Krevelen and P. Hoftijer, "Studies of gas absorbtion-I Liquid film resistance to gas in scrubbers," *Recueil: Journal of the Royal Netherlands Chemical Society,* vol. 47, pp. 49-66, 1947 b.

[29] R. Semmelbauer, "Die berechnung der Schutthohe bei Absorptionvorgangen in Fullkorperkolonnen," *Chemical Engineering Science,* vol. 22, pp. 1237-1255, 1967.

[30] K. Onda, E. Sada and Y. Murase, "Liquid-side mass transfer coefficients in packed towers," *American institute of chemcial engineers Journal,* vol. 5, no. 2, pp. 235-239, 1959.

[31] K. Onda, H. Takeuchi and Y. Koyama, "Effect of packing material on the wetted surface area," *Chemical Engineering journal of Japan,* vol. 31, pp. 126-134, 1967.

[32] K. Onda, H. Takeuchi and Y. Okumoto, "Mass transfer coefficients between gas and liquid phases in packed columns," *Chemcial Engineering Journal of Japan,* vol. 1, pp. 56-62, 1968.

[33] J. Bravo and J. R. Fair, "Generalized correlation for mass transfer in packed distillation columns," *Industrial Engineering Chemcial Process Design and Development,* vol. 21, pp. 162-170, 1982.

[34] J. Fair and J. Bravo, "Distillation columns containing structured packing," *Chemical Engineering Progress,* vol. January, pp. 19-29, 1990.

[35] N. Kolev, "Wirksame Austauschflache von Fullkoperschuttungen," *Verfahrenstechnik,* vol. 7, no. 3, pp. 71-75, 1973.

[36] N. Kolev, "Wirkungsweise von Fullprperschuttengen," *Chemcial Engineering Technology,* vol. 48, no. 12, pp. 1105-1112, 1976.

[37] J. Zech and A. Mersmann, "Liquid flow and liquid phase mass transfer in irrigated packed columns," *International Chemcial Engineerings Symposium Series,* vol. 56, pp. 39-47, 1979.

[38] R. Billet and M. Schultes, "Prediction of mass transfer columns with dumped and arranged Packings," *Transactions of the Institution of Chemical Engineers,* vol. 77, no. A, pp. 498-504, 1999.

[39] J. R. Fair and J. G. Stichlmair, Distillation: Principles and Practice, New York: Wiley-VCH, 1998.

[40] J. Mackowiak, "Pressure Drop in Irrigated Packed Columns," *Chemical Engineering Processing,* vol. 29, pp. 93-105, 1991.

[41] J. Mackowiak, "Extended channel model for prediction of the pressure drop in single-phase flow in packed columns," *Chemical Engineering Research and Design,* vol. 87, pp. 123-134, 2009.

[42] R. Billet and M. Schultes, "Prediction of mass transfer columns with dumped and aranged packing," *Institute of Chemical Engineers,* vol. 77, no. A, pp. 498-504, 1999.

[43] E. Sørensen, Absorption adn Distillation, IChemE, Technology and Engineering, 2006.

[44] spl H. Franken, "Establishement of a supercritical plant and the hydrodynamics of supercritical countercurrent columns," Stellenbosch University Master's Thesis, Stellenbosch, 2014.

[45] R. Billet and J. Mackowiak, "Flussigkeitsseitiger Stoffubergang bei der Absorption in Fullkorperkolonnen und ihr verfahrenstechnischer VErgeleich," *Chemie Technik,* vol. 6, no. 11, pp. 455-461, 1977.

[46] R. Stockfelth and G. Brunner, “Holdup, Pressure Drop, and Flooding in Packed Countercurrent Columns for the Gas Extraction,” *Industrial Engineering Chemical Research,* vol. 40, pp. 347-356, 2001.

[47] K. McNulty and C. Hsieh, “Hydraulic Performance and Efficiency of Koch Flexipac Structured Packings,” *AIChE Annual Meeting,* 1982.

[48] L. Spiegel and W. Meier, “Correlations of the performance charactaristics of the various mellapak types,” *International Chemical Engineering Symposium Series,* vol. 104, pp. 203-215, 1987.

[49] L. Robbins, “Improve Pressure-Drop Prediction with a New Correlation,” *Chemical Engineering Procceedings,* vol. 87, 1991.

[50] F. Heymes, P. Demouster, F. Charbit, J. Fanlo and P. Moulin, “Hydrodynamics and mass transfer in a packed column: Case of toluene absorption with a viscous absorbent,” *Chemical Engineering Science,* vol. 61, pp. 5094-5106, 2006.

[51] J. Rocha and J. Bravo, ““Distillation Columns Containing Structured Packings: A Comprehensive Model for Their Performance. 2. Mass-Transfer Model,” *Industrial Engineering Chemical Research,* vol. 36, p. 1660, 1996.

[52] R. Billet and M. Schultes, “Predicting Mass Transfer in Packed Columns,” *Chemical Engineering Technologt,* vol. 16, pp. 1-9, 1993.

[53] J. Maćkowiak, ““Extended channel model for prediction of pressure drop in single-phase flow in packed columns,” *Chemical Engineering Research and Design,* vol. 87, pp. 123-134, 2009.

[54] J. Maćkowiak, “Determination of Flooding Gas Velocity and Liquid Hold-up at Flooding in Packed Columns for Gas/Liquid Systems”,” *Chem. Eng. Technol,* vol. 13, no. 1, pp. 184-196, 1990.

[55] J. Mackowiak, Fluid Dynamics of Packed Columns: Principles of the Fluid Dynamic Design of Columns for Gas/Liquid and Liquid/Liquid Systems, C. Hall, Ed., Springer Science & Business Media, 2009.

[56] J. Mackowiak, “Determination of Flooding Gas Velocity and Liquid Hold-up at Flooding in Packed Columns for Gas/Liquid Systems,” *Chemical Engineering Technology,* vol. 13, pp. 184-196, 1990.

[57] B. Azzopardi, 2006, New York: Begell House., Gas-liquid Flows.

[58] A. Cartellier and J. Achard, "Local phase detection probes in fluid/fluid twophase flows," *Review of Scientific Instruments,* vol. 62, pp. 279-303, 1990.

[59] O. Jones and J. Delhaye, "Transient and statistical measurement techniques for two-phase flows.," *International Journal of Multiphase Flow,* vol. 3, pp. 89-119, 1976.

[60] M. K. Islam, T. D. Purdie, N. D. Bernard, A. Harmideh, J. Siewerdsen and D. Jaffray, "Patient dose from kilovoltage cone beam computed tomography imaging in radiation therapy," *Medical Physics,* vol. 33, no. 6, pp. 1573-1582, 2006.

[61] Z. Wang, A. Afacan, K. Nandakuma and K. Chuang, "Porosity distribution in random packed columns by gamma ray densitometry," *Chemical Engineering and Processing,* vol. 40, pp. 209-219, 2001.

[62] F. Yin, A. Afacan, K. Nandakumar and K. Chuang, "Liquid Holdup Distribution in Packed Columns: Gamma Ray Tomography and CFD Simulation," *CEP,* vol. 41, pp. 473-483, 2002.

[63] M. Schubert, A. Bieberle, F. Barthel, S. Boden and U. Hampel, "Advanced Tomographic Techniques for Flow Imaging in Columns with Flow Distribution Packings," *Chemie Ingenieur Technik,* vol. 83, no. 7, pp. 979-995, 2011.

[64] J. Nilsson and S. Riedel, Electric Circuits, 10th ed., Pearson, 2014.

[65] T. R. Kuphaldt, Lessons in Electronic CircuitsL AC, Design Science, 2007.

[66] E. Hubert and C. Wolkersdorfer, "Establishing a conversion factor between electrical conductivity and total dissolved solids in South African mine waters," *Water SA,* vol. 41, no. 4, pp. 490-500, 2015.

[67] S. Gelhaus and W. LaCourse, "Measurement of Electrolytic Conductance," in *Ewing's Analytical Instrumentation Handbook*, Boca Raton, CRC Press, 2004, pp. 561-580.

[68] Engineering Institute of technology, "Different types of capacitors," [Online]. Available: https://www.eit.edu.au/resources/different-types-of-capacitors/. [Accessed 05 03 2021].

[69] P. Evans, "The engineering mindset," 27 10 2019. [Online]. Available: https://theengineeringmindset.com/inductors-explained/. [Accessed 02 02 2021].

[70] D. W. Green and R. H. Perry, Perry's Chemical Engineers Handbook, 8th Edition ed., McGraw Hill, 2007.

[71] D. Lide, CRC Handbook of Chemistry and Physics, 85th ed., Boca Raton, Florida: CRC Press, 2005, pp. 6-155 - 6-177..

[72] S. Mohadeseh and Y. Brent, "Electrical Resistance Tomography (ERT) applications to Chemical Engineering," *Chemical Engineering Research and Design,* vol. 91, pp. 1625-1645, 2013.

[73] S. Huang, A. Plaskowski, C. Xie and M. Beck, "Tomographic imaging of two-component flow using capacitance sensors," *Journal of Physics E: Scientific Instruments,* vol. 22, pp. 173-177, 1989.

[74] W. Yang and T. York, "New ac-based capacitance tomography system," *IEEE Proceedings - Science, Measurement and Technology,* vol. 146, pp. 47-53, 1999.

[75] T. Dyakowski, J. Hale, A. Jaworski, N. White, A. Nowakowski, G. Meng, and S. Rwifa, "Dual-modality probe for Characterisation of heterogeneous mixtures," *IEEE Sensors Journal,* vol. 5, pp. 134-138, 2005.

[76] B. Hoyle, X. Jia, F. Podd, H. Schlaberg, H. Tan, M. Wang, R. West, R. Williams, and T. York, "Design and application of a multi-modality process tomography system.," *Measurement Science and Technology,* vol. 12, pp. 1157-1165, 2001.

[77] H. Tapp, A. Peyton, E. Kemsley and R. Wilson, "Chemical engineering applications of electrical process tomography," *Sensors and Actuators,* vol. 92, pp. 17-24, 2003.

[78] S. Mohadeseh and Y. Brent, "3-Dimensional spatial monitoring of tanks for the milk processing industry using electrical resistance tomography," *Journal of Food Engineering,* vol. 105, pp. 312-319, 2011.

[79] M. J. da Silva,. E. N. dos Santos and P. Tiago, "High - speed multichannel impedance measuring system," *ACTA IMEKO,* vol. 1, no. 1, pp. 36-41, 2012.

[80] A. Muzen and M. C. Cassanello, "Liquid holdup in columns packed with structured packings Countercurrent vs. cocurrent operation," *Chemical Engineering Scienc,* vol. 60, pp. 6226-6234, 2005.

[81] Y. Li and M. Soleimani, "Imaging conductive materials with high frequency electrical capacitance tomography," *Measurement,* vol. 46, pp. 3355-3361, 2013.

[82] L. Peng, J. Ye, G. Lu and W. Yang, "Evaluation of effect of number of electrodes in ECT sensors on image quality," *IEEE Sensor Journal,* vol. 12, pp. 1554-1565, 2012.

[83] T. R. Kuphaldt, Lessons in Electronic Circuits: DC, Design Science, 2006.

[84] T. R. Kuphaldt, Lessons in Electronic Circuits: Semiconductors, Design Science, 2009.

[85] J. S. Ling, W. Moebs and J. Sanny, University Physics Volume, Pressbooks, 2019.

[86] H. M. Prasser, A. Böttger and J. Zschau, "A new electrode-mesh tomograph for gas-liquid flows," *Flow Measurement and Instrumentation,* vol. 9, pp. 111-119, 1998.

[87] M. I. Montrose, EMC and the Printed Circuit Board: Design, Theory, and Layout Made Simple, Wiley-IEEE Press, 2004.

[88] "Eagle Documentation," Autodesk, [Online]. Available: http://eagle.autodesk.com/eagle/documentation. [Accessed 01 05 2021].

[89] E. Uys, S. Lamprecht, C. Schwarz, A. Burger, I. Nieuwoudt, A. Erasmus and J. Knoetze, "Establishing a facility for the hydrodynamic characterisation of distillation column internals," Stellenbosch University, Stellenbosch, 2010.

[90] W. Wangjiraniran, Y. Motegi, S. Richter, H. Kikura, M. Aritomi and K. Yamamoto, "Intrusive effect of wire mesh tomography on gas–liquid flow measurement.," *Journal of Nuclear Science and Technology,* vol. 40, pp. 932-940., 2003.

[91] H. Prasser, D. Scholz and C. Zippe, "Bubble size measurement using wire-mesh sensors," *low Measurement and Instrumentation,* vol. 12, pp. 299-312, 2001.

[92] A. Hoffmann, J. Mackowiak, A. Gorak, M. Haas, J. Loning, T. Runowski and K. Hallenberger, "Standardization of mass transfer measurements: A basis for description of Absorption Processes," *Chemical Engineering Research and Design,* vol. 85, no. A1, pp. 40-49, 2007.

[93] A. A. Ibrahim, "Experimental Study of Liquid Distribution in Packed Column," *Journal of King Saud University - Engineering Sciences,* vol. 10, no. 2, pp. 271-283, 1998.

[94] TCI, "Ningbo TCI Environmental Protection Co. Ttd," TCI, [Online]. Available: http://www.rubbersealing.com/TCI/images/upload/File/Metal%20Intalox%20Saddle%20Ring.pdf. [Accessed 24 05 2021].

[95] ChinaJinti, "Metal Saddle Ring Product No: (JT-MSR)," Jinti, [Online]. Available: http://www.ceramic-honeycombs.com/metal/Metal_Intalox_Saddle_Ring_Tower_Packing.htm. [Accessed 24 05 2021].

[96] H. Z. Kister and J. R. Haas, "Entrainment from Sieve Trays in the Froth Regime," *Industrial and Engineering Chemistry Research,* vol. 27, no. 12, pp. 2331-2341, 1988.

[97] H. Z. Kister, W. V. Plnctewsk and J. F. Chrlstopher, "Entrainment from Sieve Trays Operating in the Spray Regime," *Industrial & Engineering Chemistry Process Design and Development,* vol. 20, no. 3, pp. 528-532, 1981.

[98] A. Koziol and J. Mackowiak, "Liquid entrainment in tray columns with downcomers," *Chemical Engineering Process,* vol. 27, pp. 145-153, 1990.

[99] E. Cussler, Diffusion Mass tranfer in fluid systems, Cambridge: University of Cambridge Press, 1984.

[100] T. K. Sherwood, R. L. Pigford and C. R. Wilke, Chemical Engineering Series: Mass Transfer, New York: Mcgraw Hill, 1975.

[101] M. J. Lockett, Distillation Tray Fundementals, Cambridge University Press, 1986.

[102] K. J. Arwikar and O. C. Sandall, "Liquid phase mass tranfer resistance in a small-scale packed distillation column," *Chemical Engineering Science,* vol. 35, no. 11, pp. 2337-2343, 1980.

[103] W. Bereiter, "Druckverlust und Flussigkeitsseitiger Stoffaustausch in Sulzer Gewebpackungen," ETH Zurich, Zurich, 1975.

[104] R. Billet, "Fluiddynamisches Verhalten und Wirksamkeit von Gengenstromapparaten fur Gas-Flussig Systemen bei flussigkeitsseitigem Stoffubergangswiderstand," Ruhr-Universitat Bochum, Bochum, 1983.

[105] R. Billet and J. Mackowiak, "Neuatige Fullkorper aus Kunststoffen fur thermische Stofftrennverfahren," *Chemie Technik,* vol. 9, no. 5, pp. 219-226, 1980.

[106] K. Bornhutter and A. Mersmann, “Stoffubergang mit modernen Fullkorpern grosser Abmessungen,” *Chemcial Engineering Technology,* vol. 63, no. 2, pp. 132-133, 1991.

[107] T. H. Chilton and A. P. Colburn, “Distillation and Absrotption in packed columns - A conenient design and correlation method,” *Industrial Engineering Chemistry,* vol. 37, no. 3, pp. 255-260, 1935.

[108] C. M. Cooper, R. J. Christl and L. C. Peery, “Packed tower performance at high liquid rates,” *Transactions of the American Institute for chemcial Engineers,* vol. 37, pp. 979-996, 1941.

[109] R. Coughlin, “Effect of Liquid-Packing surface interactions on gas absorption anf flooding in a packed column,” *American Institute of Chemcial Engineers,* vol. 15, no. 5, pp. 654-659, 1969.

[110] P. Danckwerts and A. Guillham, “The design of gas absorbers I-Method for predicting rates of absorption with chemical reaction in packed columns, and tests with 1 1/2 in raschig rings,” *Transactions of the institute of chemcial engineers,* vol. 44, pp. 42-54, 1966.

[111] P. Danckwerts and S. Rizvi, “The design of absorbers. Part II : Effective interfacial areas for several types of packing,” *Transaction of the Institute of Chemical Engineers,* vol. 44, pp. 124-127, 1971.

[112] P. Deckwarts and M. Sharma, “The absorption of carbon dioxide in solutions of alkalis amines (with some notes on the hydrogen sulphide and carbonyl sulphide),” *The Chemcial Engineers,* vol. 44, pp. 244-280, 1966.

[113] M. Delaloye, U. Von Stockar and X. Lu, “The inflaunce of the viscosity on the liquid-phase mass transfer resistance in packed columns,” *The Chemcial Engineering Journal,* vol. 47, pp. 51-61, 1991.

[114] S. W. Dharwadkar and S. B. Sawant, “Mass transfer and hydrodynamic characteristics of tower packings larger than 0.025m nominal size,” *The Chemical Engineering Journal,* vol. 31, pp. 15-21, 1985.

[115] J. Echarte, H. Campana and E. Brignole, “Effective areas and liquid film mass transfer coefficients in packed columns,” *Industrial Engineering chemical Process Design and Development,* vol. 23, no. 2, pp. 349-354, 1984.

[116] R. Higbie, “The rate of absorption of a pure gas into a still lqiuid during short periods of exposure,” *Transactions of the American Institute of Chemical Engineers,* vol. 31, pp. 365-389, 1935.

[117] E. Knoedler and C. Bonilla, “Vacuum degasification in a packed column,” *Chemcial Engineering Progress,* vol. 50, no. 3, pp. 125-133, 1954.

[118] H. Koch, L. Stutman, H. Blum and L. Hutchings, “Gas absorption: Liquid transfer coefficients for the carbon dioxide air-water system,” *Chemcial Engineering Progress,* vol. 45, no. 11, pp. 677-682, 1949.

[119] P. Krotzsch, “Measurements of liquid-phase mass transfer in packed columns,” *German Chemcial Engineering,* vol. 5, pp. 131-139, 1982.

[120] V. Linek, P. Petricek, P. Benes and P. Braun, “Effective interfacial area and liquid side mass transfer coeffieints in absorbtion columns packed with hydrophilised and untreated plastic packings,” *Chemical Engineering Research and Design,* vol. 62, no. 1, pp. 13-21, 1984.

[121] R. Mangers and A. Ponter, “Effect of viscosity on liquid film resistance to mass transfer in a packed column,” *Indsutrial Engineering Chemical Process Design and Development,* vol. 19, no. 4, pp. 530-537, 1980.

[122] J. Merchuk, “Mass transfer charcteristics of a column with small plastic rings,” *Chemcial ENgineering Science,* vol. 35, pp. 743-745, 1980.

[123] D. Mohunta, A. Vaidyanathan and G. Laddha, “Effective interfacial areas in packed columns,” *Indian Chemcial Engineer,* no. April, pp. 39-42, 1969 a).

[124] D. Mohunta, A. Vaidyanathan and G. Laddha, “Prediction of liquid phase mass transfer coefficients in columns packed with raschig rings,” *Indian Chemcial Engineers,* no. July, pp. 73-79, 1969 b).

[125] W. Norman, Absorption , Distillation and Cooling towers, New York: John Wiley and Son's, 1961.

[126] F. Rixon, “The absorption of carbon dioxide in and the desorption from water using packed towers,” *Transaction of the institute for Chemcial Engineering,* vol. 26, pp. 119-130, 1948.

[127] B. Sahay and M. Sharma, “Effective interfacial area and liquid and gas side mass transfer coefficients in a packed column,” *Chemcial Engineering Science,* vol. 28, pp. 41-47, 1973.

[128] T. Sherwood and F. Holloway, “Performance of packed tower-Liquid film data for several packings,” *Transaction of the American Institute of Chemcial Engineering,* vol. 36, pp. 181-182, 1940.

[129] J. Vivan, P. Brain and V. Krukonis, “Gas absorbtion in packed columns: liquid phase resistance in loading region,” *American Institute of Chemical Engineering,* vol. 13, no. 1, pp. 174-175, 1967.

[130] J. Vivian and C. King, “The mechanism of liqioud -phase resistance to gas absorbtion in packed columns,” *American Institute for Chemical Engineering,* vol. 10, no. 2, pp. 221-227, 1964.

[131] F. Yoshida and T. Koyanagi, “Liquid phase mass transfer rates and effective interfacial area in packed absorption columns,” *Industrial Engineering Chemistry,* vol. 50, no. 3, pp. 365-374, 1958.

[132] M. H. De Brito, “Gas absorption experiments in a pliot plant column with the sulzer structured packing Mellapak,” Lausanne EPFL: PHD Thesis, Lausanne, 1992.

[133] M. Lockett, Distillation tray Fundementals, New York: Cambridge University Press, 1986.

[134] V. Linek, J. Sinkule and V. Janda, “Design of Packed Aeration Towers to strip Volitile Organic Contaminants from water,” *Water Research,* vol. 32, no. 4, pp. 1264-1270, 1998.

[135] C. Wang, M. Perry, G. T. Rochelle and A. F. Seibert, “Packing Characterisation: Mass Transfer Properties,” *Energy Procedia,* vol. 12, pp. 23-32, 2012.

[136] F. Zuiderweg, “Sieve Trays: A view on state of teh art,” *Chemical Engineering Science,* vol. 37, no. 10, pp. 1441-1464, 1982.

[137] K. Krummrich, *Quoted in Chemcial Week,* no. 24, p. 18, 1984.

[138] A. Underwood, “Fractional Distillation of Multicomponent Mixtures,” *Chemical Engineering Progress,* vol. 4, p. 603, 1948.

[139] A. Underwood, “Fractional Distillation of Multicom-ponent Mixtures: Calculation of Minimum Reflux Ratio,” *Journal of the Institute of Petroleum,* vol. 32, p. 614, 1946.

[140] E. Gilliland, “Multicomponent Rectification Estimation of the Number of Theoretical Plates as a Function of the Reflux Ratio,” *Industrial Engineering Chemistry,* vol. 32, pp. 1220-1223, 1940.

[141] M. Fenske, “Fractionation of Straight-run Pennsylvania Gasoline,” *Industrial Engineering Chemistry,* vol. 32, no. 5, pp. 482-485, 1932.

[142] C. Kavanaugh and R. Trussell, “Design of aeration towers to strip volatile contaminants from drinking water,” *Journal of the American Water Works Association,* no. 72, pp. 684-692, 1980.

[143] D. L. Jones, “PCB Design tutorial,” 2004.

[144] Boegger, “Metal Intalox Saddle - an Acr-Shape Random Packing,” Boegger, [Online]. Available: https://www.tower-packing.org/products/towerpacking/randompacking/metal-intalox-saddle.html. [Accessed 24 05 2021].

[145] D. Toye, P. Marchot, M. Crine, A. Pelsser and G. L’Homme, “Local measurements of void fraction and liquid holdup in packed columns using X-ray computed tomography,” *Chemical Engineering and Processing,* vol. 37, p. 511–520, 1998.

11. APPENDIX A: PACKED COLUMN

11.1 EXPERIMENTAL SETUP ACCURACIES

Table 11.1 : Packed column measurement accuracies based on Minne [5]

Parameter	Measurement Range	Max Error	Units
Gas mass flowrate	293 – 3292	182	$kg.h^{-1}$
Vapour flow factor	0.51 – 6.11	0.32	$(m.s^{-1}).(kg.m^{-3})$
Low liquid volumetric flow rate	0 – 2	0.018	$m^3.h^{-1}$
High liquid volumetric flow rate	4.38 – 14.90	0.43	$m^3.h^{-1}$
Bed Pressure drop	5 – 2266	11	$Pa.m^{-1}$
Liquid hold-up	0.0094 – 0.3254	0.0083	$m^3.m^{-3}$
Entrainment rate	0 – 52	1.76	feed %

11.2 EXPERIMENTAL PROCEDURE

This report considered a simplified experimental procedure to that of Minne [5] , owed to the absence of drop-out liquid hold-up and entrainment measurements. The specific start-up procedures of the blower and pump are available in Minne [5]. Future users are advised to consult this document for a rigorous operating manual of the basic valve combinations etc.

11.2.1 LIQUID LOADINGS

Demineralized water was obtained from the department utilities. Initial density, viscosity, conductivity and surface tension measurements were taken after each loading. Additional conductivity measurements were taken daily to assume minimized variance between runs after loading. The loaded water was discarded after set of packing.

The ethylene glycol used in this study was used previously by Minne [5]. To prevent contamination, the complete liquid body was filtered with a 200-micron filter both before loading and unloading. Liquid physical properties were taken before each loading after at least an hour of mixing through the column.

11.2.2 PACKING LOADINGS

Prior to use, the packing was cleaned with an 85% isopropanol mixture. The aforementioned mixture was pumped through the system for 90 minutes at 5 $m^3.h^{-1}$ (est.). Upon completion, the column was air dried for 24hours and the vapour vented to the atmosphere.

11.2.3 EIT CALIBRATIONS

Upon completion of the liquid loading phase, the system was heated to and allowed to equilibrate to 25°C. Samples were taken from the sump and used to generate the calibration curves. The temperature of the samples was recorded as well as the conductivity of the demineralized water.

11.2.4 START-UP

- The liquid body was heated to 25°C, through liquid recirculation between the heat exchanger and sump.
- Continuity tests were conducted daily on each line to ensure that there were no shorts between the electrodes and that the connections were stable
- The signal generator was set to either 20kHz or 10MHz, depending on whether capacitance or conductivity was evaluated. All capacitance measurements were taken at an input voltage of 1.9V, while the conductivity input voltage was based on the conductivity within the sump.
- Baseline capacitance (empty column) measurements were taken prior to each days runs. To evaluate the effective "Zero" of air.
- After the air baseline was established, the liquid was allowed to recirculate through the column. The liquid loading of $4.4 m^3.h^{-1}$ was used to wet the packing and establish temperature equilibrium at 25°C. This step was repeated between each run at $6 m^3.m^{-2}.h^{-1}$ to ensure complete wetting of the packing.

11.2.5 EXPERIMENTAL

- Liquid and vapour loadings were set to the required set-points and allowed 20 minute to equilibrate.
- After 20 minutes, steady state was checked through temperature and pressure stability. If the stability was deemed insufficient, increments of 10 minutes were added.
- After sufficient stability, the EIT sensor was allowed 120s of measurement while the inlet, outlet temperatures and pressures were logged. Additional data included pressure drop and liquid and vapour loadings.

12. APPENDIX B: ELECTRONICS

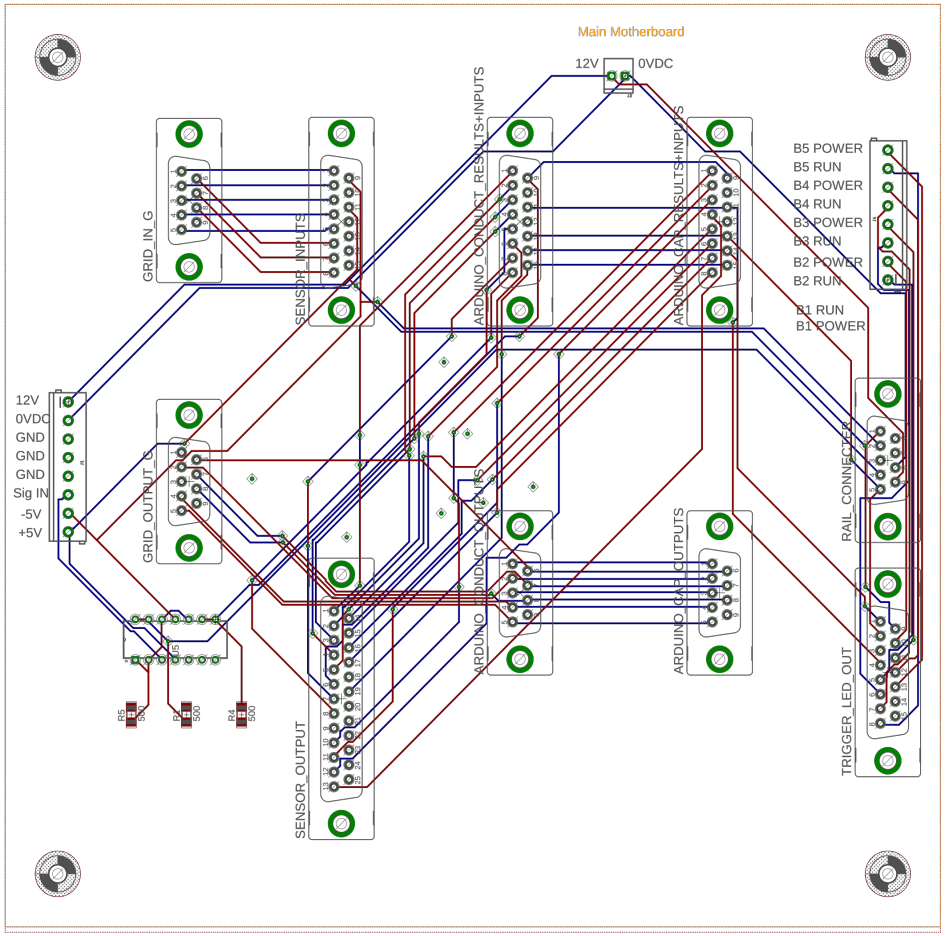

Figure 12.1 : Main motherboard PCB

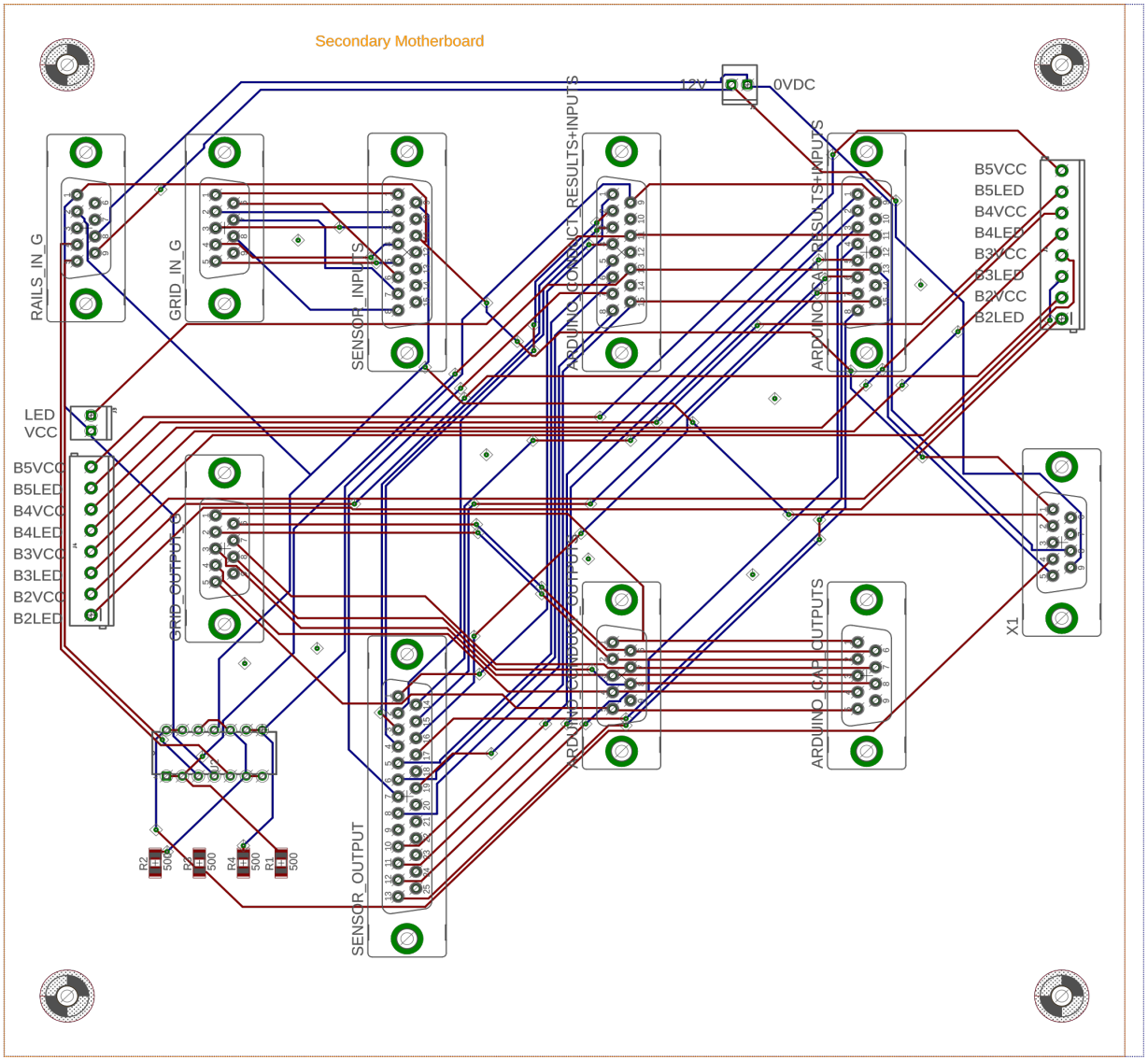

Figure 12.2: Slave motherboard PCB

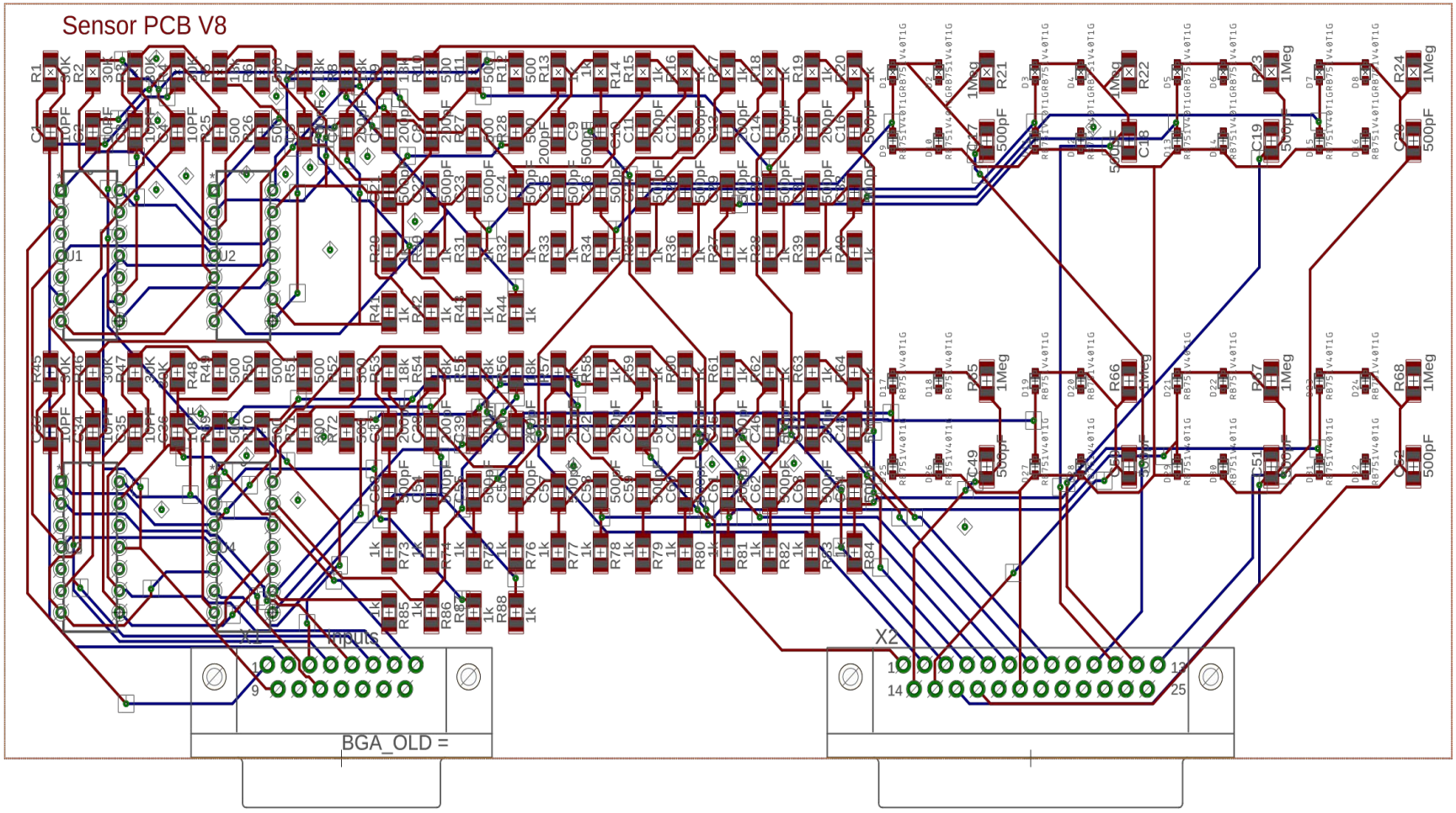

Figure 12.3: Auto-balancing bridge PCB

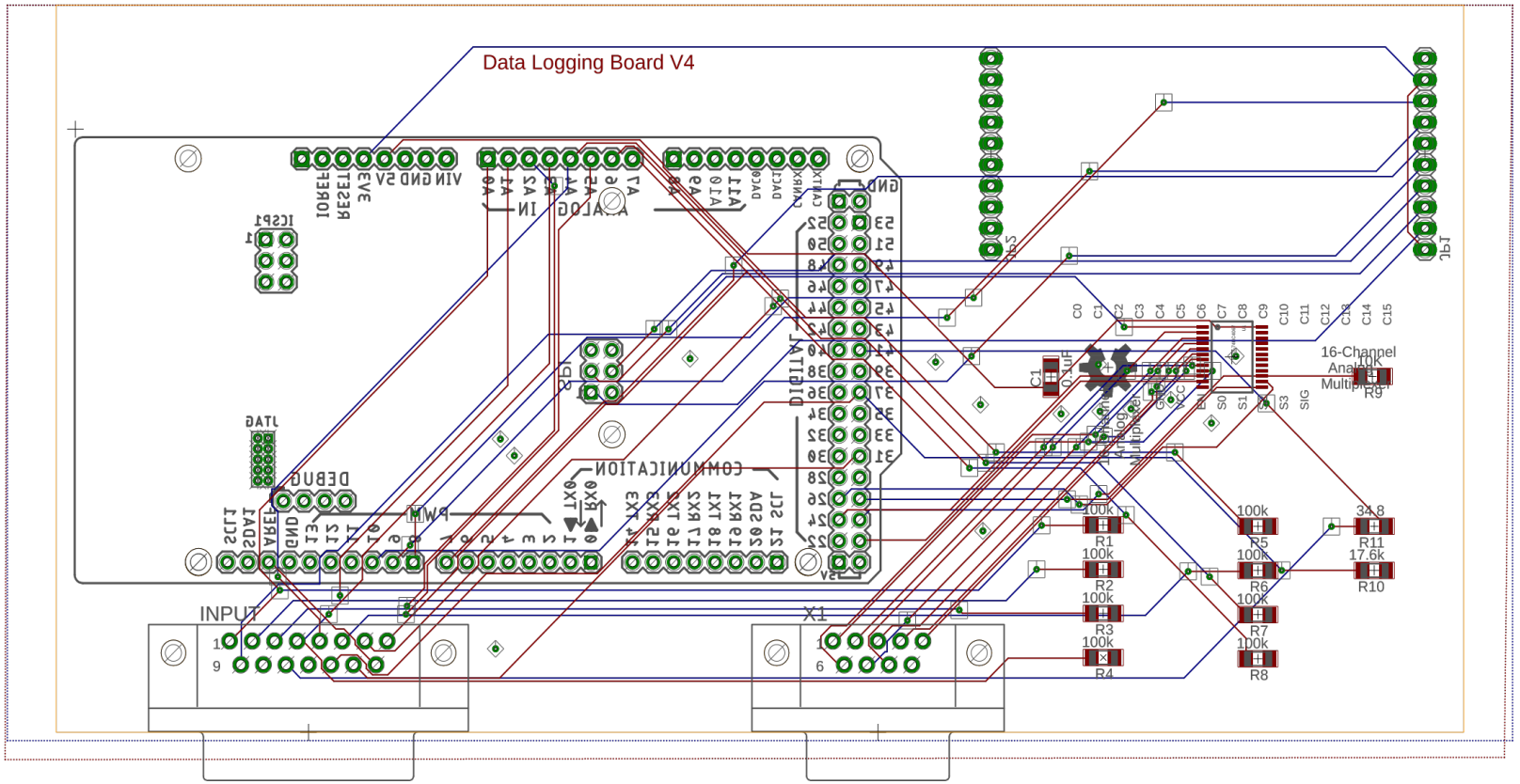

Figure 12.4: Arduino PCB

12.1 PCB TESTING

12.1.1.1DE-MUX

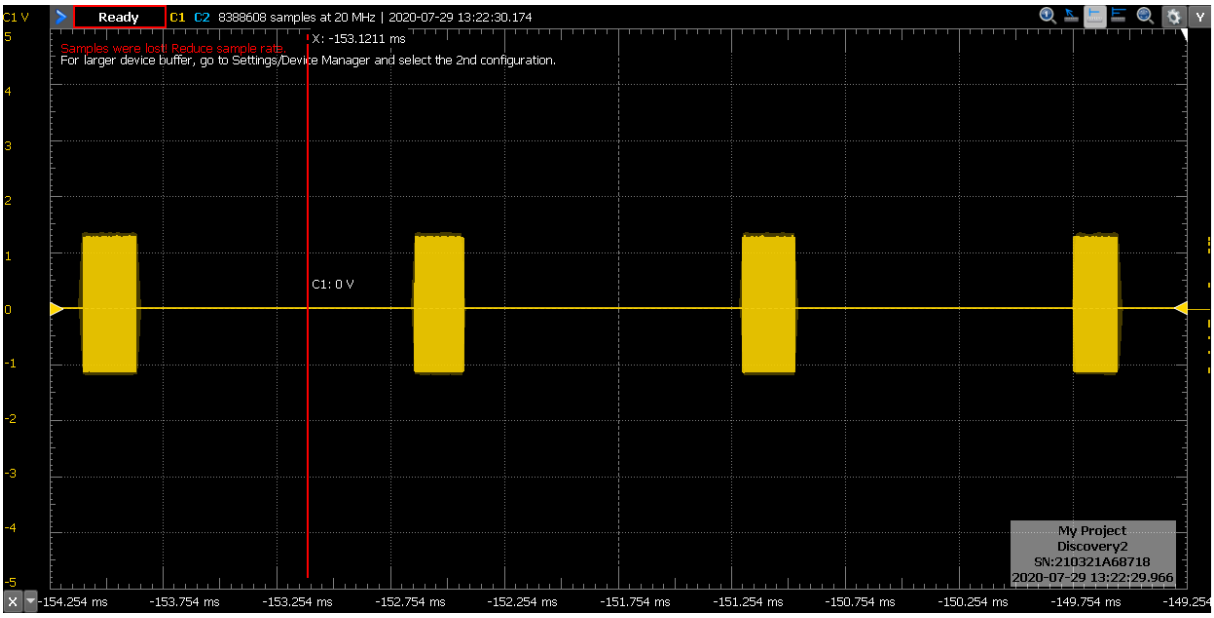

Figure 12.5: De-mux timing

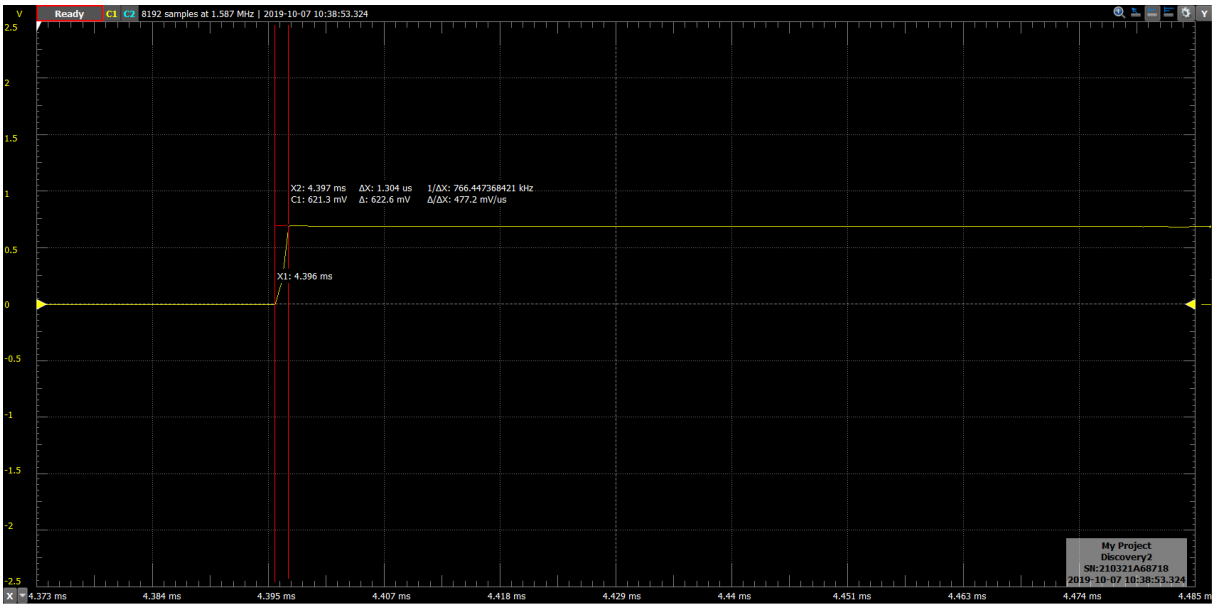

Figure 12.6: Mux- switching time

12.1.1.2 CAPACITOR LOADING TIMES DUE TO SAMPLE AND HOLD CIRCUITRY

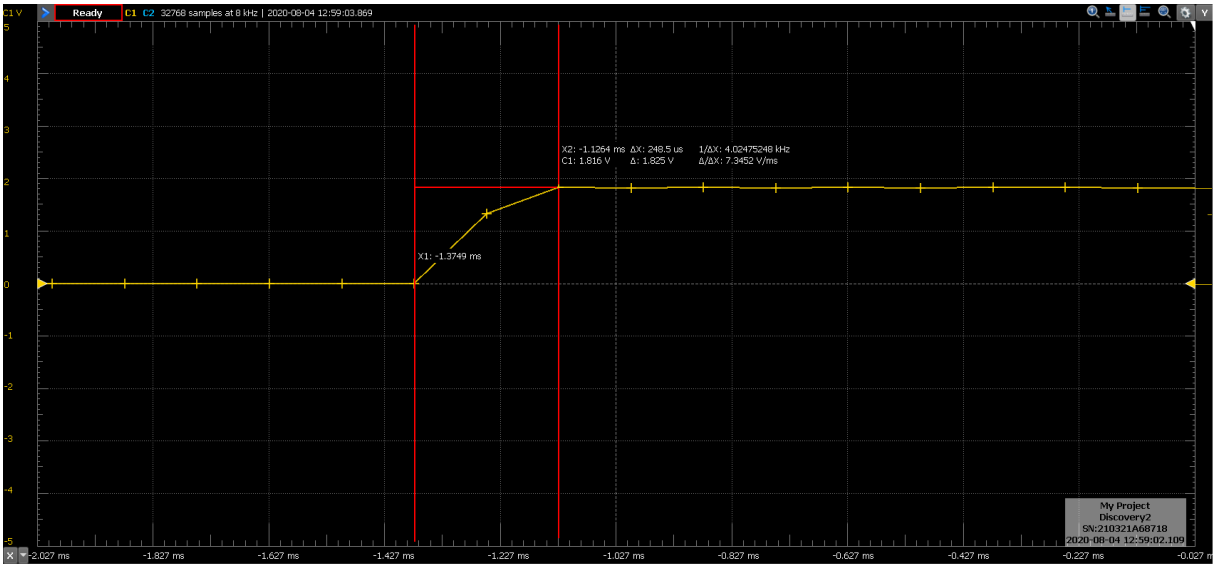

Figure 12.7: Response time of capacitance circuitry

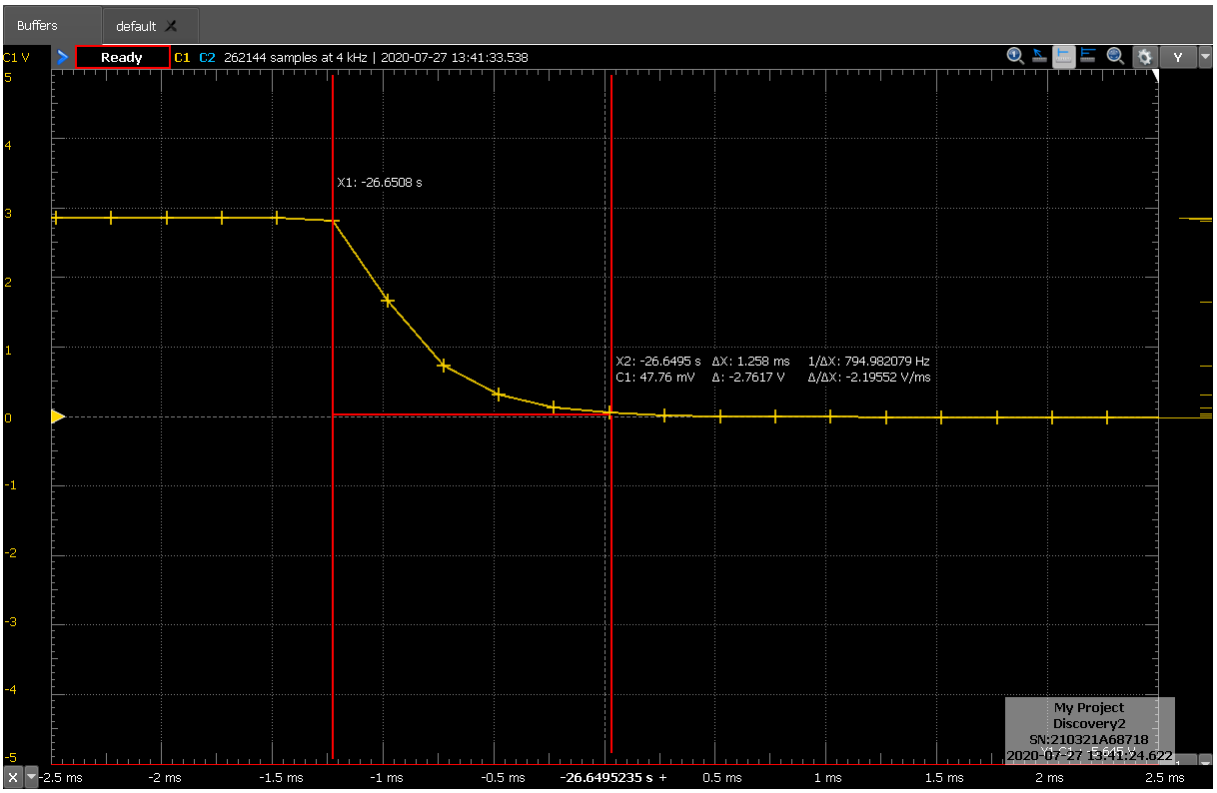

Figure 12.8: De-loading time of capacitance circuitry

12.2 CIRCUIT LINEARITY

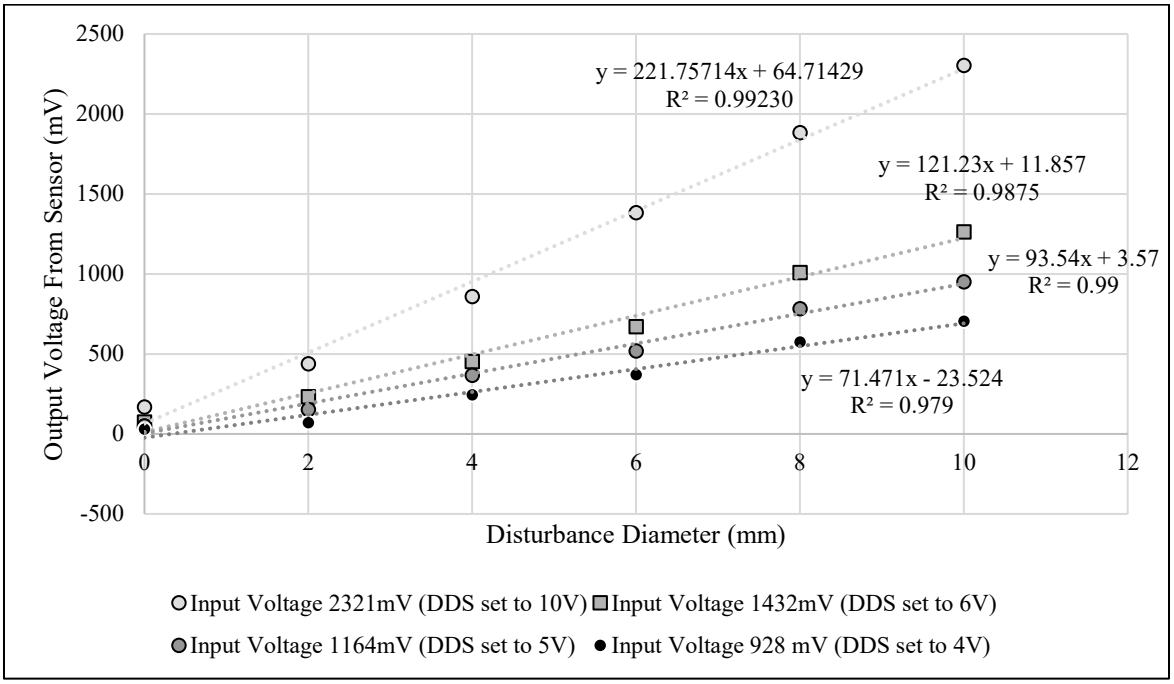

Figure 12.9: Capacitance linear voltage response to input voltage.

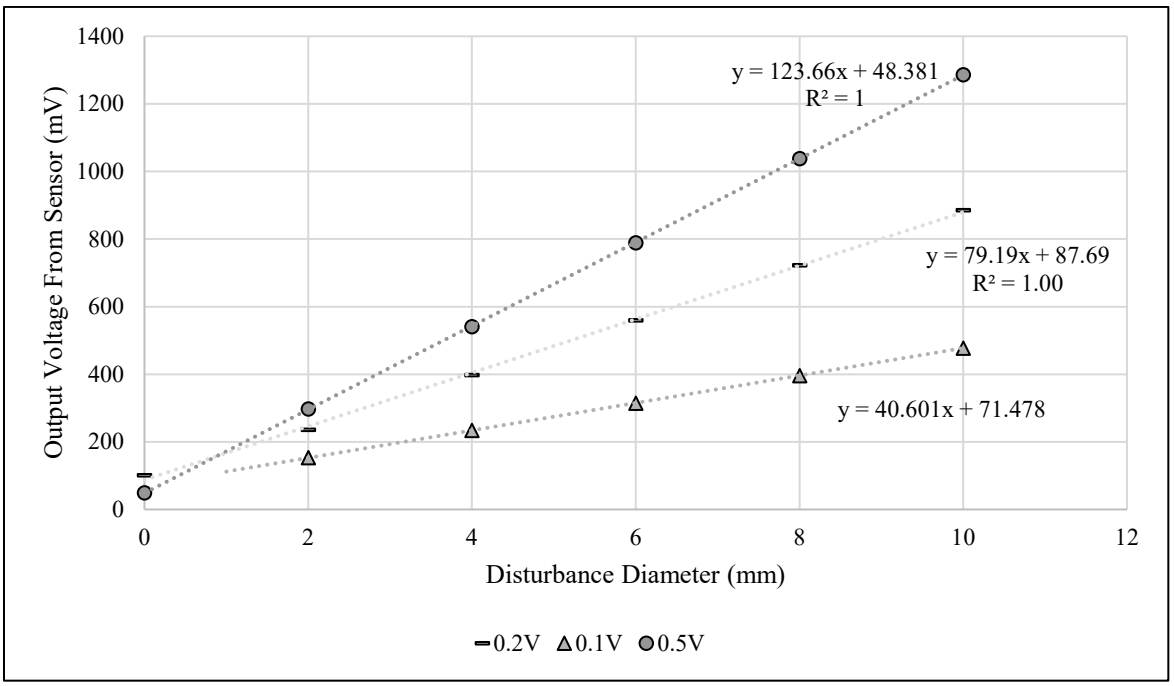

Figure 12.10: Conductivity linear voltage response to varying input voltage .

12.3 GRID TESTING

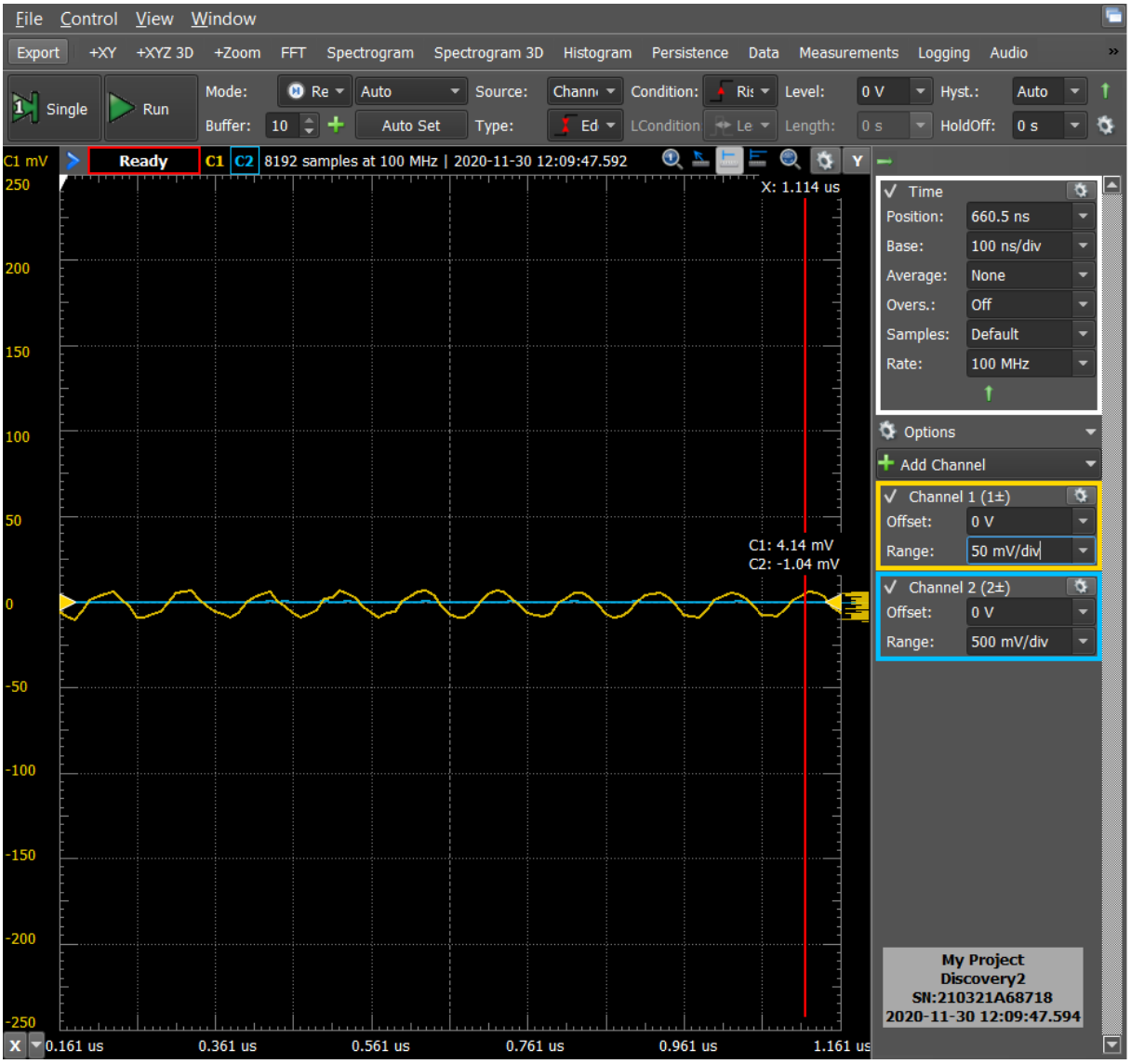

Figure 12.11: Grid harmonics without excitation signal. F_v **= 1.8 and L=98m^{3}m^{-2}h^{-1}.**

12.4 WIRE-MESH EXPLANATION

The wire-mesh methodology is widely used in electrical engineering, most notably in the capacitive touch screens found in modern smartphones. In essence:

- Horizontal electrodes are activated one at a time and cycled from top to bottom, in the attached figure from 1 to 7.
- The vertical electrodes are constantly measured along with the number (1-7) of the active electrodes.
- This method produces the cartesian vector coordinates of the disturbance. In the examined case, the red droplet.

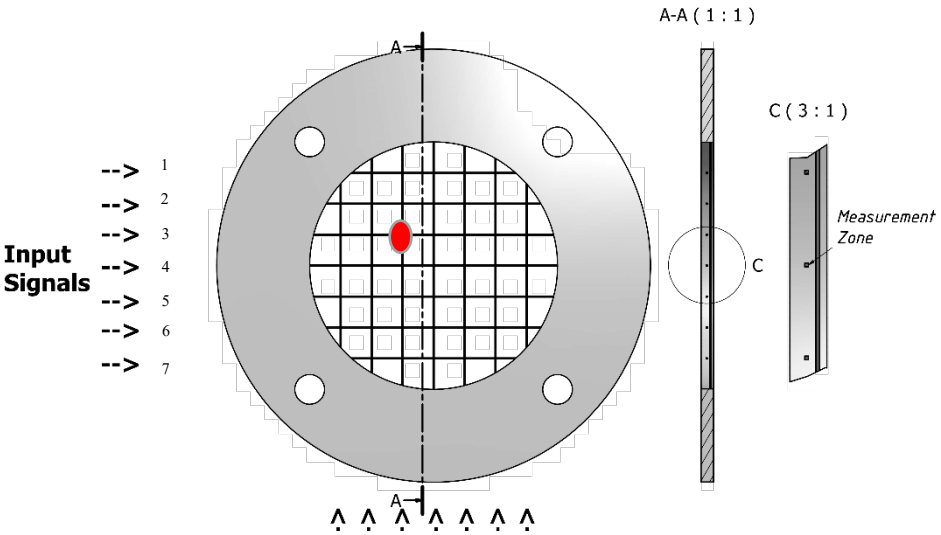

Figure 12.12: Wire-mesh grid

12.5 POWER DELIVERY PROBLEMS

Conventional electronic circuitry, and specifically signal generators operate on a current limiting principal. These systems are consequently bound by equations 13.1 and 13.2 where the current (I) is varied based on the parameters of impedance and voltage. The DDS used in this study was rated at 5W (P).

$$V = I.Z \tag{12.1}$$

$$P = V * I = 5 = V * I \tag{12.2}$$

Owing to the age and extended use of the ethylene glycol, conductivities rose to near 10µS/cm. The larger than expected resistance in parallel with the capacitance, consequently reduced the impedance (Z) and increased the expected the voltage to keep from burnout. This behaviour was recorded on the 1.5" packings as the experiments considered finer distributions (larger hold-up). The increased number of paralleled disturbances, consequently, exponentially decrease the impedance and therefore increase the current demand.

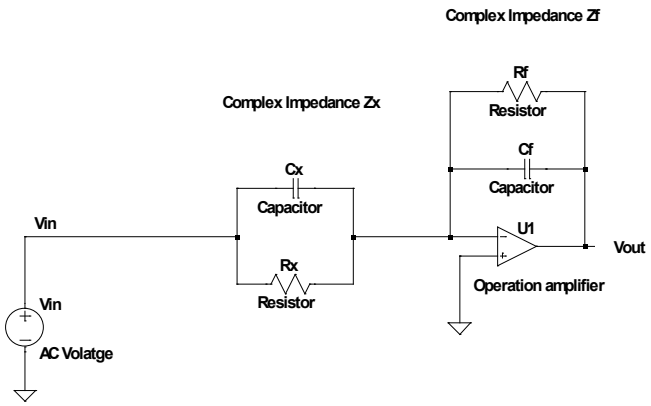

Figure 12.13: Impedance

The voltage dropping was experimentally evaluated as instability on the input signal on the $37 m^3 m^{-2} h^{-1}$ Intalox® Ultra size O runs. This led to author to disregard the 1.5" packing characterisation. Future evaluations consequently require a high-power signal generator. At the time of this study however, one could not be sourced.

The aforementioned reduction in resistance leading to increased current, is best exemplified in electrical heating elements. Larger power elements consequently use smaller resistances where 1.5kW and 3kW elements respectively have 32Ω and a 17 Ω resistances.

13. APPENDIX C: COMPUTATIONAL

13.1 MATLAB VERSION

MATLAB Version: 9.7.0.1319299 (R2019b) Update 5

MATLAB License Number: 40558920

Operating System: Microsoft Windows 10 Pro Version 10.0 (Build 19042)

Java Version: Java 1.8.0_202-b08 with Oracle Corporation Java HotSpot(TM) 64-Bit Server VM mixed mode

---

MATLAB	Version 9.7	(R2019b)
Simulink	Version 10.0	(R2019b)
Computer Vision Toolbox	Version 9.1	(R2019b)
Control System Toolbox	Version 10.7	(R2019b)
Curve Fitting Toolbox	Version 3.5.10	(R2019b)
DSP System Toolbox	Version 9.9	(R2019b)
Data Acquisition Toolbox	Version 4.0.1	(R2019b)
Database Toolbox	Version 9.2	(R2019b)
Deep Learning Toolbox	Version 13.0	(R2019b)
Fuzzy Logic Toolbox	Version 2.6	(R2019b)
GPU Coder	Version 1.4	(R2019b)
Global Optimization Toolbox	Version 4.2	(R2019b)
Image Acquisition Toolbox	Version 6.1	(R2019b)
Image Processing Toolbox	Version 11.0	(R2019b)
Instrument Control Toolbox	Version 4.1	(R2019b)
MATLAB Coder	Version 4.3	(R2019b)
Optimization Toolbox	Version 8.4	(R2019b)
Parallel Computing Toolbox	Version 7.1	(R2019b)
Partial Differential Equation Toolbox	Version 3.3	(R2019b)
Signal Processing Toolbox	Version 8.3	(R2019b)
Statistics and Machine Learning Toolbox	Version 11.6	(R2019b)
Symbolic Math Toolbox	Version 8.4	(R2019b)

13.2 COMPUTATIONAL REQUIREMENTS

Four separate i7 (windows 10) Pc's were used:

- 1 x i7 4770k
- 1 x i7 7700HQ
- 2 x i7 3770s

All Pc's were equipped with 16GB of Ram and each used 200GB of SSD space as cache or virtual memory. Each experimental run took between 4 and 10 hours to process.

14. APPENDIX D GRAPHICAL RESULTS

The proceeding section presents the distribution-based results collected using the EIT characterisation.

14.1 LIQUID HOLD-UP

14.1.1 AIR/WATER

14.1.1.12.5" INTALOX ULTRA™ (O)

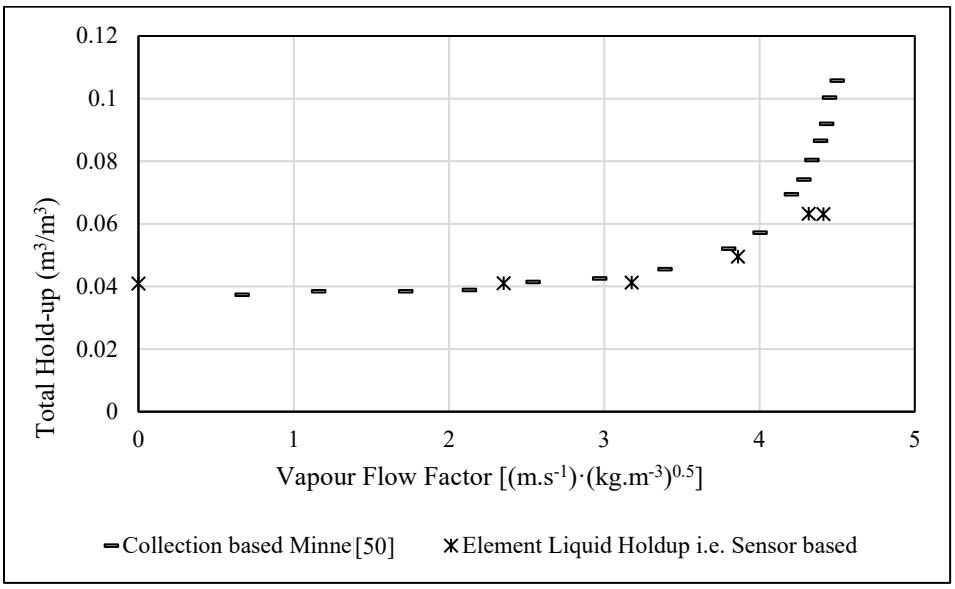

Figure 14.1: Intalox® Ultra size O liquid holdup vs element liquid holdup; water/air; 37 $m^3m^{-2}h^{-1}$.

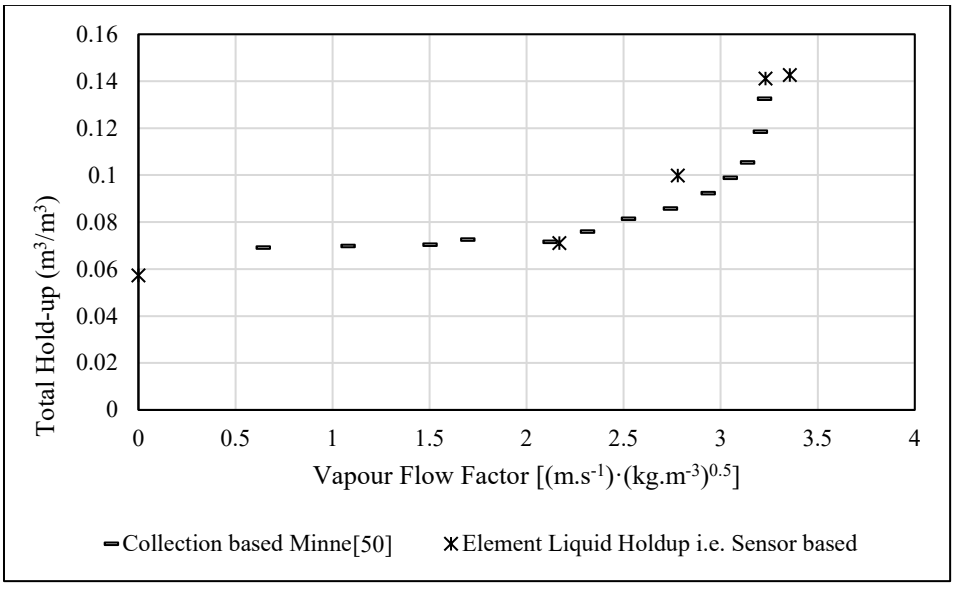

Figure 14.2: Intalox® Ultra size O liquid holdup vs element liquid holdup; water/air; 98 $m^3m^{-2}h^{-1}$;

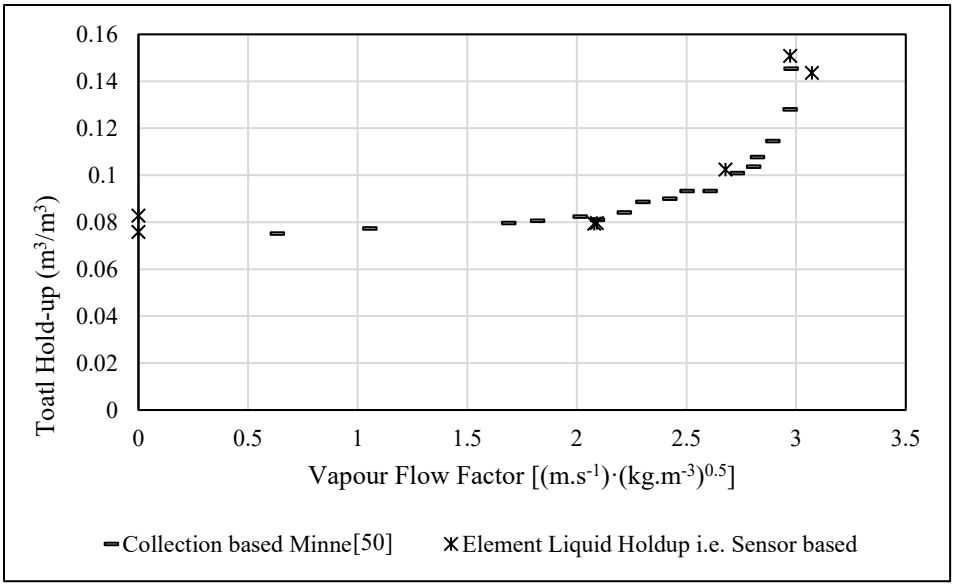

Figure 14.3: Intalox® Ultra size O liquid holdup vs element liquid holdup; water/air; 122 $m^3m^{-2}h^{-1}$;

14.1.1.22" INTALOX INTALOX® ULTRA (L)

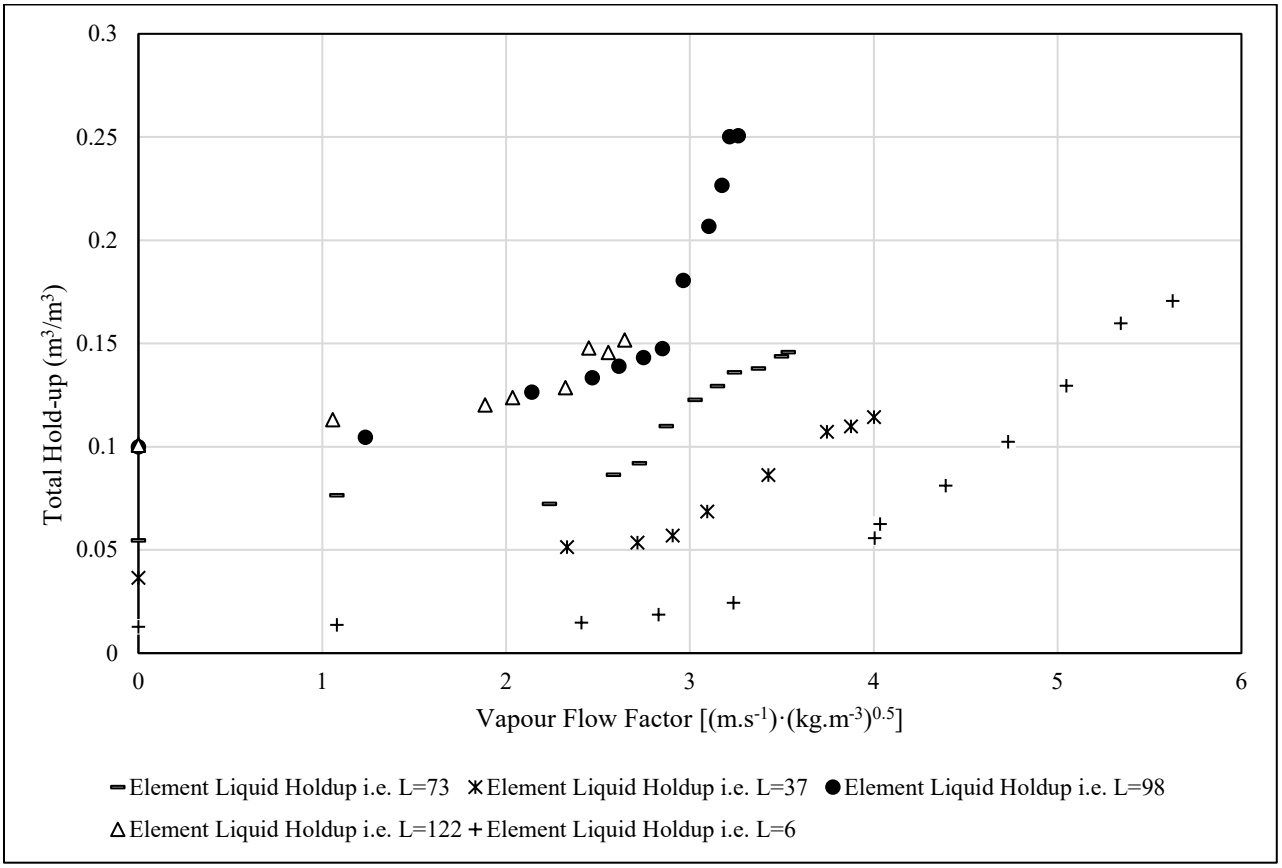

Figure 14.4: Intalox® Ultra L; element liquid hold-up; air / water

14.1.1.3 2” FLEXIRING®

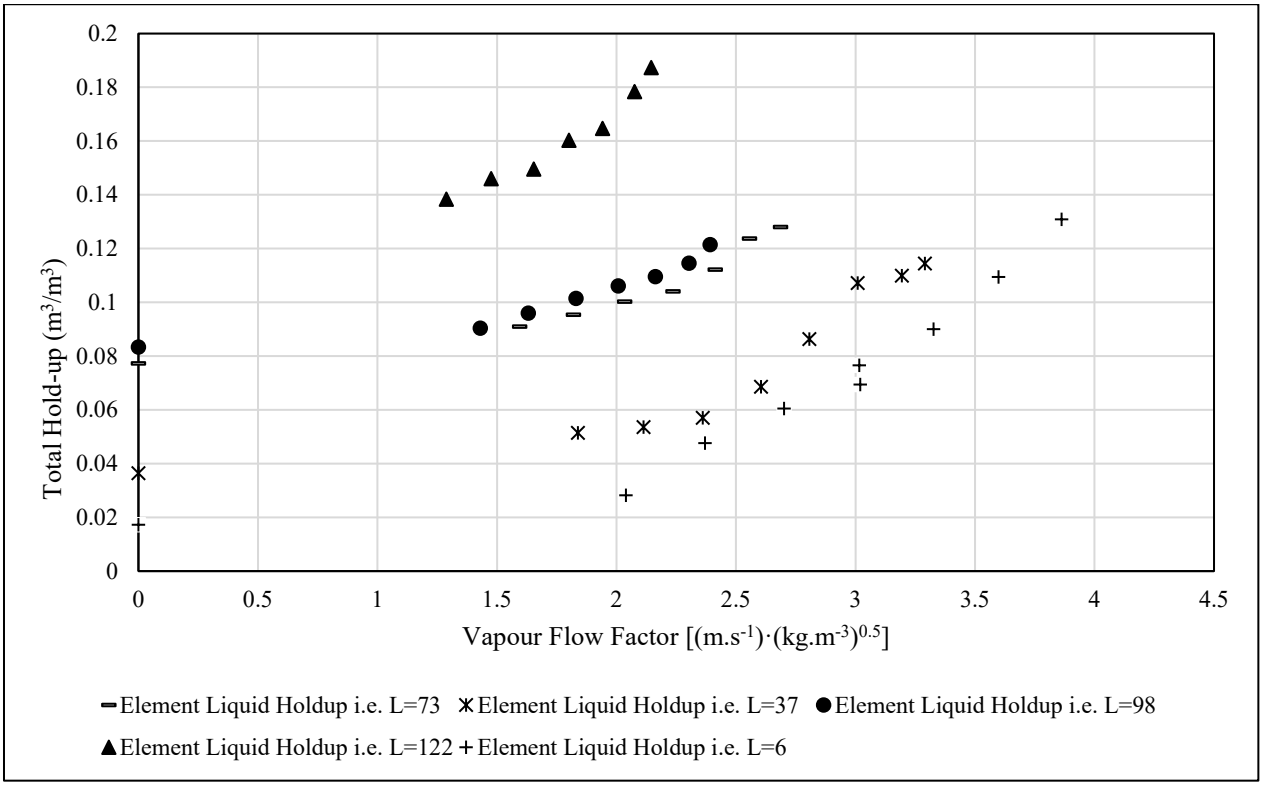

Figure 14.5 : 2” FlexiRing® element liquid hold-up; air / water

14.1.1.41.5” INTALOX INTALOX® ULTRA (A)

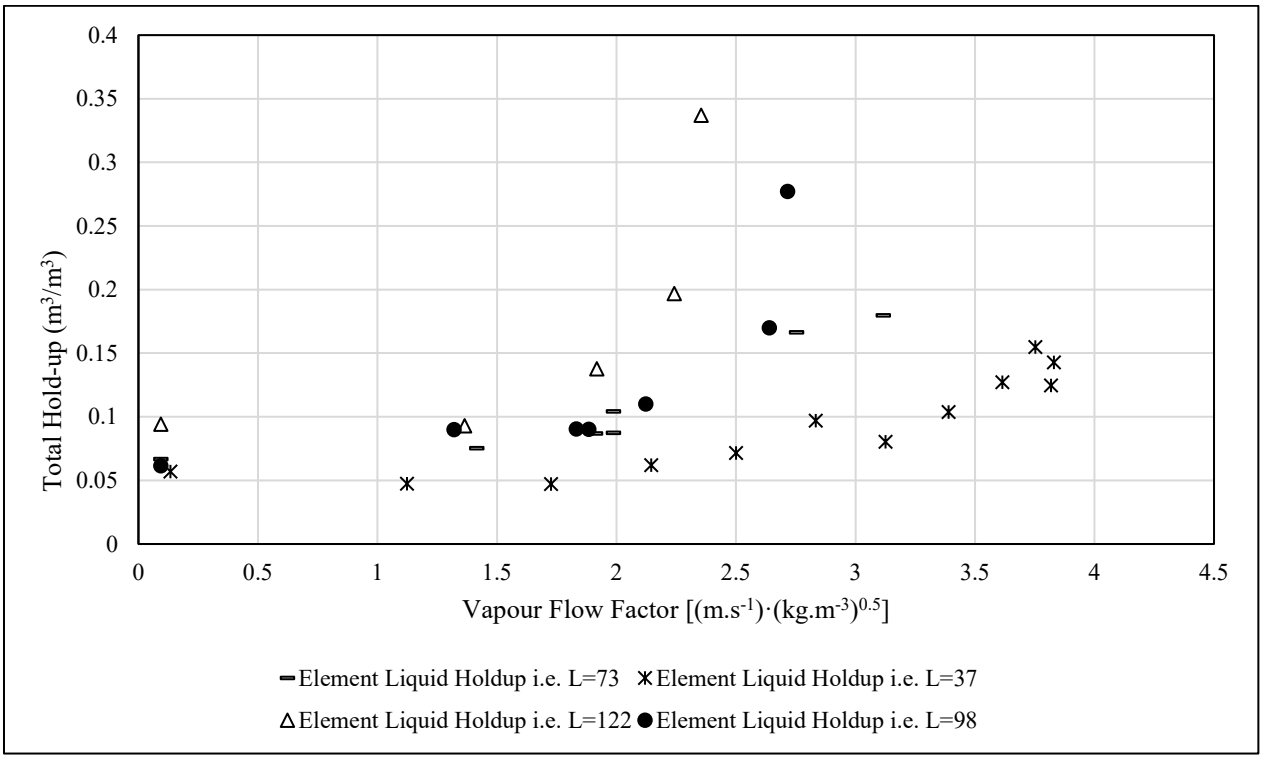

Figure 14.6: Intalox® Ultra A; element liquid hold-up; air / water

14.1.2 AIR/ETHYLENE GLYCOL

14.1.2.12" INTALOX® ULTRA (L)

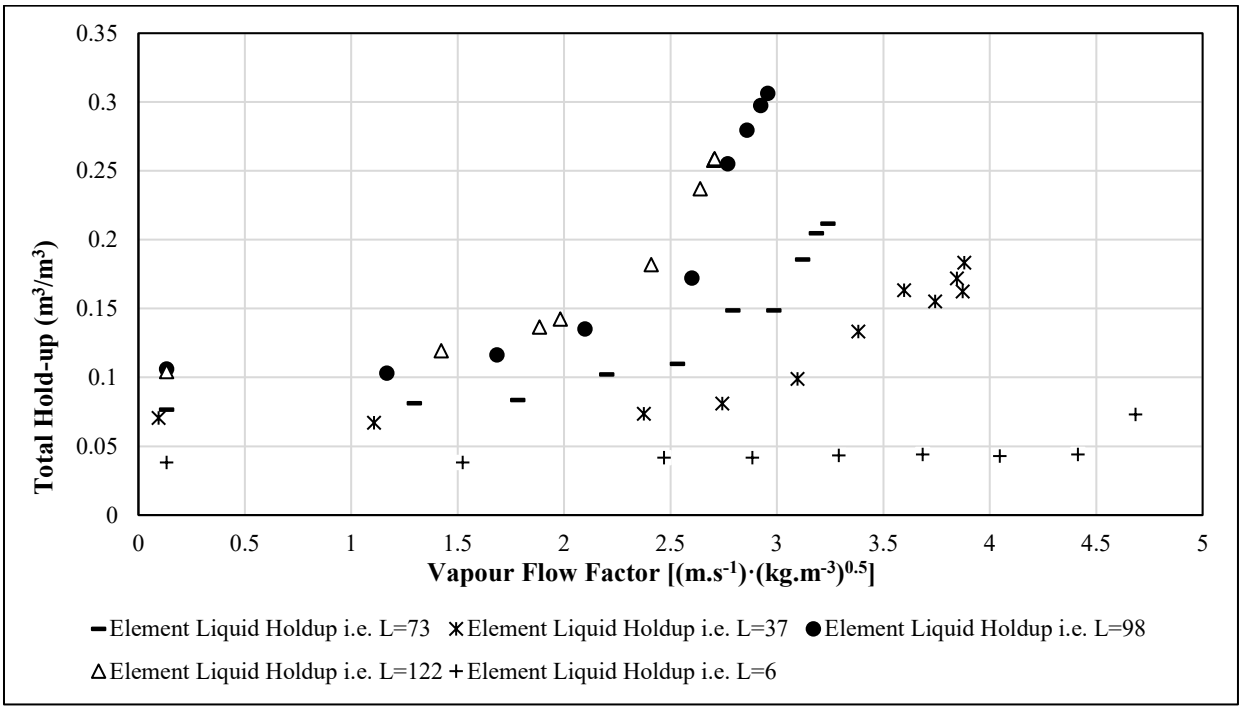

Figure 14.7: Intalox® Ultra L element liquid hold-up; air/ ethylene glycol

14.1.2.22" FLEXIRING®

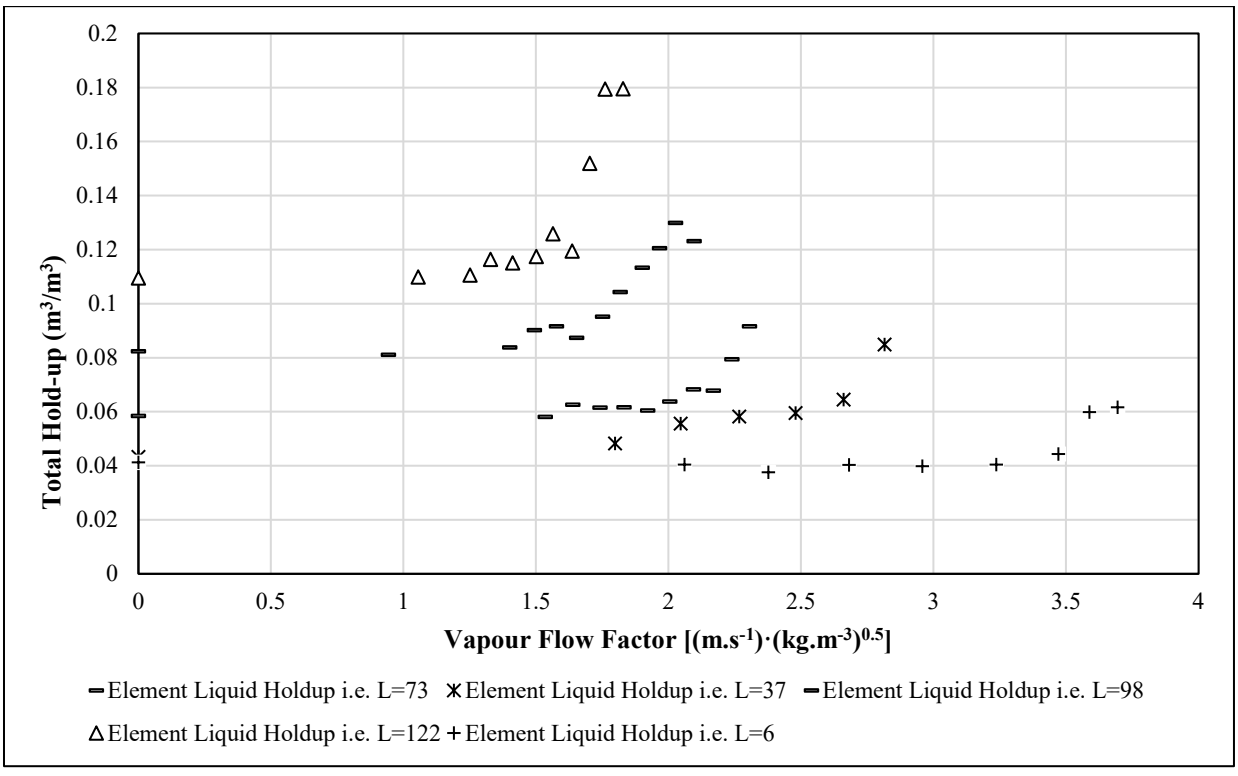

Figure 14.8: 2" FlexiRing®; element liquid hold-up; air/ ethylene glycol

14.2 VOLUME BASED CDF: EFFECTS OF VAPOUR

14.2.1 2.5" INTALOX® ULTRA (O)

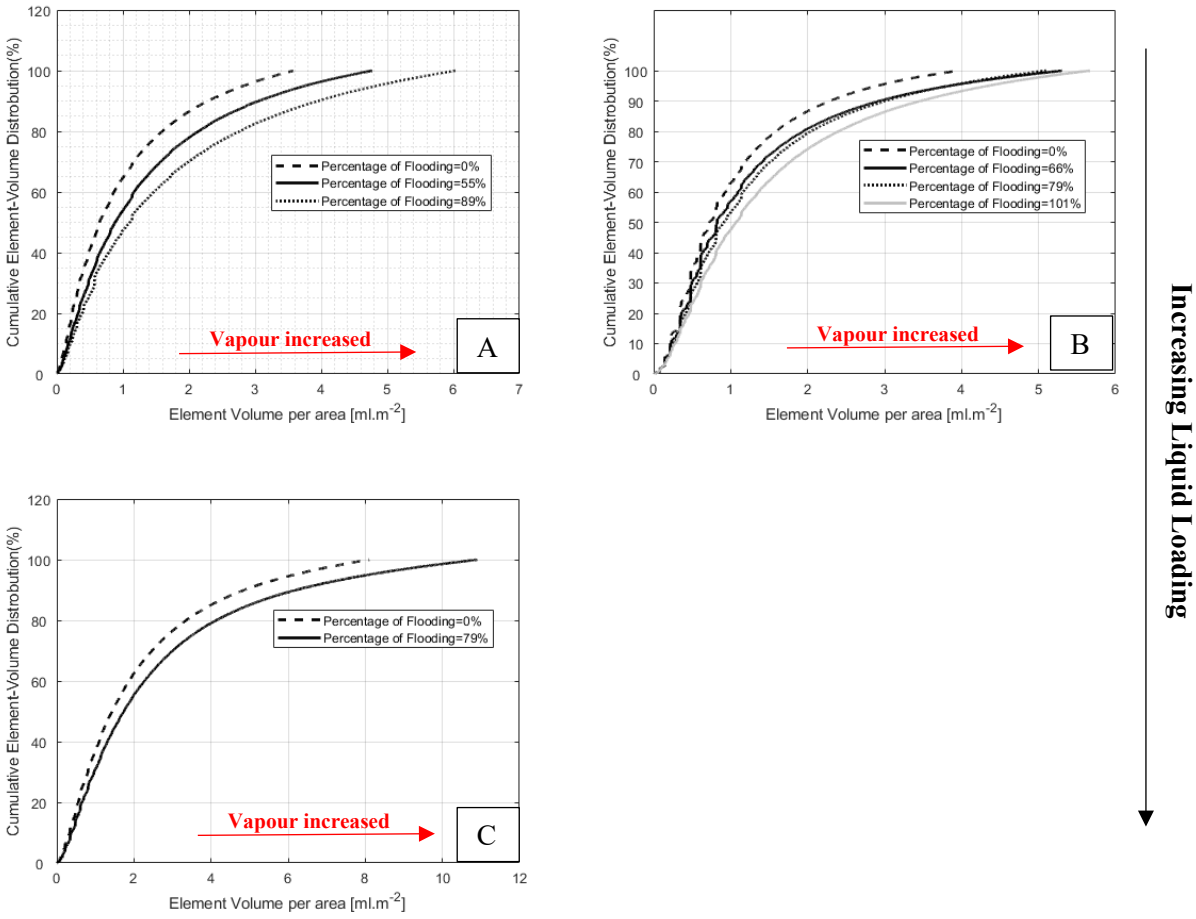

Figure 14.9: Cumulative IPL element-volume distributions using air / water and Intalox® Ultra size O A) 37 $m^3.m^{-2}.h^{-1}$; B) 73 $m^3.m^{-2}.h^{-1}$; C) 122 $m^3.m^{-2}.h^{-1}$;

14.3 AREA BASED CDF

14.3.1 IPL ELEMENT-SURFACE AREA: WATER WITHOUT VAPOUR

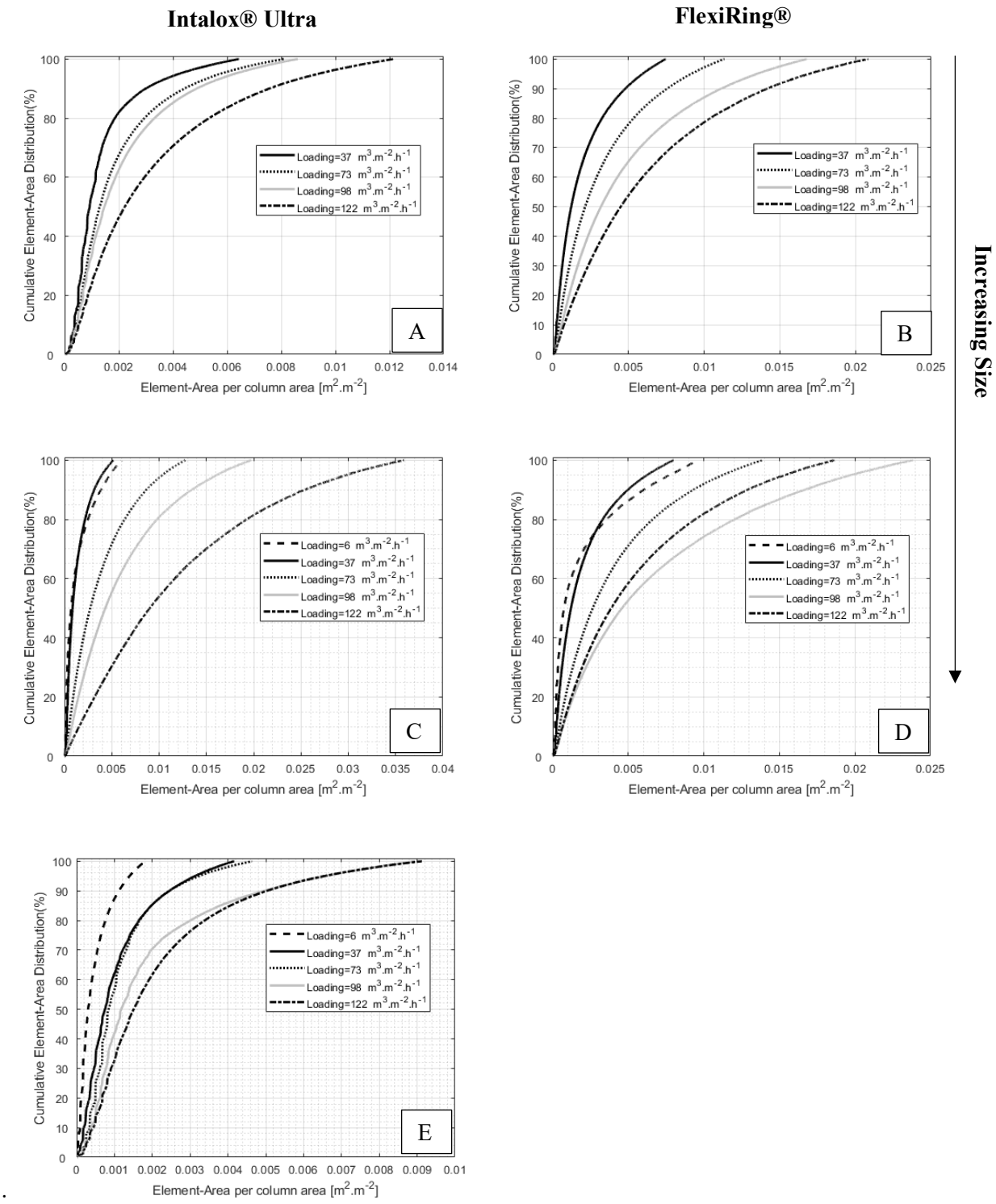

.

Figure 14.10 : Cumulative IPL element-surface area distributions using air / water at zero vapour loading A) Intalox® Ultra size A; B) 1.5" FlexiRing®; C) Intalox® Ultra size L; D) 2" FlexiRing® ; e) Intalox® Ultra size O;

14.3.2 WATER: 1.5" FLEXIRING® AND INTALOX® ULTRA A

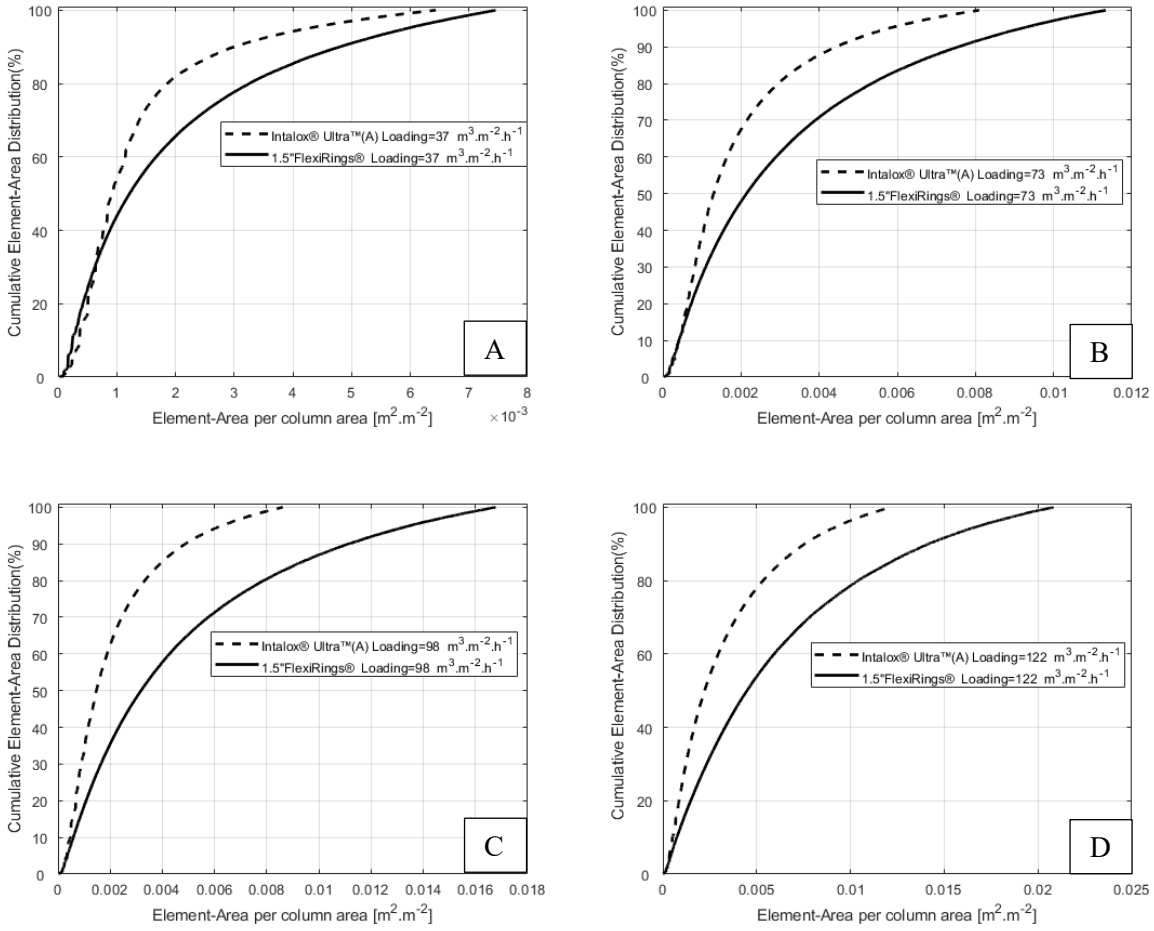

Figure 14.11 : Cumulative IPL element-surface area distributions using air / water at zero vapour loading considering Intalox® Ultra size A vs. 1.5" FlexiRing® @ A) 37 $m^3.m^{-2}.h^{-1}$; B) 73$m^3.m^{-2}.h^{-1}$; C) 98$m^3.m^{-2}.h^{-1}$; D) 122$m^3.m^{-2}.h^{-1}$;

14.3.3 WATER: 2" FLEXIRING® AND INTALOX® ULTRA L

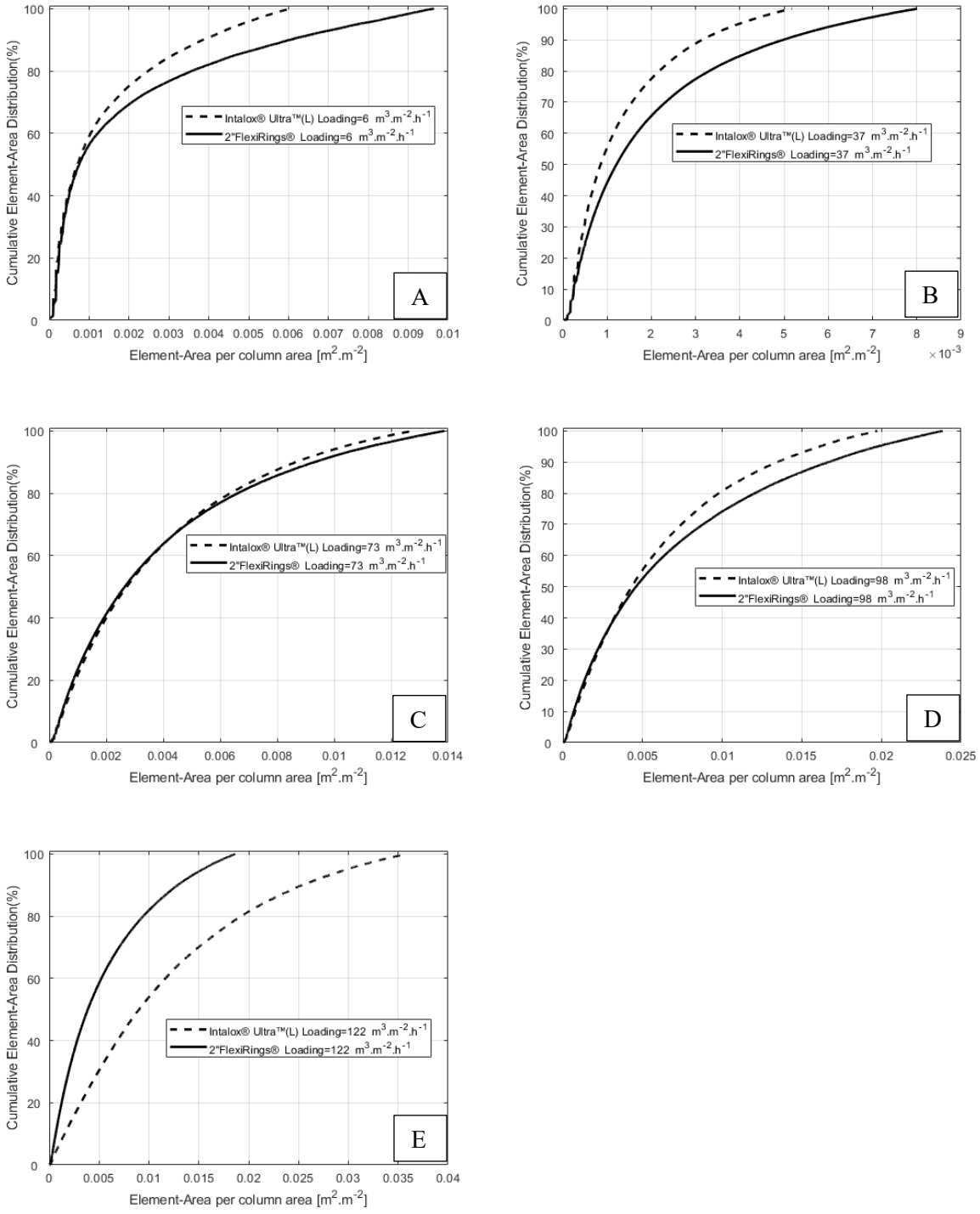

Figure 14.12: Cumulative IPL element-surface area distributions using air / water at zero vapour loading considering Intalox® Ultra size L vs. 2" FlexiRing® @ A) 6m^3.m^{-2}.h^{-1}; B) 37 m^3.m^{-2}.h^{-1}; C) 73m^3.m^{-2}.h^{-1}; D) 98m^3.m^{-2}.h^{-1}; E) 122m^3.m^{-2}.h^{-1};

14.3.4 CHARACTERISATION BASED ON VARYING PACKING SIZE: WATER

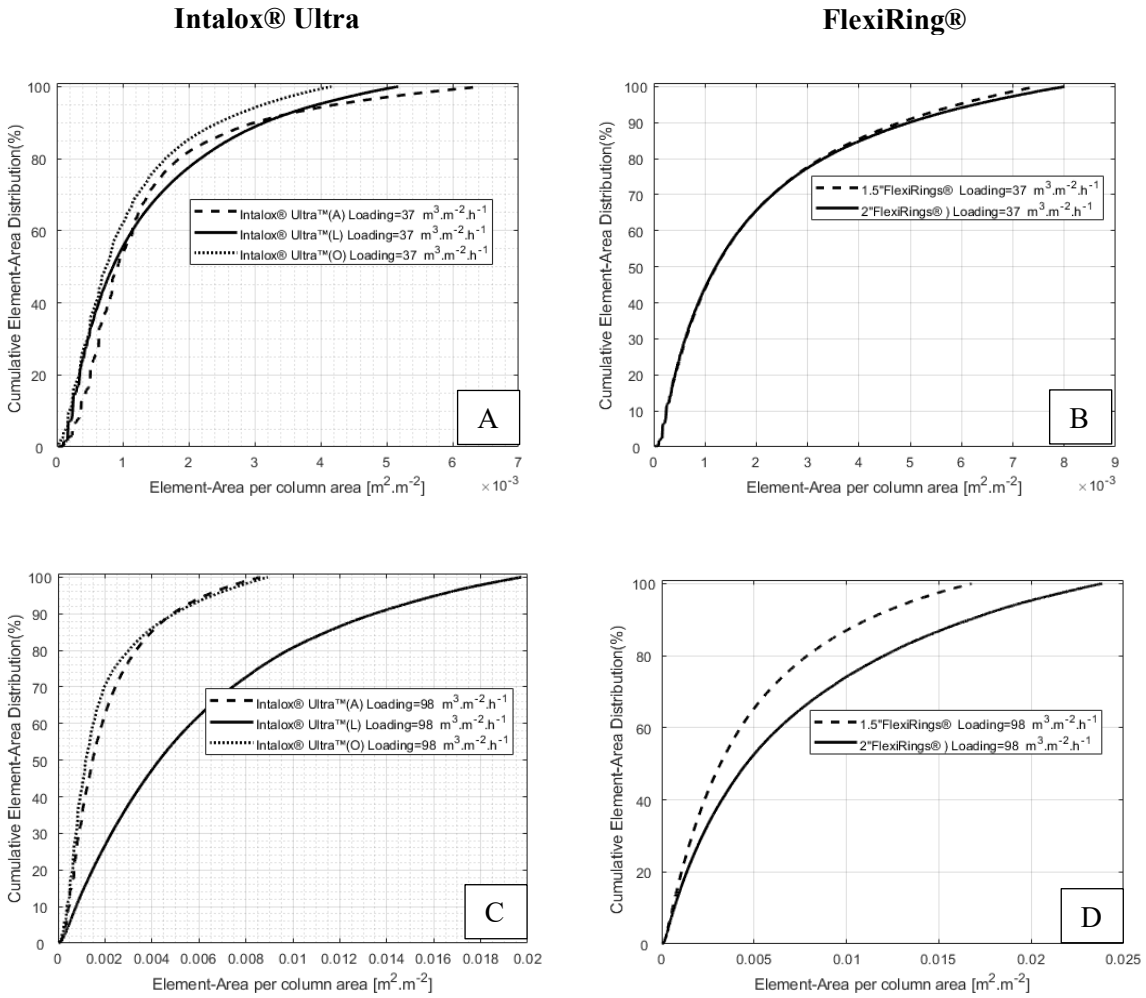

Figure 14.13 : Cumulative IPL element-surface area distributions using water at zero vapour loading A) Intalox® Ultra sizes A, L and O @ 37 $m^3.m^{-2}.h^{-1}$; B) 1.5" &2" FlexiRing® @ 37 $m^3.m^{-2}.h^{-1}$; C) Intalox® Ultra sizes A, L and O @ 98 $m^3.m^{-2}.h^{-1}$ D) 1.5" &2" FlexiRing® @ 98 $m^3.m^{-2}.h^{-1}$.

14.3.5 IPL ELEMENT-SURFACE AREA: ETHYLENE GLYCOL

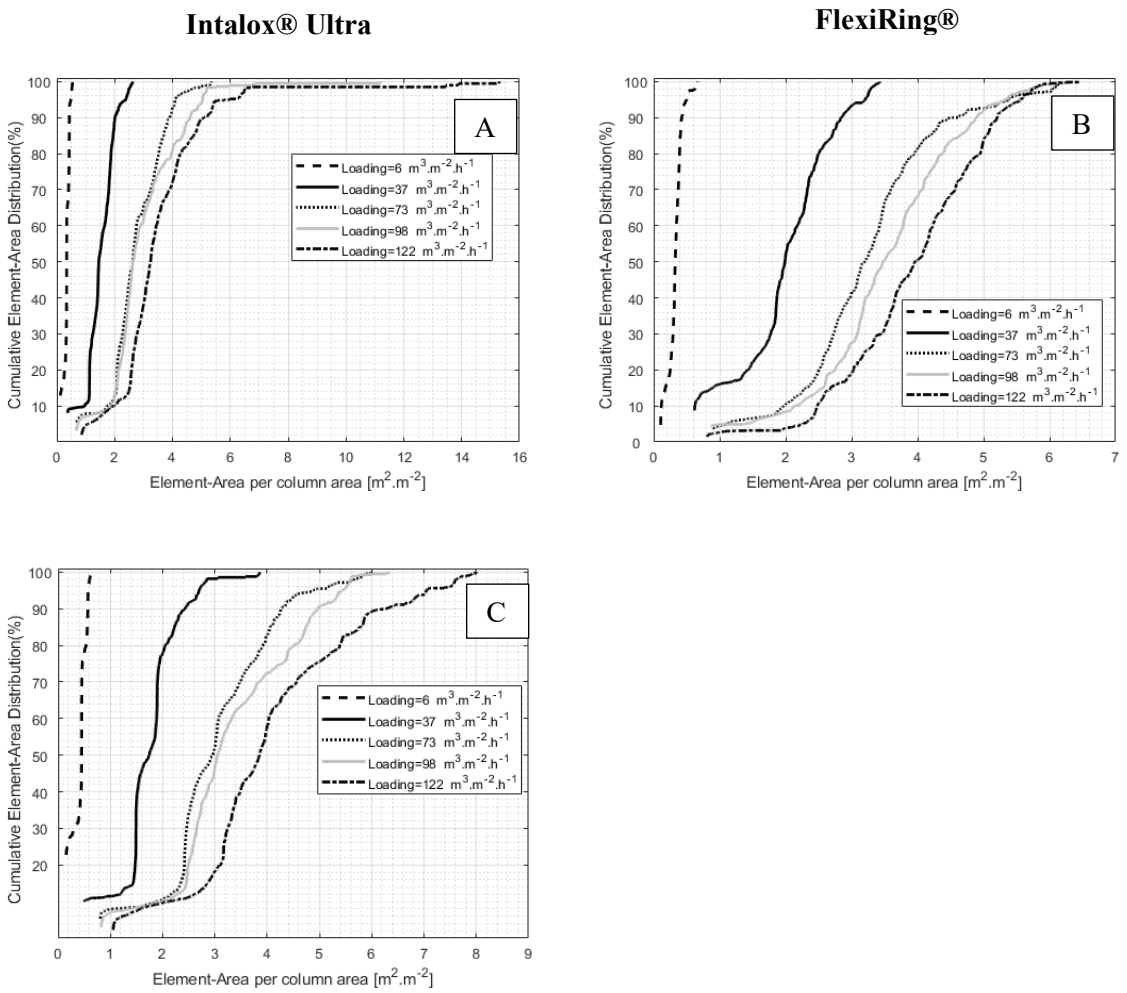

Figure 14.14 : Cumulative IPL element-surface area distributions using air / ethylene glycol at zero vapour loading; A) Intalox® Ultra size L; B) 2" FlexiRing® ; C) Intalox® Ultra size O.

14.3.6 ETHYLENE GLYCOL: 2" FLEXIRING® AND INTALOX® ULTRA L

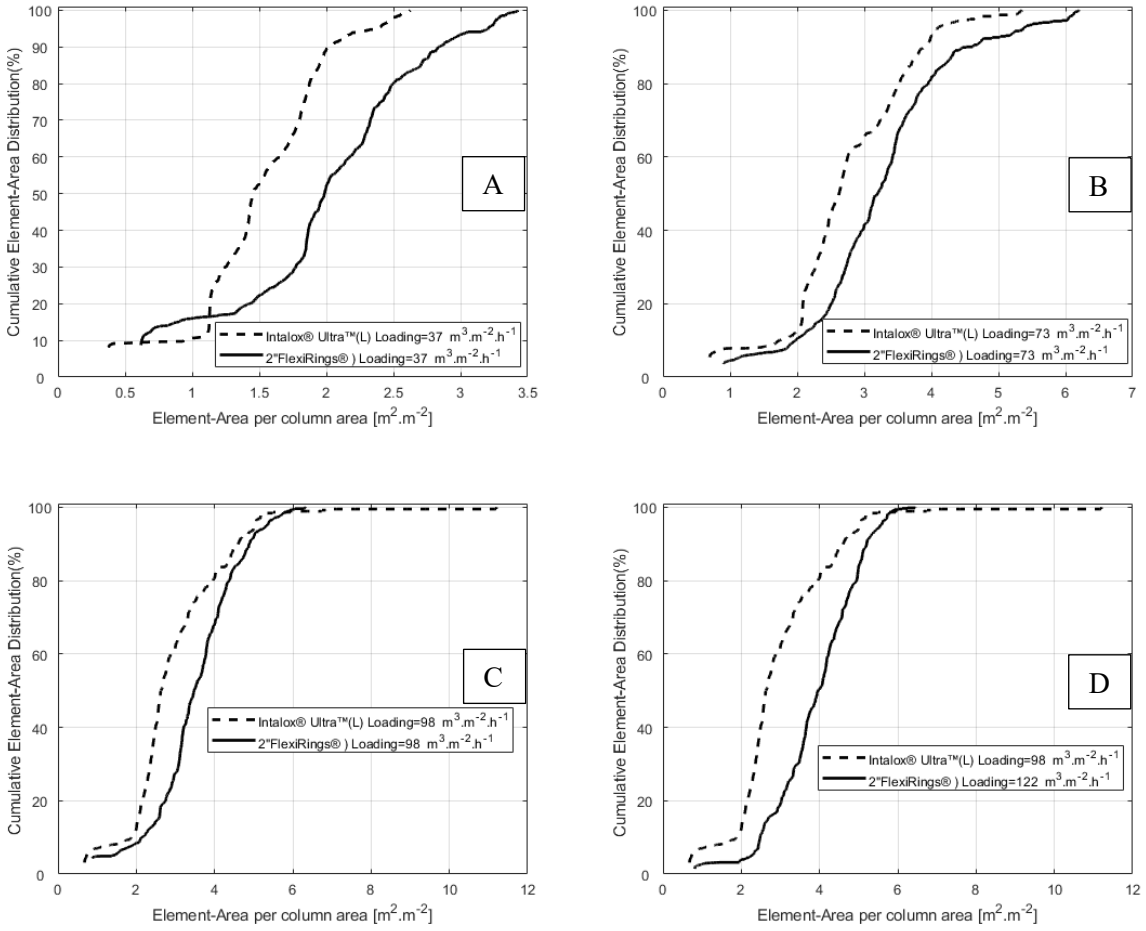

Figure 14.15 : Cumulative IPL element-surface area distributions using air/Ethylene Glycol at zero vapour loading considering Intalox® Ultra size L vs. 2" FlexiRing® @ A) 37 $m^3.m^{-2}.h^{-1}$; B) 73$m^3.m^{-2}.h^{-1}$; C) 98$m^3.m^{-2}.h^{-1}$; D) 122$m^3.m^{-2}.h^{-1}$.

14.4 IPL ELEMENT-SURFACE AREA-CDF: EFFECTS OF VAPOUR

14.4.1 AIR/WATER: 2" FLEXIRING® AND INTALOX® ULTRA L

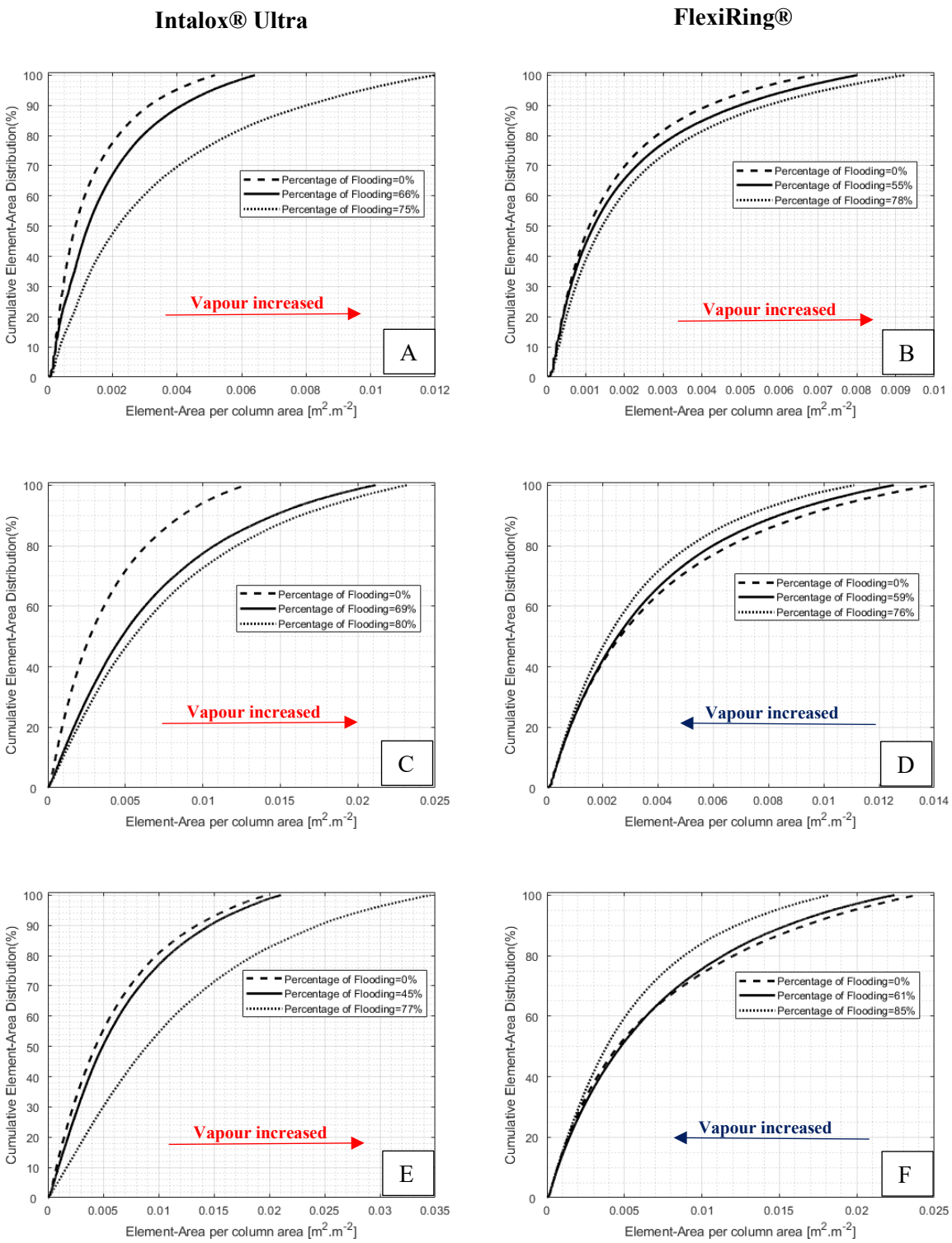

Figure 14.16: Cumulative IPL element-surface area distributions for air / water; A) Intalox® Ultra size L @ 37 $m^3.m^{-2}.h^{-1}$; B) 2" FlexiRing® @ 37 $m^3.m^{-2}.h^{-1}$; C) Intalox® Ultra size L @ 73 $m^3.m^{-2}.h^{-1}$; D) 2" FlexiRing® @ 73 $m^3.m^{-2}.h^{-1}$; E) Intalox® Ultra size L @ 98 $m^3.m^{-2}.h^{-1}$; F) 2" FlexiRing® @ 98 $m^3.m^{-2}.h^{-1}$.

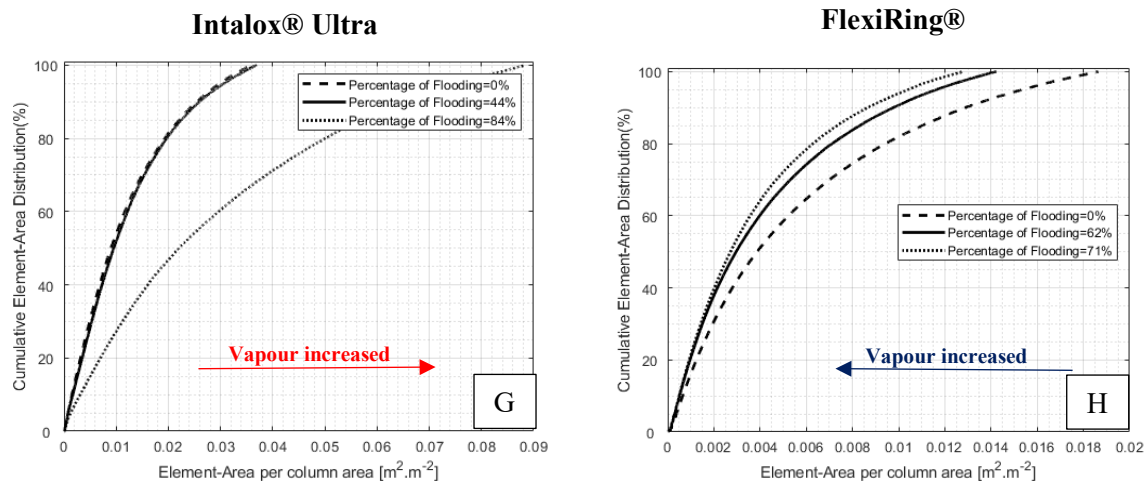

Figure 14.17: Figure 14.16 Continues; G) Intalox® Ultra size L @ 122 $m^3.m^{-2}.h^{-1}$; H) 2" FlexiRing® @ 122 $m^3.m^{-2}.h^{-1}$.

14.4.2 AIR/WATER: 1.5" FLEXIRING® AND INTALOX® ULTRA A

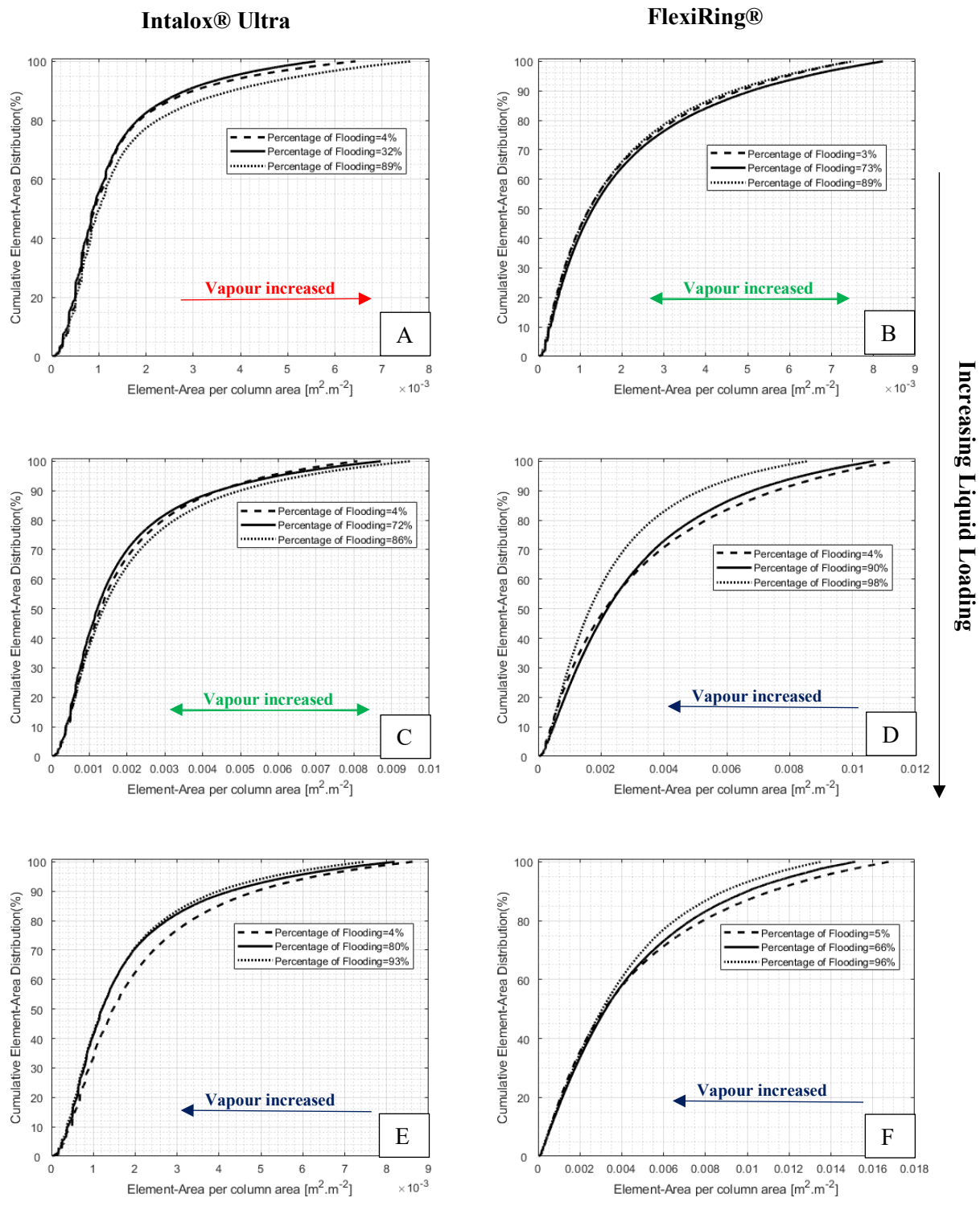

Figure 14.18 : Cumulative IPL element-surface area distributions for air water; A) Intalox® Ultra size A @ 37 $m^3.m^{-2}.h^{-1}$; B) 1.5" FlexiRing® @ 37 $m^3.m^{-2}.h^{-1}$; C) Intalox® Ultra size A@ 73 $m^3.m^{-2}.h^{-1}$; D) 1.5" FlexiRing® @ 73 $m^3.m^{-2}.h^{-1}$; E) Intalox® Ultra size A@ 98 $m^3.m^{-2}.h^{-1}$; F) 1.5" FlexiRing® @ 98$m^3.m^{-2}.h^{-1}$.

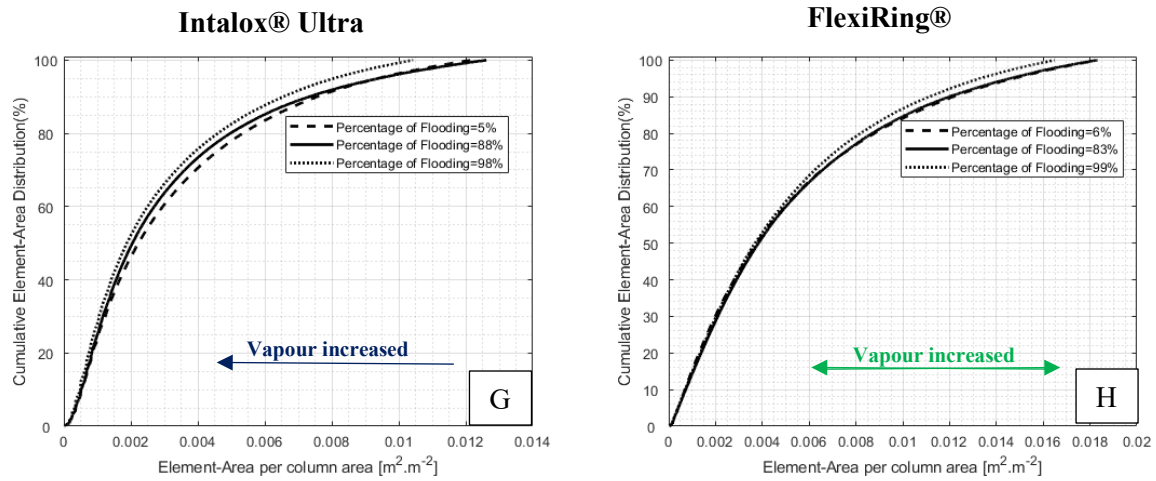

Figure 14.19 : Figure 14.18 Continues; G) Intalox® Ultra size A @ 122 $m^3.m^{-2}.h^{-1}$; H) 1.5" FlexiRing® @ 122$m^3.m^{-2}.h^{-1}$.

14.4.3 AIR/WATER: 2.5" INTALOX® ULTRA (O)

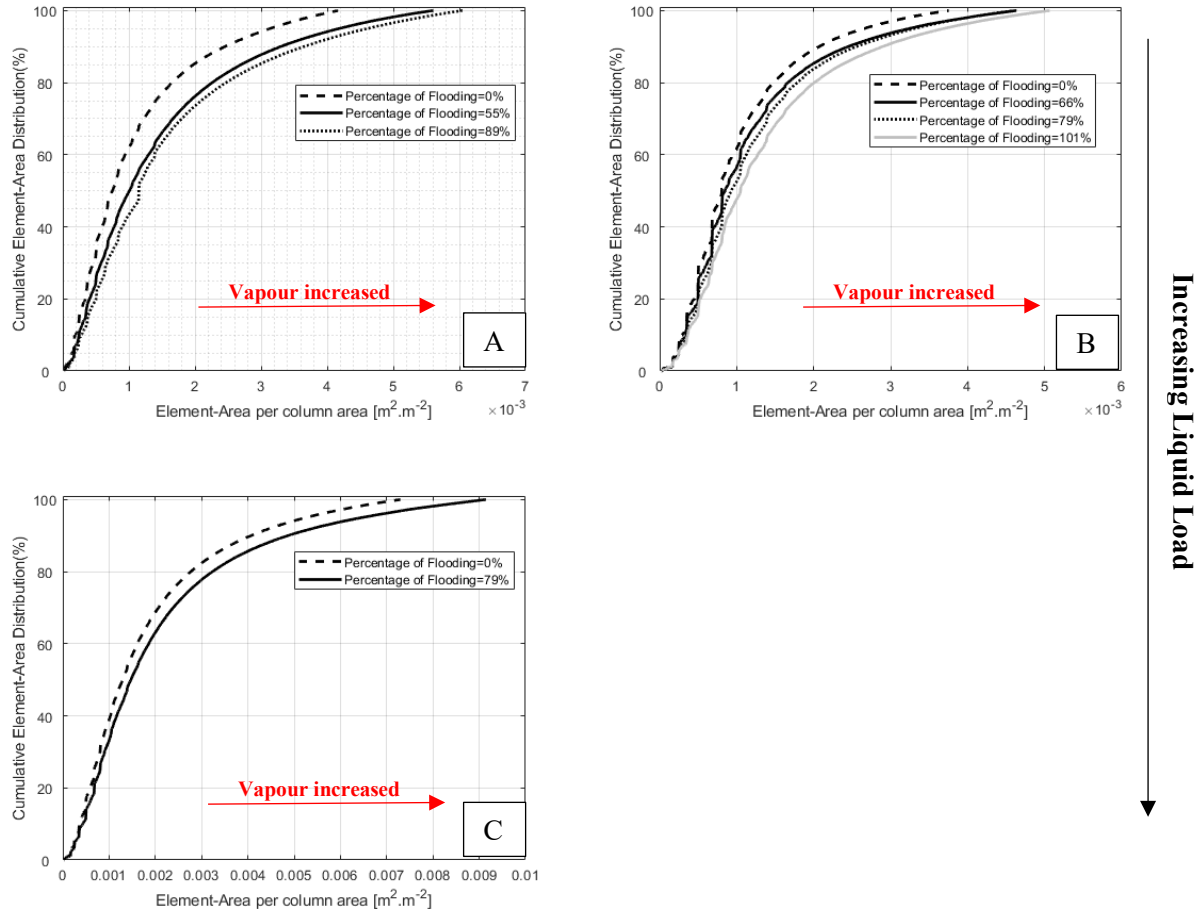

Figure 14.20: Cumulative IPL element-surface area distributions using air / water and Intalox® Ultra size O A) 37 $m^3.m^{-2}.h^{-1}$; B) 73 $m^3.m^{-2}.h^{-1}$; C) 98 $m^3.m^{-2}.h^{-1}$;

14.4.4 ETHYLENE GLYCOL/AIR:2" FLEXIRING® AND INTALOX® ULTRA L

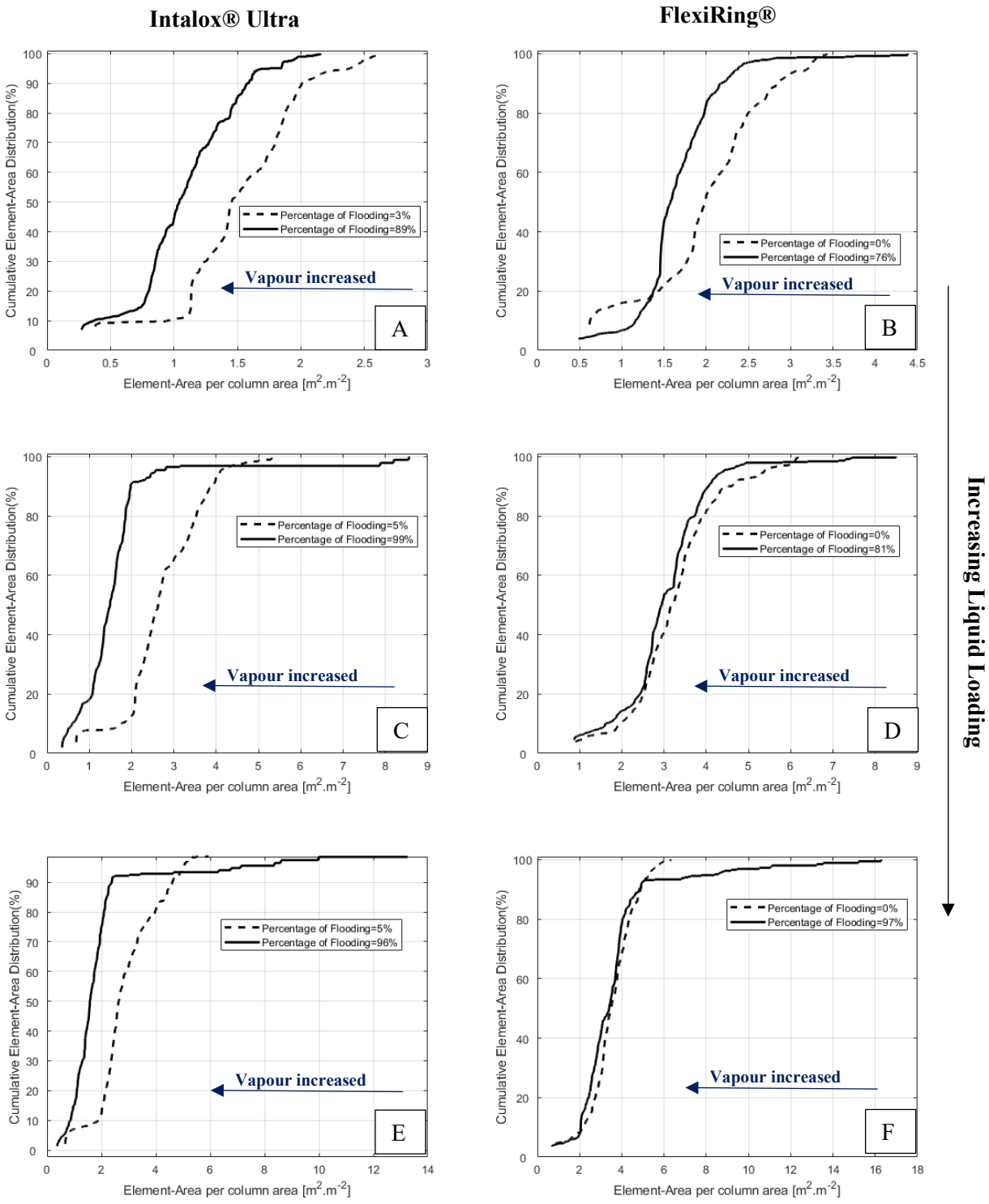

Figure 14.21: Cumulative IPL element-surface area distributions for air/ ethylene glycol; A) Intalox® Ultra size L @ 37 $m^3.m^{-2}.h^{-1}$; B) 2" FlexiRing® @ 37 $m^3.m^{-2}.h^{-1}$; C) Intalox® Ultra size L@ 73 $m^3.m^{-2}.h^{-1}$; D) 2" FlexiRing® @ 73 $m^3.m^{-2}.h^{-1}$; E) Intalox® Ultra size L@ 98 $m^3.m^{-2}.h^{-1}$; F) 2" FlexiRing® @ 98$m^3.m^{-2}.h^{-1}$;

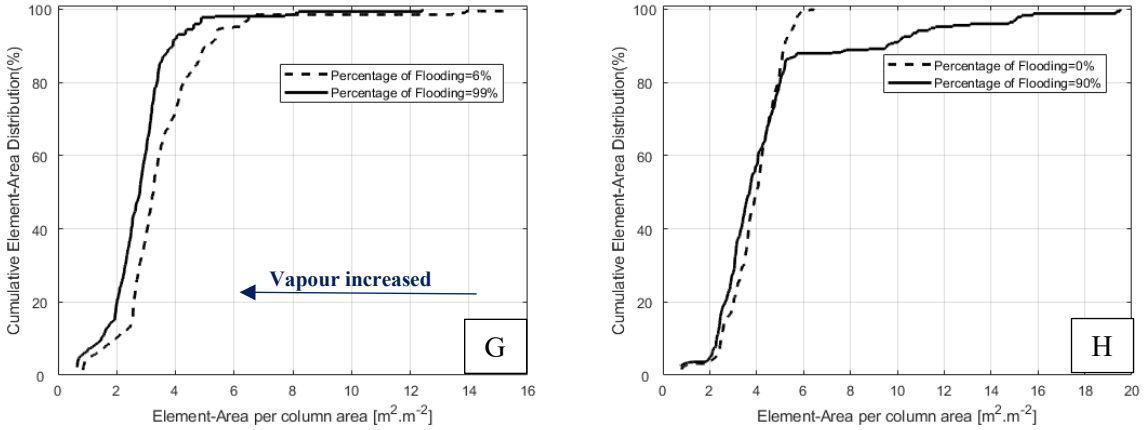

Figure 14.22: Figure 14.21 Continues; G) Intalox® Ultra size L@ 122 $m^3.m^{-2}.h^{-1}$; H) 2" FlexiRing® @ 122$m^3.m^{-2}.h^{-1}$.

14.5 NUMBER BASED CDF

14.5.1 IPL ELEMENT-VOLUME

14.5.1.1 IPL ELEMENT-VOLUME: WATER WITHOUT VAPOUR

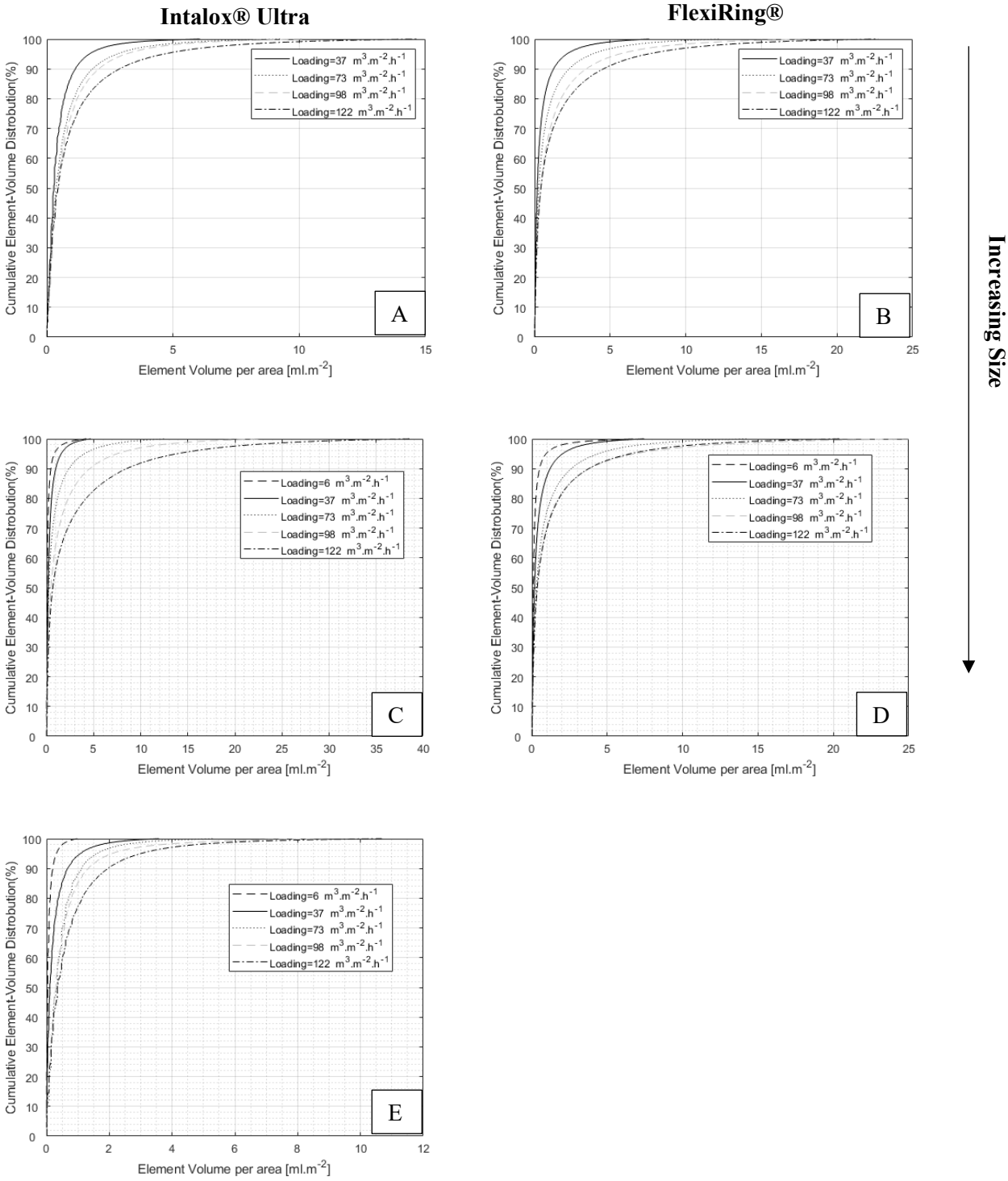

Figure 14.23: Cumulative IPL element-volume distributions using air / water at zero vapour loading A) Intalox® Ultra size A; B) 1.5" FlexiRing®; C) Intalox® Ultra size L; D) 2" FlexiRing® ; E) Intalox® Ultra size L;

14.5.1.2. IPL ELEMENT-VOLUME: ETHYLENE GLYCOL WITHOUT VAPOUR

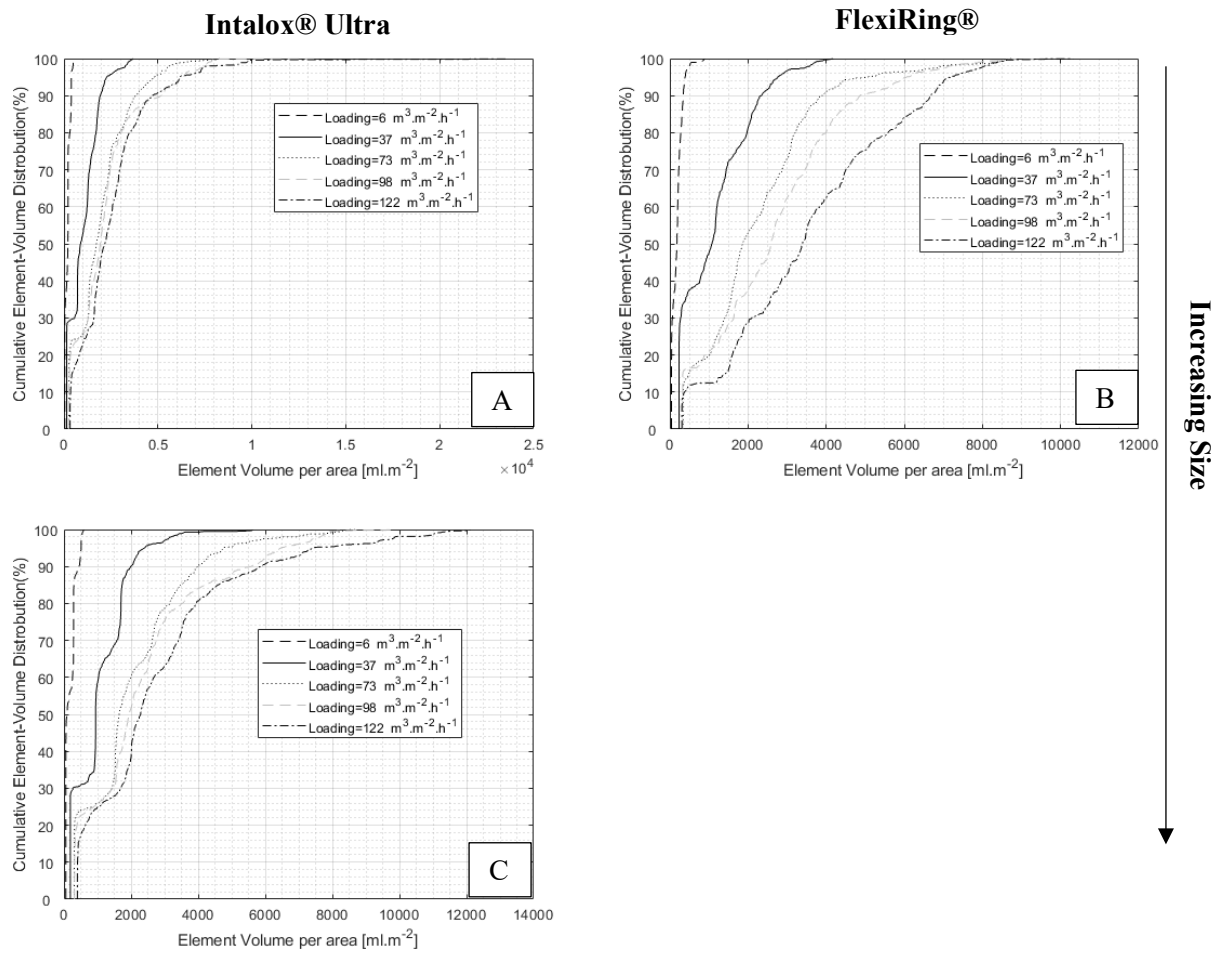

Figure 14.24: Cumulative IPL element-volume distributions using air / ethylene glycol at zero vapour loading; A) Intalox® Ultra size L; B) 2" FlexiRing® ; C) Intalox® Ultra size O.

14.5.1.3. VAPOUR LOADING: AIR/WATER 2" FLEXIRING® AND INTALOX® ULTRA L

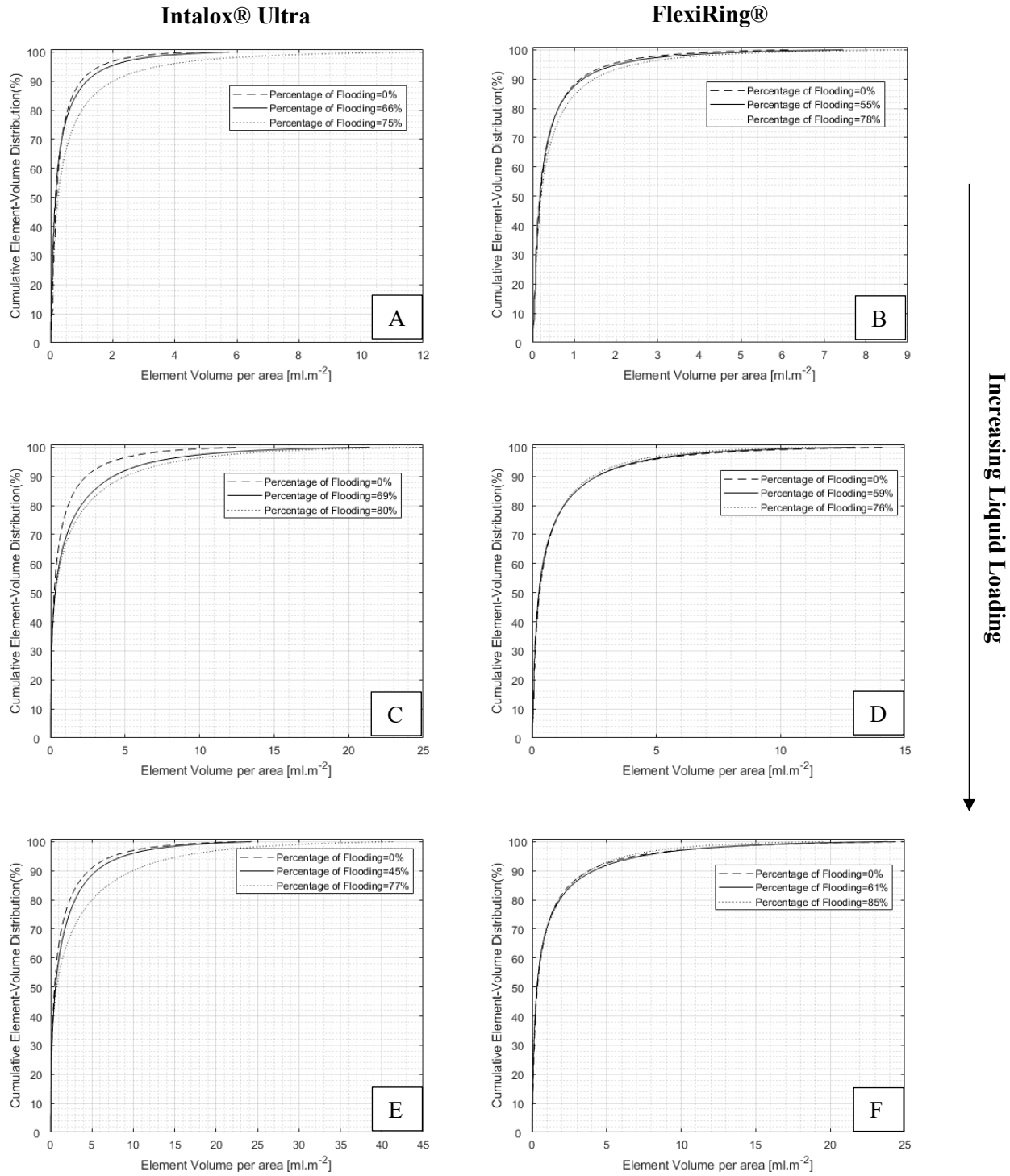

Figure 14.25 : Cumulative IPL element-volume distributions for air water; A) Intalox® Ultra size L @ 37 $m^3.m^{-2}.h^{-1}$; B) 2" FlexiRing® @ 37 $m^3.m^{-2}.h^{-1}$; C) Intalox® Ultra size L @ 73 $m^3.m^{-2}.h^{-1}$; D) 2" FlexiRing® @ 73 $m^3.m^{-2}.h^{-1}$; E) Intalox® Ultra size L @ 98 $m^3.m^{-2}.h^{-1}$; F) 2" FlexiRing® @ 98 $m^3.m^{-2}.h^{-1}$;

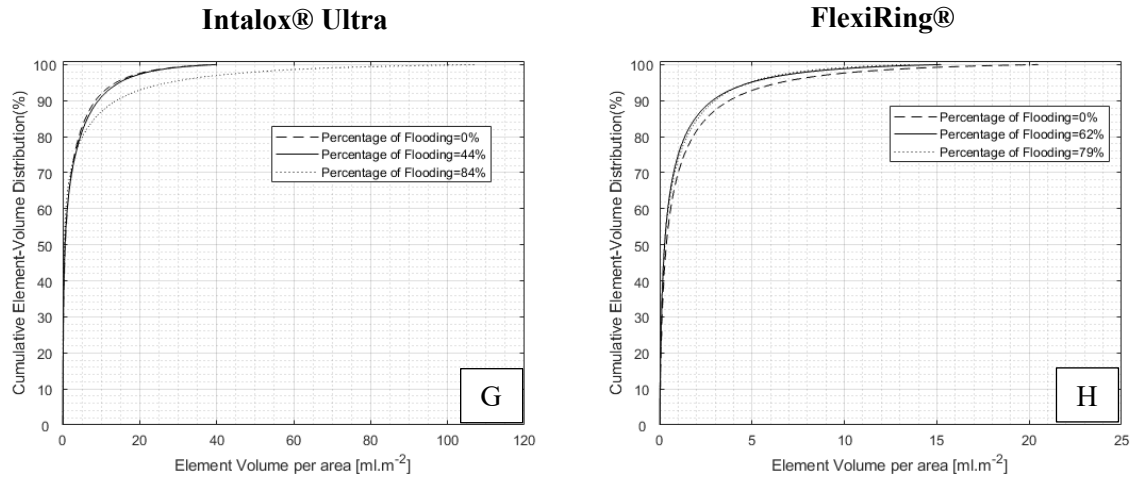

Figure 14.26: Figure 14.25 Continues; G) Intalox® Ultra size L @ 122 $m^3.m^{-2}.h^{-1}$; H) 2" FlexiRing® @ 122 $m^3.m^{-2}.h^{-1}$;

14.5.1.4. VAPOUR LOADING: AIR/WATER 1.5" FLEXIRING® AND INTALOX® ULTRA A

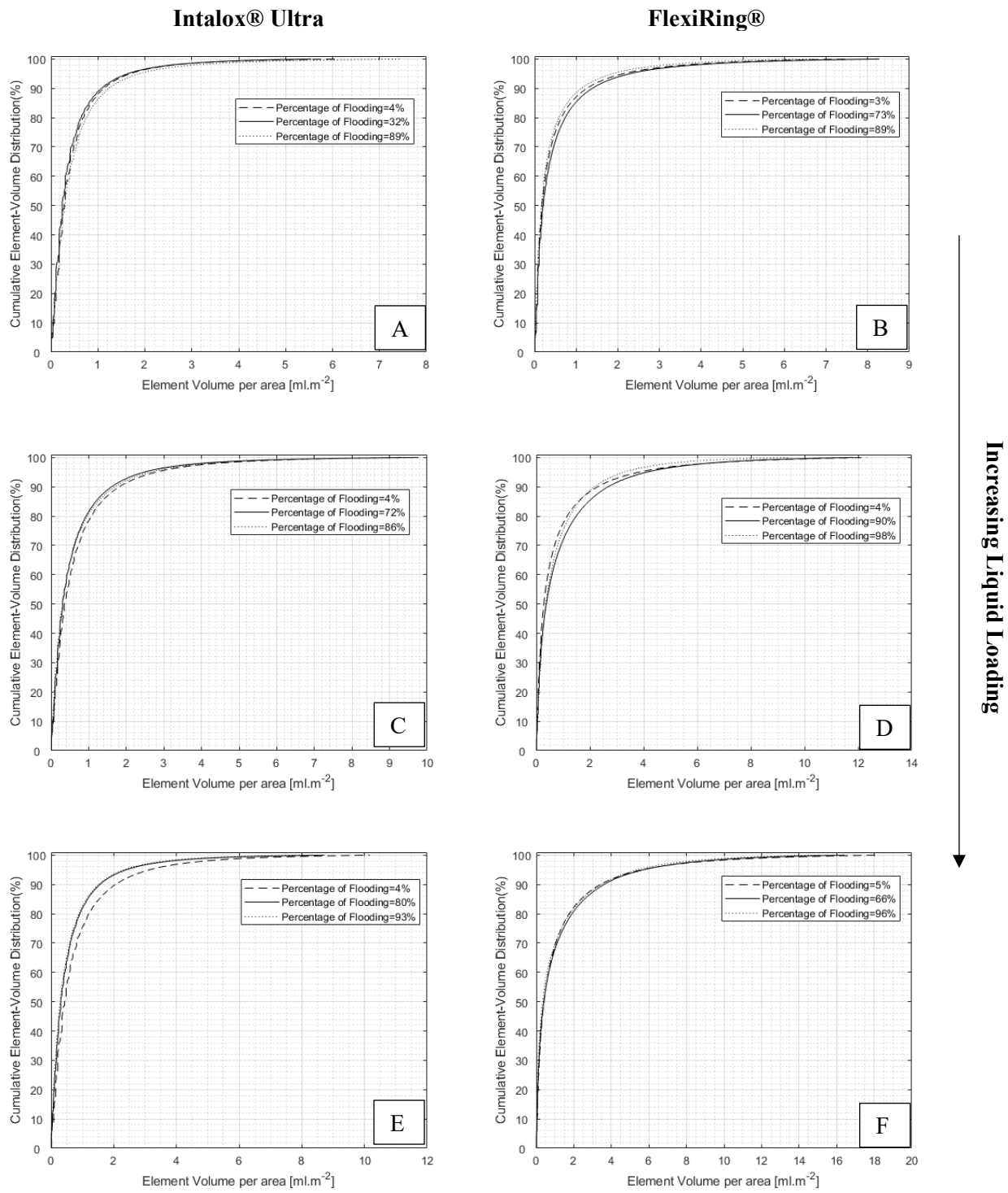

Figure 14.27 : Cumulative IPL element-volume distributions for air water; A) Intalox® Ultra size A @ 37 $m^3.m^{-2}.h^{-1}$; B) 1.5" FlexiRing® @ 37 $m^3.m^{-2}.h^{-1}$; C) Intalox® Ultra size A@ 73 $m^3.m^{-2}.h^{-1}$; D) 1.5" FlexiRing® @ 73 $m^3.m^{-2}.h^{-1}$; E) Intalox® Ultra size A@ 98 $m^3.m^{-2}.h^{-1}$; F) 1.5" FlexiRing® @ 98$m^3.m^{-2}.h^{-1}$;

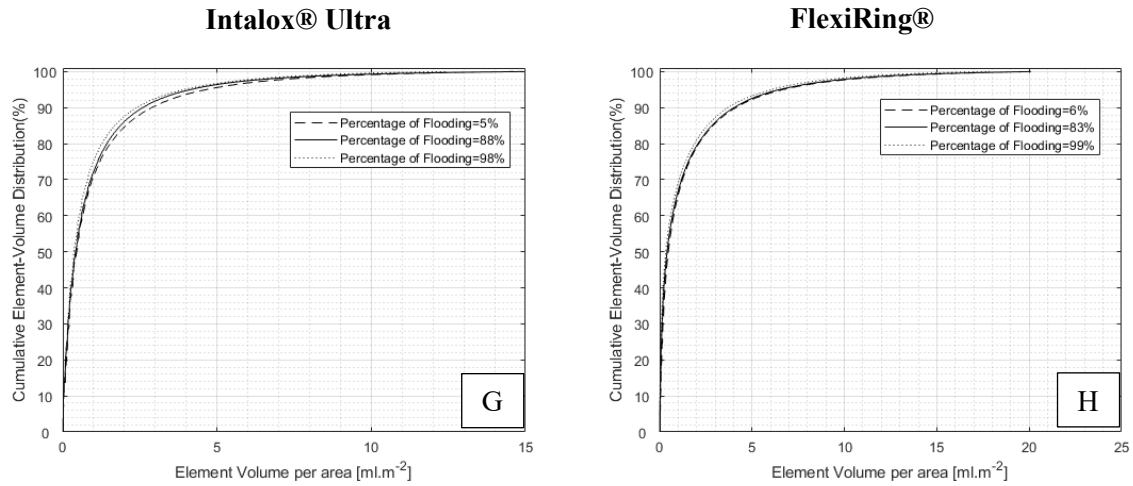

Figure 14.28: Figure 14.27 Continues; G) Intalox® Ultra size A @ 122 $m^3.m^{-2}.h^{-1}$; H) 1.5" FlexiRing® @ 122$m^3.m^{-2}.h^{-1}$.

14.5.1.5. VAPOUR LOADING: AIR/WATER INTALOX® ULTRA O

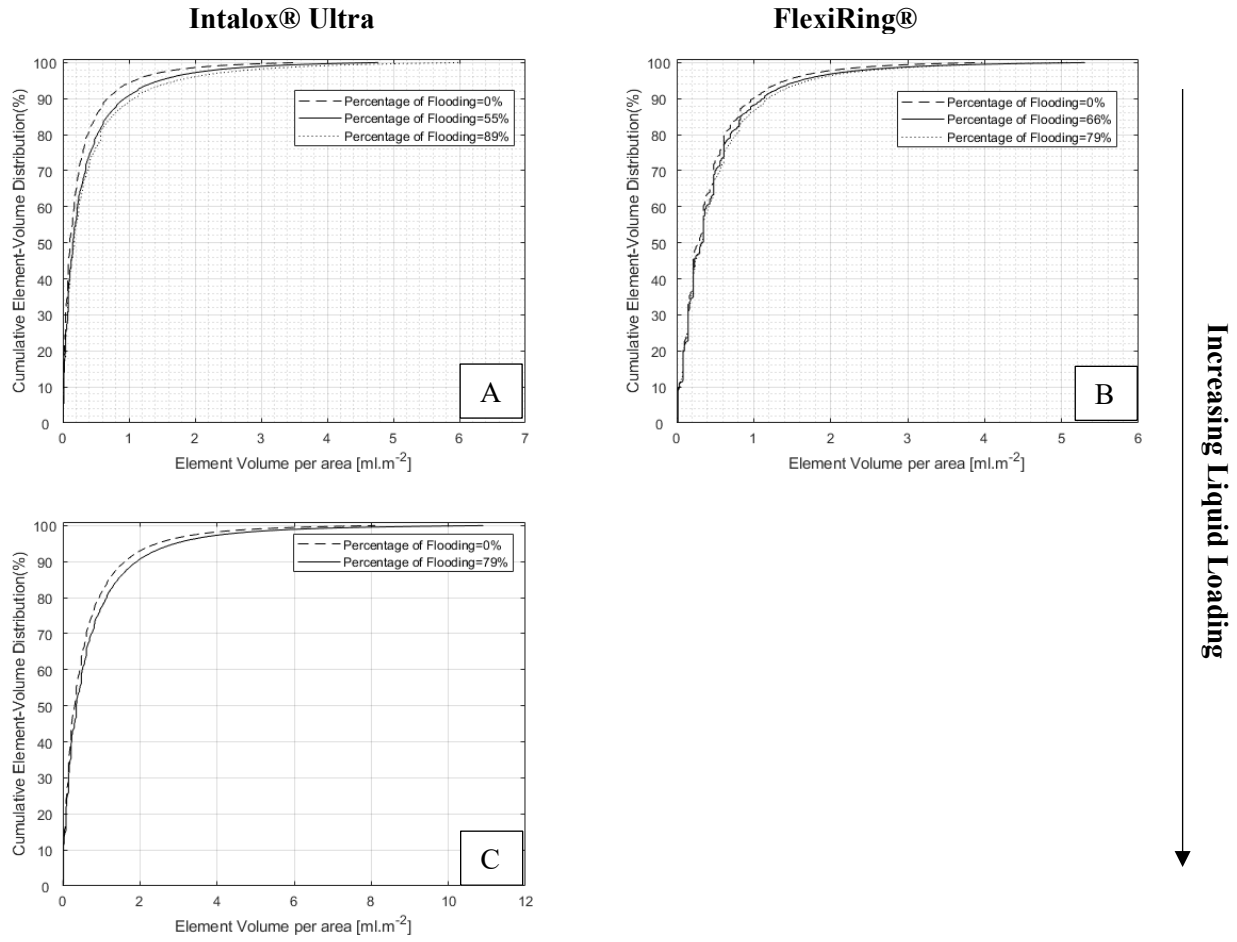

Figure 14.29: Cumulative IPL element-volume distributions using air / water and Intalox® Ultra size O A) 37 $m^3.m^{-2}.h^{-1}$; B) 73 $m^3.m^{-2}.h^{-1}$; C) 122 $m^3.m^{-2}.h^{-1}$;

14.5.2 IPL ELEMENT-SURFACE AREA

14.5.2.1. IPL ELEMENT-SURFACE AREA: WATER WITHOUT VAPOUR

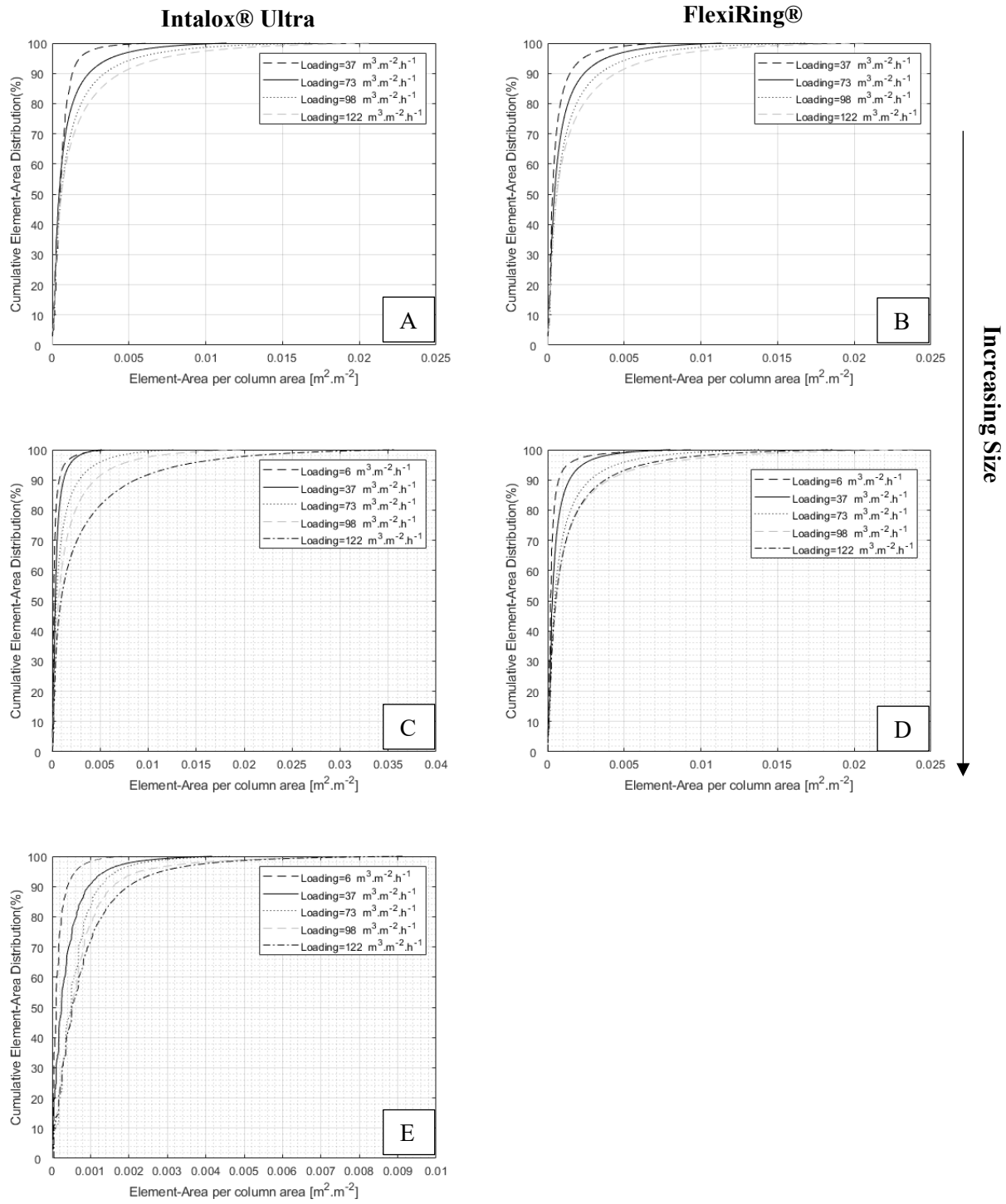

Figure 14.30 : Cumulative IPL element-surface area distributions using air / water at zero vapour loading A) Intalox® Ultra size A; B) 1.5" FlexiRing®; C) Intalox® Ultra size L; D) 2" FlexiRing® ; E) Intalox® Ultra size L;

14.5.2.2. IPL ELEMENT-SURFACE AREA: ETHYLENE GLYCOL WITHOUT VAPOUR

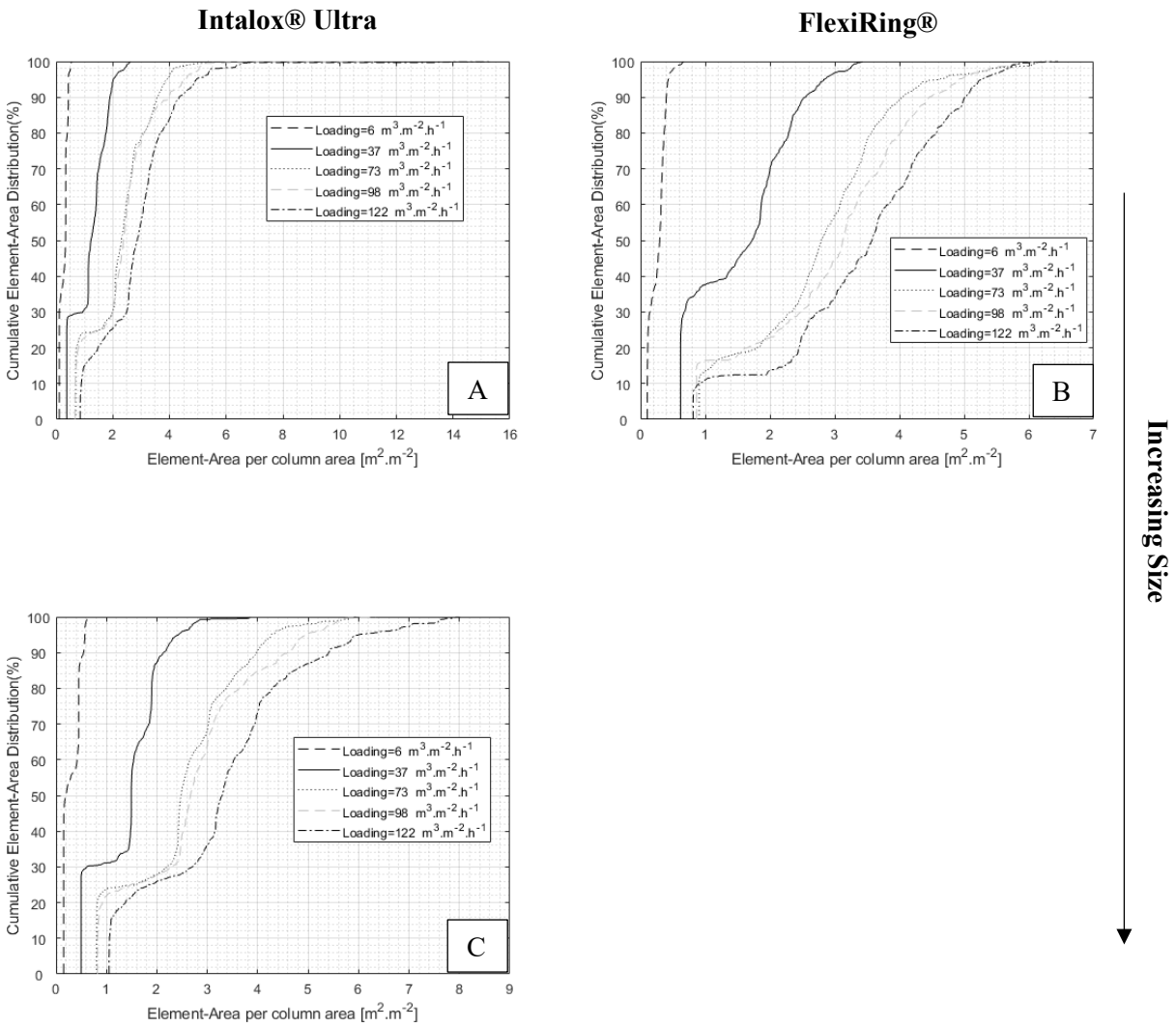

Figure 14.31: Cumulative IPL element-surface area distributions using air / ethylene glycol at zero vapour loading; A) Intalox® Ultra size L; B) 2" FlexiRing® ; C) Intalox® Ultra size O.

14.5.2.3. VAPOUR LOADING: AIR/WATER 2" FLEXIRING® AND INTALOX® ULTRA L

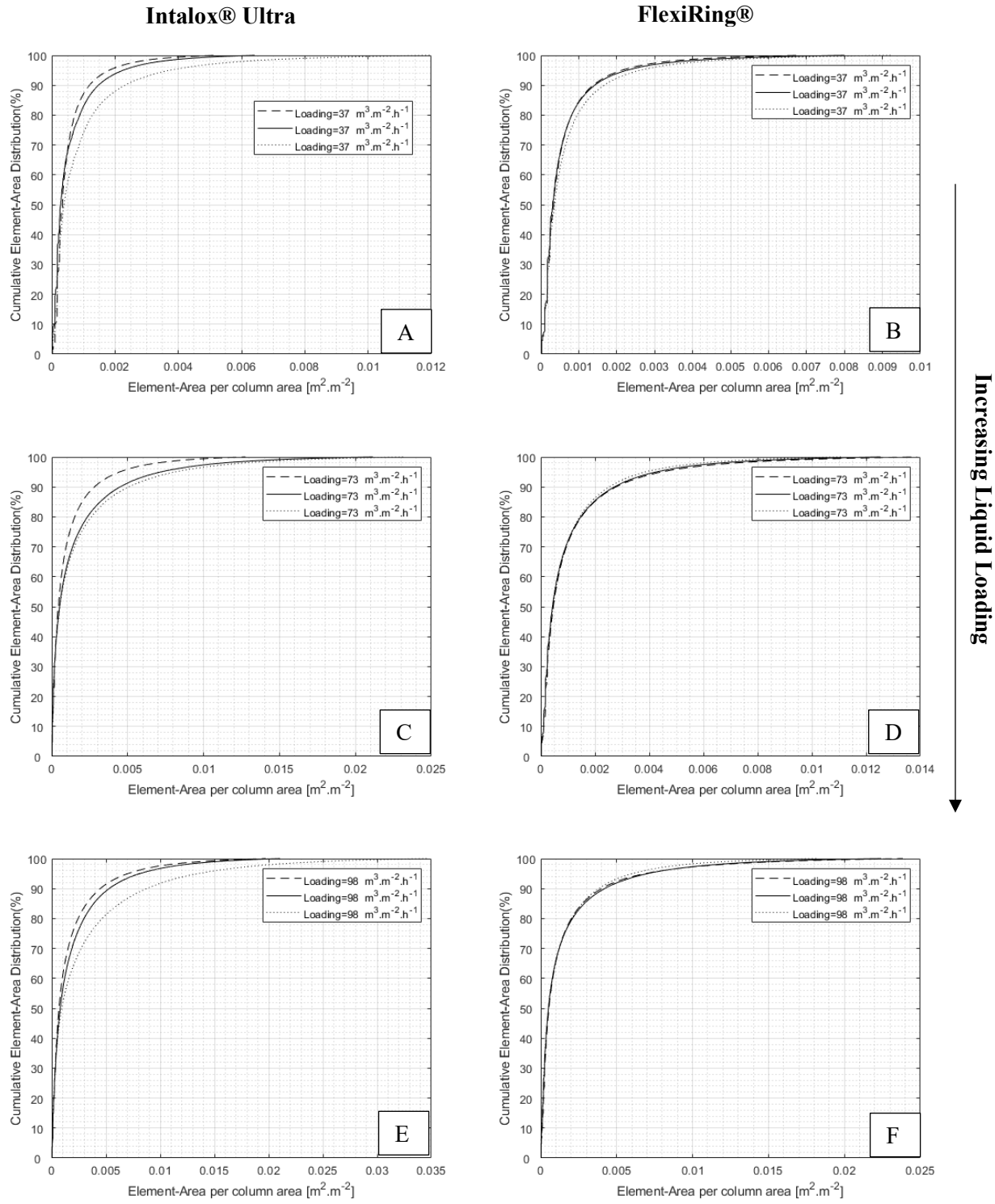

Figure 14.32: Cumulative IPL element-surface area distributions for air water; A) Intalox® Ultra size L @ 37 $m^3.m^{-2}.h^{-1}$; B) 2" FlexiRing® @ 37 $m^3.m^{-2}.h^{-1}$; C) Intalox® Ultra size L @ 73 $m^3.m^{-2}.h^{-1}$; D) 2" FlexiRing® @ 73 $m^3.m^{-2}.h^{-1}$; E) Intalox® Ultra size L @ 98 $m^3.m^{-2}.h^{-1}$; F) 2" FlexiRing® @ 98 $m^3.m^{-2}.h^{-1}$;

.

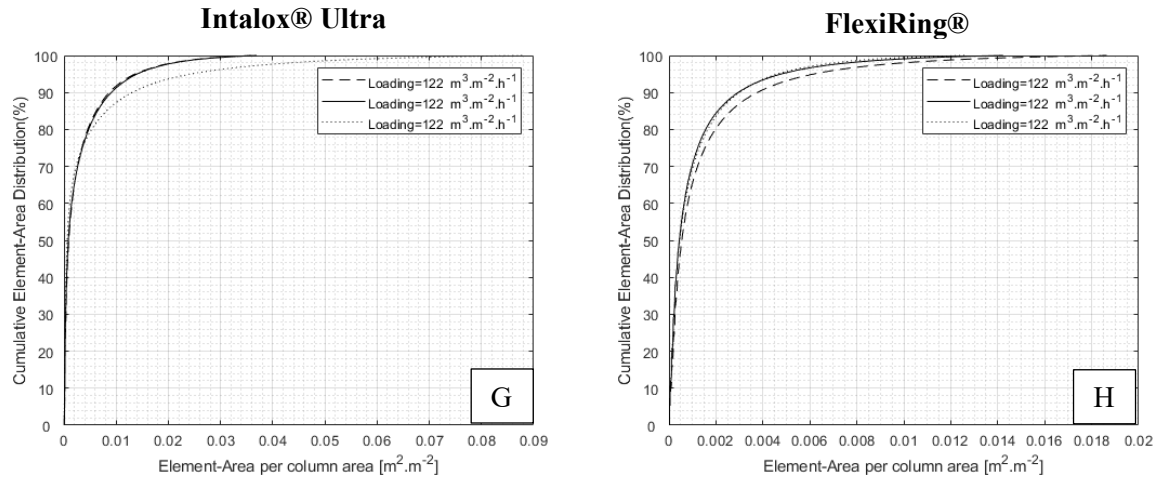

Figure 14.33: Figure 14.32 Continues; G) Intalox® Ultra size L @ 122 $m^3.m^{-2}.h^{-1}$; H) 2" FlexiRing® @ 122 $m^3.m^{-2}.h^{-1}$;

14.5.2.4. VAPOUR LOADING: AIR/WATER 1.5" FLEXIRING® AND INTALOX® ULTRA A

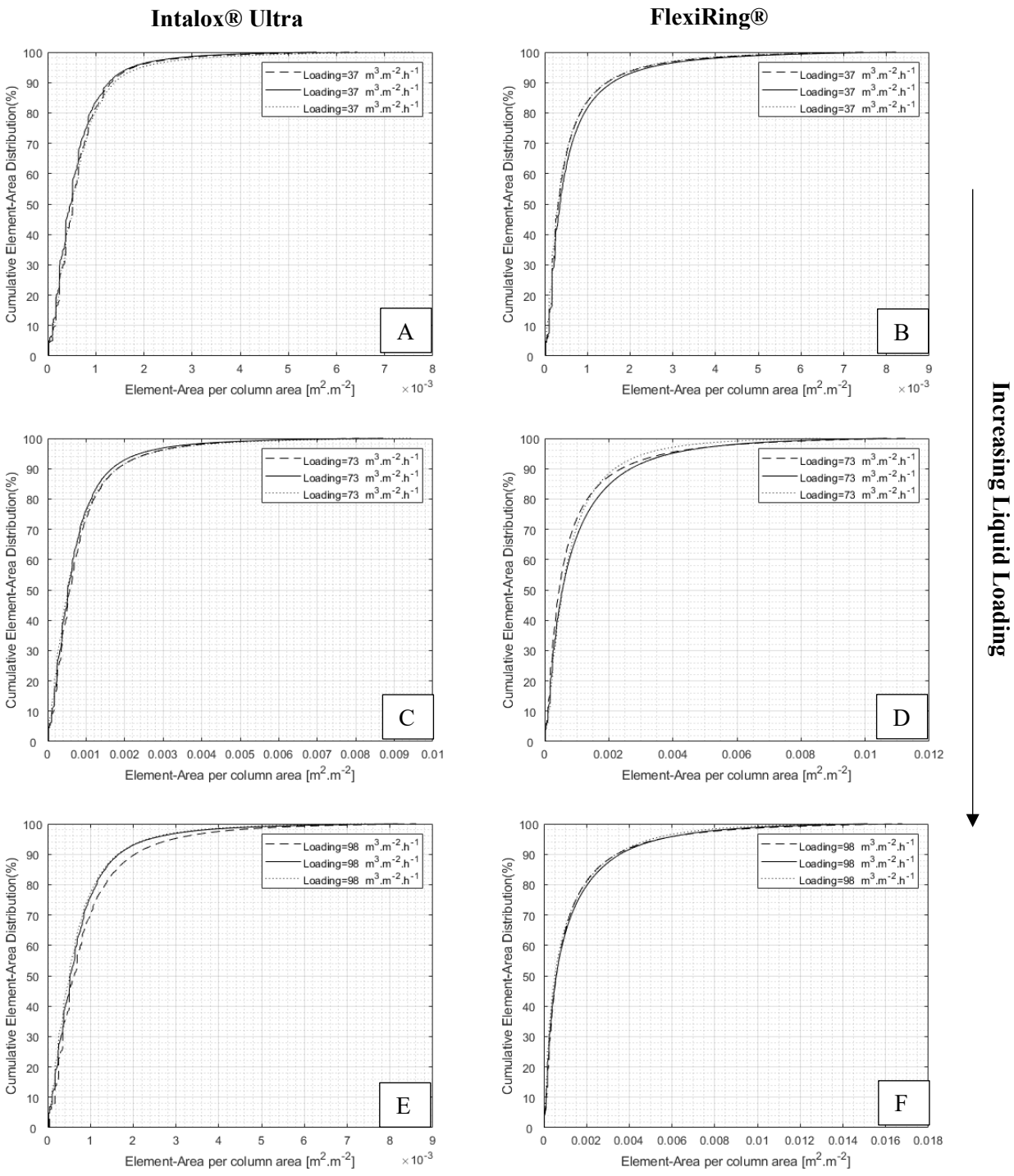

Figure 14.34: Cumulative IPL element-surface area distributions for air water; A) Intalox® Ultra size A @ 37 $m^3.m^{-2}.h^{-1}$; B) 1.5" FlexiRing® @ 37 $m^3.m^{-2}.h^{-1}$; C) Intalox® Ultra size A@ 73 $m^3.m^{-2}.h^{-1}$; D) 1.5" FlexiRing® @ 73 $m^3.m^{-2}.h^{-1}$; E) Intalox® Ultra size A@ 98 $m^3.m^{-2}.h^{-1}$; F) 1.5" FlexiRing® @ 98$m^3.m^{-2}.h^{-1}$;

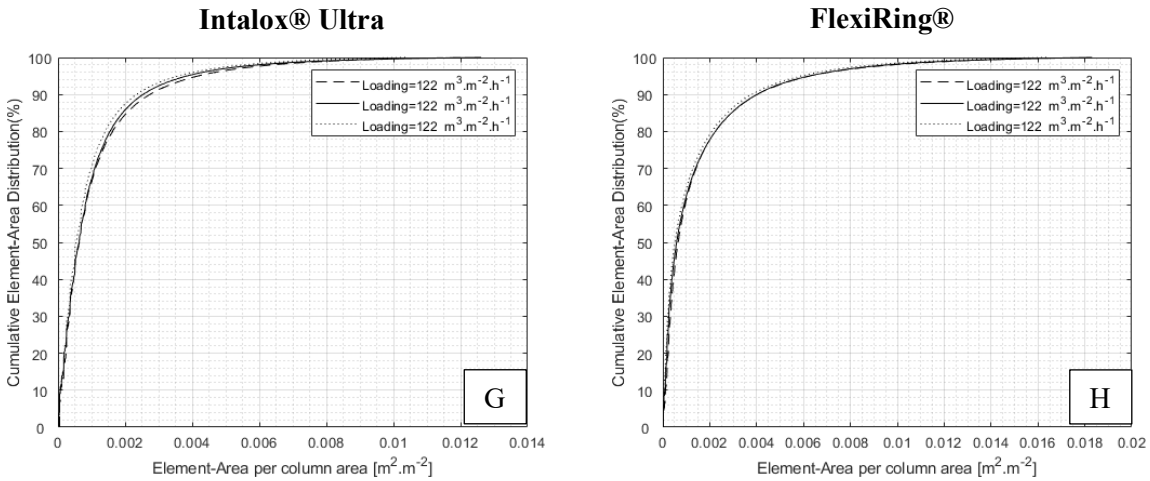

Figure 14.35: Figure 14.34 Continues; G) Intalox® Ultra size A @ 122 $m^3.m^{-2}.h^{-1}$; H) 1.5" FlexiRing® @ 122$m^3.m^{-2}.h^{-1}$.

14.5.2.5. VAPOUR LOADING: AIR/WATER INTALOX® ULTRA O

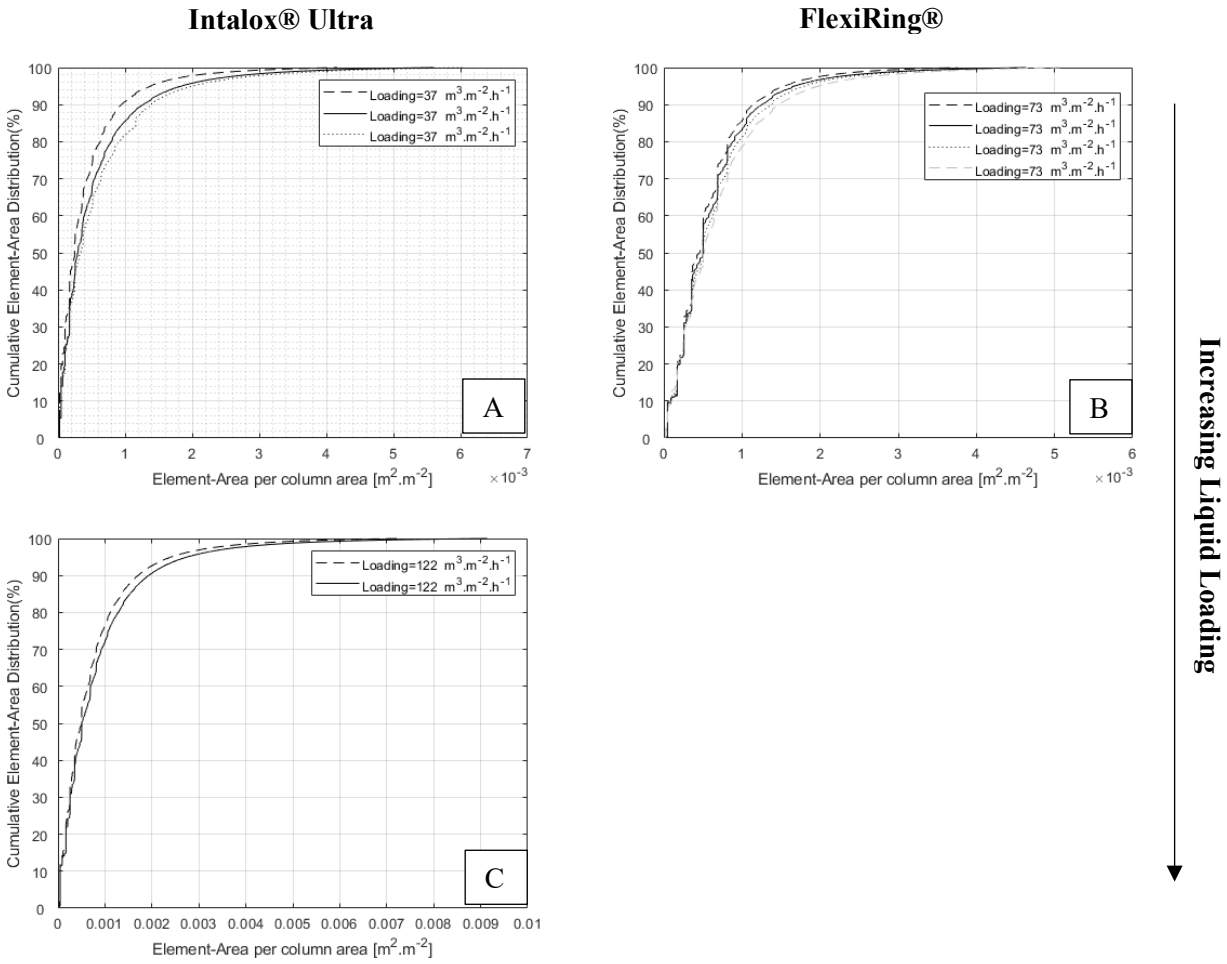

Figure 14.36: Cumulative IPL element-surface area distributions using air / water and Intalox® Ultra size O A) 37 $m^3.m^{-2}.h^{-1}$; B) 73 $m^3.m^{-2}.h^{-1}$; C) 122 $m^3.m^{-2}.h^{-1}$;

14.6 PROBABILITY DENSITY FUNCTIONS

14.6.1 ELEMENT VOLUME: WATER WITHOUT VAPOUR

14.6.1.11.5" FLEXIRING®

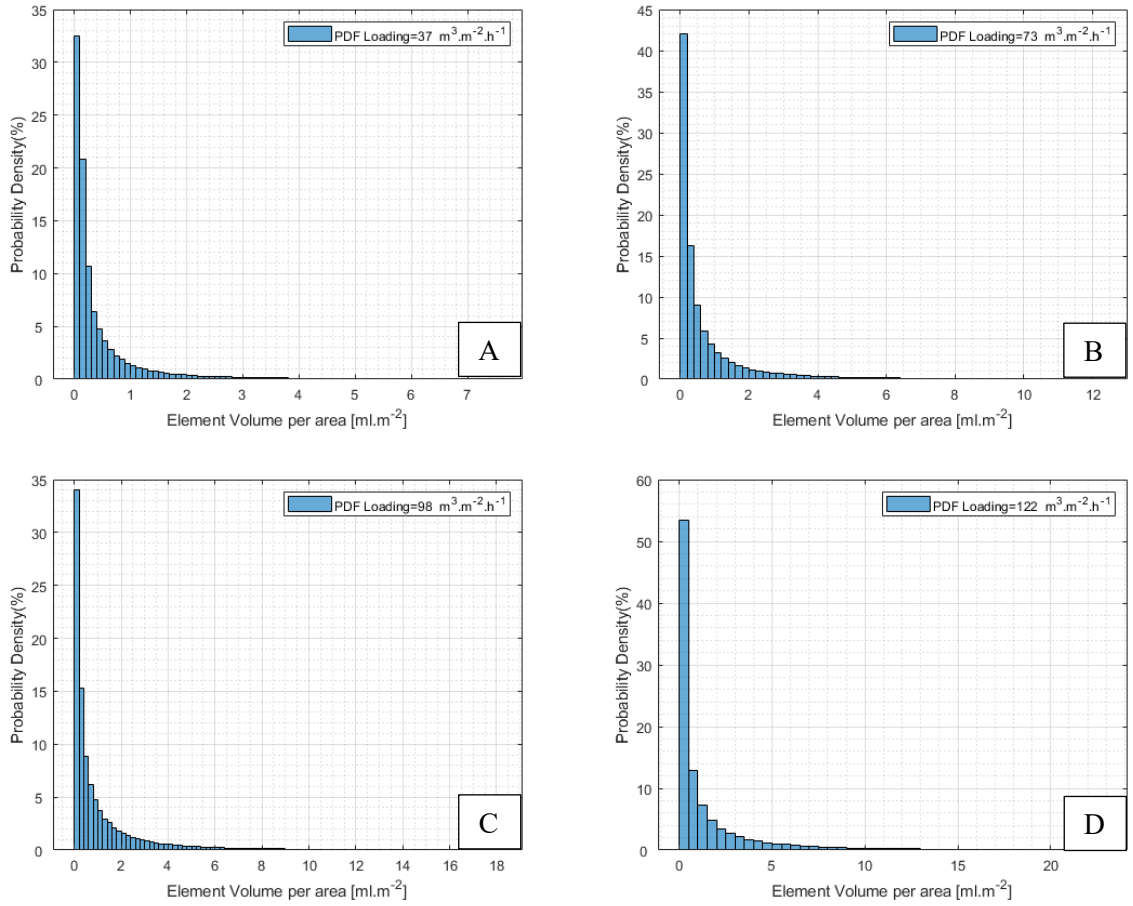

Figure 14.37 : Probability density function for the air / water system using 1.5" FlexiRing® A) 37 $m^3.m^{-2}.h^{-1}$; B) 73 $m^3.m^{-2}.h^{-1}$; C) 98 $m^3.m^{-2}.h^{-1}$; D) 122$m^3.m^{-2}.h^{-1}$;

14.6.1.21.5" INTALOX® ULTRA (A)

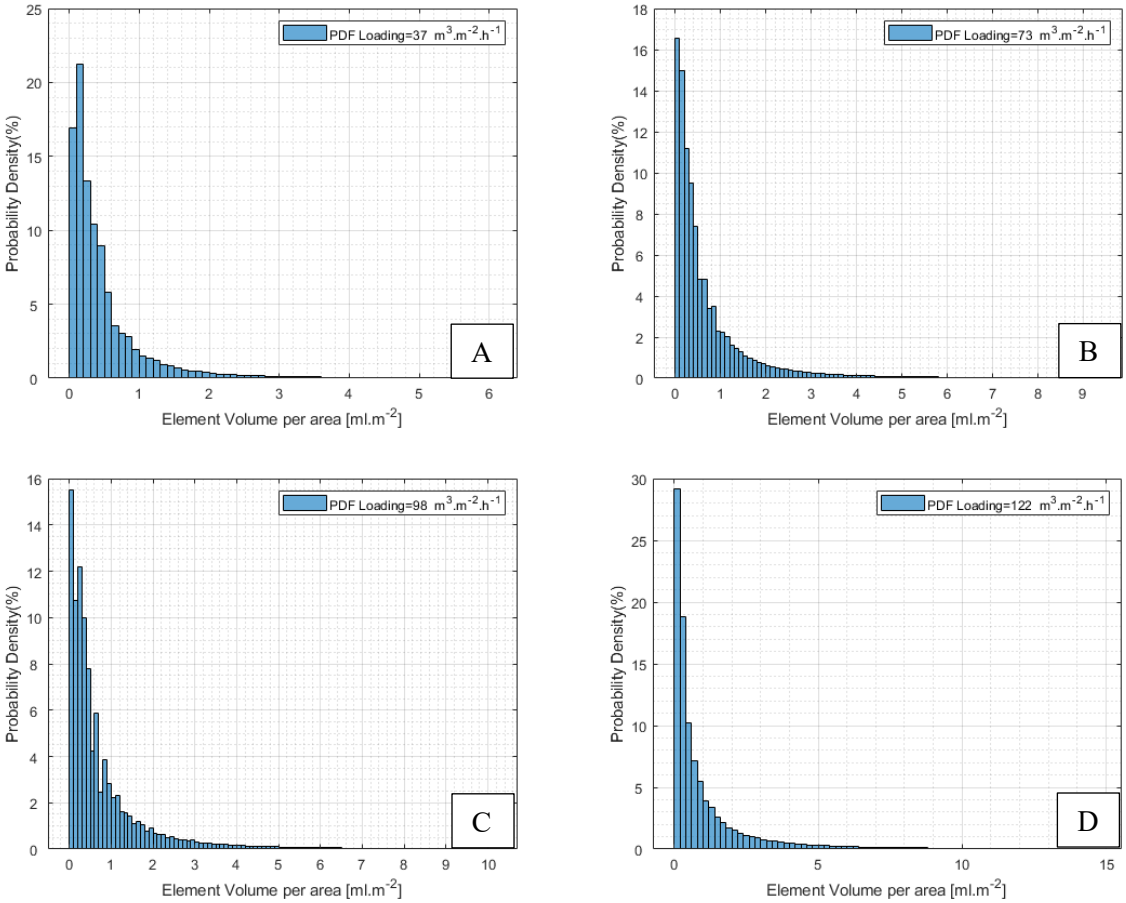

Figure 14.38: Probability density function for the air / water system using 1.5" Intalox® Ultra A) 37 $m^3.m^{-2}.h^{-1}$;B) 73 $m^3.m^{-2}.h^{-1}$;C) 98 $m^3.m^{-2}.h^{-1}$ D) 122$m^3.m^{-2}.h^{-1}$;

14.6.1.32" INTALOX® ULTRA (L)

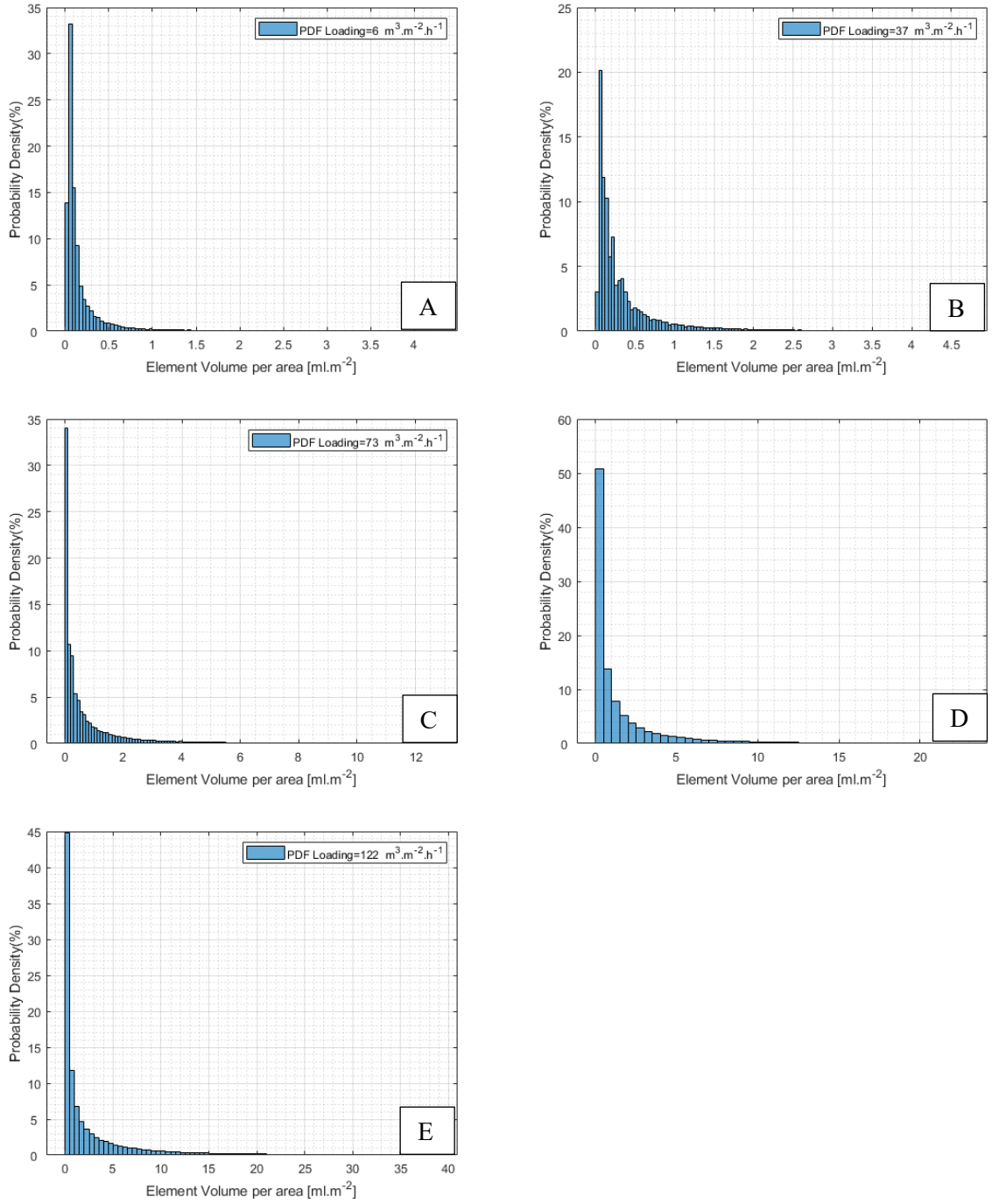

Figure 14.39 : Probability density function for the air / water system using 2" Intalox® Ultra; A) 6 $m^3.m^{-2}.h^{-1}$; B) 37 $m^3.m^{-2}.h^{-1}$;C) 73 $m^3.m^{-2}.h^{-1}$;D) 98 $m^3.m^{-2}.h^{-1}$ E) 122$m^3.m^{-2}.h^{-1}$;

14.6.1.42" FLEXIRING®

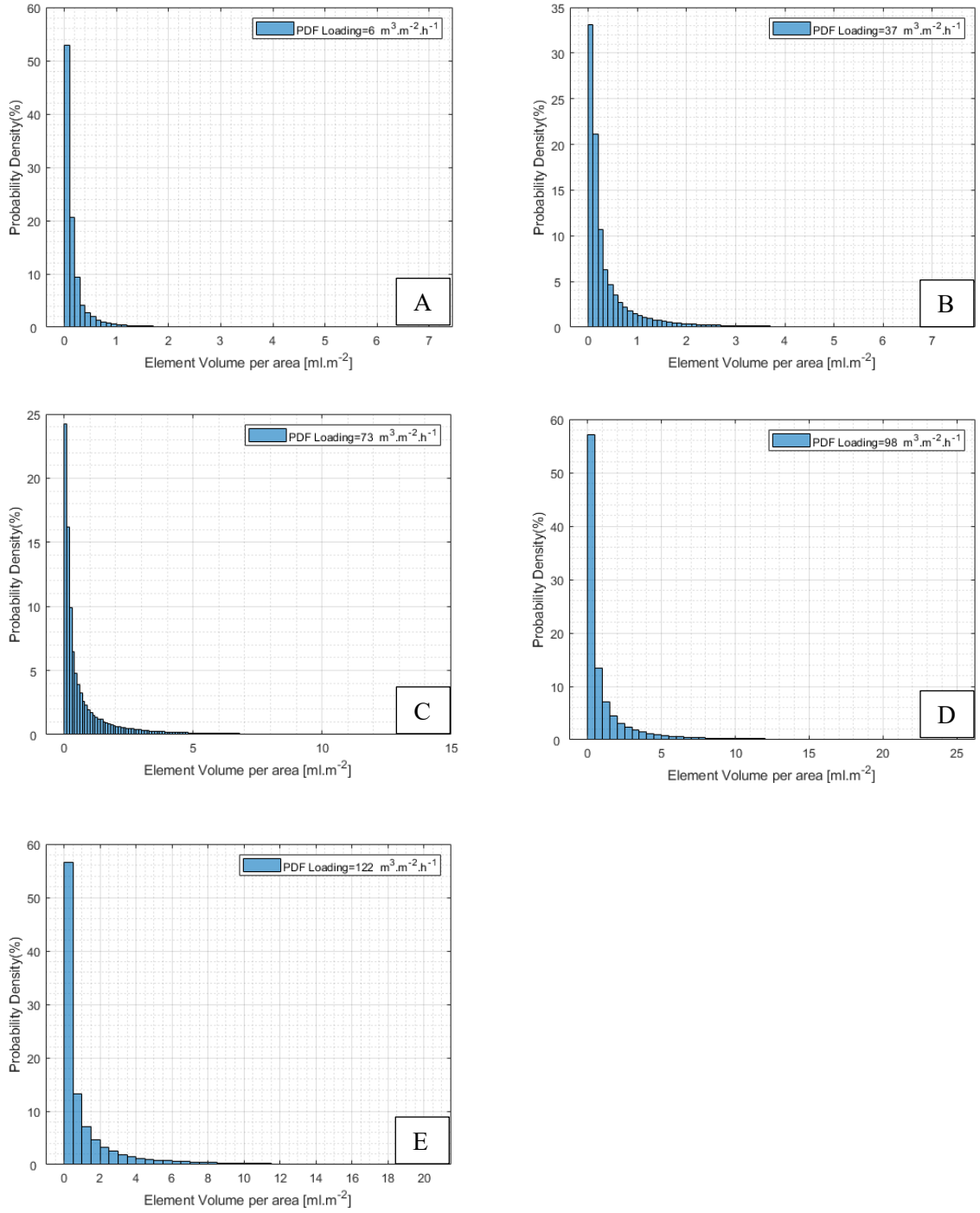

Figure 14.40: Probability density function for the air / water system using 2" FlexiRing® A) 6 $m^3.m^{-2}.h^{-1}$; B) 37 $m^3.m^{-2}.h^{-1}$;C) 73 $m^3.m^{-2}.h^{-1}$;D) 98 $m^3.m^{-2}.h^{-1}$ E) 122$m^3.m^{-2}.h^{-1}$;

14.6.1.52.5" INTALOX® ULTRA (O)

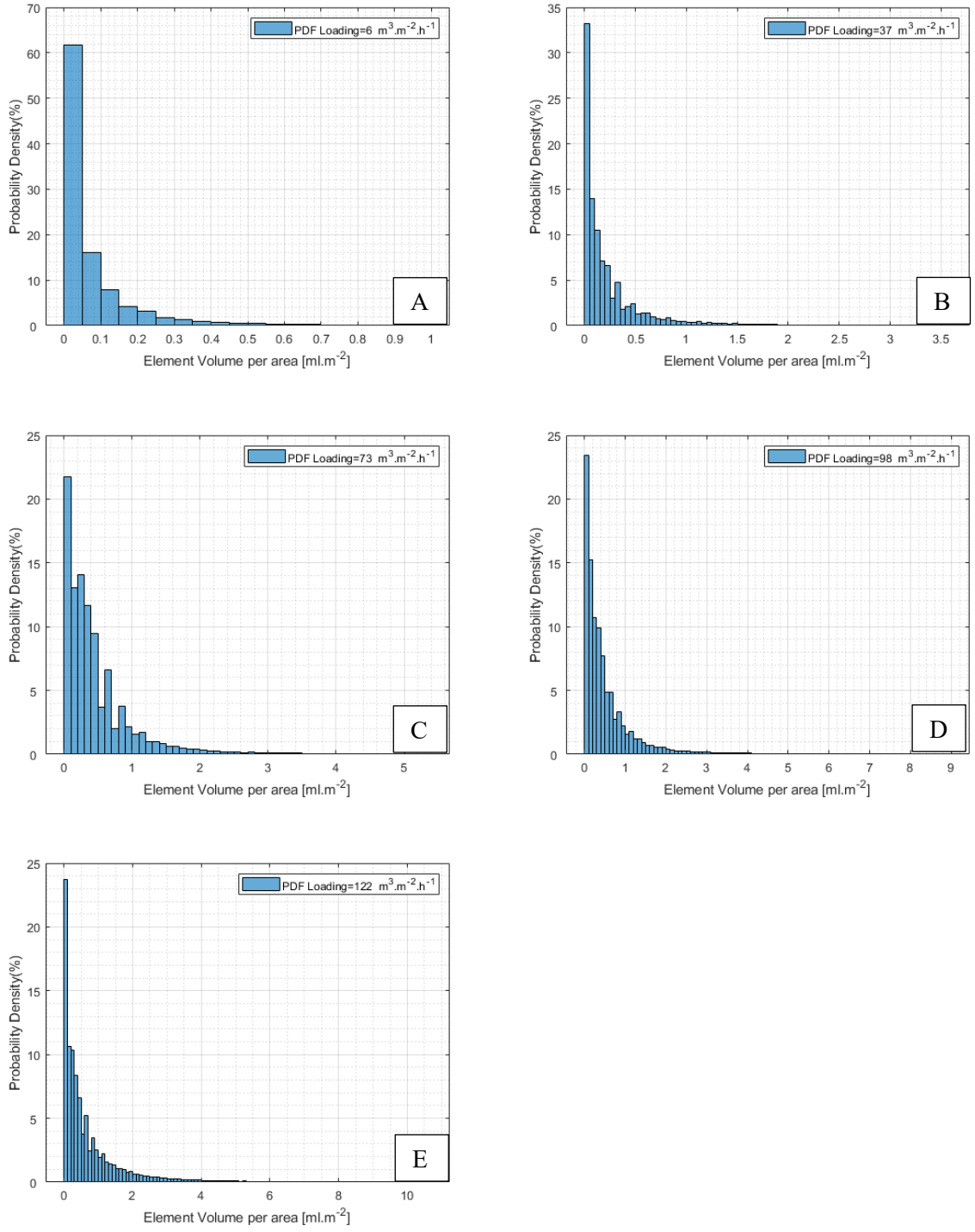

Figure 14.41: Probability density function for the air / water system using 2.5" Intalox® Ultra; A) 6 $m^3.m^{-2}.h^{-1}$; B) 37 $m^3.m^{-2}.h^{-1}$;C) 73 $m^3.m^{-2}.h^{-1}$;D) 98 $m^3.m^{-2}.h^{-1}$ E) 122$m^3.m^{-2}.h^{-1}$;

14.7 DISTRIBUTION ANALYSIS

The succeeding section evaluated the distribution behaviour of the packed column experimental setup from Lamprecht [2], with the liquid distributor from Minne [50]. The evaluation showed:

- Improved distribution with liquid loading. The more enclosed designed was adjudged to be more forgiving towards the distributor.
- That the either the column or liquid distributor may suffer from levelling issues. This stems from the liquid preferentially reporting to the right(graph) side of the column. The aforementioned requires evaluation.

14.7.1 WATER: 2" FLEXIRING®

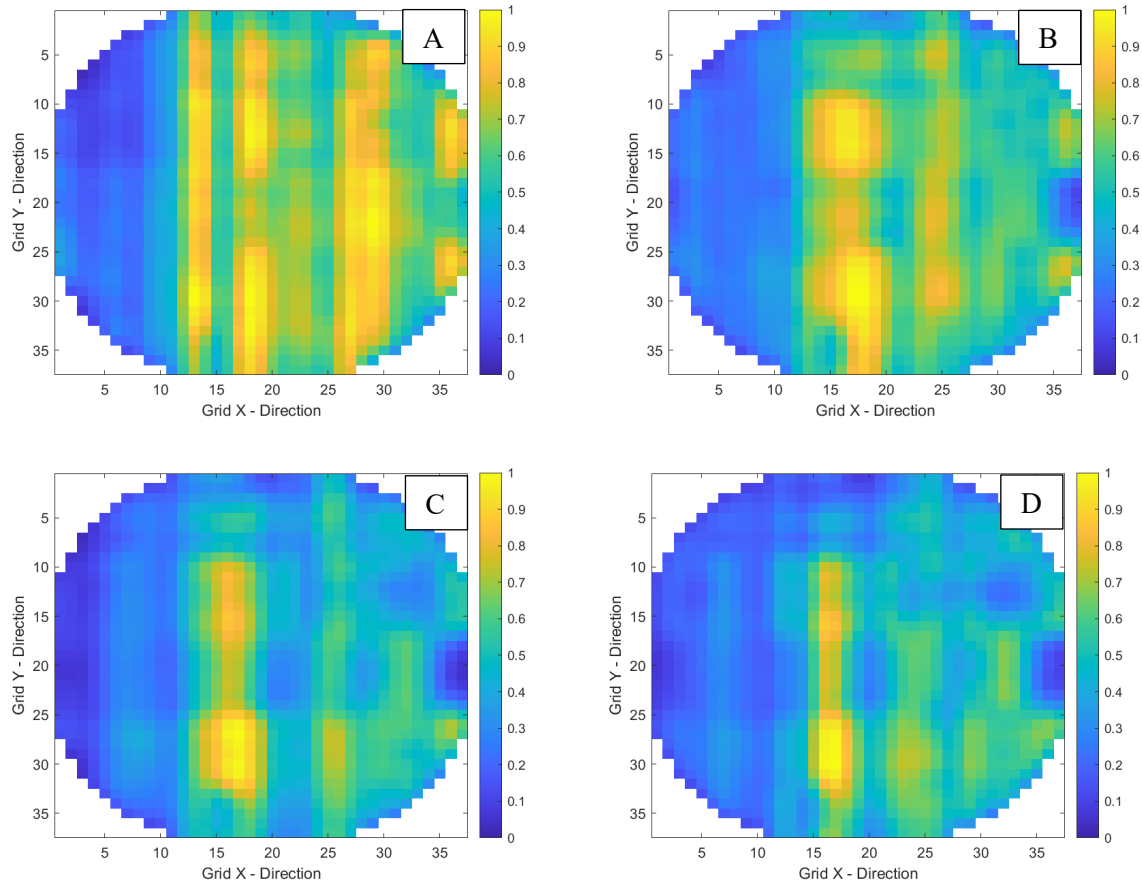

Figure 14.42 : 2" FlexiRing® distribution with water. A) 37 $m^3.m^{-2}.h^{-1}$; B) 73 $m^3.m^{-2}.h^{-1}$; C) 98 $m^3.m^{-2}.h^{-1}$; D) 122 $m^3.m^{-2}.h^{-1}$.

14.7.2 WATER: INTALOX® ULTRA L

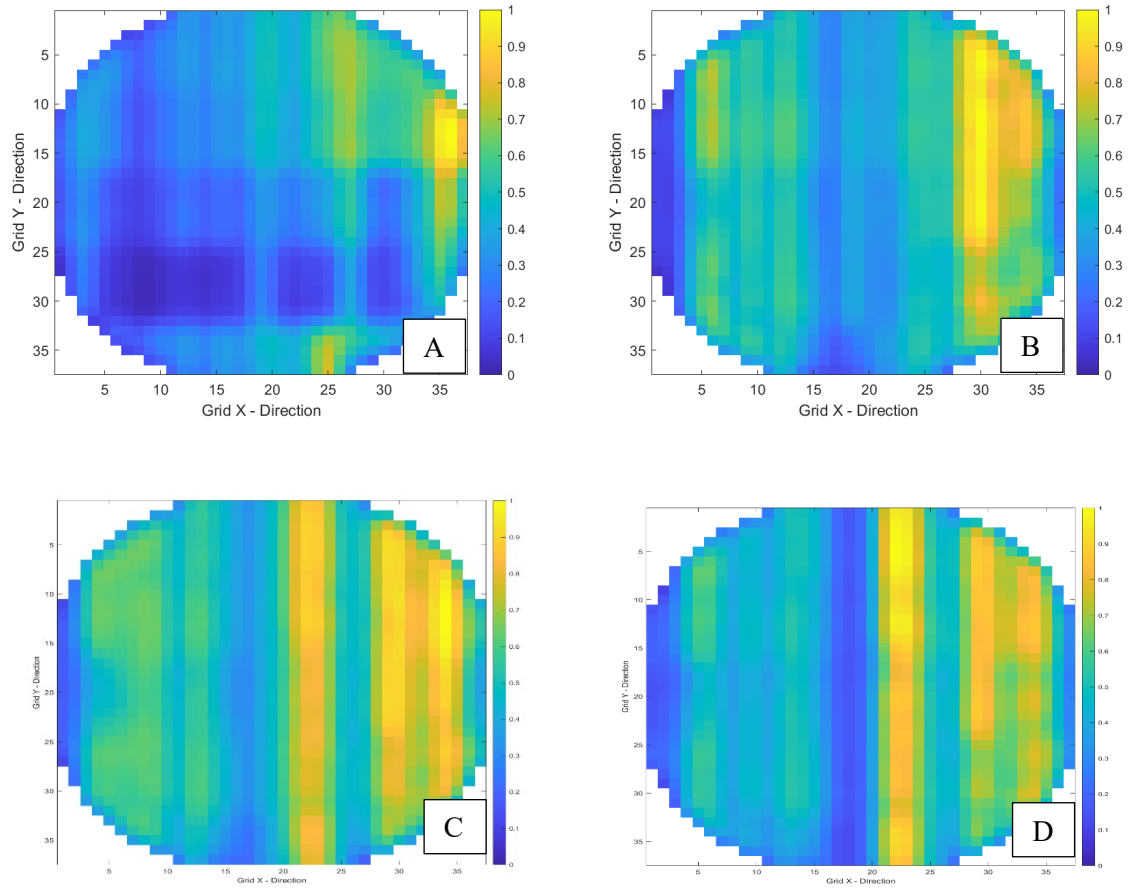

Figure 14.43: Intalox® Ultra L distribution with water. A) 37 $m^3.m^{-2}.h^{-1}$; B) 73 $m^3.m^{-2}.h^{-1}$; C) 98 $m^3.m^{-2}.h^{-1}$; D) 122 $m^3.m^{-2}.h^{-1}$.

14.7.3 WATER: INTALOX® ULTRA A

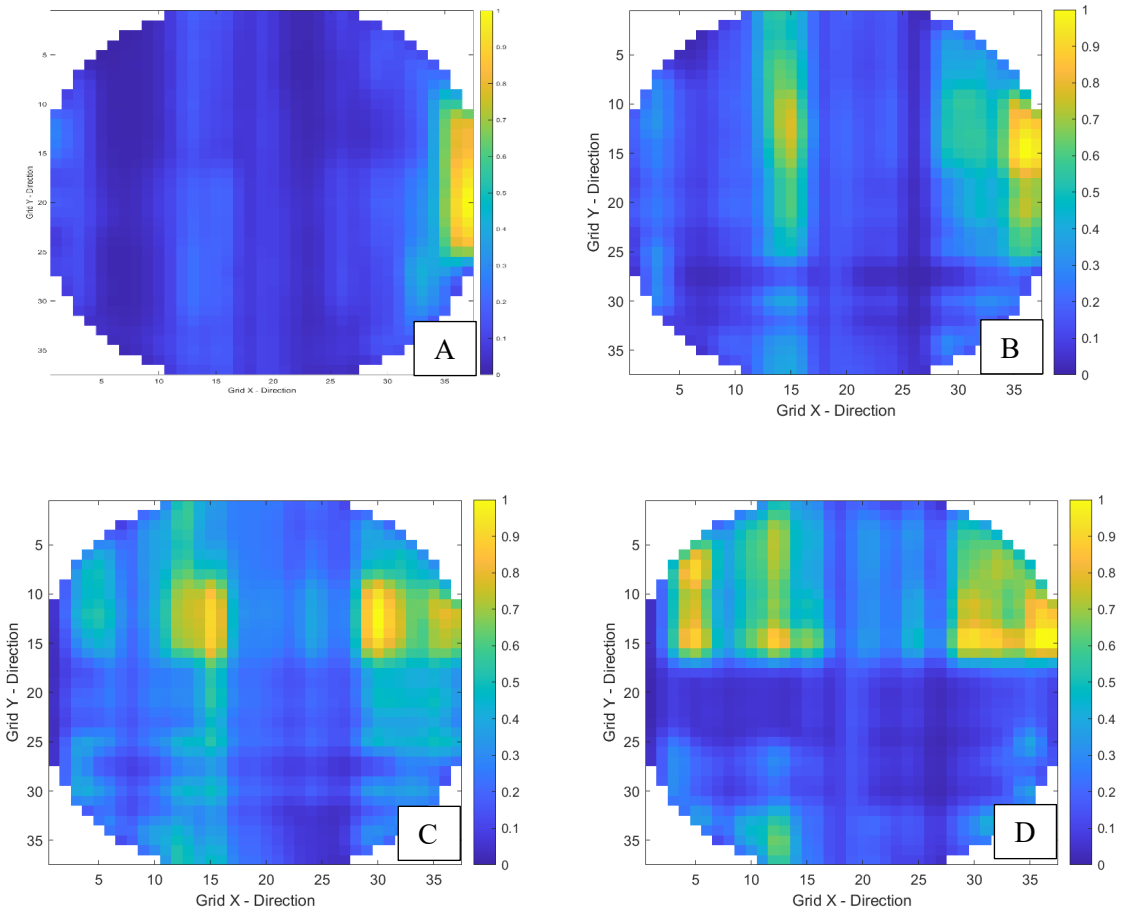

Figure 14.44: Intalox® Ultra A distribution with water. A) 37 $m^3.m^{-2}.h^{-1}$; B) 73 $m^3.m^{-2}.h^{-1}$; C) 98 $m^3.m^{-2}.h^{-1}$; D) 122 $m^3.m^{-2}.h^{-1}$.

14.7.4 WATER: 1.5" FLEXIRING®

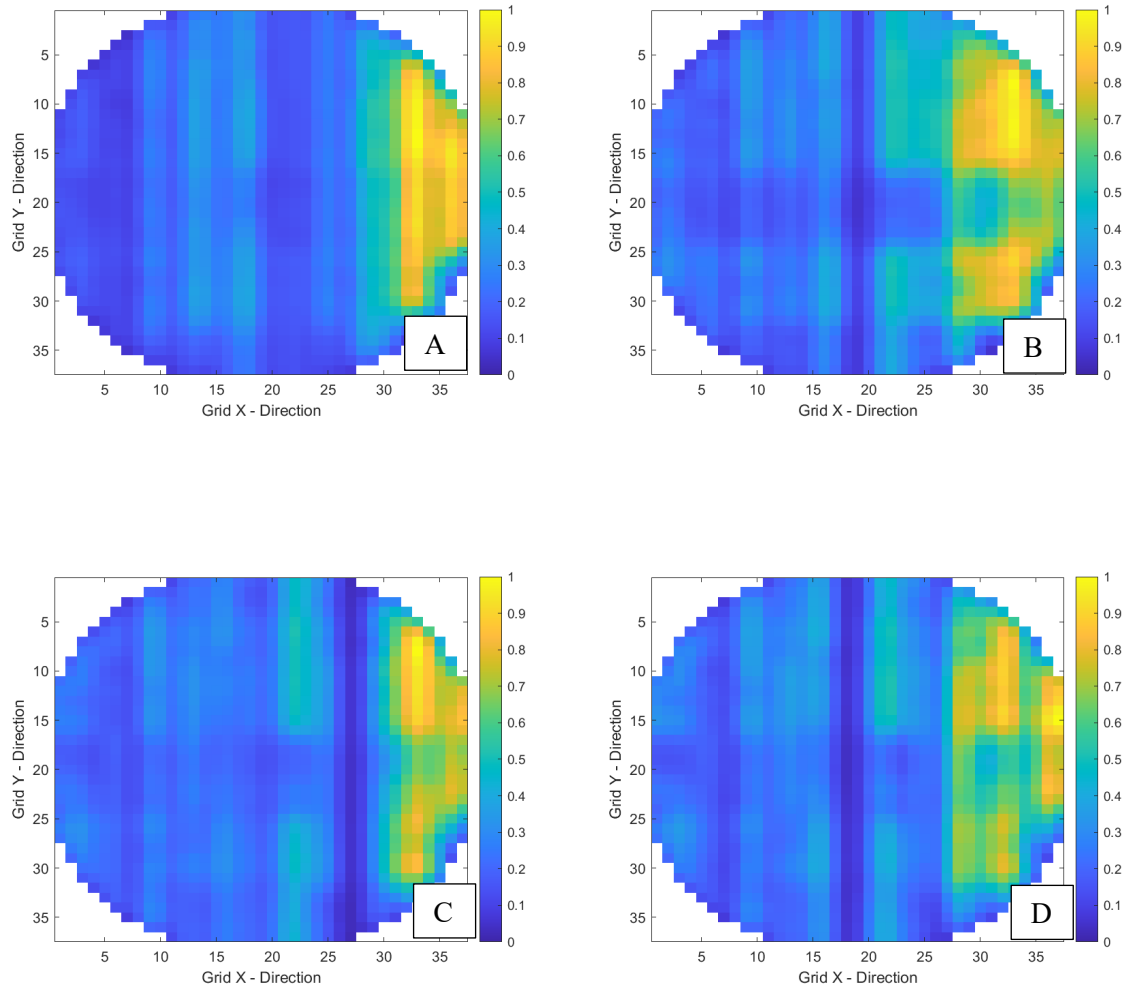

Figure 14.45: 1.5" FlexiRing® distribution with water. A) 37 $m^3.m^{-2}.h^{-1}$; B) 73 $m^3.m^{-2}.h^{-1}$; C) 98 $m^3.m^{-2}.h^{-1}$; D) 122 $m^3.m^{-2}.h^{-1}$.

14.8 APPENDIX E: THREE-DIMENSIONAL INTERACTIVE PROJECTIONS

This section presents interactive three-dimensional models of the experimental setup, and is intended for electronic copies only. The reader is advised to allow display of the 3D images (Right click, Enable display and trust this document).

Functions within the 3D space include:

- Pan/Rotation and zoom
- Make components transparent for better viewing angle of the internals
- Custom cross-sectionals
- Measurements using an interactive ruler.

14.8.1 LIQUID DISTRIBUTOR

14.8.2 FULL COLUMN

14.8.3 WIRE-MESH GRID

14.8.4 HOLDUP GRID

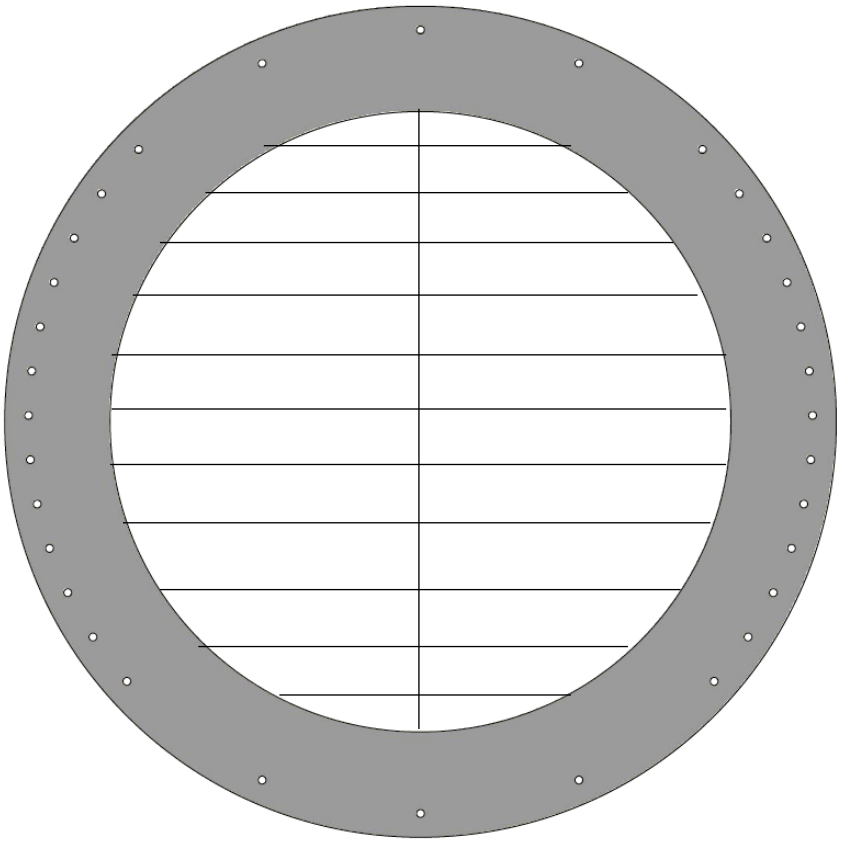

Vertical spacing = 30 mm